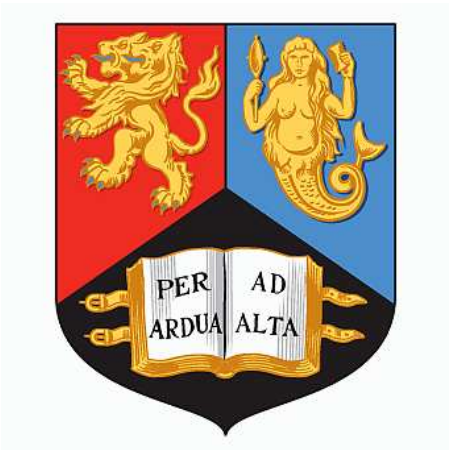
Searches for Rare and Flavour-Violating Exclusive Decays of the Higgs and Z Bosons with the ATLAS Experiment

Robert James Ward

Thesis submitted for the degree of

Doctor of Philosophy



Particle Physics Group,

School of Physics and Astronomy,

University of Birmingham.

8th June 2023

UNIVERSITY OF
BIRMINGHAM

University of Birmingham Research Archive

e-theses repository

This unpublished thesis/dissertation is copyright of the author and/or third parties. The intellectual property rights of the author or third parties in respect of this work are as defined by The Copyright Designs and Patents Act 1988 or as modified by any successor legislation.

Any use made of information contained in this thesis/dissertation must be in accordance with that legislation and must be properly acknowledged. Further distribution or reproduction in any format is prohibited without the permission of the copyright holder.

Abstract

The latest searches for the rare exclusive Higgs and Z boson decays to a vector quarkonium state and a photon in the $\mu^+\mu^-\gamma$ final state are presented. These searches probe the magnitude and the sign of the Higgs boson coupling to bottom- and charm-quarks using 139 fb^{-1} of ATLAS data collected at $\sqrt{s} = 13$ TeV. The observed data are compatible with the expected backgrounds and the 95% confidence level upper limits on the branching fractions of the Higgs boson decays into $J/\psi\,\gamma$, $\psi(2S)\,\gamma$, and $\Upsilon(1S, 2S, 3S)\,\gamma$ are found to be 2.0×10^{-4}, 10.5×10^{-4}, and $(2.5, 4.2, 3.4) \times 10^{-4}$, respectively, assuming Standard Model production of the Higgs boson. The corresponding 95% CL upper limits on the branching fractions of the Z boson decays are 1.2×10^{-6}, 2.4×10^{-6}, and $(1.1, 1.3, 2.4) \times 10^{-6}$. The sensitivities of the searches for the flavour-violating exclusive decays of the Higgs boson to $D^*\,\gamma$ and the Z boson decays to $D^0\,\gamma$ and $K_s\,\gamma$ are also presented. These searches probe potential flavour-violating couplings of the Higgs and Z bosons using 135 fb^{-1} of ATLAS data collected at $\sqrt{s} = 13$ TeV. The expected 95% CL upper limits on the branching fractions of each decay are $13.2^{+5.4}_{-3.7} \times 10^{-4}$ for $H \to D^*\,\gamma$, $3.0^{+1.2}_{-0.8} \times 10^{-6}$ for $Z \to D^0\,\gamma$, and $2.7^{+1.2}_{-0.7} \times 10^{-6}$ for $Z \to K_s\,\gamma$. In addition, a study of the feasibility to measure the track reconstruction efficiency of the ATLAS inner detector in dense environments, using boosted J/ψ and ϕ decays in the $\mu^+\mu^-$ final state, is presented. These environments are relevant in the exclusive Higgs and Z boson decays.

Acknowledgements

The more I came to think about the acknowledgements the more people I realised there are to thank. I originally started writing these about a week before the deadline, but I quickly found myself rambling for far too long. I now find myself here again in the final hour, as this is the last thing I need to do before I finally submit. I will try to keep the acknowledgements brief in the name of saving ink, disk space, and submitting on time, so apologies if I don't name you directly!

To get the ball rolling I'd like to start on the physics side of life. Kostas, your advice and supervision have been instrumental in getting me through this PhD, even if it is sometimes humbling. There have been many times along the way where I've gone a bit astray and you've set me straight back on the right path. My special thanks go to Rhys and Andy as well: Rhys, for instilling the importance of a good technical knowledge right from the very start, and Andy, for all of those many occasions where I stressed over something trivial but you stopped the presses anyway to help me out right away. I would also like to thank the full Birmigham Higgs group for all your support with my research over the years, the Birmingham gas lab group for giving me a much needed break from my ATLAS woes, and those of you in my PhD year who have humoured me throughout all of my unsolicited rants about pointless things. I'd also like to thank the University of Birmingham Welsh Society for the strong community you have given me throughout my time at the university. Helping to set this society up was one of the best decisions I have ever made. Of course there are many others of you that have helped me along the way that I've not had a chance to mention. After all, I've been at this university for 8 years now!

On the real life side of things I'd like to start by thanking all my friends back home, in particular Dylan, Adam, Matt, and Joe: our frequent conversations about anything and everything have kept me from falling too far into the PhD pit. I'd also like to thank my family for always being there, and in particular my immediate family, Mum, Dad, Michelle, Gareth, and you as well Geraint, as you basically are immediate family, let's

be honest. Gareth, your advice and experience throughout the years has been vital. Those extra five years you have on me are a great resource to help guide me on my way. Emmalene, thank you for putting up with me throughout this whole PhD experience, and the undergrad experience too for that matter, I don't know how I would have coped you weren't right there with me every day keeping me going.

Most importantly, and who could forget them, I would like to thank the European Research Council (ERC) who funded this project under the European Union's Horizon 2020 research and innovation programme under grant agreement no 714893 (ExclusiveHiggs).

Declaration of Author's Contribution

This thesis represents the work that I have undertaken as part of the ATLAS experiment over the course of my post-graduate studies. The ATLAS Collaboration consists of many people, and much of the work presented here would not be possible without the work of others, especially those who implemented the triggers for the searches in this thesis and earlier iterations of the analysis frameworks, and those that have supervised my research along the way.

Chapter 1 is an introduction to the thesis. Chapter 2 covers a theoretical background of the Standard Model, the experimental status of the Higgs boson properties, and the motivation and status of the exclusive decay searches, each relevant to understand the content of the thesis. Chapter 3 describes the ATLAS experiment as a whole. These background chapters are written based on information from many sources, referenced throughout, that are not my own work. In particular Ref. [1], a textbook on particle physics, was used to write the description of the Standard Model. Chapter 4 discusses a performance study that I conducted as part of the clustering and tracking in dense environments (CTIDE) group. This work was the qualification task for me to gain ATLAS authorship and was a standalone study that I conducted in full. Chapter 5 discusses the completed searches for the rare exclusive decays of the Higgs and Z bosons to a quarkonium state and a photon. I have contributed in all aspects of this analysis as part of a small team, and I am a primary editor for the paper. Chapter 6 discusses the ongoing searches for several flavour-violating exclusive decays of the Higgs and Z bosons. For these I the primary developer, and I have adapted and upgraded the analytical tools from previous exclusive decays searches for use in these channels. Finally, Chapter 7 is a conclusion and summary of the studies presented in this thesis.

In addition to the work presented in this thesis, I helped with the implementation of the exclusive decay triggers for Run 3 and played a role in managing the Monte Carlo samples for both the CTIDE group and the Exclusive Higgs group.

Perfect is the enemy of perfectly adequate.

Contents

1 Introduction **8**

2 Theoretical Background and Experimental Status **10**
2.1 The Standard Model of Particle Physics 10
2.1.1 The Electromagnetic Force and Quantum Electrodynamics 11
2.1.2 The Strong Force and Quantum Chromodynamics 12
2.1.3 The Weak Force and Electroweak Unification 13
2.1.4 The Brout-Englert-Higgs Mechanism 15
2.1.5 Fermion Mass Generation 18
2.2 Properties of the Higgs Boson 18
2.2.1 Production and Decay at the Large Hadron Collider 19
2.2.2 Measurements at the Large Hadron Collider 21
2.3 Exclusive Decays of Massive Bosons to a Meson and a Photon 23
2.3.1 Higgs Boson Decays 24
2.3.2 Vector Boson Decays 27
2.3.3 Experimental Results 29

3 The ATLAS Experiment at the CERN Large Hadron Collider **32**
3.1 The Large Hadron Collider 32
3.1.1 Luminosity and Pile-up 34
3.2 The ATLAS Detector 37
3.2.1 Magnet System 39
3.2.2 Inner Detector 41
3.2.3 Electromagnetic Calorimeter 43
3.2.4 Hadronic Calorimeter 45
3.2.5 Muon Spectrometer 46
3.3 Data Acquisition and Physics Performance 48
3.3.1 Data Acquisition and Triggers 48
3.3.2 Tracks and Vertices 49
3.3.3 Photons and Electrons 50
3.3.4 Muons 52
3.4 Software and Simulation 54

4 Feasibility Study for a Data-Driven Measurement of Inner Detector Track Reconstruction Efficiency in Dense Environments **57**
4.1 Analytical Investigation of Charged Particle Separation 60
4.1.1 Bending of Charged Particles in the Magnetic Field 60
4.1.2 Separation between Charged Particle Pairs 62
4.2 Monte Carlo Estimate of Track Reconstruction Efficiency 63
4.2.1 Event Generation and Selection 65
4.2.2 Procedure and Results 66
4.3 Prototype Analysis using $J/\psi \to \mu^+\mu^-$ Decays 73
4.3.1 Event Selection and Categorisation 74
4.3.2 Signal Modelling 77
4.3.3 Background Modelling 80
4.3.4 Results 82
4.4 Feasibility of using $\phi \to \mu^+\mu^-$ Decays 86

4.5 Further Considerations for the Tag-and-Probe Method . . . 87
4.6 Outlook . . . 93

5 Searches for H and Z Boson Decays into a Vector Quarkonium State and a Photon 96
5.1 Event Selection . . . 99
5.1.1 Data Sample and Triggers . . . 99
5.1.2 Selection Requirements . . . 101
5.1.3 Event Categorisation . . . 103
5.2 Signal Modelling . . . 104
5.2.1 Event Generation and Simulation . . . 104
5.2.2 Signal Acceptance and Efficiency . . . 108
5.2.3 Signal Shape and Resolution . . . 113
5.2.4 Systematic Uncertainties . . . 117
5.3 Exclusive Background Modelling . . . 121
5.3.1 Event Generation and Simulation . . . 122
5.3.2 Analytical Shapes of $m_{\mu^+\mu^-\gamma}$ and $m_{\mu^+\mu^-}$ . . . 123
5.3.3 Systematic Uncertainties . . . 126
5.4 Inclusive Background Modelling . . . 127
5.4.1 Generation and Validation Region Selection Criteria . . . 130
5.4.2 Non-Parametric Data-Driven Method for $m_{\mu^+\mu^-\gamma}$ . . . 131
5.4.3 Analytical Shape of $m_{\mu^+\mu^-}$ . . . 139
5.4.4 Systematic Uncertainties . . . 141
5.5 Statistical Procedure and Results . . . 144
5.5.1 Construction of the Likelihood Function . . . 144
5.5.2 Observed Significances and Upper Limits . . . 148
5.5.3 Interpretation in κ Framework . . . 153

6 Searches for Flavour-Violating H and Z Boson Decays with a Displaced Vertex: $H \to D^*\gamma$, $Z \to D^0\gamma$, and $Z \to K_s\gamma$ 158
6.1 Event Selection . . . 160
6.1.1 Data Sample and Triggers . . . 160
6.1.2 Selection Requirements . . . 162
6.2 Signal Modelling . . . 163
6.2.1 Event Generation and Simulation . . . 164
6.2.2 Signal Acceptance and Efficiency . . . 166
6.2.3 Signal Shape and Resolution . . . 167
6.3 Background Modelling . . . 167
6.3.1 Generation and Validation Region Selection Criteria . . . 171
6.3.2 Non-Parametric Data-Driven Method . . . 171
6.3.3 Systematic Uncertainties . . . 175
6.4 Statistical Procedure and Results . . . 177
6.4.1 Construction of the Likelihood Function . . . 177
6.4.2 Expected Sensitivity . . . 179

7 Conclusion 181

1 Introduction

The Higgs boson, H, is responsible for the mass generation of particles in the Standard Model (SM), and it continues to be a core topic in particle physics since its discovery in 2012 [2, 3] by the ATLAS [4] and CMS [5] experiments. This landmark discovery was made possible by the high-energy proton–proton collisions produced at the Large Hadron Collider (LHC) [6] at CERN. So far, all measurements of the Higgs boson are consistent with predictions by the SM [7, 8], but many of its couplings are not yet established, and although the SM is the most complete theory embodying our current understanding of fundamental particles and forces, it leaves many questions unanswered such as the role of gravity, the heirarchy problem and the origin of dark matter. A large experimental effort at the LHC is dedicated to understanding the properties of the Higgs boson and performing precision tests of the SM.

The ATLAS experiment covers a wide range of searches of exclusive Higgs boson decays to a meson and a photon, which offer an alternative probe of the Higgs boson couplings to quarks. Similarly, searches for exclusive decays of the Z and $W^{\pm}$ bosons of the weak force to a meson and a photon provide a window into a unique set of QCD measurements due to their large masses. The exclusive decays form dense environments in the detector. It is important to evaluate the performance of the ATLAS detector in these conditions to fully understand the physics searches. This thesis discusses searches for several exclusive Higgs and Z boson decays to a meson and a photon at the ATLAS experiment and an investigation of the performance of the ATLAS inner detector in dense environments relevant in the exclusive decays, as well as the necessary background to understand each of these studies.

The SM and the experimental status of the Higgs boson are discussed in Chapter 2, as well as an overview of the searches for rare and flavour-violating exclusive decays. This is followed by a description of the ATLAS experiment in Chapter 3. Chapter 4 covers a performance study investigating the feasibility to measure the ATLAS inner detector di-track reconstruction efficiency in dense environments using a data-driven approach. These

environments are relevant for the exclusive decays of the H and Z bosons discussed in this thesis. The latest searches for the rare Higgs and Z boson decays to a quarkonium state and a photon are presented in Chapter 5, where the quarkonium states include the charmonium $J/\psi, \psi(2S)$ states, and bottomonium $\Upsilon(1S, 2S, 3S)$ states. These decay channels have sensitivity to the Higgs boson c- and b-quark Yukawa couplings. The expected sensitivities of the searches for flavour-violating decays of Higgs and Z bosons to a flavoured meson and a photon are discussed in Chapter 6, including $H \to D^* \gamma$, $Z \to D^0 \gamma$, and $Z \to K_s \gamma$. These decay channels each involve a displaced vertex and have sensitivity to potential flavour-violating couplings of the Higgs and Z bosons. A summary of the studies presented in this thesis is discussed in Chapter 7.

2 Theoretical Background and Experimental Status

The study of high energy physics using particle colliders aims to improve our understanding of the fundamental particles and forces in our universe. This chapter gives an overview of the theoretical background and experimental status relevant to the studies presented in this thesis. The SM is described in Section 2.1 and the expected properties of the SM Higgs boson are described in Section 2.2 along with the experimental status of the investigation of the properties of the observed Higgs boson. Section 2.3 describes the motivation and current experimental status of the study of the exclusive decay modes of the Higgs and vector bosons to a meson and a photon.

2.1 The Standard Model of Particle Physics

The Standard Model (SM) of particle physics is the combination of several theories to provide the most complete description of the fundamental particles of the universe and their interactions, excluding gravity [9–12]. The SM is a quantum field theory (QFT) with a symmetry under locally gauge invariant transformations of the $\mathrm{SU}(3)_C \times \mathrm{SU}(2)_L \times \mathrm{U}(1)_Y$ gauge group. The $\mathrm{SU}(3)_C$ group describes the strong interaction whilst the $\mathrm{SU}(2)_L \times \mathrm{U}(1)_Y$ group describes the electroweak interaction, which is the unification of the electromagnetic and weak forces. In the SM, matter consists of fermions which have a spin of $\frac{1}{2}$ and obey Fermi-Dirac statistics and the Pauli Exclusion Principle, which states that no two fermions can share the same quantum numbers. These are split into three generations which differ in mass, and complementary to each fermion is its associated anti-fermion. These have the same mass as their fermion counterparts but opposite quantum numbers, such as charge. The fundamental forces are mediated by the gauge bosons which have a spin of 1 and obey Bose-Einstein statistics. The particles of the SM and their properties are summarised in Figure 2.1. The final piece to the Standard Model is the Higgs boson, a spin-0 scalar boson proposed to explain the origin of mass of the $W^{\pm}$ and Z bosons [13–18]. This section describes each of the three fundamental forces included in the SM, and the completion of the model by the introduction of the Brout-Englert-Higgs mechanism

to provide the intermediate vector bosons and the fermions with mass.

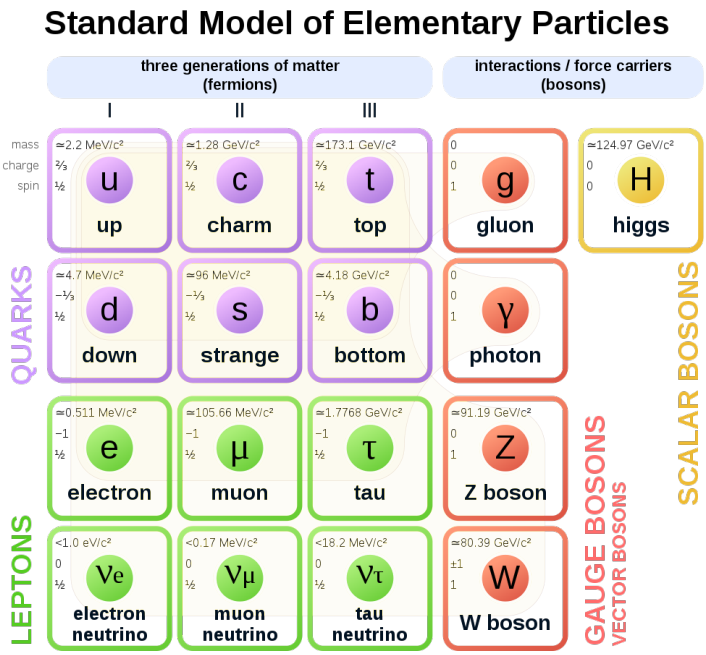


Figure 2.1: Elementary particles of the Standard Model and their properties [19].

2.1.1 The Electromagnetic Force and Quantum Electrodynamics

Charged fermions experience the electromagnetic (EM) force, which is carried by the photon, γ, and is a symmetry based on the conservation of electric charge. Electric charge is one-dimensional and can either be positive (+) or negative (-). The EM force is responsible for keeping negatively charged electrons bound to positively charged nuclei in atoms, and an example of an EM interaction is γ-decay, the emission of a photon from an excited nucleus, $N^* \rightarrow N + \gamma$.

The QFT describing the EM force is the most simple of the SM, and is called quantum electrodynamics (QED). At low energies it is described by the $\mathrm{U}(1)_{\mathrm{EM}}$ gauge group which is embodied in the unified electroweak $\mathrm{SU}(2)_L \times \mathrm{U}(1)_Y$ part of the SM. This is an Abelian group in that the generators of the group commute. This results in the photon being electrically neutral, and so photons do not interact with each other.

2.1.2 The Strong Force and Quantum Chromodynamics

Quarks experience the strong force, which is propagated by the gluon, g, and can be understood by the introduction of colour charge, which is exchanged in the interaction. Colour charge is analagous to the electric charge of QED, but rather than two possible values (+, -), colour charge has six possible values split across three colours. These are red $(R, \bar{R})$, green $(G, \bar{G})$, and blue $(B, \bar{B})$, where a bar over the symbol denotes the equivalent anti-colour. Quarks carry colour, whereas leptons are colour-neutral. Quarks have colour (q_R, q_G, q_B) and anti-quarks are have anti-colour $(\bar{q}_{\bar{R}}, \bar{q}_{\bar{G}}, \bar{q}_{\bar{B}})$. The strong force is responsible for the binding of protons and neutrons in atomic nuclei; it is significantly stronger than the EM force and overpowers the EM repulsion between the positively charged protons. An example of a strong interaction is α-decay, the emission of a Helium nucleus ($^4_2$He), consisting of two protons and two neutrons, from an unstable nucleus such as Uranium-238 ($^{238}_{92}$U) in its decay to Thorium-234, ($^{234}_{90}$Th), $^{238}_{92}\mathrm{U} \rightarrow ^{234}_{90}\mathrm{Th} + ^4_2\mathrm{He}$.

The QFT describing the strong force is called quantum chromodynamics (QCD), which is described by the $\mathrm{SU}(3)_C$ gauge group of the SM. Unlike QED, this is a non-Abelian group where the group generators do not commute. This has the result that the carriers of the strong force, the 8 gluons, carry colour charge and interact with each other. A consequence of gluon self-interaction is the phenomenon of colour confinement, where quarks are confined to bound colourless states and cannot be observed in isolation. In QED the potential energy stored in the EM field between electrically charged particles decreases with distance as $1/r$, such that the EM force decreases with particle separation as $1/r^2$. However, in QCD the field lines between two quarks are squeezed into a tube because the interactions between the gluons which carry the force are attractive. The potential energy stored in this field is proportional to the distance r between the quarks, and the strong force between them is constant regardless of distance. It would take an infinite amount of energy to separate two quarks to infinity, and therefore at large distances it becomes energetically favourable to form a new quark-antiquark pair and create two colourless states instead of increasing the length of the tube further. In this situation the two initial quarks are once again bound to colour-neutral states, and the

colour field betwen the two initial quarks is removed. A result of colour confinement is that all observable particles are colour-neutral, meaning that total colour charge of their constituents sum to zero. These composite colour-neutral particles are known as hadrons, and are formed in a process known as hadronisation. As gluons carry colour they must also only exist in bound colour-neutral states and cannot carry the strong force over macroscopic distances.

There are two common arrangements to achieve neutral colour in a hadron. The first arrangement is a quark anti-quark pair of opposite colour charge ($q_R\bar{q}_{\bar{R}}, q_G\bar{q}_{\bar{G}}, q_B\bar{q}_{\bar{B}}$). Particles of this type are called mesons and an example is the pion family, responsible for the strong nuclear interaction which binds nuclei together. The quark content of the π^+ and π^- mesons are of $(u\bar{d})$ and $(d\bar{u})$, respectively. The second arrangement is a triple quark or anti-quark combination, (q_R, q_G, q_B) or $(\bar{q}_{\bar{R}}, \bar{q}_{\bar{G}}, \bar{q}_{\bar{B}})$ respectively. Particles of this type are known collectively as baryons, and include protons (uud) and neutrons (udd) contained in atomic nuclei. Further arrangements are also possible such as tetraquarks and pentaquarks, each of which have been observed by the LHCb Collaboration [20, 21]. These contain a colour-neutral arrangement of four and five quarks respectively. The majority of the mass of hadronic particles originates from the binding energy of the strong force, rather than the mass of the constituent quarks.

2.1.3 The Weak Force and Electroweak Unification

Every fermion experiences the weak force, which is carried by the $W^{\pm}$ and Z^0 bosons. An example of a weak interaction is β-decay, the emission of an electron and a neutrino from an unstable nucleus, converting a constituent neutron into a proton, $n \rightarrow p + e^- + \bar{\nu_e}$. This is an example of the weak charged-current interaction, which violates quark flavour conservation. The weak charged-current interaction is the only force in the SM capable of changing the flavour of a quark. In the case of β-decay a d-quark in the neutron changes flavour to a u-quark, forming the proton. The W^- boson which carries the interaction subsequently decays to e^- and ν_e. The weak charged-current is also able to change quark flavour across fermion generations, which is vital in particle decay where

typically unstable heavy generations of fermion decay into the lighter, more stable lighter generations.

In the 1960s, Glashow Weinberg and Salam proposed that the weak force and the EM force are both manifestations of the same force, the electroweak force, which unify at high energy scales [9–11]. This lead to the prediction of the existence of the Z boson, which is responsible for weak neutral-current interactions that are analogous to the interactions of QED, except the Z boson is the carrier instead of the photon. Electroweak interactions are described by the $\mathrm{SU}(2)_L \times \mathrm{U}(1)_Y$ gauge group of transformations. Here, L in the $\mathrm{SU}(2)_L$ group refers to the left handed set of fermions; the weak force is chiral and only interacts with left-handed particles, which have a weak-isospin $I = 1/2$ whilst right-handed particles have a weak-isospin $I = 0$. As a result the weak charged-current also violates parity conservation. Like the $\mathrm{SU}(3)_C$ group of QCD, the $\mathrm{SU}(2)_L$ group is non-Abelian such that the carriers of the weak force interact with each other. The variable Y of the $\mathrm{U}(1)_Y$ group refers to the weak hypercharge, a quantum number that relates to the third component I_3 of weak-isospin as well as the electric charge Q, where

$$Q = I_3 + \frac{1}{2}Y.$$

Electric charge is conserved in electroweak interactions. Local gauge invariance in $\mathrm{SU}(2)_L \times \mathrm{U}(1)_Y$ transformations results in four gauge bosons: B for the $\mathrm{U}(1)_Y$ group and W_1, W_2 and W_3 for the $\mathrm{SU}(2)_L$ group. These gauge bosons mix to produce the physical gauge bosons $W^{\pm}, Z$ and γ, where

$$W^{\pm} = \frac{1}{\sqrt{2}}\left(W_1 \mp iW_2\right)$$

and

$$\begin{pmatrix} \gamma \\ Z \end{pmatrix} = \begin{pmatrix} \cos\theta_W & \sin\theta_W \\ -\sin\theta_W & \cos\theta_W \end{pmatrix} \begin{pmatrix} B \\ W_3 \end{pmatrix}.$$

The value θ_W is known as the weak mixing angle, which is an observable quantity. With EW theory alone, each of these bosons are predicted as massless. This is true of the photon, γ, but the $W^{\pm}$ and Z bosons have mass, confirmed by their discoveries by the UA1 and UA2 experiments [22–25] in the 1980s. The current world average measurements of these masses are $m_W = (80.379 \pm 0.012)$ GeV and $m_Z = (91.1876 \pm 0.0021)$ GeV, respectively [26].[1]

2.1.4 The Brout-Englert-Higgs Mechanism

To solve the issue of non-zero $W^{\pm}$ and Z mass, the Brout-Englert-Higgs (BEH) mechanism was proposed [13–18]. Simply adding mass terms for the three bosons into the SM Lagrangian would break the local gauge invariance of the $\mathrm{SU}(2)_L \times \mathrm{U}(1)_Y$ gauge group, which violates a key axiom of the SM as local gauge invariance is required for the theory to be renormalisable. To resolve this, the BEH mechanism introduces a new complex $\mathrm{SU}(2)_L$ doublet scalar field into the SM Lagrangian with a characteristic non-zero vacuum expectation value. This breaks the symmetry of the $\mathrm{SU}(2)_L$ group whilst maintaining overall gauge invariance. This complex doublet scalar field ϕ has the form

$$\phi = \begin{pmatrix} \phi^+ \\ \phi^0 \end{pmatrix} = \frac{1}{\sqrt{2}} \begin{pmatrix} \phi_1 + i\phi_2 \\ \phi_3 + i\phi_4 \end{pmatrix},$$

where, to generate masses of the EW gauge bosons, one scalar field must be electrically neutral, ϕ^0, and the other must be electrically charged, ϕ^+ (with a conjugate $(\phi^+)^* = \phi^-$). The contribution to the SM Lagrangian is

$$\mathcal{L}_H = (D_\mu \phi)^\dagger (D^\mu \phi) - V(\phi),$$

where the first term describes the interaction of the EW bosons with the Higgs field in terms of the covariant derivative D_μ. The second term is the associated Higgs potential.

[1] A recent measurement of the $W^{\pm}$ boson mass of $m_W = 80.433 \pm 0.009$ by the CDF Collaboration [27] is a topic of high-interest in the particle physics community at the moment, as this measurement significantly disagrees with the current world average and predictions by the SM.

This has the form

$$V(\phi) = \mu^2(\phi^\dagger\phi) + \lambda(\phi^\dagger\phi)^2,$$

where μ^2 is a mass parameter and λ is a self-interaction parameter, which obeys $\lambda > 0$ for the potential to have a finite minimum. For $\mu^2 > 0$ the minumum of this potential, the ground state in the vacuum, occurs in the state when both fields $\phi^+ = \phi^0 = 0$, meaning the the vacuum expectation value is zero. In this situation the vacuum is also symmetric. However, in the case where $\mu^2 < 0$, a potential with a characteristic 'mexican hat' shape is formed as shown in Figure 2.2. In this case the minimum of the potential, or the vacuum state, is not when both fields are zero but rather when

$$\phi^\dagger\phi = -\frac{\mu^2}{2\lambda} = \frac{v^2}{2},$$

where $v = \sqrt{-\mu^2/\lambda}$ is the vacuum expectation value (vev), and $v \neq 0$. This leads to a set of infinitely degenerate minima in the shape of a circle. However the physical vacuum state must choose a particular value on this circle, breaking the symmetry. This is known as spontaneous symmetry breaking, and for the SM BEH mechanism the photon must remain massless, such that only the electrically neutral scalar field ϕ^0 is chosen to have the non-zero vev. The corresponding vacuum state is

$$\phi = \frac{1}{\sqrt{2}} \begin{pmatrix} 0 \\ v + h \end{pmatrix},$$

where h is the SM scalar Higgs field which has a corresponding spin-0 scalar Higgs boson, H.

The result of including this additional doublet in the theory results in the $W^\pm$ and Z bosons gaining mass whilst the photon remains massless. In the SM the couplings of the $W^\pm$ and Z bosons, collectively referred to as the intermediate vector bosons, V, are

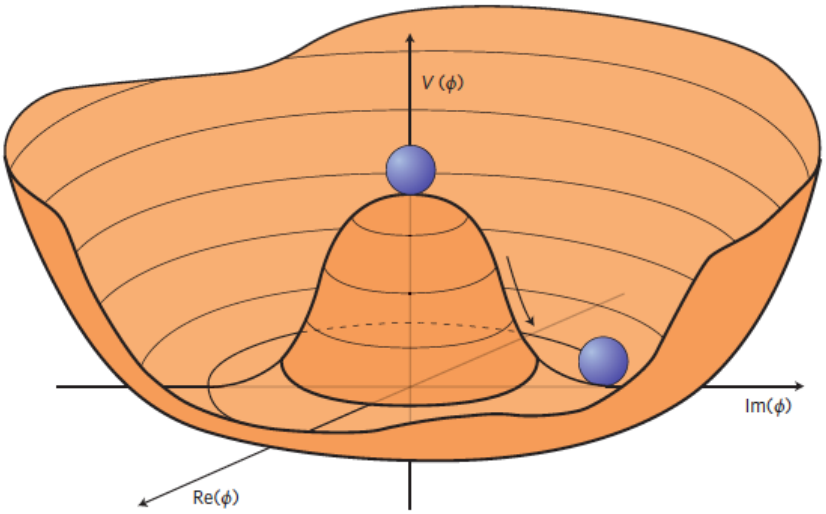


Figure 2.2: An illustration of the Higgs potential [28].

proportional to their mass squared. The value is given by

$$g_V = 2\frac{m_V^2}{v},$$

where m_V is the mass of the vector boson and $v \approx 246$ GeV is the vacuum expectation value of the Higgs field. The masses of the $W^{\pm}$ and Z bosons are related to the weak mixing angle θ_W by the relation

$$\frac{m_W}{m_Z} = \cos\theta_W.$$

Further, the self-interaction terms of the BEH mechanism in the SM gives a mass for the Higgs boson of

$$m_H = v\sqrt{2\lambda},$$

where λ is a free parameter in the SM, such that the SM does not predict a mass for the Higgs boson. As an additional benefit, the addition of the BEH mechanism to the Standard Model allows the cross section of the $W^+W^- \to W^+W^-$ scattering process to preserve unitarity at high energies, via the addition of Feynman diagrams with Higgs

boson exchange.

2.1.5 Fermion Mass Generation

The BEH mechanism generates the masses of the vector and Higgs bosons, but it does not intrinsically explain the origin of the fermion masses. To explain fermion mass in the SM, terms must be added to the SM Lagrangian in a way which preserves $\mathrm{SU}(2)_L \times \mathrm{U}(1)_Y$ gauge invariance [10, 29]. The introduction of the Higgs field ϕ via the BEH mechanism allows for the straightforward extension of the SM Lagrangian to include gauge invariant mass terms for the fermions that also describe their interactions with the Higgs boson. These terms take the form $-g_f \bar{\psi}_L \phi \psi_R + \text{h.c}$, where g_f is the Yukawa coupling of the fermion f and describes the strength of the fermion's coupling to the Higgs boson. The term h.c is shorthand for Hermitian conjugate and the terms L and R refer to the chirality of the fermion, either left- or right-handed. The term ψ represents the fermion fields. In the Standard Model, the strengths of the Yukawa couplings are linearly proportional to the mass of each fermion, with values of

$$g_f = \sqrt{2}\frac{m_f}{v},$$

where m_f is the mass of the fermion. The Standard Model thus gives concrete predictions for the couplings of the Higgs boson to fermions, and measurements of the Yukawa couplings, which can be substantially modified in BSM theories, provide stringent tests of the SM.

2.2 Properties of the Higgs Boson

The Standard Model predicts the existence of a Higgs boson but does not predict its mass. In 2012 the ATLAS [4] and CMS [5] collaborations reported the observation of a boson with a mass of approximately 125 GeV [2, 3] which served as an ideal candidate for the SM Higgs boson. So far measurements of the properties of this Higgs boson are consistent with the predictions by the SM and have confirmed its role in the spontaneous

breaking of electroweak symmetry, and the mass generation of the Z and $W^{\pm}$ bosons and the third generation fermions [7, 8]. This section describes the predicted production and decay mechanisms for a SM Higgs boson as well as the properties of the observed boson measured at the Large Hadron Collider (LHC) [6].

2.2.1 Production and Decay at the Large Hadron Collider

According to the SM a Higgs boson with mass 125 GeV has a lifetime of $\tau_H \approx 1.6 \times 10^{-22}$ s and a natural width of $\Gamma_H = 4.14 \pm 0.02$ MeV [30], and its spin-parity quantum numbers are $J^P = 0^+$. A collection of Feynman diagrams of Higgs boson production modes is shown in Figure 2.3, and the production cross section versus LHC centre-of-mass energy (CM) is shown in Figure 2.4. During Run 2 the LHC ran at a CM energy of $\sqrt{s} = 13$ TeV. At this energy the most dominant production mechanism, at 87% [30], is gluon-gluon fusion (ggH), where two gluons fuse through a quark loop to produce a H. The second most dominant mechanism at 7% is vector boson fusion (VBF), where two vector bosons ($W^{\pm}$ or Z) fuse to produce a H. This mechanism provides a discriminant tag of two hadronic jets with a large rapidity gap, which can lead to increased sensitivity for searches with hadronic final states. The third mechanism is Higgs boson production with an associated vector boson at 4%, where a $W^{\pm}$ or Z is produced that subsequently radiates a H (WH and ZH respectively, VH collectively). This production mechanism can be tagged based on the decay of the associated vector boson. The fourth production mechanism is the production of a Higgs boson with an associated top-quark pair ($t\bar{t}H$) or bottom-quark pair ($b\bar{b}H$), which each contribute about 1% to the total H production. Associated production of a H with other types of quarks, such as a charm-quark pair, are possible but these contributions are negligible due to the small coupling of the Higgs boson to the lighter quark flavours. The final common production mechanism is the production of a Higgs boson with a single top quark (tH), which accounts for about 0.05% of the total production cross section.

Figures 2.3 and 2.4 also show Feynman diagrams and branching ratios, respectively, for the common decay modes of a SM Higgs boson with mass near 125 GeV, which account

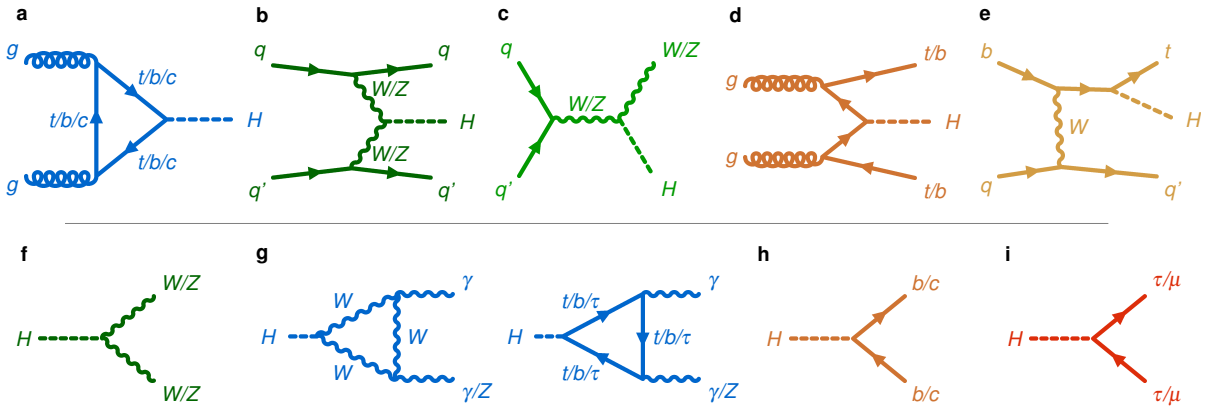
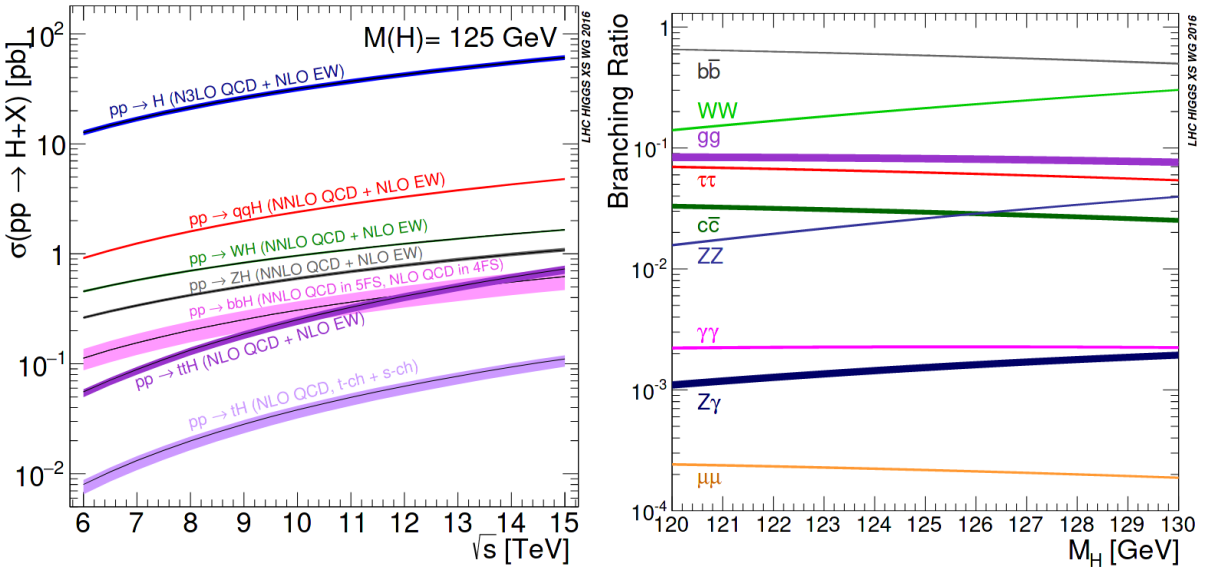


Figure 2.3: Feynman diagrams of the dominant production mechanisms at the LHC (top row) and decay modes (bottom row) of the Standard Model Higgs boson. From left-to-right the production mechanism in (a) is gluon–gluon fusion (ggH), (b) is vector boson fusion (VBF), (c) is associated production with a massive vector boson (VH), (d) is associated production with a t- or b-quark pair ($t\bar{t}H$ and $b\bar{b}H$), and (e) is the associated production with a single t-quark (tH). From left-to-right the decay mode in (f) is the decay into a pair of vector bosons $H \to WW(ZZ)$, (g) is the decay to a pair of photons or a photon and a Z boson ($H \to \gamma\gamma(Z\gamma)$) which occurs either via quark loops or W boson loops, (h) is the decay to a pair of b- or c-quarks ($H \to b\bar{b}(c\bar{c})$), and (i) is the decay to a pair of τ-leptons or muons ($H \to \tau^+\tau^-(\mu^+\mu^-)$). From Ref. [7].



(a) (b)

Figure 2.4: The SM Higgs boson (a) production cross sections as a function of LHC centre-of-mass energy, and (b) branching ratios as a function of Higgs boson mass around 125 GeV [30].

for over 90% of H decays [30]. For Higgs boson mass of 125 GeV, decays into gauge bosons make up 22% of the branching fraction for $H \to WW$, 3% for $H \to ZZ$, 0.2% for $H \to \gamma\gamma$ and 0.2% for $H \to Z\gamma$. Although the photon is massless the decays involving photons can occur via quark or W boson loops. Decays into fermions make up 58% of the branching fraction for $H \to b\bar{b}$, 6% for $H \to \tau^+\tau^-$, 3% for $H \to c\bar{c}$, and 0.02% for $H \to \mu^+\mu^-$. Decays into pairs of lighter fermions are also possible, but the branching ratios decrease proportionally with the square of the fermion mass such that these decays are very rare in the SM.

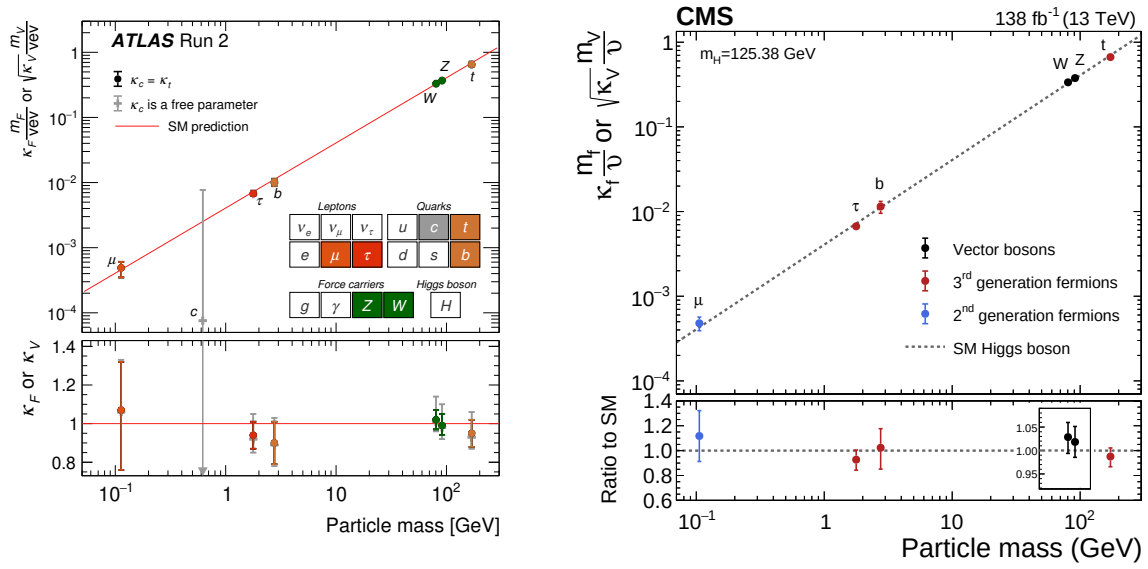
2.2.2 Measurements at the Large Hadron Collider

The Higgs boson was discovered primarily through its diboson decay channels $H \to ZZ$, $H \to WW$ and $H \to \gamma\gamma$ [2, 3], confirming its couplings with the Z and $W^\pm$ bosons and its effective coupling to photons. Since its discovery, the number of observed Higgs boson at the LHC has increased by a factor of 30 [7, 8] and many precision studies of its properties have been conducted to investigate whether it is consistent with the SM prediction primarily though its bosonic decay modes, in particular $H \to \gamma\gamma$ and $H \to ZZ^* \to 4\ell$. Several measurements of the Higgs boson mass have been conducted, where the value $m_H = 125.09 \pm 0.21(\text{stat.}) \pm 0.11(\text{syst.})$ GeV was measured using the combined Run 1 measurements from ATLAS and CMS [31]. The latest measurement from the ATLAS experiment, which uses both Run 1 and Run 2 data, is $m_H = 124.97 \pm 0.24$ GeV [32] whilst the latest measurement from the CMS experiment is $m_H = 125.38 \pm 0.14$ GeV [33]. The ATLAS and CMS collaborations have performed precision measurements of the total Higgs boson cross section and have found this to be in agreement with the SM prediction [34–37]. These studies also look at the differential Higgs boson cross sections, such as versus Higgs boson transverse momentum, which can be used to set indirect constraints on Higgs boson couplings: modified couplings, such as to b- and c-quarks, can alter these distributions as they modify how the Higgs boson is produced at the LHC. Through studies of the diboson decay modes of the observed Higgs boson, it was observed that the discovered boson is consistent with the spin-0 hypothesis of the SM, and the spin-1

and spin-2 hypotheses are excluded at confidence levels (CL) in excess of 99.9% [38, 39]. In these analyses it was also observed that the charge conjugation and parity (CP) properties are consistent with the CP-even state in the SM, such that the quantum numbers of the observed boson are $J^{\mathrm{PC}} = 0^{++}$, although small admixtures of non-SM CP-even or CP-odd states are still allowed. Limits on the lifetime the Higgs boson are obtained through indirect measurements of its natural width [38–42] and recently the CMS Collaboration measured $\Gamma_H = 3.2^{+2.4}_{-1.7}$ MeV, in agreement with the SM, using off-shell and on-shell Higgs boson production [43]. Searches for the bosonic decays $H \to \gamma^*\gamma \to \ell\ell\gamma$ with a low-mass dilepton pair [44, 45] have been performed by ATLAS and CMS, where the ATLAS Collaboration reported the first evidence for the process. Further searches for the bosonic decay mode $H \to Z\,\gamma$ [45–47] have been conducted by each collaboration, but this process has not yet been observed.

For the Higgs boson couplings to fermions, the ATLAS and CMS collaborations have observed the associated production of Higgs bosons with t-quark pairs, confirming its coupling to top quarks [48, 49]. Each collaboration has also observed Higgs boson decays into a pair of b-quarks [50, 51] and τ-leptons [52, 53], where the τ-lepton decay channel is also used for precision measurements of the Higgs boson production cross sections. These confirm all of the Higgs boson couplings to the third-generation charged fermions and are in agreement with SM expectactions. More recently, evidence has been reported for the Higgs boson couplings to muons via $H \to \mu^+\mu^-$ with a 3σ significance by the CMS Collaboration, and a smaller significance of 2σ by the ATLAS Collaboration [54, 55], the first evidence for the Higgs boson couplings to second-generation charged fermions. Direct searches have been performed for $H \to c\bar{c}$ by both ATLAS and CMS [56–59], as have searches for $H \to e^+e^-$ [60, 61], but these have not yet been observed and no further experimental evidence currently exists for the Higgs boson couplings to the first- and second- generation fermions. Figure 2.5 summarises the experimental measurements of the Higgs boson coupling strengths to the bosons and fermions using the κ framework for coupling modifiers [62]; these are relative coupling strength parameters where $\kappa = g_f/g_f^{\mathrm{SM}}$ and values of $\kappa = 1$ correspond to the SM expectation. Here g_f is the Yukawa coupling

strength of the Higgs boson to a given fermion and g_f^{SM} is the value of the Yukawa coupling strength in the SM as described in Section 2.1.5. Current measurements are consistent with the SM.



(a) (b)

Figure 2.5: The measured coupling modifiers of the Higgs boson to fermions and massive gauge bosons from the (a) ATLAS [7] and (b) CMS [8] experiments versus particle mass. The κ-framework is used to represent the coupling strengths where $\kappa = 1$ corresponds to the SM expectation. The value $v \approx 246$ GeV is the vacuum expectation value of the BEH field and m refers to the mass of the particle. For the massive $W^{\pm}$ and Z bosons the square root of the coupling modifier is plotted such that it has a linear proportionality to mass as predicted in the SM. The values on each plot show are the values of the κ coupling modifiers after a combined fit. For the ATLAS result two fit scenarios are shown, one where κ_c is fixed to $\kappa_c = \kappa_t$ and a second where κ_c is free in the fit.

Searches for potential BSM couplings of the Higgs boson have also been performed by ATLAS and CMS, such as searches for flavour-changing neutral currents via the t-quark decays $t \to cH$ and $t \to uH$ [63–66], and the lepton-flavour-violating decays $H \to e\mu$, $H \to e\tau$ and $H \to \mu\tau$ [60, 67, 68]. However, no evidence for these flavour-violating couplings has been found.

2.3 Exclusive Decays of Massive Bosons to a Meson and a Photon

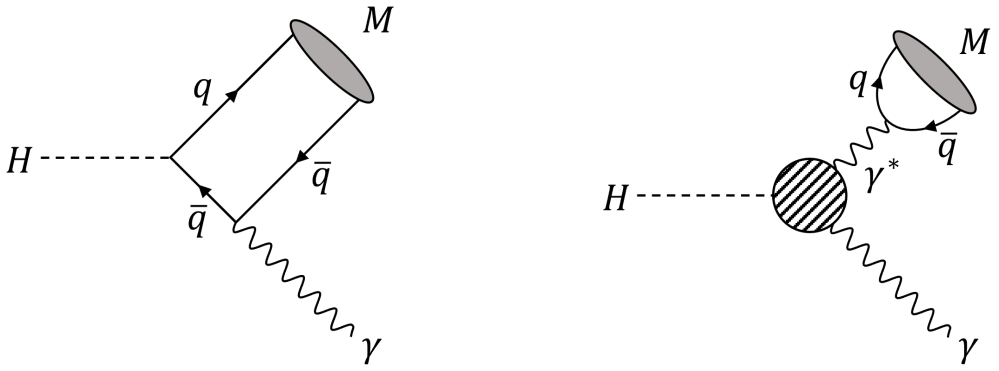
The most direct method to probe the quark couplings of the Higgs and vector bosons, the Z and the $W^{\pm}$ bosons of the weak force, is via their decays to pairs of quarks, which are detected through their formation of QCD jets. The colliding proton beams at the LHC

create huge sources of multi-jet QCD backgrounds, which makes it challenging to isolate potential signals. This motivates the search for exclusive decays with distinct signatures in the detector as an alternative probe to the properties of the bosons. This section describes the physics motivation to search for exclusive decays of the Higgs, Z, and $W^{\pm}$ bosons to a meson and a photon, as well as a summary of the current experimental standing of these decay channels, for which the ATLAS experiment plays a major role.

2.3.1 Higgs Boson Decays

Radiative decays of the Higgs boson to light mesons offer an alternative probe to the quark Yukawa couplings [69–76]. Although their branching fractions are small compared to inclusive $H \to q\bar{q}$ decays, decays of the type $H \to \mathcal{M}\gamma$, where $\mathcal{M}$ is a flavourless vector meson, offer a clean signal to suppress the large multi-jet backgrounds at the LHC because the decay topologies include a resonance in both the Higgs boson mass and the meson mass, as well as a high p_T photon appearing approximately back-to-back with the meson candidate. There are two primary contributions to the decay amplitude in the SM, shown in Figure 2.6. The 'direct' amplitude occurs via the quark Yukawa coupling whilst the 'indirect' amplitude occurs at the one-loop level through the $H \to \gamma^*\gamma$ decay, where the virtual photon then fragments to form the meson. The two processes destructively interfere, and despite being loop-induced, the indirect amplitude typically dominates. Only the direct amplitude is sensitive to the quark Yukawa coupling, but because the two processes interfere the decay channels are sensitive not only to the magnitude of the quark Yukawa couplings but to their sign as well.

Exclusive SM decays of the Higgs boson to a photon and a heavy quarkonium meson state, $H \to \mathcal{Q}\gamma$, offer a probe of the magnitude and the sign of the b- and c-quark Yukawa couplings [69–71]. For g_c, the relevant charmonium states are J/ψ and $\psi(2S)$; for g_b the relevant bottomonium states are $\Upsilon(nS)(n = 1, 2, 3)$. Similarly, exclusive SM decays of the Higgs boson to a photon and a light vector meson state, $H \to \mathcal{V}\gamma$, offer a probe of the magnitude and sign of the s-, u- and d-quark Yukawa couplings [71]. The decay $H \to \phi\gamma$ is sensitive to the Higgs boson coupling to the strange quark, and the decays



(a) Direct amplitude (b) Indirect amplitude

Figure 2.6: Feynman diagrams depicting the $H \to \mathcal{M}\,\gamma$ process, where $\mathcal{M}$ is a flavourless meson. The hatched circle in (b) denotes a set of one-loop diagrams.

$H \to \rho\gamma$ and $H \to \omega\gamma$ are sensitive to the up- and down-quark couplings. The expected branching fractions of each of these decays in the SM are shown in Table 2.1 [71, 73, 74]. The Higgs boson couplings to c-, s-, u-, and d-quarks have not yet been confirmed in experiment. The b-quark coupling has been confirmed in experiment as discussed in 2.2, however the $\Upsilon(1S, 2S, 3S)$ decay channels are particularly sensitive to deviations in the b-quark Yukawa coupling from the Standard Model prediction because of an almost perfect cancellation between the direct and indirect amplitudes, leading to small branching fractions compared to the other exclusive decay channels.

Table 2.1: Calculations of the expected branching fractions for the rare $H \to \mathcal{M}\,\gamma$ decay channels. The values for the quarkonium decay channels, $\mathcal{Q} = J/\psi, \psi(2S), \Upsilon(1S, 2S, 3S)$, are taken from Refs. [73, 74]. The values for the light meson decay channels, ϕ, ρ, ω, are taken from Ref. [71].

Decay Channel	SM Expectation
$\mathcal{B}(H \to \Upsilon(1S)\,\gamma)$	$5.22^{+2.02}_{-1.70} \times 10^{-9}$
$\mathcal{B}(H \to \Upsilon(2S)\,\gamma)$	$1.42^{+0.72}_{-0.57} \times 10^{-9}$
$\mathcal{B}(H \to \Upsilon(3S)\,\gamma)$	$0.91^{+0.48}_{-0.38} \times 10^{-9}$
$\mathcal{B}(H \to J/\psi\,\gamma)$	$2.99^{+0.16}_{-0.15} \times 10^{-6}$
$\mathcal{B}(H \to \psi(2S)\,\gamma)$	$1.03 \pm 0.06 \times 10^{-6}$
$\mathcal{B}(H \to \phi\,\gamma)$	$2.31 \pm 0.11 \times 10^{-6}$
$\mathcal{B}(H \to \rho\,\gamma)$	$1.68 \pm 0.08 \times 10^{-5}$
$\mathcal{B}(H \to \omega\,\gamma)$	$1.48 \pm 0.08 \times 10^{-6}$

Deviations in the quark Yukawa couplings from the SM expectations can lead to significant enchancements in the branching fractions of the exclusive $H \to \mathcal{M}\,\gamma$ decays,

particularly for the bottomonium decays [77]. Such deviations can arise in theories beyond-the-SM (BSM), which are reviewed in Ref. [30]. These include the introduction of subdominant sources of electroweak symmetry breaking [78], the Froggatt–Nielsen mechanism with a single Higgs doublet [79], the Randall–Sundrum models [80], new physics with the minimal flavour violation framework [81], the Giudice–Lebedev Higgs-dependent Yukawa couplings model [82], and the possibility of the Higgs boson being a composite pseudo-Nambu-Goldstone boson [83].

$H(Z) \to \mathcal{M}\gamma$ decays can also provide a probe to potential flavour-violating Yukawa couplings, where $\mathcal{M}$ is instead an electrically neutral, flavoured meson such as D^* or K^*. Decays of this type are forbidden at tree-level in the SM as they violate quark-flavour conservation. Table 2.2 shows the SM calculations for the branching fractions of the inclusive flavour violating decays $H \to q\bar{q}'$ which occur at the one-loop level through $W^\pm$ loops [84]; in the case of the flavour-violating $H \to \mathcal{M}\,\gamma$ decays, one quark must further radiate a photon and hadronise with the other quark to form the flavoured meson, such that the SM expectations of the exclusive decays are expected to be significantly lower, although they have not been calculated in the literature. The flavour-violating decay channels have the advantage that there is no contribution from the indirect amplitude in the SM at one-loop level seen in the rare exclusive decays, as this would require a flavour-violating decay of a photon. As the branching fractions for these decay channels are so small in the SM, any observation at the LHC would imply new physics such as the existence of flavour-violating Yukawa couplings of the Higgs boson.

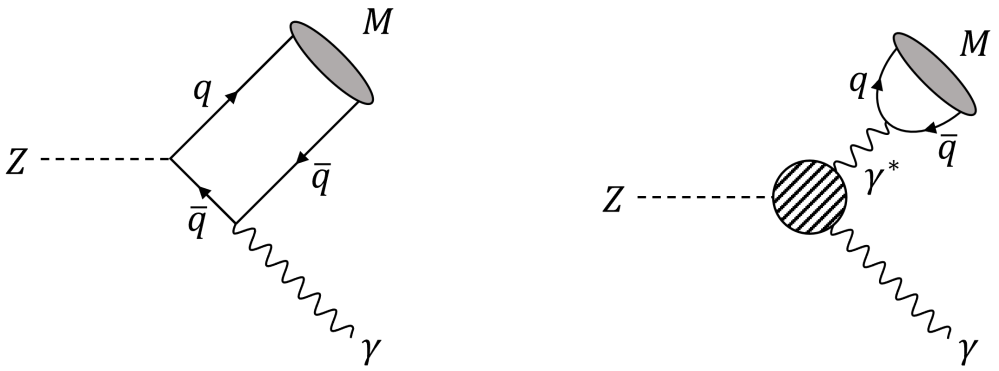
Table 2.2: Calculations of the expected branching fractions for inclusive flavour-violating $H \to q\bar{q}'$ decays in the Standard Model, taken from Ref. [84]. Each branching fraction is a sum of the two charge conjugate contributions $q\bar{q}' + \bar{q}q'$.

Decay Channel	SM Expectation
$\mathcal{B}(H \to uc)$	5.00×10^{-20}
$\mathcal{B}(H \to ds)$	1.19×10^{-11}
$\mathcal{B}(H \to db)$	5.16×10^{-9}
$\mathcal{B}(H \to sb)$	1.15×10^{-7}

2.3.2 Vector Boson Decays

The Z boson production cross section at the LHC [85] at $\sqrt{s} = 13$ TeV is approximately 1000 times larger than the Higgs boson production cross section [30, 86], which allows rare Z boson decays to be probed to much smaller branching fractions than analogous H boson decays to the same final state. Radiative decays of the type $Z \to \mathcal{M}\gamma$ have similar contributions from direct and indirect amplitudes in the SM, shown in Figure 2.7. The indirect amplitude is smaller in the Z decays compared to the H decays, leading to overall smaller branching fractions in the SM in general, with the exception of the bottomonium decays. These are shown in Table 2.1 [87–89], where the same mesons are considered as for the $H \to \mathcal{M}\gamma$ decays. These decay channels not only offer complementary reference channels to the $H \to \mathcal{M}\gamma$ decays to help in the development of analysis strategies, but they are useful in studies of the QCD factorisation approach in the SM. Since the power corrections in terms of the ratio of QCD energy scale to vector-boson mass are small in $Z \to \mathcal{M}\gamma$ decays, the light-cone distribution amplitudes (LCDAs) of the mesons can be probed in a theoretically clean region where power corrections are in control [88]. This is not possible in other applications of the QCD factorisation approach, such as in B-hadron decays. Similarly to the exclusive Higgs boson decays, choosing a flavoured meson in the decay $Z \to \mathcal{M}\gamma$ such as D^0 or K_s, allows potential flavour-violating couplings of the Z bosons to quarks to be probed, which are also forbidden at tree-level in the SM as flavour-changing neutral currents are not allowed at this level. The SM branching fractions of these decays have not yet been calculated in the literature, but they are expected to be significantly smaller than the $\mathcal{O}(10^{-8})$ branching fractions for the decays in Table 2.3 as two quarks of different flavour must be produced in the processes to be able to form the D^0 or K_s mesons. This is possible in the SM only with the addition of $W^\pm$ loops, similarly to the flavour-violating $H \to q\bar{q}$ decays in Table 2.2. As a result, any observation at the LHC would imply new physics.

Searches for $W^\pm$ boson decays to a meson and a photon are also useful in the QCD factorisation approach [88], however as the $W^\pm$ bosons are charged, decays directly analogous to the H and Z decay channels are not possible. The SM branching fractions for



(a) Direct amplitude

(b) Indirect amplitude

Figure 2.7: Feynman diagrams depicting the $Z \to \mathcal{M}\,\gamma$ process, where $\mathcal{M}$ is a flavourless meson. The hatched circle in (b) denotes a set of one-loop diagrams.

Table 2.3: Calculations of the expected branching fractions for the rare $Z \to \mathcal{M}\,\gamma$ and $W^{\pm} \to \mathcal{M}^{\pm}\,\gamma$ decay channels in the Standard Model. The values for the quarkonium decay channels, $\mathcal{Q} = J/\psi, \psi(2S), \Upsilon(1S, 2S, 3S)$, are taken from Ref. [89]. The values for the light meson decay channels, ϕ, ρ, ω, are taken from Ref. [88], as are the values for the $W^{\pm} \to \mathcal{M}^{\pm}\,\gamma$ decay channels.

Decay Channel	SM Expectation
$\mathcal{B}(Z \to \Upsilon(1S)\,\gamma)$	$4.80^{+0.26}_{-0.25} \times 10^{-8}$
$\mathcal{B}(Z \to \Upsilon(2S)\,\gamma)$	$2.44^{+0.14}_{-0.13} \times 10^{-8}$
$\mathcal{B}(Z \to \Upsilon(3S)\,\gamma)$	$1.88^{+0.11}_{-0.10} \times 10^{-8}$
$\mathcal{B}(Z \to J/\psi\,\gamma)$	$8.96^{+1.51}_{-1.38} \times 10^{-8}$
$\mathcal{B}(Z \to \psi(2S)\,\gamma)$	Not available
$\mathcal{B}(Z \to \phi\,\gamma)$	$1.04 \pm 0.12 \times 10^{-8}$
$\mathcal{B}(Z \to \rho\,\gamma)$	$4.19 \pm 0.47 \times 10^{-9}$
$\mathcal{B}(Z \to \omega\,\gamma)$	$2.82 \pm 0.40 \times 10^{-8}$
$\mathcal{B}(W^{\pm} \to \pi^{\pm}\,\gamma)$	$4.00 \pm 0.83 \times 10^{-9}$
$\mathcal{B}(W^{\pm} \to \rho^{\pm}\,\gamma)$	$8.74 \pm 1.91 \times 10^{-9}$
$\mathcal{B}(W^{\pm} \to K^{\pm}\,\gamma)$	$3.25 \pm 0.69 \times 10^{-10}$

the decays to $\pi^{\pm}\gamma$, $\rho^{\pm}\gamma$ and $K^{\pm}\gamma$ are shown in Table 2.3 [88]. In the case of the $W^{\pm}$ decays there is no indirect amplitude, as similarly for the flavour-violating decays of the H and Z bosons, this would require a photon to undergo a flavour-violating decay, which is forbidden in the SM.

2.3.3 Experimental Results

Several searches for the exclusive Higgs, Z and $W^{\pm}$ boson decays to a meson and a photon have been conducted at the LHC. The initial searches for the Higgs and Z boson decays to $J/\psi\,\gamma$ and $\Upsilon(1S, 2S, 3S)\,\gamma$ by ATLAS were performed using the Run 1 dataset [90], as well as for their decays to $\phi\,\gamma$ [91]. These searches were updated using the partial 2015–2016 Run 2 dataset of up to 36.1 fb^{-1} collected at $\sqrt{s} = 13$ TeV, where the $\mathcal{Q}\,\gamma$ search was updated to include the $\psi(2S)\,\gamma$ final state [92] and the $\phi\,\gamma$ search also included the H and Z boson decays to $\rho\,\gamma$ [93]. The most recent ATLAS result for the exclusive decays searches for the H and Z boson decays to $\mathcal{Q}\,\gamma$ and uses the full Run 2 dataset of 139 fb^{-1} collected at $\sqrt{s} = 13$ TeV [94]. These searches are presented in full in Chapter 5 The latest 95% confidence level (CL) upper limits on the branching fractions on each decay channel from these searches are summarised both in Table 2.4 and in Figure 2.8. These are the world-leading limits on each decay channel. The CMS experiment has searched for the decay $H \to J/\psi\,\gamma$ using the Run 1 dataset [95], and later searched for both H and Z boson decays to $J/\psi\,\gamma$ using the partial Run 2 dataset, yielding 95% CL upper limits of 7.6×10^{-4} and 1.4×10^{-6}, respectively, from 35.9 fb^{-1} of data collected at $\sqrt{s} = 13$ TeV [96]. The CMS experiment has also searched for the decay $W^{\pm} \to \pi^{\pm}\gamma$ using the full Run 2 dataset of 137 fb^{-1} collected at $\sqrt{s} = 13$ TeV and reported a 95% CL upper limit of 1.5×10^{-5} [97]. Finally, the LHCb experiment has searched for the decay $Z \to D^0\,\gamma$ using 2.0 fb^{-1} of data collected at $\sqrt{s} = 13$ TeV, yielding a 95% CL upper limit of 2.1×10^{-3} [98].

Searches for the rare decays $H(Z) \to \omega\,\gamma$ and $W^{\pm} \to (\pi^{\pm}, \rho^{\pm}, K^{\pm})\,\gamma$ at ATLAS are ongoing, as well as for the flavour-violating decays $H \to (D^*, K^*)\,\gamma$ and $Z \to (D^0, K_s)\,\gamma$. The current status of the searches for $H \to D^*\,\gamma$, $Z \to D^0\,\gamma$, and $Z \to K_s\,\gamma$ is presented

Table 2.4: Limits at 95% CL on the branching fractions for each of the $H(Z) \to \mathcal{M}\gamma$ decays searched for by the ATLAS experiment.

	95% CL Branching Fraction Upper Limit	
Decay Channel	Z Decay	H Decay
$\Upsilon(1S)\gamma$	1.1×10^{-6}	2.5×10^{-4}
$\Upsilon(2S)\gamma$	1.3×10^{-6}	4.2×10^{-4}
$\Upsilon(3S)\gamma$	2.4×10^{-6}	3.4×10^{-4}
$J/\psi\gamma$	1.2×10^{-6}	2.0×10^{-4}
$\psi(2S)\gamma$	2.4×10^{-6}	10.5×10^{-4}
$\phi\gamma$	0.9×10^{-6}	4.8×10^{-4}
$\rho\gamma$	25×10^{-6}	8.8×10^{-4}

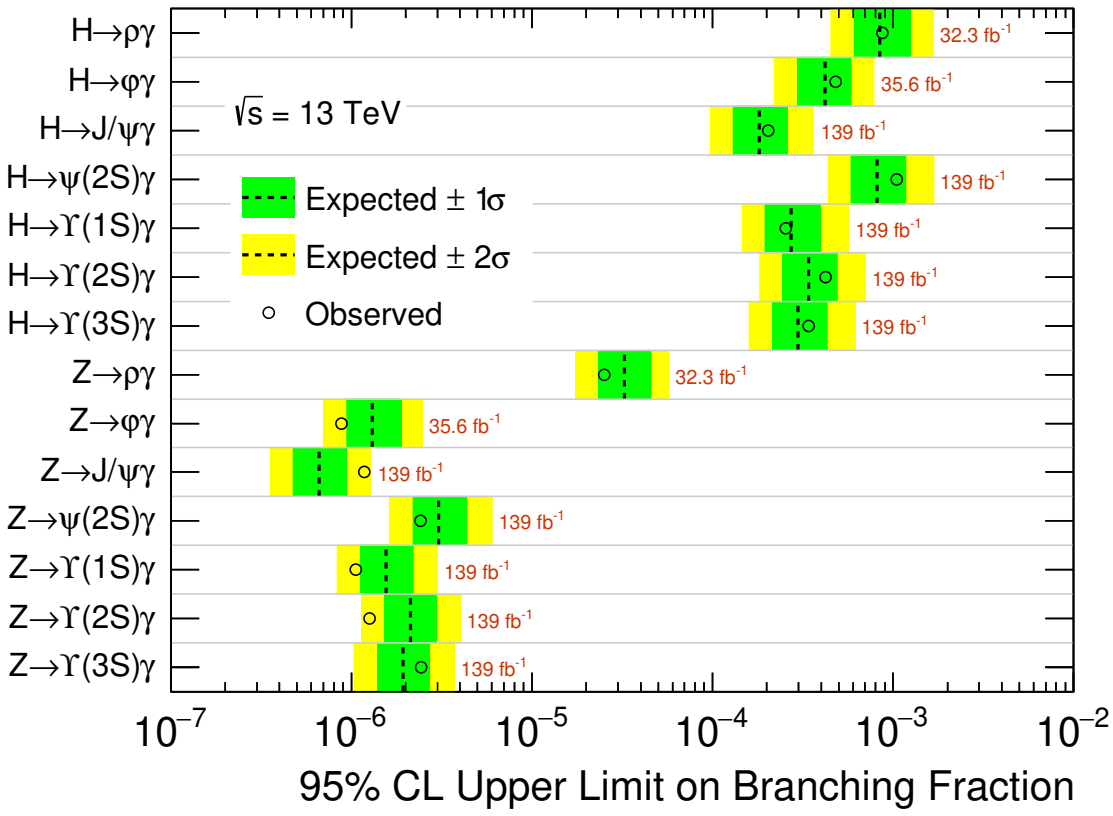


Figure 2.8: Summary of the 95% CL upper limits on Higgs and Z boson branching fractions for exclusive decays to a meson and a photon from the ATLAS experiment, assuming Standard Model Higgs boson production. Each limit is the world-leading result. The limits on $H(Z) \to \mathcal{Q}\gamma$ are from Ref. [94] whilst the limits on $H(Z) \to \phi\gamma$ and $H(Z) \to \rho\gamma$ are taken from Ref. [93].

in Chapter 6. In addition to the searches for exclusive decays of the Higgs and massive vector bosons to a meson and a photon, similar exclusive decays searches involving a meson have been conducted by ATLAS and CMS. For ATLAS, these include searches for $H \to Z\,J/\psi$ and $H \to Z\,\eta_c$ [99]. For CMS, these include searches for $H \to Z\,\phi$ and $H \to Z\,\rho$ as well as searches for Higgs and Z boson decays into pairs of J/ψ or $\Upsilon(1S, 2S, 3S)$ vector quarkonium states [100].

3 The ATLAS Experiment at the CERN Large Hadron Collider

ATLAS, one of four major experiments located on the Large Hadron Collider (LHC) ring at CERN, is a general purpose particle physics detector. This chapter describes the operation of the LHC in Section 3.1 which provides the high energy proton–proton (pp) collisions for ATLAS, which described in Section 3.2. The data acquisition and triggers for ATLAS are described in Section 3.3, including the physics performance for particles relevant in rare exclusive decays, and the software which ATLAS uses in to process of data and simulate events is described in Section 3.4.

3.1 The Large Hadron Collider

The Large Hadron Collider [6] is a circular collider and the highest-energy particle accelerator ever built, with a circumference of 27 km. It is situated approximately 100 m underground on the Swiss-French border at CERN, inside of the tunnel used previously for the Large Electron-Positron (LEP) collider which operated from 1989 until 2000. It is a synchrotron designed to accelerate protons up to 7 TeV in two counter-rotating beams, and to collide them head-on at several interaction points (IP) around the detector where experiments measure the properties of the collisions. As protons are approximately 2000 times more massive than electrons, significantly less energy is lost due to synchrotron radiation. As a result, the LHC is capable of accelarating protons to much higher energies compared to the electrons and positrons at LEP, despite them having the same circumference. As well as pp collisions, the LHC is also capable of colliding heavy ions such as lead ions which can be used in further physics studies.

The LHC is the last element in the CERN accelerator complex, shown in Figure 3.1, a chain of machines which accelerate protons to increasingly higher energies. Many of these machines have their own set of experiments for physics studies at lower energies. Protons are originally sourced from bottles of hydrogen gas, which are stripped of their electrons, and then accelerated to 50 MeV by Linac2, a type of linear accelerator. These are then

injected into the Proton Synchrotron Booster (PSB) which accelerates the protons to 1.4 GeV before injecting them into the Proton Synchrotron (PS), which accelerates them to 25 GeV. From there, protons are injected into the Super Proton Synchrotron (SPS) where they are accelerated to 450 GeV. Finally, they are transferred into the LHC in two separate beams, one travelling clockwise and the other anticlockwise, where they are accelerated further. During Run 2 the proton beams were accelerated up to 6.5 TeV, the record at the time, to provide collisions with a total centre-of-mass energy of $\sqrt{s} = 13$ TeV. Protons are sent to the LHC in bunches, which are groups of approximately 10^{11} protons, and the LHC is designed to handle 2808 bunches per beam which circulate for approximately 10 hours. These bunches are spaced 25 ns apart (corresponding to a distance of ~ 7.5 m) and give rise to approximately one-billion collisions per second.

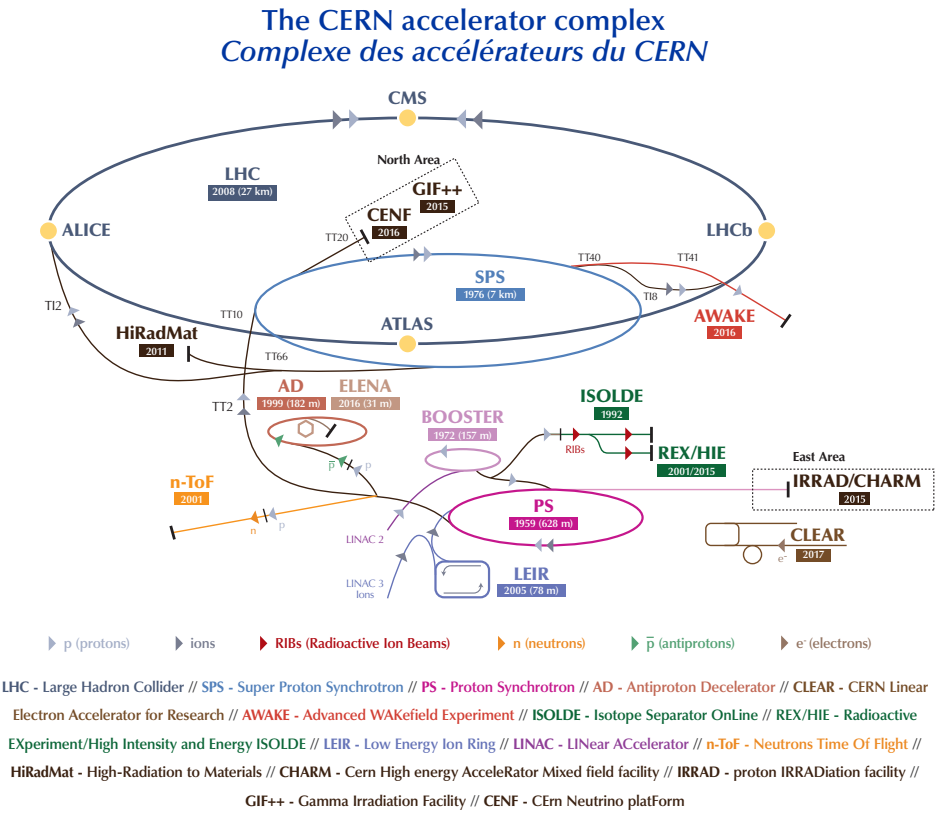


Figure 3.1: The CERN particle accelerator complex in 2018 at the end of Run 2. The LHC (dark blue line) is the last ring in a chain of particle accelerators. ©2018–2022 CERN.

The LHC itself is not a perfect circle but is made up of eight arcs and eight straight sections called insertions. The accelerator features of a variety of magnets, 9593 in total,

to optimise the trajectory of the protons. The main types are the dipole magnets for the bending of particle trajectories, and the quadrupole magnets for the focusing of the beams to maximise the number of collisions. There are 1232 main dipole magnets, which operate at 1.9 K using superfluid helium, and 392 main quadrupole magnets. The LHC also features of eight superconducting radiofrequency (RF) cavities per beam, which accelerate the protons in bunches. These operate at a temperature of 4.5 K. The LHC operates under a vacuum pressure of 10^{-13} to avoid collisions with gas molecules.

Particles collide at four IPs, shown in Figure 3.2, where the main particle experiments lie. The ATLAS (A Large Toroidal LHC ApparatuS) [4] and CMS (Compact Muon Solenoid) [5] experiments are situated at opposite sides of the LHC ring, and serve as the two general-purpose particle physics experiments. The LHCb (Large Hadron Collider beauty) [101] experiment specialises in the study of the small matter-antimatter asymmetry in the interactions of B-hadrons, which are hadrons containing b-quarks. The ALICE (A Large Ion Collider Experiment) [102] experiment specialises in the study of lead-ion collisions to investigate the properties of quark-gluon plasma, a high-energy state of matter where quarks and gluons are no longer confined inside hadrons.

3.1.1 Luminosity and Pile-up

To maximise the potential for studying physics processes it is beneficial to have high statistics. The event rate for a given physics process at a particle accelerator is given by

$$\frac{dN}{dt} = L\sigma,$$

where σ is the cross section for the process, which is determined by the underlying physics and is a measure of the probability for an interaction of a particular type to occur. Cross section is typically measured in barns, where b = 10^{-28} m^2. The quantity L is known as the instantaneous luminosity, which is a measure of the intensity of the collisions in the accelerator in cm^{-2}s^{-1} or b^{-1}s^{-1}, and is determined by the properties of the machine producing the interactions. The LHC is designed to have a peak instantaneous luminosity

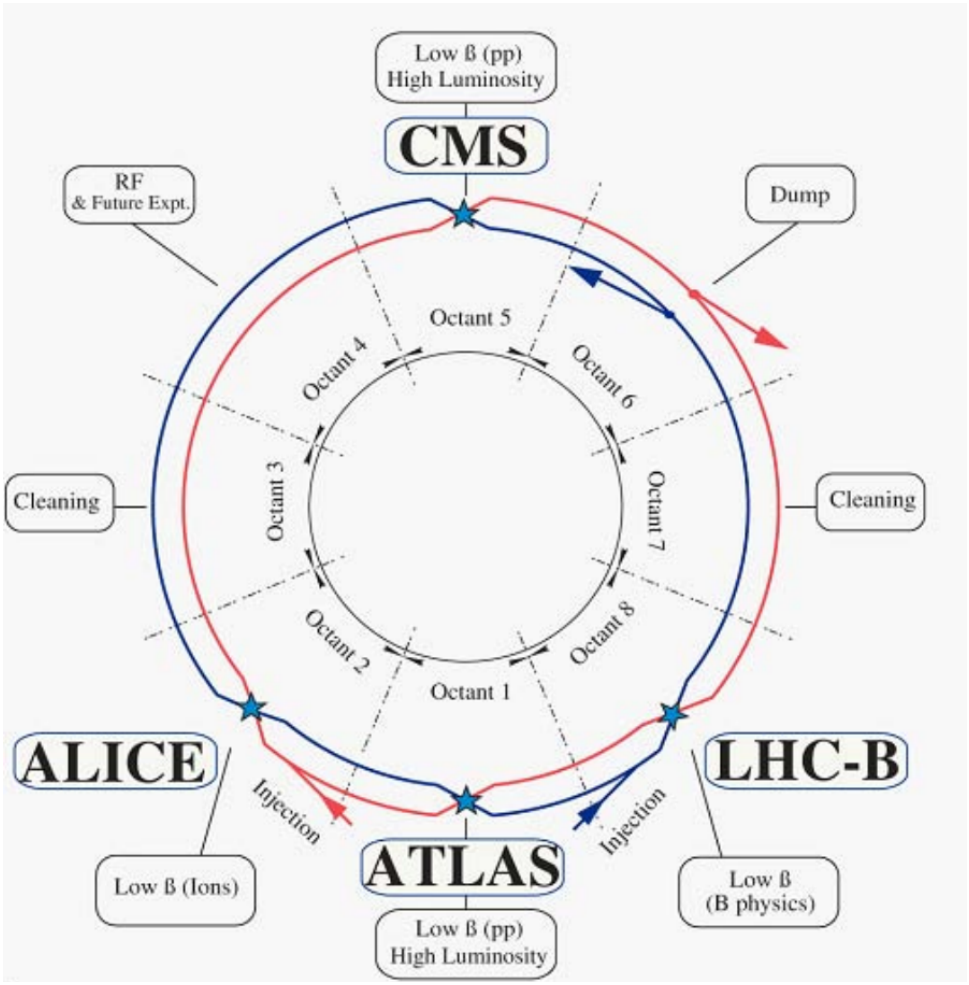


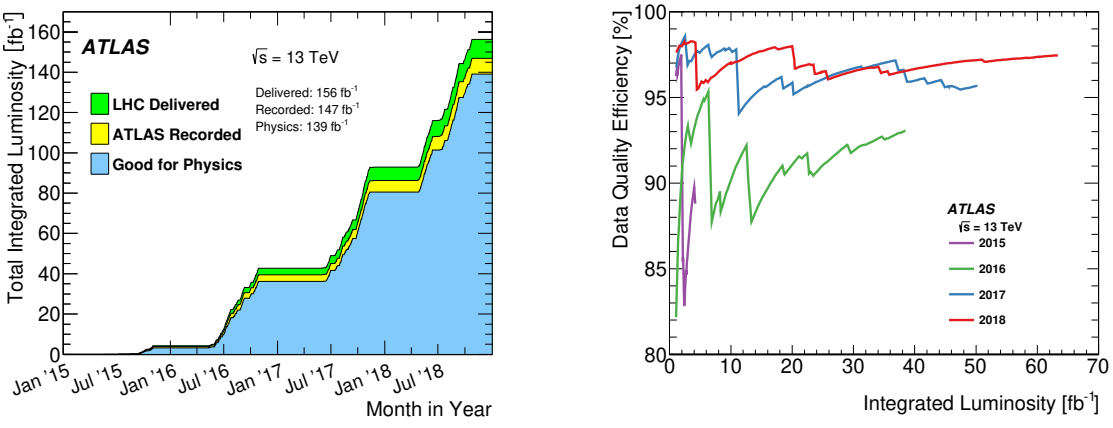
Figure 3.2: Schematic layout of the LHC. The red (clockwise) and blue (anticlockwise) lines denote the path of the two counter rotating beams, which collide at four interaction points where the primary experiments of the LHC lie [6].

of $\sim 1.2 \times 10^{34}$ cm^{-2}s^{-1} [6].

Another useful quantity to describe the capability of a particle accelerator to deliver events is the integrated luminosity $\mathcal{L}$, which is the integral of L with time measured in cm^{-2} or b^{-1},

$$\mathcal{L} = \int L \cdot dt.$$

This is a measure of the total number of events $N = \mathcal{L}\sigma$ delivered throughout the operation of a detector. Figure 3.3 shows the cumulative integrated luminosity recorded at $\sqrt{s} = 13$ TeV as Run 2 of the LHC progressed, with a total of 139 fb^{-1} of data good for physics delivered to ATLAS by the end of 2018 [103]. Figure 3.3 also shows the fraction of events versus $\mathcal{L}$ which meet the data quality requirements [103] to be used in physics analyses. The result of assessing ATLAS data and applying data quality requirements is the 'Good Runs List' (GRL) for each year of data taking. This is a list of luminosity blocks (LB) which are certified as good for physics analyses and it is designed to filter out any data compromised by anomalous conditions in the detector. The total good-for-physics integrated luminosity which is the sum of the LBs that are present in the GRLs.



(a) (b)

Figure 3.3: The cumulative integrated luminosity delivered by the LHC to ATLAS between 2015–2018, where (a) shows the delivered luminosity versus time, and (b) shows the cumulative portion of events that meet the data quality requirements versus total integrated luminosity for each year of operation during Run 2 [103].

One consideration when operating particle experiments at higher luminosities is the pile-up, which is the number of pp interactions in the same or neighbouring bunch crossings. This can reduce the efficiency for event reconstruction as the more events that occur in the detector at a given time, the harder it is to resolve each event individually. For example particles from different pp interactions can overlap in the detector components. Figure 3.4 shows the average number of events per bunch crossing for each year of operation during Run 2, which changed from about 13 pp interactions per bunch crossing in 2015 to about 36 in 2018 as the instantaneous luminosity at the LHC increased.

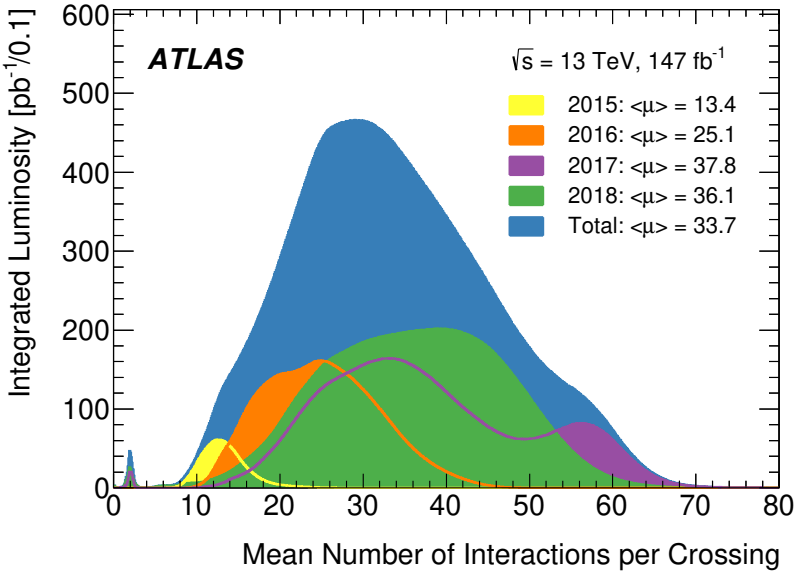


Figure 3.4: The pile-up of the interactions in the ATLAS detector throughout different run periods [103].

3.2 The ATLAS Detector

The ATLAS detector [4], shown in Figure 3.5, is a multipurpose particle detector designed for a wide range of physics, from studies of the Higgs boson, the top quark, and precision measurements of the Standard Model, to searches for exotic BSM physics such as for dark matter and supersymmetry. It has an approximately forward–backward symmetric cylindrical geometry and a coverage of nearly 4π in solid angle around the interaction point (IP) for event reconstruction. With a length of 46 m and a diameter of 25 m, it is the largest-volume detector for a particle collider in the world. It has a mass of

approximately 7,000 tonnes and is situated in a cavern 100 m underground.

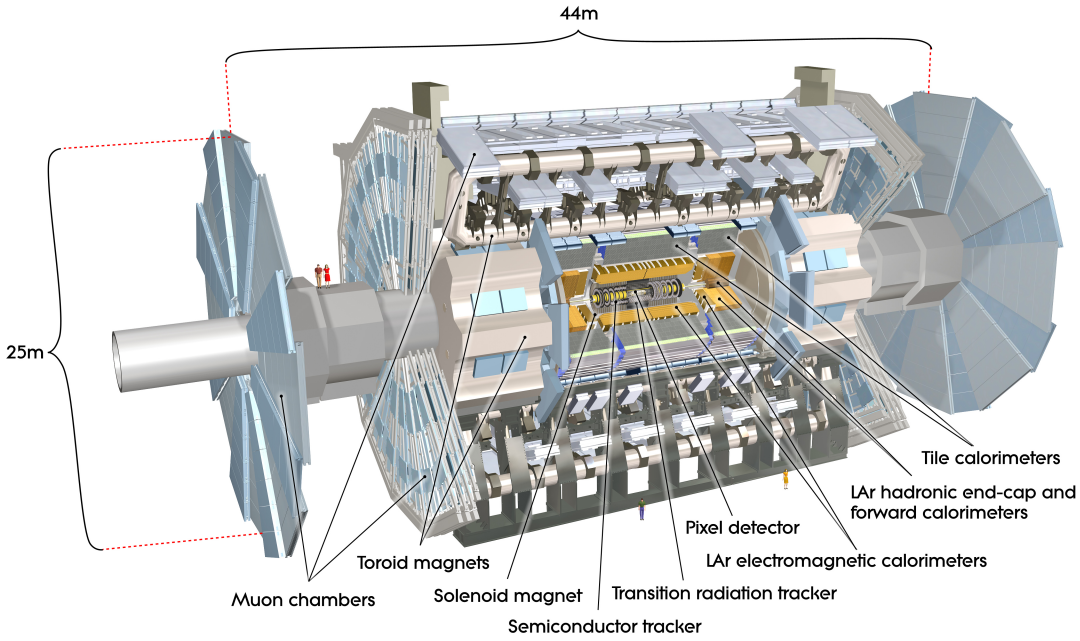


Figure 3.5: The layout of the whole ATLAS detector [4]. ATLAS Experiment ©2008 CERN.

The detector itself consists of six separate subsystems to measure the momentum, trajectory and energy of particles, which are wrapped in concentric layers around the IP. From innermost to outermost systems, these are the pixel detector, semiconductor tracker (SCT), and transition radiation tracker (TRT) of the inner detector (ID), followed by the electromagnetic and hadronic calorimeters, and finally the muon spectrometer (MS). The three subsystems that make up the ID are designed for the precision tracking of charged particles, the calorimeters are designed to measure the energy of both charged and neutral particles, and the MS is designed for the tracking of muons, which are able to pass through the entire detector geometry. Integrated alongside the detection subsystems is a magnet system designed to bend the paths of charged particles through the Lorentz force, which is used to measure both their momenta and their charges. This consists of the solenoid magnet to provide a magnetic field for the ID, and the toroid magnets to provide a magnetic field for the MS. This section describes each of these components in more detail.

The ATLAS experiment uses a right-handed coordinate system with its origin set to

the IP in the centre of the detector, and the z-axis along the beam pipe of the LHC. The x-axis points from the IP to the centre of the LHC ring, and the y-axis points upward. In the transverse plane, cylindrical coordinates are used in (r, ϕ), where r is the radius and ϕ is the azimuthal angle about the z-axis. In the longitudinal plane the quantity pseudorapidity, η is used, which is defined in terms of the polar angle θ as $\eta = -\ln[\tan(\theta/2)]$. This value is invariant to Lorentz boosts along the z-axis.

Several useful quantities to describe properties of particles in the detector are defined with respect to these coordinate systems. The rapidity, y, is defined as

$$y = \frac{1}{2} \ln \left(\frac{E + p_z}{E - p_z} \right),$$

where E is the energy of the particle and p_z is the momentum of the particle along the z-axis. In the limit of high energy, y approaches η. The angular separation between two particle tracks, ΔR, in (η, ϕ) is defined as $\Delta R = \sqrt{(\Delta\phi)^2 + (\Delta\eta)^2}$, where $\Delta\phi$ is the difference between the azimuthal angle, $\phi_{1,2}$, coordinates of the two tracks, wrapped into the range $-\pi$ to π, and $\Delta\eta$ is the difference between the pseudorapidities, $\eta_{1,2}$, of the two tracks. The transverse momentum of a track, p_{T}, is the momentum of the particle in the transverse plane and is defined as $p_{\mathrm{T}} = \sqrt{(p_x)^2 + (p_y)^2}$, where p_x and p_y are the momenta of the particle along the x- and y-axes, respectively. Adding p_z in quadrature with p_{T} gives the magnitude $|\vec{p}|$ of the total momentum of the particle, $|\vec{p}| = \sqrt{(p_x)^2 + (p_y)^2 + (p_z)^2}$.

3.2.1 Magnet System

The momentum and charge of particles in the ATLAS detector are measured by bending their trajectories with magnetic fields through the ATLAS magnet systems [104]. This is done through the use of two different types of superconducting magnetic systems called the toroidal magnet systems, split into the barrel [105] and endcap [106], and the central solenoidal magnet system [107]. These systems are cooled to approximately 4.5–4.6 K to provide the necessary magnetic field strengths, a temperature which is achieved within a day of cooling for the solenoid magnet and five weeks of cooling for the larger toroid

magnets.

The central solenoid magnet surrounds the inner detector at the core of the experiment, and provides an axial magnetic field. It is 5.8 m long, with an inner diameter of 2.46 m, an outer diameter of 2.56 m, and a total mass of 5.7 tonnes, 5.4 T of which are from the coils themselves. The small thickness is designed to minimise the amount of interactions between the magnet and particles in the detector, as this information cannot be recorded. Despite being so thin it provides a 2 T magnetic field to the ID, achieved by embedding roughly 10 km of niobium–titanium (NbTi) superconducting wire inside pure aluminium (Al) strips. It stores an energy of 40 MJ with an energy-to-mass ratio of 7.4 kJ/kg, and has an operational current of 7.73 kA.

The toroid magnets surround the entire detector and provide a magnetic field to bend the trajectories of muons in the muon spectrometer. The toroid magnets are split into one large magnet surrounding the barrel of the ATLAS detector, and two further magnets which are situated at each end of the experiment in the endcaps of the detector. The central barrel toroid is the largest toroidal magnet ever built, with a length of 25.3 m, an inner diameter of 9.4 m, an outer diameter of 20.1 m, and a total mass of 830 tonnes. It provides a magnetic field for the range $|\eta| < 1.4$ and consists of eight coils each individually encased in stainless-steel vacuum vessels and provides an average magnetic field strength of approximately 0.5 T, achieved with roughly 56 km of NbTi wire. The total energy stored by the barrel toroid is 1.08 GJ, which has an operational current of 20.5 kA. The two endcap toroids are designed to bend the trajectories of muons leaving the detector near the beam pipe, and have a total mass of 239 tonnes each, with inner diameters of 1.65 m, outer diameters of 10.7 m, and lengths of 5.0 m. Each endcap toroid consists of eight coils which share a common cryostat and provides an average magnetic field strength of approximately 1.0 T, achieved with 13 km of NbTi wire per toroid, for the range $1.6 < |\eta| < 2.7$. The total energy stored by each endcap toroid is 0.25 GJ, and each has an operational current of 20.5 kA, similarly to the barrel toroid. The field integral of the toroids ranges between 2.0–6.0 Tm across most of the detector, and in the transition region $1.4 < |\eta| < 1.6$ the magnetic field is provided by a combination of the

barrel toroid and the endcap toroids.

3.2.2 Inner Detector

The inner detector [108, 109] is the innermost subsystem of the ATLAS detector and provides measurements close to the interaction point. Its primary purpose is to measure the momenta of charged tracks produced at the IP and to identify the production vertices of primary and secondary charge particles, based on the ionisation of the sensitive material by charged tracks. The layout of the ID consists of three main sections, and is shown in Figure 3.6. From smaller-to-larger radii three sections are the silicon pixel detector, the semiconductor tracker (SCT), and the transition radiation trackers (TRT). The entire ID is surrounded by the superconducting solenoid magnet, and is immersed in an approximately uniform 2 T axial magnetic field for the measurements of charged particle momenta. During the first long shutdown (LS1), before data-taking started in 2015 for Run 2, an additional pixel detector was installed inside the innermost layer of the ID called the insertable B-layer (IBL) [110, 111], exploiting the now-smaller beam pipe to obtain an additional measurement closer to the IP. The specific dimensions of each component are shown in Figure 3.7, including the newly installed IBL. The ID is split into the barrel at small pseudorapidity and the endcap at large pseudorapidity. In total the ID is 6.2 m long, with an inner radius of just 33.5 mm and an outer radius of 1.1 m. Overall the pixel detectors and SCT cover a pseudorapidity range $|\eta| < 2.5$ for tracking and the TRT covers a range $|\eta| < 2.0$ for tracking and the identification of electrons.

The silicon pixel detector [113] is the first point of detection in ATLAS, and consists of three layers of silicon pixel modules. Including the IBL, the four pixel detector layers typically provide three to four precise measurements per charged particle track, with a precision of 10 µm in r–ϕ and 115 µm in z for the barrel, and r for the endcaps. In total there are approximately 92 million pixels in the pixel detector, with a granularity of $50\times250\,\mu\text{m}^2$ in (ϕ, z) for the IBL, and $50\times400\,\mu\text{m}^2$ for the outer three layers. The four layers in the barrel contain 1736 sensor modules in total and the three layers in each

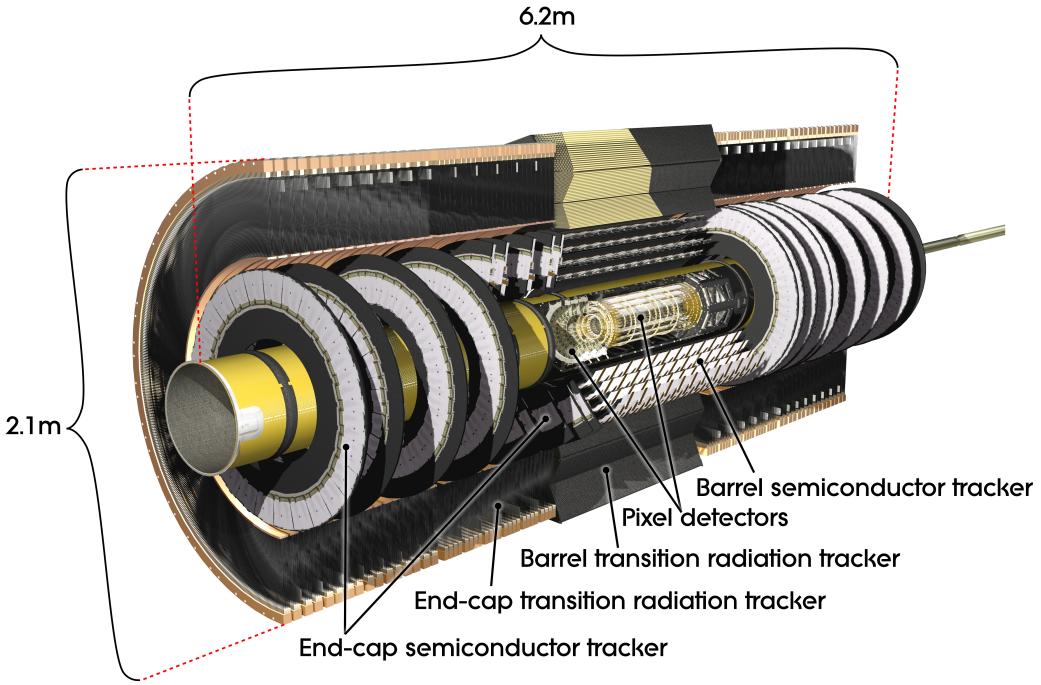


Figure 3.6: The layout of the ATLAS inner detector [4]. ATLAS Experiment ©2008 CERN.

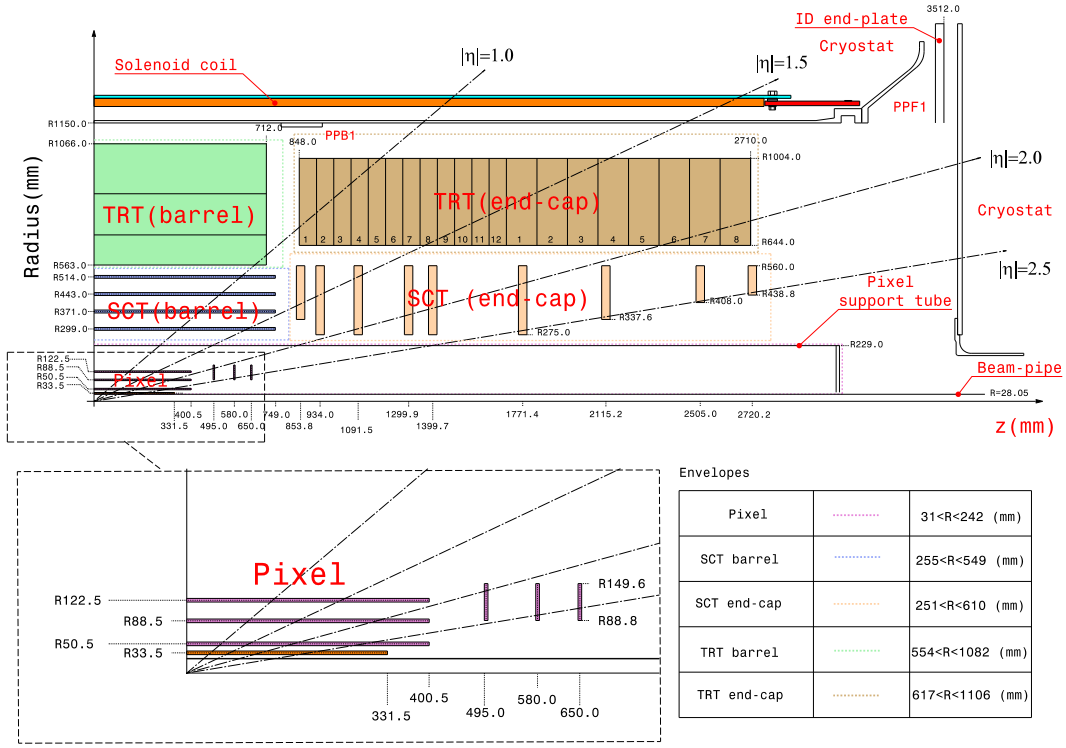


Figure 3.7: A schematic diagram of the layout of one quadrant of the ATLAS inner detector for Run 2 in the r–z plane [112].

endcap contains 288 modules. The innermost layers of the pixel detectors enhance the reconstruction of secondary vertices.

The SCT surrounds the pixel detector and contains eight strip layers, paired into four stereo strips, and typically provides up to eight measurements per track with a resolution of 17 µm in r–ϕ and 580 µm in z for the barrel, and r for the endcaps. In total there are approximately 6.3 million readout channels in the SCT, with a readout strip every 80 µm on the silicon. There are 4088 two-sided sensor modules in total. The SCT allows the impact parameters of each track to be measured and provides vertexing for heavy-flavour tagging and τ-lepton tagging.

The TRT surrounds the SCT and is made up of many layers of gas-filled drift tubes called straws. There are 300,000 straws each 4 mm in diameter with 30 µm gold-plated tungsten wires in their centres. The gas mixture used in the straws is primarily xenon (Xe), carbon dioxide (CO_2) and oxygen (O_2), with a ratio of Xe:CO_2:O_2 (70% : 27% : 3%) and a pressure of 5–10 mbar. During Run 1 of the LHC significant gas leaks were observed in the LHC. Many of these were repaired for Run 2, but for modules which still have leaks, an argon (Ar) mixture of Ar:CO_2:O_2 (70% : 27% : 3%) is used to mitigate the loss of Xe [114]. In the barrel region the straws are 144 cm long and are divided into two halves at $\eta \approx 0$. In the endcaps the straws are 37 cm long and are arranged radially in wheels. The total number of readout channels for the TRT is roughly 351,000, with approximately 35 measurements per track. Unlike the pixel detector and SCT, the TRT only provides information about the r–ϕ coordinates of the track, with a precision of 130 µm. However, the TRT is able to discern electrons from other charged particles such as pions, based on the fraction of hits for a given track (approximately 30) that lie above a high-energy threshold, corresponding to transition radiation.

3.2.3 Electromagnetic Calorimeter

The calorimetery system [115], shown in Figure 3.8, consists of high-density materials designed to absorb both charged and neutral particles, and active layers which measure the energy that they lose as they traverse the detector. The calorimeters are able to stop

most known particles, with the exception of muons and neutrinos, and are split into two components which cover a range of $|\eta| < 4.9$ in total.

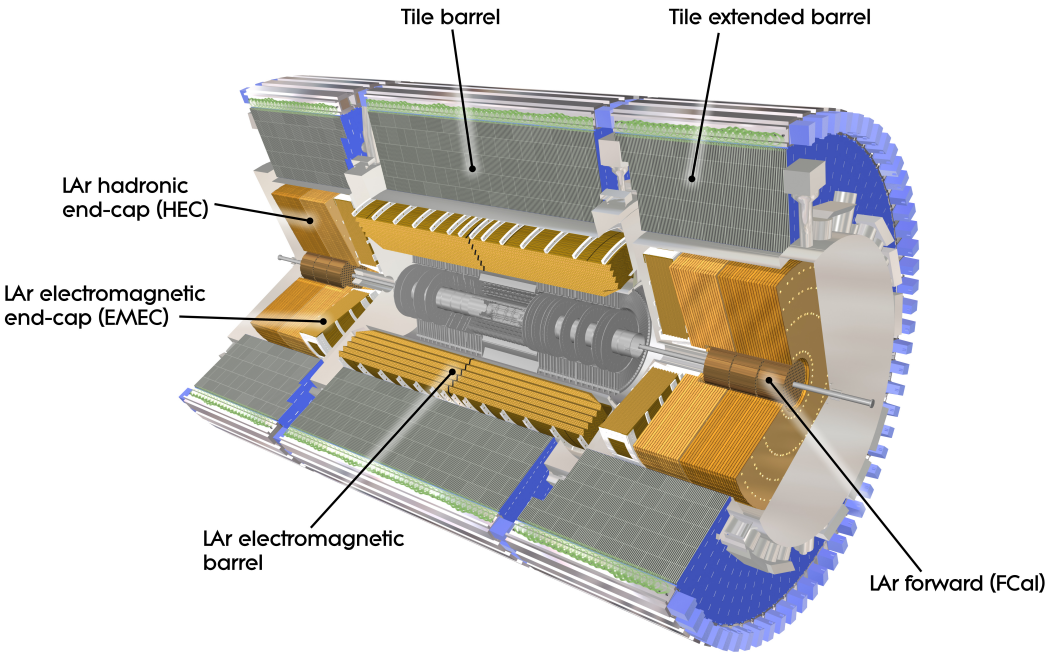


Figure 3.8: The layout of the ATLAS calorimeter system [4]. ATLAS Experiment ©2008 CERN.

The first component is the electromagnetic (EM) calorimeter [116], and is the inner of the two calorimeter systems. This is specialised in measuring the energy deposits of electromagnetic particles in the region $|\eta| < 3.2$, namely electrons, positrons and photons. The EM calorimeter consists of high-granularity (liquid argon) LAr sampling calorimeters with lead (Pb) absorbers and a characteristic accordion geometry, where the ionisation of the LAr from the showers produced by incoming particles produces an electric current which is used to measure the energy of the original particle. It is divided into a barrel component for $|\eta| < 1.475$ and two endcap components for $1.375 < |\eta| < 3.2$. To keep the argon in a liquid state, the LAr calorimeters are cooled to a temperature of 89 K. The EM calorimeter shares a common vacuum vessel with the central solenoid magnet to reduce the number of vacuum walls, minimising interactions in the support structure which cannot be measured, and provides a complete symmetry in ϕ without any cracks. The barrel part is separated into two halves at $z = 0$ with a separation of 4 mm and has

roughly 100,000 readout channels. Each endcap is separated into two coaxial wheels with an inner wheel covering $1.375 < |\eta| < 2.5$ and an outer wheel covering $2.5 < |\eta| < 3.2$, and each endcap has roughly 62,000 readout channels. In the range $|\eta| < 2.5$ for precision physics, the EM calorimeter is separated into three layers, whereas for the range of the endcap outer wheels, $2.5 < |\eta| < 3.2$, the calorimeter is separated into two layers. The coverage from $3.1 < |\eta| < 4.9$ is provided by the forward calorimeter, which consists of a LAr module with a copper (Cu) absorber optimised for EM calorimetry. An additional thin LAr presampler covers the range $|\eta| < 1.8$ to correct for energy losses upstream of the calorimeter. This consists of an active LAr layer with a thickness of 1.1 cm in the barrel region, covering $|\eta| < 1.52$ with 7808 readout channels, and 0.5 cm in the endcap region, covering $1.5 < |\eta| < 1.8$ with 1536 readout channels each.

3.2.4 Hadronic Calorimeter

The second of the calorimeters is the hadronic calorimeter [117], which surrounds the EM calorimeter. This is specialised in measuring the energy deposits of hadronic particles, such as pions, kaons, neutrons and protons, which do not deposit all of their energy in the EM calorimeter. In the region $|\eta| < 1.7$ the hadronic calorimeter is made of a high density material consisting of layers of steel and plastic scintillating tiles, and is called the tile calorimeter. As particles hit the steel they cause showers of particles which produce photons in the scintillating material. The photons are collected and converted into an electric current with an intensity proportional to the original particle's energy. The tile calorimeter is separated into the barrel region for $|\eta| < 1.0$ and two extended barrel regions for $0.8 < |\eta| < 1.7$. Each component has an inner radius of 2.28 m, an outer radius of 4.25 m, and are divided into 64 modules azimuthally and segmented into three layers radially.

The hadronic calorimeters in the endcaps use LAr technology with a Cu absorber and cover the range $1.5 < |\eta| < 3.2$, with some overlap in $|\eta|$ between both the tile calorimeter and the hadronic forward calorimeters to reduce the drop in material density in the transition regions. There are two independent wheels per endcap, located directly

behind the endcap calorimeters of the EM calorimeter. The hadronic and EM calorimeter endcaps share a crysostat for the cooling of the LAr. Each of the two endcap hadronic calorimeters are built from 32 identical wedge shaped modules and are divided into two segments in depth to give four layers per endcap, and have an inner radius of 0.475 m (except for in the overlap region with the forward calorimeter, where the inner radius is 0.372 m) and an outer radius of 2.03 m. The coverage from $3.1 < |\eta| < 4.9$ is provided by the forward calorimeter, which consists of two LAr modules with a tungsten (W) absorber optimised for hadronic calorimetry.

3.2.5 Muon Spectrometer

The outermost layer of the ATLAS detector is the muon spectrometer [118], shown in Figure 3.9. It specialises in the identification and reconstruction of muons, which are able to escape the ID and the calorimeters. It measures their deflection by the magnetic field generated by the superconducting toroidal magnets, where the field integral ranges from 2.0–6.0 Tm. It is separated into four subsystems, called the thin-gap chambers (TGC), resistive-plate chambers (RPC), monitored drift tubes (MDT) and the cathode strip chambers (CSC).

The MDTs and CSCs are designed for precision tracking of muons and cover a range of $|\eta| < 2.7$. The MDTs are arranged in three main layers and primarily cover the barrel region of the detector for $|\eta| < 2.7$, where the innermost layer covers $|\eta| < 2.0$. There are 354,000 drift tubes in total, spread across 1150 chambers. Each chamber consists of three to eight layers of drift tubes operated at 3 bars of pressure with a gas mixture of Ar:CO_2 (93% : 7%), and achieve an average resolution of 80 µm per tube and about 35 µm per chamber. The CSCs are a type of multiwire proportional chamber with cathods segmented into strips in orthogonal directions, and cover the endcap region with high granularity between $2.0 < |\eta| < 2.7$ where the background rate is higher. There are 31,000 channels per endcap, spread across 32 chambers each. The resolution of each chamber is 40 µm in the bending plane and roughly 5 mm in the transverse plane.

The RPCs and TGCs are used for triggering and an additional measurement of the co-

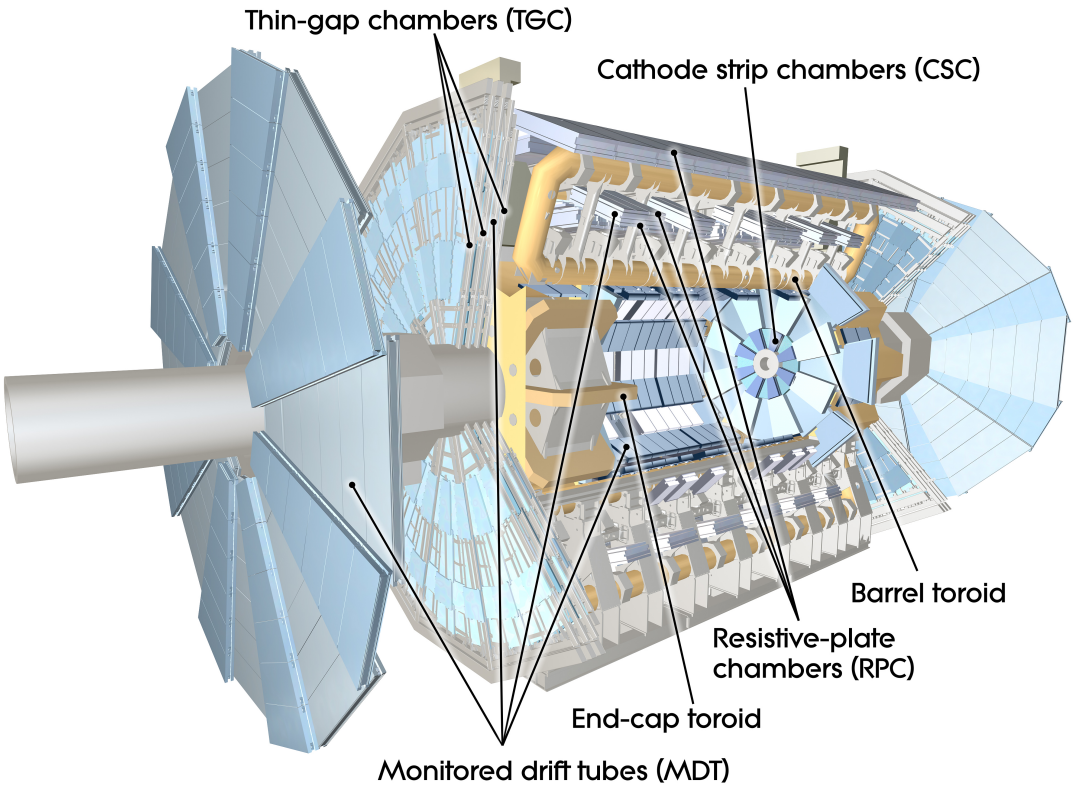


Figure 3.9: The layout of the ATLAS muon spectrometer [4]. ATLAS Experiment ©2008 CERN.

ordinates of each muon in ϕ, which is in the non-bending plane, and η which is in the bending plane. The precision-tracking chambers are specialised in the measurement of the η coordinate of each muon. These are matched with the η coordinates measured by the trigger system, and the ϕ coordinate measured by the trigger system is subsequently adopted as the second coordinate of the muon. The trigger chambers also provide information for the identification of bunch crossings due to their time resolution of 15–25 ns and to provide well defined p_{T} thresholds. The muon trigger system covers a range $|\eta| < 2.4$, where coverage in the barrel for $|\eta| < 1.05$ is provided by the RPCs and coverage in the endcap for $1.05 < |\eta| < 2.4$ is provided by the TGCs. The TGCs additionally cover the range up to $1.05 < |\eta| < 2.7$ for measurements of the second coordinate. In total there are 373,000 channels in the RPCs spread across 606 chambers, and 318,000 channels in the TGCs spread across 3588 chambers.

3.3 Data Acquisition and Physics Performance

Raw information measured by the ATLAS detector needs to be processed to determine which events should be retained for further analysis, as well as for the reconstruction and identification of physics objects in passing through the detector resulting from the collisions. This section describes the methods ATLAS uses to trigger on and record interesting events and a selection of algorithms and processes used to reconstruct and identify physics objects that are relevant in the scope of this thesis.

3.3.1 Data Acquisition and Triggers

With a bunch crossing rate of 25 ns and an average of 36 *pp* interactions per bunch crossing in 2018, the ATLAS detector must cope with approximately 1.6 B collisions per second, which corresponds to a data volume of approximately 60 TB every second. Only a small fraction of these collisions contain interesting information for use in further studies. To reduce the huge amount of data flowing through the detector to manageable levels, ATLAS employs a two-level trigger system to pick events with interesting characteristics [119, 120]. The layout of the trigger and data acquisition system (TDAQ) used throughout Run 2 is shown in Figure 3.10.

The first-level trigger (L1) is hardware based and works on a basic subset of information from the calorimeters and muon spectrometer. This decides whether or not to keep an event within 2.5 µs of an it occuring, and reduces the data flow from 40 MHz down to a level of 100 kHz, which is passed on to the software-based second-level trigger. The second-level trigger, also known as the high-level trigger (HLT), uses the full information of each event measured by the detector and performs detailed analyses of the information from the specific detector regions using a farm of approximately 40,000 CPU cores. In roughly 200 µs the HLT is able to filter the 100 kHz of data to a rate of 1 kHz for permanent storage. The stored events are then able to be used in detailed analyses offline. Throughout Run 2 approximately 1500 individual event selections were available in the trigger menu, where the bandwidth and chosen physics signatures of each trigger reflect the physics goals of the experiment.

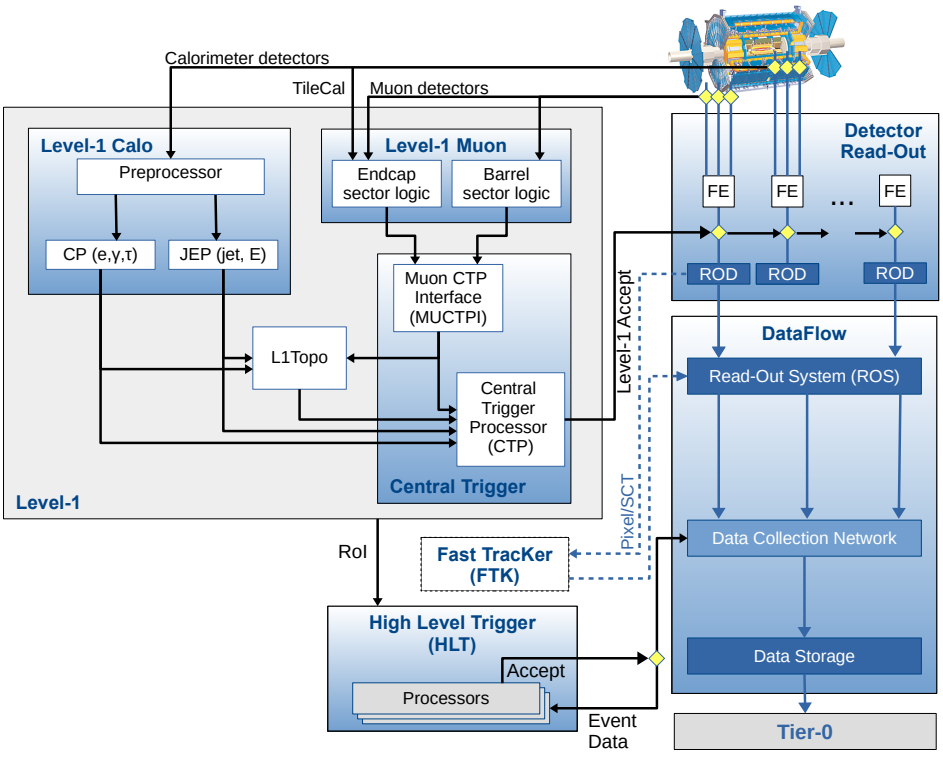
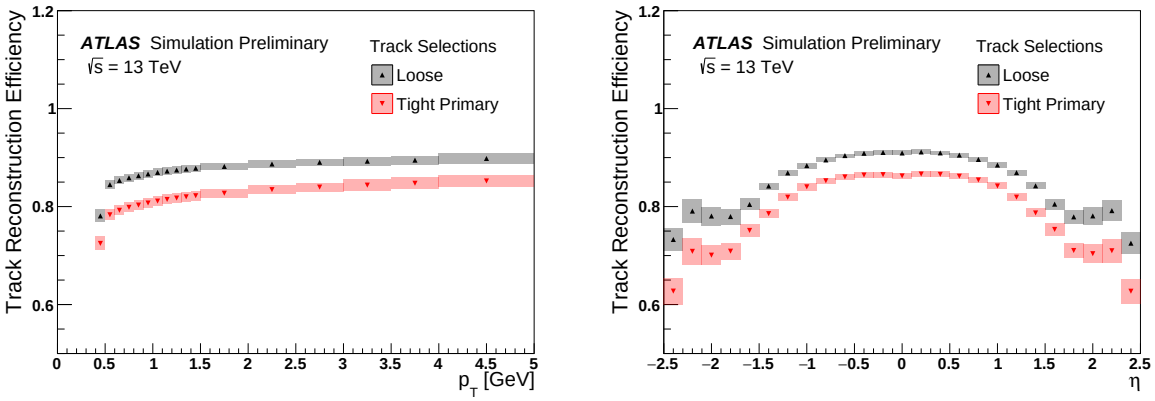


Figure 3.10: A flowchart of the ATLAS trigger and data acquisition system operating throughout Run 2 [120].

3.3.2 Tracks and Vertices

The reconstruction of charged particle tracks is primarily performed by the ID. Tracks which reach the detector consist primarily of electrons, protons, pions, kaons and muons. Most other particles decay in the beam pipe before they can reach the ID. Track reconstruction is performed through a sequence of algorithms that use measurements from the different components of the ID [121, 122], and can reconstruct tracks with $p_{\mathrm{T}} > 400$ MeV and $\eta < 2.5$. The first stage is the inside-out pattern recognition sequence which seeds tracks starting from the pixel detectors and performs hit finding into the outer edge of the ID using a combinatorial Kalman filer [123]. The second stage is the ambiguity solver which resolves fake and overlapping track candidates found during the crude pattern recognition. The third stage extends the tracks from the silicon detectors into the TRT. A complementary outside-in pattern recognition sequence is also used starting from the TRT and moving towards the pixel detectors. This is particularly helpful in resolving secondary particles such as from displaced $K_s \to \pi^+\pi^-$ decays or photon conversions

($\gamma \to e^+e^-$) which don't always have hits in the silicon detectors. Figure 3.11 shows the ID track reconstruction efficiency versus track p_{T} and η using minimum bias events. The loose and tight requirements are based on both the kinematic requirements on p_{T} and η above, and on the number of hits and holes (missing hits) of the track in the silicon detectors. The selections are defined in Ref. [124].



(a) (b)

Figure 3.11: The efficiency of the ATLAS inner detector to reconstruct tracks (a) versus track p_{T} and (b) versus track η [124].

Primary vertices in ATLAS, the vertices of the pp collisions themselves, are reconstructed using an iterative vertex finding algorithm described in Ref. [125], split into two stages. The first stage is the primary vertex finding algorithm which is designed to associate tracks with vertex candidates, the second is the χ^2-based vertex fitting algorithm which is designed to reconstruct the position of the vertex with its corresponding error matrix. The fitting stage also refits the tracks associated with the vertex to constraining them to originate from the interaction point. Vertices are seeded in the finding stage by searching for a global maximum in the z coordinates of tracks in an event. Tracks which are incompatible with this vertex by more than 7σ are used to seed new vertices. The vertex reconstruction efficiency versus number of tracks in the event is shown in Figure 3.12.

3.3.3 Photons and Electrons

Photons and electrons are reconstructed with similar methods in ATLAS, as both interact in the EM calorimeter to form showers. The main difference is that electrons additionally

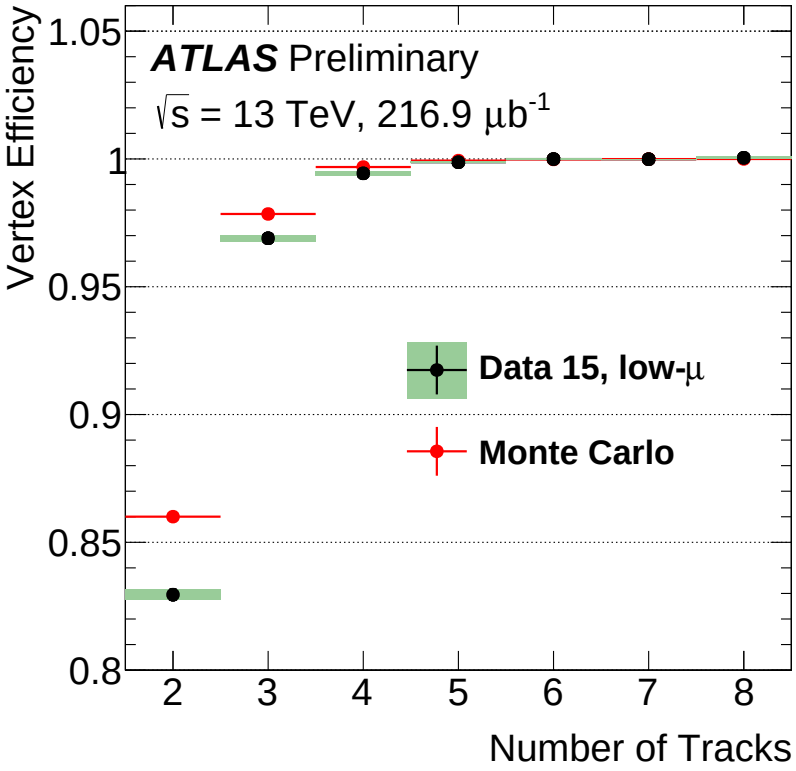
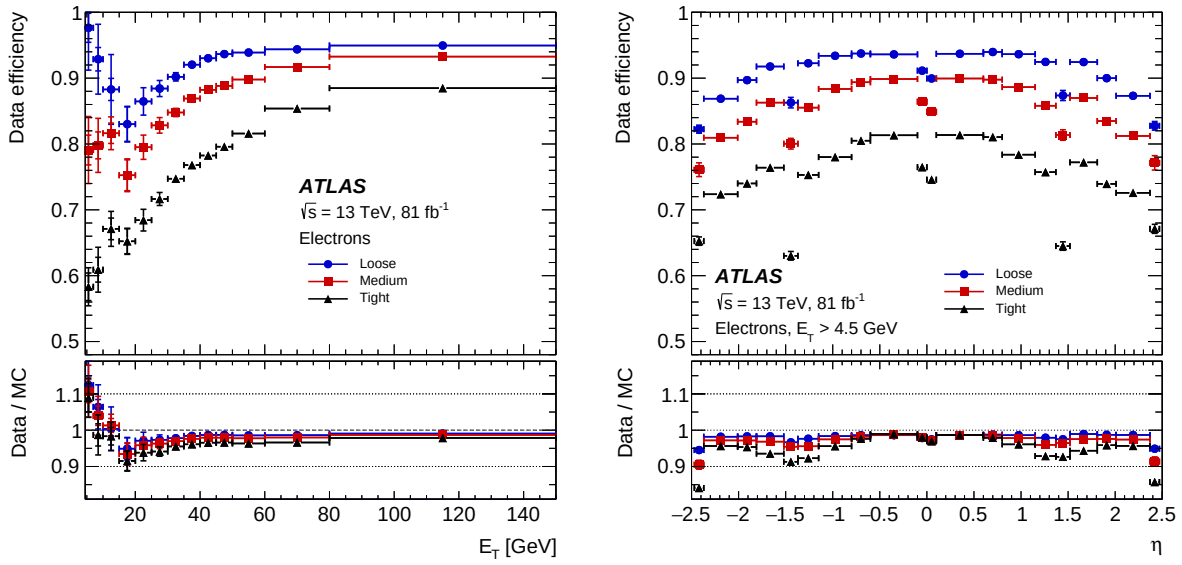


Figure 3.12: The efficiency of vertex reconstruction in ATLAS versus number of tracks in the event in low-μ data, where μ is the average number of interactions per bunch crossing [126].

leave a track in the ID. Photon candidates are either converted, where they interact in the ID and are converted into a pair of electrons, $\gamma \to e^+e^-$, or unconverted where they only interact in the EM calorimeter. Electron and photon reconstruction is performed in the region $|\eta| < 2.47$ and is based on clusters of energy deposits in the EM calorimeter [127]. Clusters that match a reconstructed ID track which is consistent with originating from an electron produced at the IP are classed as electrons. Clusters without matching ID tracks are classed as unconverted photons. Clusters matched to a single ID track consistent with a photon conversion or a two-track vertex consistent with a photon conversion are classed as converted photons, including requirements on the number of hits in the innermost pixel detector layers and the number of high-threshold hits in the TRT.

Three identification criteria which vary in purity are defined for electrons, based on likelihood-methods using information from both the EM calorimeter and the ID. In order of most-to-least pure, these are 'tight', 'medium', and 'loose', and are defined in detail in Ref. [128]. Both calorimeter-based and track-based isolation variables are used in

electron identification. Figure 3.13 shows the reconstruction efficiency for each electron identification criteria versus p_{T} and η.



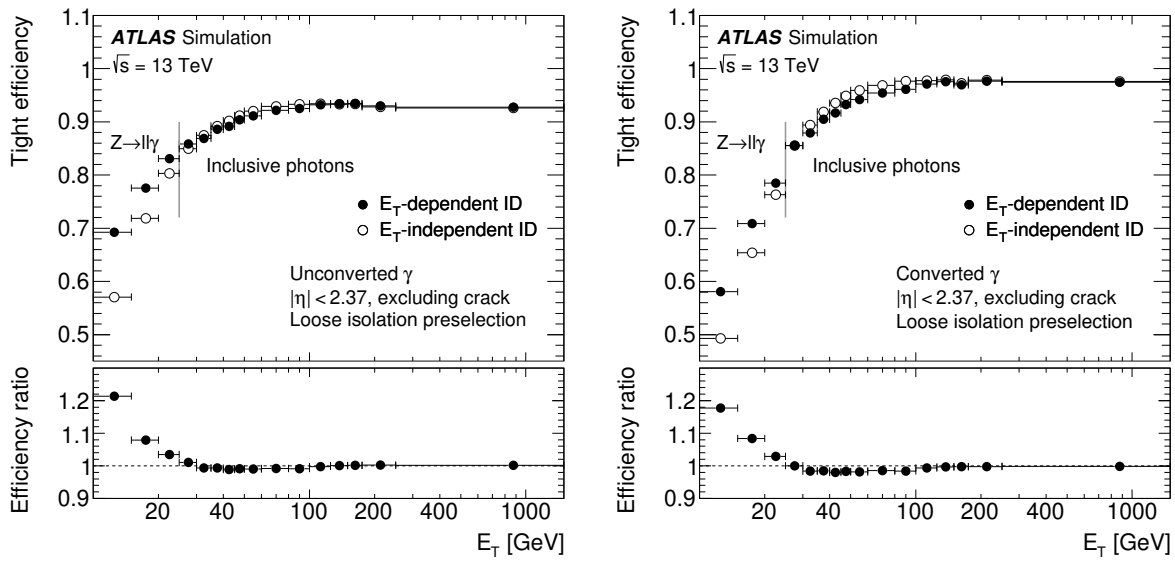
(a) (b)

Figure 3.13: The efficiency of the ATLAS inner detector to reconstruct electrons (a) versus track p_{T} and (b) versus track η [129].

Two identification criteria are defined for photons based on the shapes of the showers in the calorimeter as well as isolation criteria. These are 'tight' and 'loose', and are defined in detail in Ref. [130]. Figure 3.14 shows the reconstruction efficiency of tight photons versus E_{T} for both converted and unconverted photon candidates.

3.3.4 Muons

Muons are the only particles other than neutrinos that are able to reach the muon spectrometer. Reconstruction of muons is first performed independently in the ID and the MS, and the information from each component is combined to form the final muon tracks that are used in physics analyses [131]. In the ID, muons are reconstructed like any other charged particle track. In the MS, muons are reconstructed by searching for hit patterns in each muon chamber to form track segments using Hough transforms [132]. Muon candidates are built from fitting together hits from track segments in different layers of the MS and an overlap removal procedure is used to resolve which tracks to assign each hit.



(a) (b)

Figure 3.14: The efficiency of the ATLAS inner detector to reconstruct (a) unconverted photons and (b) converted photons versus E_{T} [129].

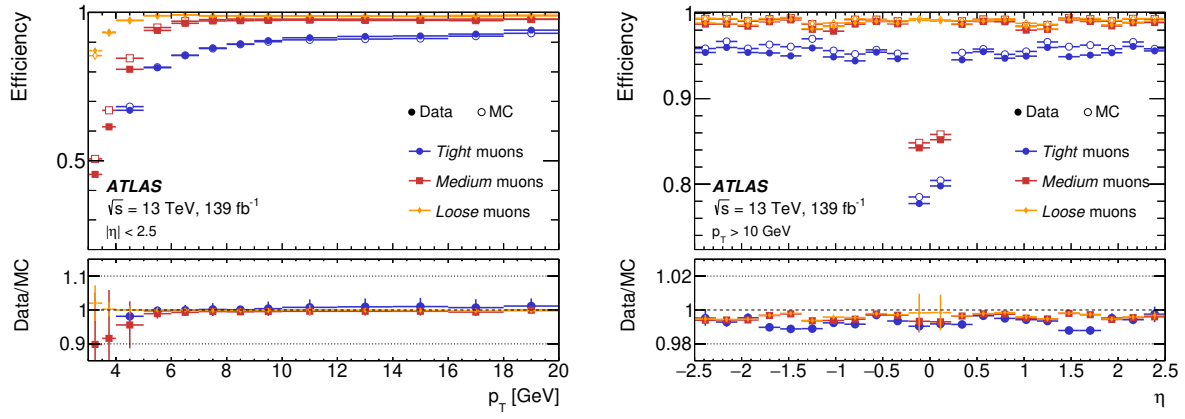
The combined ID-MS reconstruction is performed using information from the ID, MS, and the calorimeters. There are four types of muon, defined depending on which detector components are used in their reconstruction. The first type is the combined (CB) muon, where full tracks are reconstructed independently in the ID and the MS, and a combined track is formed using a global refit where MS hits can either be added or removed to the track candidate. Most CB muons are formed with an outside-in pattern recognition approach starting from the MS and extrapolated inwards to match an ID track, but an inside-out pattern recognition is also used as a complementary approach, starting from the ID and extrapolating outwards. The second type is the segment-tagged (ST) muon, where ID tracks are classified as a muon if they match at least one track segment in the MDT or CSC chambers when extrapolated to the MS. These are used when muons only cross one layer of the MS, such as low-p_{T} muons or muons which fall in MS regions with low acceptance. The third type is the calorimeter-tagged (CT) muon, where a track in the ID is identified as a muon if it is matched to an energy deposit in the calorimeters which are consistent with a minimum-ionising particle. This type of muon is optimised for the region $|\eta| < 0.1$ where the MS is only partially instrumented. The fourth type of muon is the extrapolated (ME) muon, where the MS has not matched an ID track but

is loosely compatible with originating from the IP when the track is extrapolated, taking into account energy lost in the calorimeters. This type of muon is used to extend the acceptance of muon reconstruction into the range $2.5 < |\eta| < 2.7$ which is outside of the geometric acceptance of the ID. If an ID track is shared between muons of several types, preference is given to CB muons which are the highest purity, then to ST muons and finally to CT muons.

Muons are further categorised according to several identification criteria which have varying purity, and are useful depending on the requirements of the specific physics analysis. The three inclusive identification criteria are 'medium', 'loose' and 'tight', whilst a fourth 'high-p_{T}' criteria is provided for muons with $p_{\mathrm{T}} > 100$ GeV which is optimised for searches for high-mass Z' and W' resonances [133, 134]. The full selection criteria is presented in Ref. [131], but in general medium muons are the default identification criteria used in analyses. These minimise systematic uncertainties associated with muon reconstruction and only include CB and ME muon tracks. The loose selection criteria maximises reconstruction efficiency whilst still providing good quality muon tracks, and include all types of muon tracks. This criteria is optimised specifically for Higgs boson candidates in the four-lepton final state [135] and all CB and ME muons that satisfy the medium criteria are included in the loose selection. The tight selection criteria maximises the purity of the muons at the expense of some efficiency, and only CB muons are inclued. Figure 3.15 shows the performance of the ATLAS experiment in reconstructing muons in the loose, medium, and tight categories versus muon p_{T} and muon η [136].

3.4 Software and Simulation

The interpretation, reconstruction and analysis of data obtained by the detector is a vital part of the ATLAS experiment, and is largely based on software. For this purpose the Athena framework was developed [137, 138], which is built primarily on the Gaudi framework [139]. Analyses are typically structured such that Athena is used to process bulk data from the experiment and select relevant information; the output of this is often a more manageable ROOT [140] file that is used for the final studies, depending on the



(a) (b)

Figure 3.15: The efficiency of the ATLAS inner detector to reconstruct muons (a) versus track p_{T} and (b) versus track η [136].

particular investigation.

Reconstructed information from the experiment is stored in the 'AOD' data format, which contains the full information of each event. Before they are used in any analyses a second processing is often used, known as derivation, to reduce the information stored to just that useful in the specific physics analysis. The derivations perform selections on the events to either skim them (reject the event entirely), slim them (reduce the number of variables stored in an event for each object to only that which is necessary in the analysis), or thin them (remove physics objects that are unnecessary). The primary advantage of these derived AODs, known as DAODs, are their small size compared to full AODs, making them significantly easier to handle.

The simulation of physics events plays an important role towards understanding of the response of the ATLAS detector. The Monte Carlo (MC) technique is vital in the simulation of events, and can be achieved through the use of particle generators, such as Pythia8 [141, 142] and Sherpa [143], which generate physics events at truth level. Once generated, truth-level events can be simulated in the ATLAS detector using Geant4 [144, 145] and processed with the ATLAS tracking software in Athena. Many packages are available for this purpose, which vary in computation time and detail. The most detailed simulation of ATLAS, called full-sim, fully simulates each event through the detector geo-

metry with GEANT4. However, to save on computational time, some faster simulations exist such as ATLFAST-II [146], which simulates the ID and the MS with GEANT4 but uses a parameterised approach to simulate the response of the calorimeters. Once simulated, events are reconstructed with the same techniques used to process real physics events and can be studied using the same analytical tools.

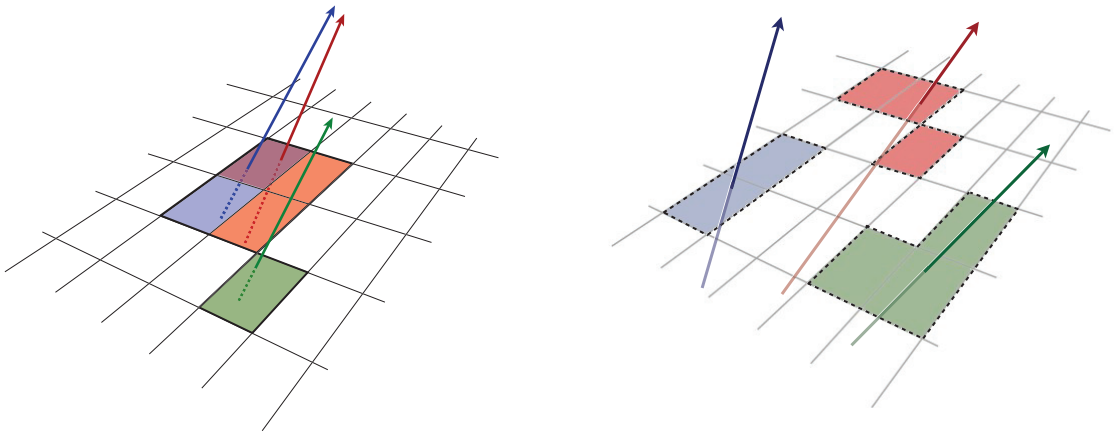
4 Feasibility Study for a Data-Driven Measurement of Inner Detector Track Reconstruction Efficiency in Dense Environments

Dense environments are regions in a detector where the separations between particles from an interaction are of the order of the granularity of the detector sensors being traversed, such that resolving the separate particles becomes challenging. With the increase of centre-of-mass energy of LHC proton–proton collisions from $\sqrt{s}$ = 7–8 TeV in Run 1 to $\sqrt{s}$ = 13 TeV in Run 2, the production rates of boosted objects such as high-p_{T} jets have increased [147, 148], and tracking in dense environments such as in the cores of these jets has grown increasingly important. Boosted objects in hadronic final states are sensitive probes to potential new physics, and in such cases studies of jet substructure could be crucial to unveil the underlying physics [149]. Physics analyses in these dense environments include signatures involving boosted, hadronically decaying τ-leptons [150, 151] and high-mass diboson resonances [40, 152–156]. In particular, the decay $\phi \to K^+K^-$ forms a two-particle dense environment [157, 158] as the small difference between the sum of masses of the two kaons and the ϕ meson mass leads to a small opening angle between the kaons, such that the two charged kaons are close to each other as they traverse the detector. The reconstruction of ϕ mesons in this decay channel is vital to measurements of CP violation in the B_s-meson decay $B_s^0 \to J/\psi\,\phi$ [159–165], as well as in searches for exclusive decays of the Higgs and Z bosons to $\phi\,\gamma$ directly relevant to this thesis [91, 93].

Events with dense environments are also important in several performance studies such as jet energy scale calibration [166], the calibration of jet mass in large radius jets [167], the determination of systematic uncertainties on the measured jet energy scale and measurements of substructure observables [168–172] distinguishing jets of different origins from each other [173–176], the identification of b-jets [177–180], and the reconstruction of hadronically decaying τ-leptons [181, 182] which is important in the context of the exclusive

Higgs and Z boson decay triggers for hadronic final states.

The dense cores of high p_{T} jets and τ-leptons are characterised by separations between charged particles on the order of the granularity of the pixels in the ATLAS inner detector such that they may overlap, as in Figure 4.1(a). The charged particles forming these merged clusters are more challenging to reconstruct compared to isolated charged parcticles that form single-particle clusters, such as in Figure 4.1(b). A neural network based approach was implemented during Run 1 to identify merged clusters created by multiple charged particles [183]. This was optimised for dense enviroments for Run 2 following a targeted overhaul of the ambiguity processing stage of the track reconstruction chain [184], motivated by the increased potential to study boosted objects due to the increase of centre-of-mass energy in Run 2 compared to Run 1.



(a) (b)

Figure 4.1: Illustration of energy deposits on a pixel sensor: (a) merged clusters, from the deposits of highly collimated charged particles, and (b) isolated, single-particle clusters. Different colours represent energy deposits from different particles, with the particle trajectories represented by the arrows. The aspect ratio of the pixels is not drawn to scale. From Ref. [185].

The performance of the ATLAS track reconstruction algorithms in dense environments was evaluated at the start of Run 2 [185–189]. In particular in Ref. [185], the efficiency to reconstruct charged particles in boosted decays that result in dense environments such as $\rho \to \pi^+\pi^-$ and $\tau \to \pi^+\pi^-\pi^\pm\nu_\tau$, as well as to reconstruct charged particles near jets, was estimated based mainly on simulation. A technique to probe the performance of track reconstruction in data, first used in Ref. [187], was used to measure the relative number

of tracks lost in reconstruction due to the collimation of charged particles in high-p_{T} jets.

Currently no data-driven method exists to measure the efficiency to reconstruct charged particles in dense environments analogous to the $\rho \to \pi^+\pi^-$ and $\tau \to \pi^+\pi^-\pi^\pm\nu_\tau$ studies with simulation, where the expected number of tracks in the final state is known. The decays $J/\psi \to \mu^+\mu^-$ and $\phi \to \mu^+\mu^-$ provide a potential opportunity to measure the track reconstruction efficiency in dense environments where two particles overlap in the detector, by exploiting the different methods to reconstruct muons in the ATLAS detector [131]. The capability of the ATLAS detector to reconstruct muon candidates both in the ID and MS independently allows for the performance of the ID to be measured based on muons reconstructed in the MS. A tag-and-probe method is investigated, similar to those used in measurements of the muon reconstruction efficiency [136], where the tag muon must be successfully reconstructed in both the ID and MS and the probe must at least be reconstructed in the MS. The test considers whether the probe muon was also reconstructed in the ID.

This chapter explores the feasibility of implementing this data-driven tag-and-probe method to measure the efficiency of the ID to reconstruct both muons in boosted $J/\psi \to \mu^+\mu^-$ and $\phi \to \mu^+\mu^-$ decays, and how this depends on the separation between the two muons by categorising events according to muon transverse momentum, p_{T}, or angular separation, $\Delta R = \sqrt{(\Delta\phi)^2 + (\Delta\eta)^2}$. Section 4.1 describes an analytical study of the dependence of charged particle separation on p_{T} and ΔR, accounting for the bending of their trajectories due to the ATLAS solenoid magnet. Section 4.2 describes a study using MC simulation to identify under which conditions track reconstruction efficiency is expected to decrease, to establish the requirements for a data-driven measurement. Section 4.3 discusses the prototype analysis of $J/\psi \to \mu^+\mu^-$ decays using 139 fb^{-1} of ATLAS proton–proton collision data collected at $\sqrt{s} = 13$ TeV, and Section 4.4 discusses the potential to of apply the same method on $\phi \to \mu^+\mu^-$ decays. Finally, Section 4.5 highlights some of the considerations to take into account in this tag-and-probe method in terms of biases and additional efficiencies that may affect the result, and the conclusions of the investigation are summarised in Section 4.6. In this context, a re-sampling

method to model the background in searches with boosted phase-spaces was developed.

4.1 Analytical Investigation of Charged Particle Separation

To fully understand any data-driven or Monte Carlo based study on the capability of the ID to successfully resolve close-by charged particles, it is important to understand from first principles the trajectory of charged particles in the detector and how this can relate to a decrease in efficiency in dense environments. This section discusses how the magnetic field in the ATLAS detector alters the trajectory of charged particles traversing the ID, as well as the separation between same and oppositely charged particles at a given radius from the interaction point. The dependence of particle separation on their p_{T} and ΔR is also studied, and this is used to predict the behaviour of the decrease in ID efficiency, under the assumption that particles that overlap more have a lower efficiency to be reconstructed as two separate tracks.

4.1.1 Bending of Charged Particles in the Magnetic Field

As discussed in Section 3.3, the Lorentz force causes charged particles to bend in magnetic fields, and the curving of charged particles in the r–ϕ plane of the ATLAS detector caused by the axial magnetic field is vital to measure their momentum. The higher the p_{T} of the particle, the harder it is to deflect for a given magnetic field strength, such that the radius of curvature of the particle is a smaller. The trajectory of a particle forms the arc of a helix as it traverses the detector. The sagitta of the arc, the distance from the midpoint of the arc to the midpoint of its chord, in the r–ϕ plane is used to measure p_{T}. The important quantity in this study is the radius of the circle that the arc traces in r–phi, called the radius of curvature r_{mag} of the particle. The calculation of the arc length of deflection, S_{mag}, caused by this bending in the axial magnetic field is summarised diagramatically in Figure 4.2.

Using the Lorentz force, the relation between r_{mag}, the p_{T} of a particle with charge q, and the magnetic field strength B is

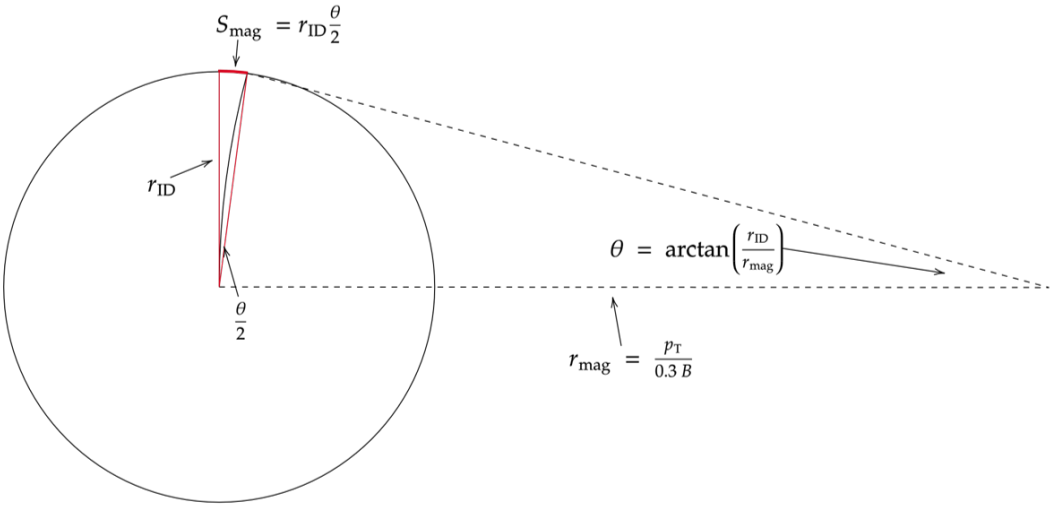


Figure 4.2: Calculation of the arc length, S_{mag}, of the deflection to a particle's trajectory caused by the axial magnetic field.

$$r_{\text{mag}} = \left|\frac{p_{\text{T}}}{qB}\right| \approx \left|\frac{p_{\text{T}}}{0.3B}\right|$$

for the specific set of units r_{mag} [m], p_{T} [GeV], q [|e|], where e is the charge of an electron, B [T] which is approximately 2 T throughought the ID, and 0.3 is a dimensional constant.[2] The charge is omitted as $q = \pm 1$ for all SM charged particles which traverse the detector. Whether the particle is positively ($q = 1$) or negatively ($q = -1$) charged does not affect the magnitude of r_{mag} but it does change the direction of the trajectory, such that particles with opposite charges will bend in opposite directions. From trigonometry, the angle of the arc θ traced out by a particle at a given radius r_{ID} in the ID is

$$\theta = \arctan\left(\frac{r_{\text{ID}}}{r_{\text{mag}}}\right).$$

Using this angle combined with the alternate segment theorem and the inscribed angle theorem of circular geometry, S_{mag} is

$$S_{\text{mag}} = r_{\text{ID}}\frac{\theta}{2} = \frac{r_{\text{ID}}}{2} \cdot \arctan\left(\frac{r_{\text{ID}}}{r_{\text{mag}}}\right) = \frac{r_{\text{ID}}}{2} \cdot \arctan\left(0.3 \cdot \frac{r_{\text{ID}}B}{p_{\text{T}}}\right).$$

[2]The true value is $c \times 10^{-9}$ where c is the speed of light in ms^{-1}.

The radius of the Insertable B-Layer (IBL), the innermost layer of the ATLAS ID, is used for the purposes of this study, such that $r_{\mathrm{ID}} = 33.5\,\mathrm{mm}$. As r_{ID} and B are fixed in the ATLAS detector, the size of S_{mag} at the IBL depends only on the p_{T} of the charged particle.

4.1.2 Separation between Charged Particle Pairs

The angular separation between two particles at their production vertex, the point where they are produced, is described by the quantity $\Delta R = \sqrt{(\Delta\phi)^2 + (\Delta\eta)^2}$, which is the sum in quadrature between the separation in azimuthal angle $\Delta\phi$ and pseudorapidity $\Delta\eta$ of the two particles. If there were no magnetic field in the ATLAS detector, the particles would travel in straight lines, and their separation in the r–ϕ plane at the IBL S_{sep} would simply be the length of the arc traced out by the angle $\Delta\phi$, $S_{\Delta\phi} = r_{\mathrm{ID}} \cdot \Delta\phi$. However, in the presence of the magnetic field, the particles are each deflected with the additional arc length $S_{\mathrm{mag}}(p_{\mathrm{T}})$. The separation between particle pairs at the IBL is therefore influenced both by their angular separation ΔR and the bending of the particles caused by the magnet, which directly depends on p_{T}. As there is no magnetic deflection in the r–η plane, particle separation in this dimension is determined only by $\Delta\eta$, such that a smaller ΔR does probe smaller particle separation in this plane.

For simplicity, the particles considered here have the same p_{T} such that the magnitude of S_{mag} is the same for each particle. In the case of two particles with the same charge, the particles bend in the same direction, such that any change in their separation due to S_{mag} cancels out, and $S_{\mathrm{sep}} = S_{\Delta\phi}$, as shown in Figure 4.3(a). In the case of two particles with opposite charges, the more relevant situation in this study, the particles bend in opposite directions such that the separation due to S_{mag} does not cancel, and $S_{\mathrm{sep}} = |2S_{\mathrm{mag}}(p_{\mathrm{T}}) + S_{\Delta\phi}(\Delta\phi)|$, where S_{mag} is defined as positive definite and the sign of $S_{\Delta\phi}$ can change depending on the charge arrangement of the two particles. A change in sign of $\Delta\phi$ is equivalent to swapping the charges of the two particles. A positive $S_{\Delta\phi}$ corresponds to the particles bending away from each other as in Figure 4.3(b); a negative $S_{\Delta\phi}$ corresponds to the particles bending towards each other as in Figure 4.3(c). When

the deflection by the magnets is small compared to the separation from $\Delta\phi$, such that $2S_{\text{mag}} < S_{\Delta\phi}$, decreasing $\Delta\phi$ (and thus ΔR) will overall reduce S_{sep} at the IBL. However if the two particles bend towards each other and $2S_{\text{mag}} = |S_{\Delta\phi}|$, they will cross over each other; decreasing $\Delta\phi$ further will result in the total separation S_{sep} increasing, as shown in Figure 4.3(d). In this case a smaller ΔR does not correspond to a smaller particle separation in the ϕ plane.

Track reconstruction efficiency decreases when the separation between particle trajectories is small in the ID as their overlap makes it more likely for merged clusters to be formed in the pixel layers, which are more difficult to resolve. Figure 4.4 shows an analytical calculation of the separation between $p_{\text{T}} = 30$ GeV particles at the IBL in $\Delta\eta$ and $\Delta\phi$, where ΔR contours are denoted as grey circles. In Figure 4.4(a) the two particles have the same charge, such that bending by the magnets has no net effect on the particle separation and the minimum separation is proportional to ΔR. Conversely, in Figure 4.4(b), the particles have opposite charge and the bending by the magnets does impact their separation. The result of this is that the minimum separation at the IBL, or in any particular layer in the ID, is offset in $\Delta\phi$. For ΔR contours outside of the minimum separation, ΔR probes the separation between particle trajectories at the IBL, but when ΔR passes through the minimum at negative $\Delta\phi$, which is at $\Delta R \approx 7 \times 10^{-3}$ for the IBL, further decreasing ΔR increases the separation between particle trajectories at r_{IBL}. At this limit ΔR is no longer proportional to particle separation. Thus for particles with the same charge the efficiency is expected to decrease with ΔR, and for oppositely charged particles the efficiency is expected to decrease with ΔR until a minimum is reached. After this minimum is reached, decreasing ΔR further means that the particles will cross over each other before reaching the ID due to the magnetic field, such that they will be further apart at the IBL and the di-track reconstruction efficiency will increase.

4.2 Monte Carlo Estimate of Track Reconstruction Efficiency

To fully benefit from a data-driven analysis, it is important to understand what simulation predicts for the ID di-track reconstruction efficiency. This study simulates pairs of

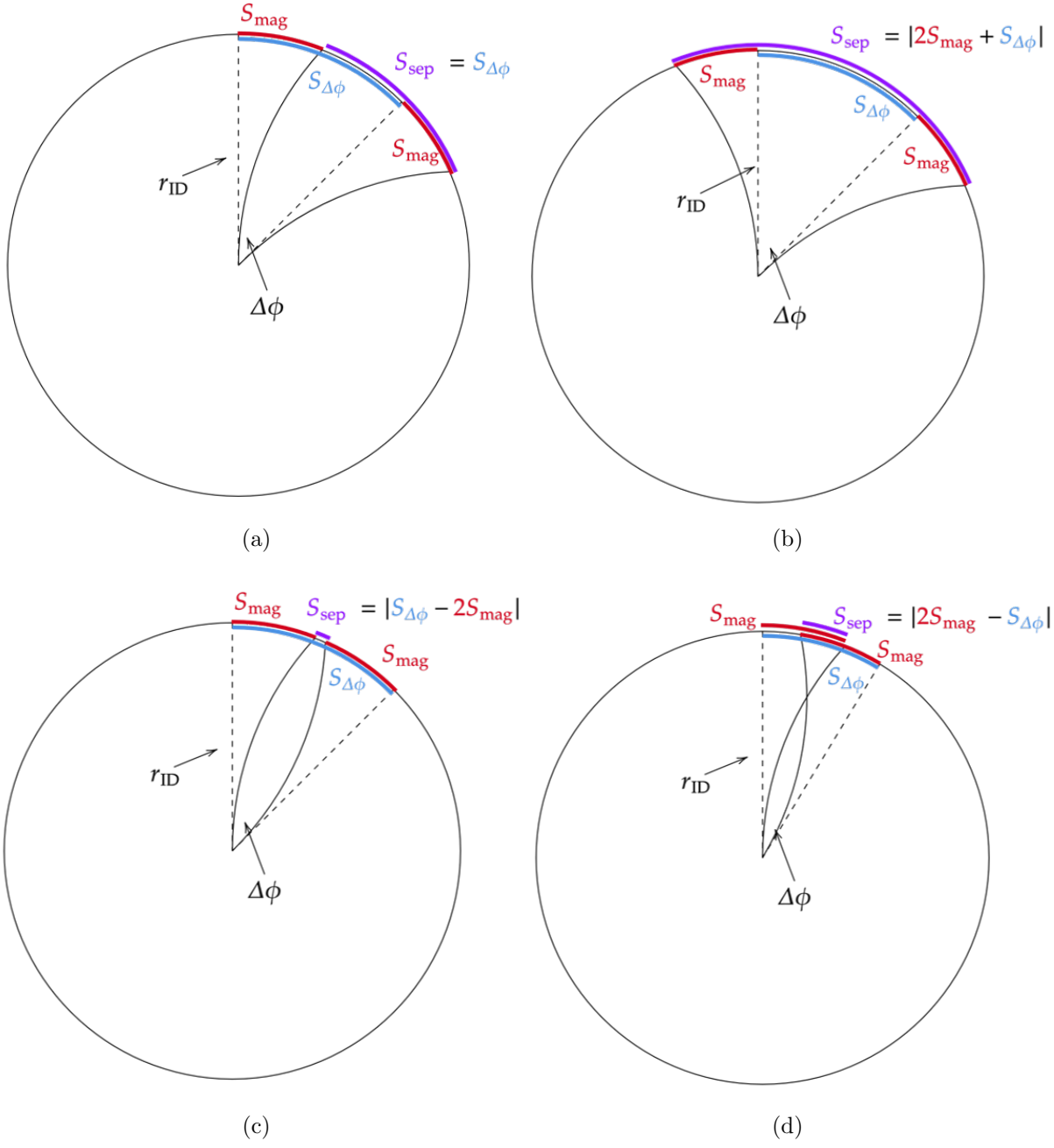
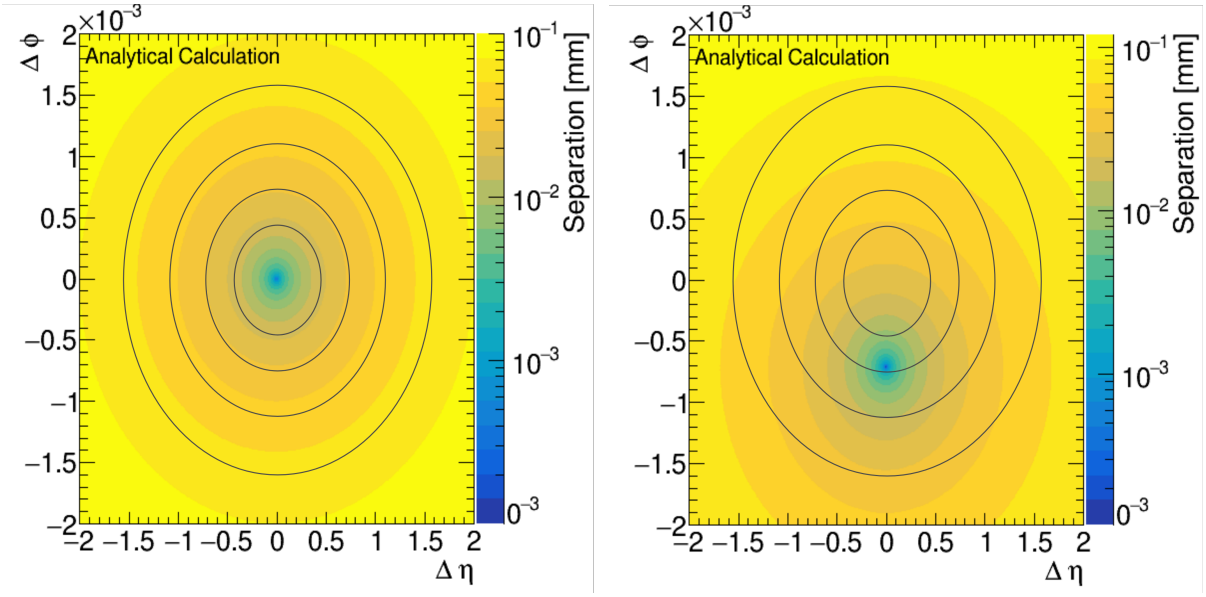


Figure 4.3: Total separation between collimated particles of the same p_{T} in the r–ϕ plane in different situations, taking to account the separation by $\Delta\phi$ and the separation caused by magnetic bending. (a) the particles have the same charge, such that the bending by the magnet has no net effect. (b) the particles have opposite charge and bend away from each other. (c) the particles have opposite charge and bend towards each other, decreasing their separation. (d) the particles have opposite charge and bend towards each other, but $\Delta\phi$ is small enough that the particles cross; decreasing $\Delta\phi$ further results in the total separation increasing.



(a) (b)

Figure 4.4: Calculation of separation between particles at the IBL at $r_{\text{ID}} = 33.5$ mm for 30 GeV particles in a 2T magnetic field in $\Delta\eta, \Delta\phi$. (a) the particles have the same charge, such that separation is dependent only on ΔR. (b) the particles have opposite charge, such that the minumum separation is offset in $\Delta\phi$ due to the bending of the particles by the magnet. The grey circles show ΔR contours.

charged particles traversing the ATLAS detector with the Monte Carlo technique, and the reconstruction efficiency of the ID is investigated. Several configurations are tested to see how the efficiency depends on the kinematic properties of the charged particle pairs, p_{T} and ΔR, but also their charge configuration (same or oppositely charged) and their species (muon or pion). This section describes how the pairs of charged particles are simulated as well as the results of the study, which are used to verify the predictions of the analytical study in Section 4.1 and to establish the requirements for a data-driven study to be sensitive to a decrease in the ID track reconstruction efficiency for close-by charged particles.

4.2.1 Event Generation and Selection

Collimated particles were generated with fixed p_{T} and ΔR using a customised Particle Gun sampler, with nothing else included in the event. The first particle is generated uniformly in ϕ and within $|\eta| < 2.7$; the second particle is generated with fixed ΔR from the first, with $\Delta\eta$ and $\Delta\phi$ sampled uniformly on the ΔR contour. The collimated particles

were simulated in the ATLAS detector with ATLFAST-II, described in Section 3.4, and reconstructed without taking pile-up into account. To estimate the reconstruction efficiency, events where both particles are within $|\eta| < 2.4$ at generator level are selected, well within the geometric acceptance of the ID.

Each sample of simulated pairs of charged particles contains 10k events, and the four p_{T} values tested are 30 GeV, 100 GeV, 500 GeV and 1 TeV, and the 19 ΔR values tested are approximately logarithmically spaced and range from 0.0001–0.2. In most cases oppositely charged muons were simulated, however for $p_{\mathrm{T}} = 30$ GeV a sample was generated with same-charge muons to investigate the effect of the bending by the magnets discussed in the analytical study. In addition to this, a sample of oppositely charged pions at $p_{\mathrm{T}} = 1$ TeV was simulated to compare the track reconstruction efficiency of pions to that of muons.

4.2.2 Procedure and Results

The number of reconstructed ID tracks is counted to see if separate tracks, or only a single merged track, were formed. The efficiency is

$$\varepsilon = \frac{n_{\mathrm{pass}}}{n_{\mathrm{fail}} + n_{\mathrm{pass}}},$$

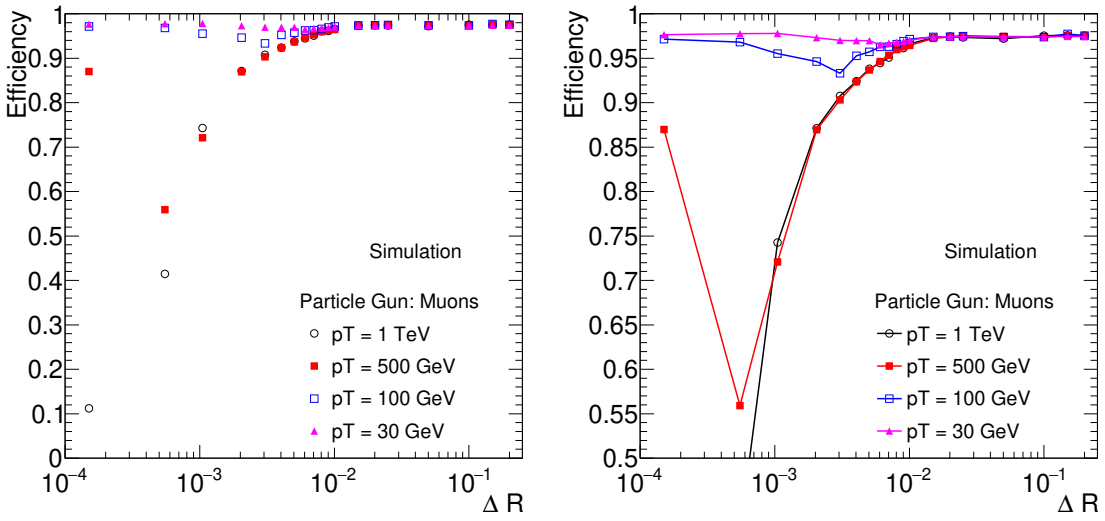
where n_{pass} is the number of events where the ID succeeded in resolving the two particles, such that the event contains two tracks, and n_{fail} is the number of events where the ID failed to resolve the two particles, such that the event contains only a single track. It should be noted that this is a di-track efficiency, where the probability to successfully discern two particles is represented by a single parameter ε.[3] For this study, the probability for the ID to reconstruct no tracks or greater than 2 tracks is negligible, such that the above are considered the only possibilities. A summary of the efficiency versus ΔR

[3]This is different to a single-track efficiency, where the probability of reconstructing any individual charged particle is $\varepsilon_{\mathrm{track}}$. In this model the probability to reconstruct both charged particles is $\varepsilon^2_{\mathrm{track}}$, one particle is $2\varepsilon_{\mathrm{track}}(1-\varepsilon_{\mathrm{track}})$, and neither particle is $(1-\varepsilon_{\mathrm{track}})^2$. This assigns an independent efficiency to the reconstruction of each particle, which is not applicable here as a decrease in efficiency depends directly on the overlap of particles in the di-track system.

is presented in Figure 4.5 for each of the tested configurations. For each curve showing oppositely charged particles, a minimum efficiency is seen in ΔR, below which reducing ΔR increases the overall separation between the trajectories of the charged particles in the ID, and therefore the efficiency. Three effects are seen when changing the muon p_{T} in Figure 4.5(a) and Figure 4.5(b). The first, predicted by the analytical study of charged particle separation at the IBL, is the shift of the minimum in ΔR at different p_{T}. The size of S_{mag} decreases as the p_{T} increases, shifting the location of the minimum S_{sep} to smaller ΔR. The second effect, which cannot be explained by the shift of minimum charged particle separation at the IBL alone, is the change in the depth of the minimum. At 30 GeV the efficiency decrease is of the order of 1%, whereas at 1 TeV the efficiency decrease is $\sim 90\%$. The ID is made up of several layers, so although a value of $\Delta\eta$, $\Delta\phi$ exists where the muons exactly overlap at the IBL, low p_{T} charged particles are more curved and will separate in the outer layers of the ID; particles with straighter trajectories stay collimated throughout the layers, lowering their efficiency to be resolved. The third effect is that the efficiency does not fully recover as ΔR is reduced below the minimum for 500 GeV and 1 TeV muons, shown by the points at smallest ΔR. This is because the width of the minimum in efficiency is finite, as seen for 30 GeV and 100 GeV muons, and at sufficiently high p_{T} the region of low efficiency begins to encompass $\Delta R = 0$, as the particle trajectories are curved less by magnetic field. In this regime, points at very small ΔR are not in a plateau of efficiency but are in the turn-on, such that the efficiency does not fully recover as ΔR approaches 0, unlike for lower p_{T} muon pairs.

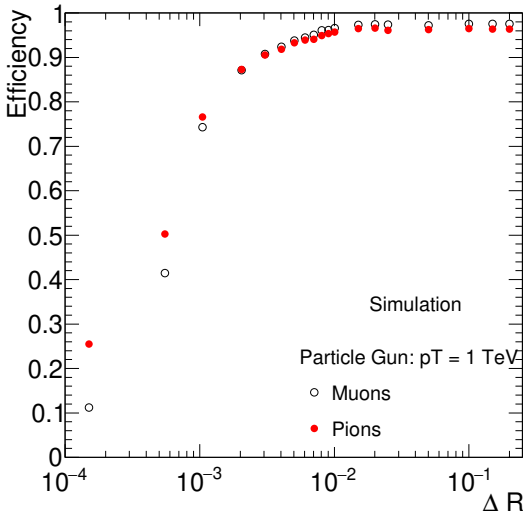
For same-charged muons in Figure 4.5(d) the bending has no net effect for the same p_T and the efficiency decreases by 80% at 30 GeV, despite the decrease being 1% for oppositely charged muons of the same momentum. This was predicted in the analytical study. Figure 4.5(c) compares muons and pions of the same transverse momentum, and shows that the behaviour of the ID reconstruction is similar for both species.

The results in Figure 4.6 show how the efficiency depends on $\Delta\eta$ and $\Delta\phi$. For oppositely charged particles, the decrease in efficiency is seen at negative $\Delta\phi$ as predicted by the analytical study. For particles with the same charge, the efficiency decrease is centred

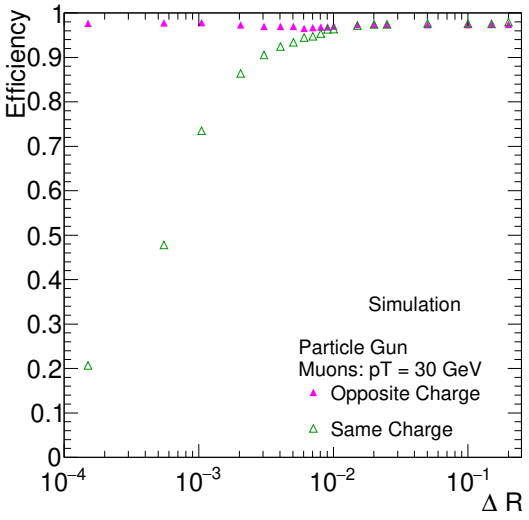


(a)

(b)



(c)



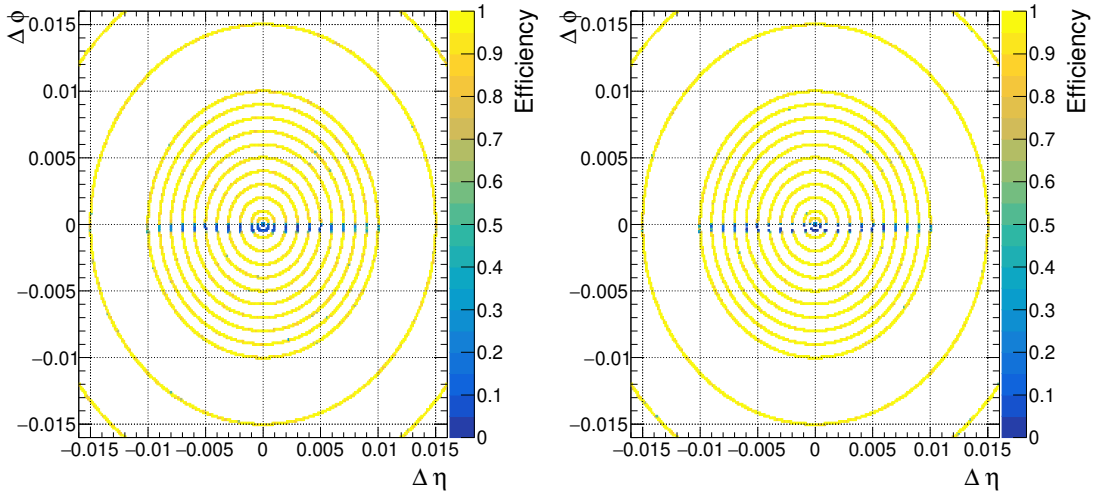
(d)

Figure 4.5: A comparison of the ID di-track reconstruction efficiency versus particle ΔR of (a) muons with various p_{T} ((b) is the same plot with added trend lines to emphasise the shift of the minimum in ΔR), (c) 1 TeV p_{T} muons and pions and (d) same and oppositely charged muons with 30 GeV p_{T}.

around $\Delta\phi = 0$ as expected. For 500 GeV and 1 TeV particles, the region of low efficiency begins to overlap with $\Delta\phi = 0$, such that the efficiency does not fully recover as ΔR approaches 0. The granularity of the pixels is smaller in ϕ than in η, which can be seen by the wider low efficiency region in $\Delta\eta$: the pixel size of the IBL is $50\times250\,\mu m^2$ in (ϕ, z), the pixel size of the three pixel detector layers is $50\times400\,\mu m^2$.

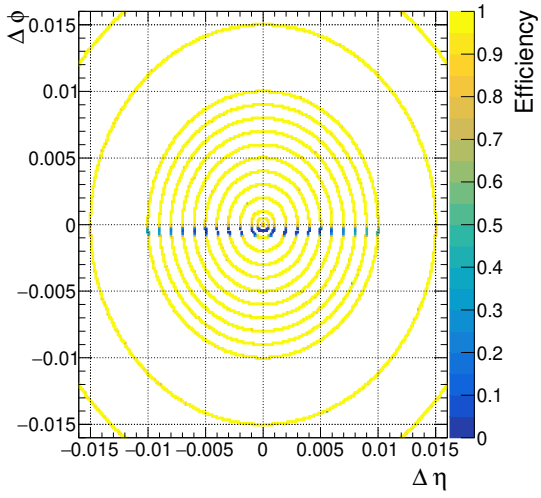
Figure 4.7 shows the invariant mass of the pairs of particles throughout this Monte Carlo study. The invariant mass of the pair m_{pair} follows the relationship $m_{\text{pair}} \propto \Delta R$ for large ΔR, with the limit at small ΔR that $m_{\text{pair}} = 2m_{\mu}$ (or $m_{\text{pair}} = 2m_{\pi}$ in the case of pions in Figure 4.7(a)). Figure 4.8 shows the efficiency versus invariant mass of the pair. Figure 4.9 shows the ID di-track reconstruction efficiency in the p_{T} of the di-particle system versus their invariant mass. To see an appreciable decrease in efficiency, low mass resonances at high p_{T} are required.

Table 4.1 compares the ΔR value of the minimum ID efficiency predicted by the analytical efficiency estimate compared with the location found by the Monte Carlo efficiency estimate. Throughout the p_{T} range the analytical prediction is an order of magnitude smaller than found in the Monte Carlo estimate. The minimum di-track reconstruction efficiency is linked to the radius, r_{cross}, at which the muon trajectories cross over each other in the ID. In the analytical study, the assumption was that $r_{\text{cross}} = 33.5$ mm corresponded to the minimum efficiency, the radius of the IBL. Extrapolating from the minimum ΔR found in the Monte Carlo estimate to calculate r_{cross}, it is found the minimum efficiency for each p_{T} occurs when the muons cross each other within the SCT. This implies that the decrease in di-track efficiency is more complicated than the analytical study alone suggests, but both studies agree in terms of the expected trends. Based on this Monte Carlo study, for a data-driven analysis to be sensitive to a decrease in ID di-track reconstruction efficiency, it must have good statistics for $\Delta R < 0.01$ and $p_{\text{T}} > 100$ GeV, and low-mass resonances are preferred.

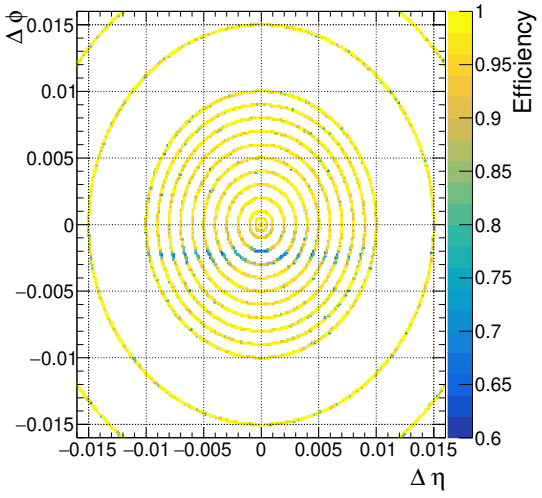


(a) 1 TeV Pions

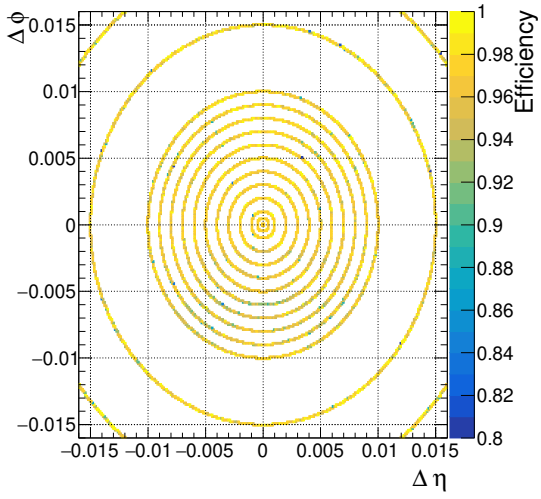
(b) 1 TeV Muons



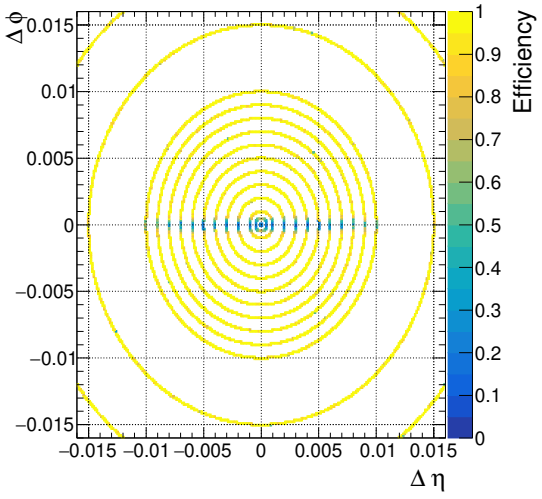
(c) 500 GeV Muons



(d) 100 GeV Muons



(e) 30 GeV Muons



(f) 30 GeV Muons (Same Sign)

Figure 4.6: ID di-track reconstruction efficiency versus $\Delta\eta$ and $\Delta\phi$ for several Particle Gun configurations. It should be noted that for (d) 100 GeV and (e) 30 GeV p_{T} muons the efficiency range is altered to highlight the fall in efficiency.

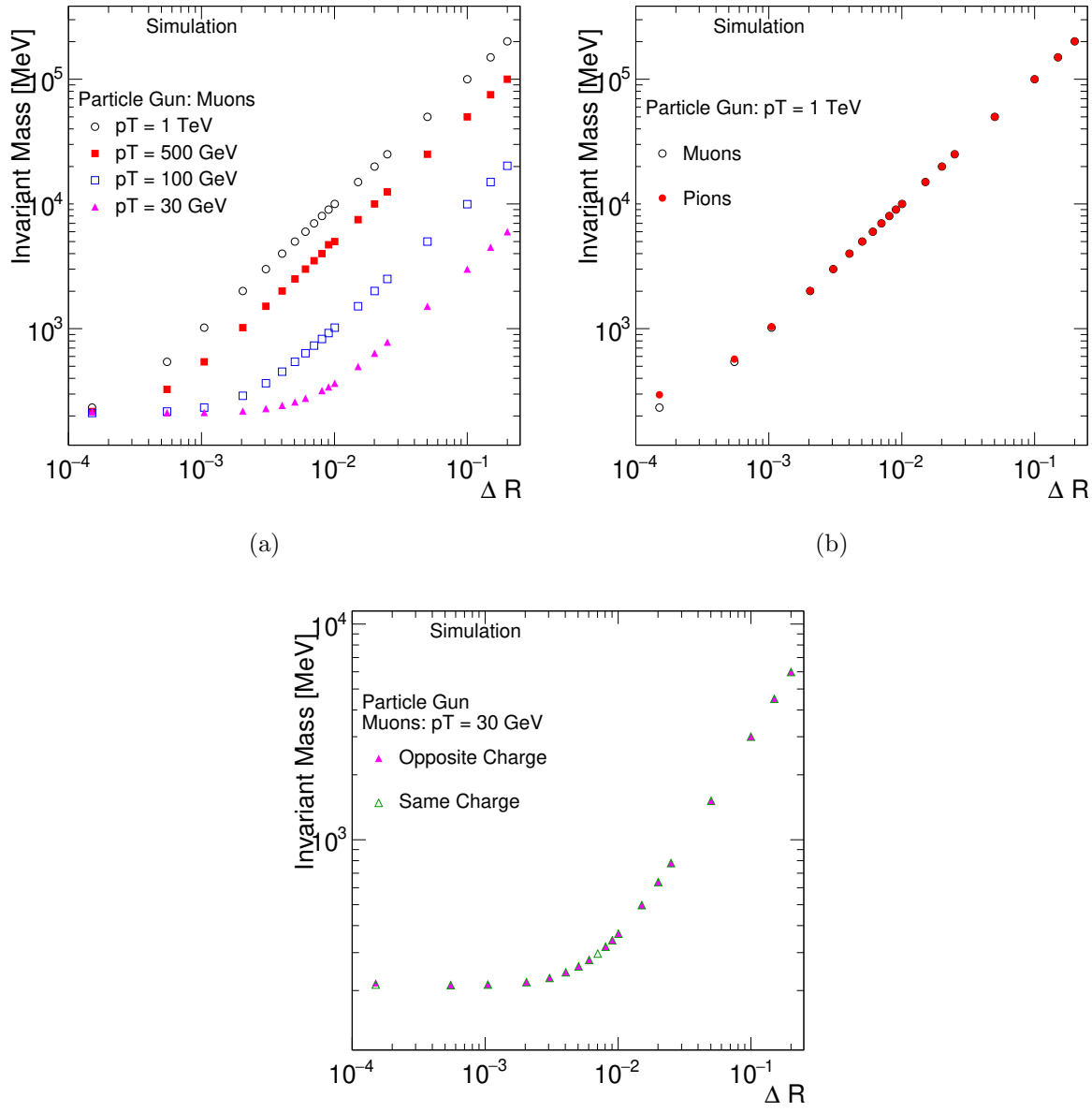
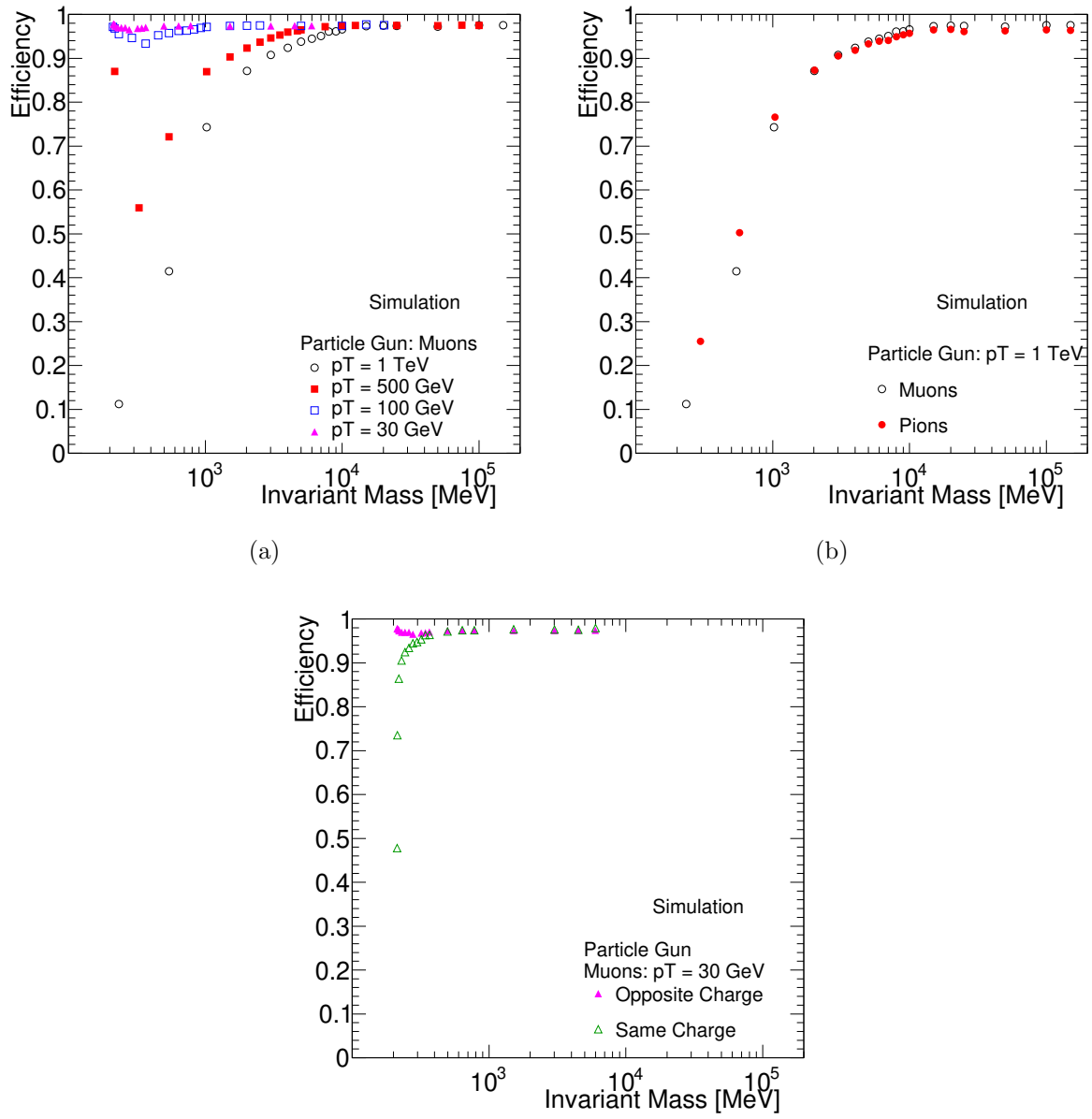


Figure 4.7: A comparison of invariant mass versus particle ΔR of (a) muons with various p_{T}, (c) 1 TeV p_{T} muons and pions and (d) same and oppositely charged muons with 30 GeV p_{T}.

Table 4.1: Comparison of the location in ΔR of the minimum ID efficiency between analytical and Monte Carlo studies. The analytical study assumes that the minimum efficiency occurs when the charged particles cross over each other at the IBL at $r_{\mathrm{cross}} = 33.5$ mm. The uncertainties in the values of the MC estimate entries are based on the spacing of the sampled points in ΔR, which are propagated through to the calculation of r_{cross}.

Muon p_{T} [GeV]	Analytical ΔR_{min}	MC Estimate ΔR_{min}	MC Estimate r_{cross} [mm]
30	6.7×10^{-4}	$(6.0 \pm 0.5) \times 10^{-3}$	300 ± 25
100	2.0×10^{-4}	$(3.0 \pm 0.5) \times 10^{-3}$	500 ± 83
500	4.0×10^{-5}	$(5.0 \pm 2.5) \times 10^{-4}$	420 ± 210
1000	2.0×10^{-5}	$(3.0 \pm 2.0) \times 10^{-4}$	500 ± 330



(a) (b)

(c)

Figure 4.8: A comparison of efficiency versus invariant mass of (a) muons with various p_{T}, (c) 1 TeV p_{T} muons and pions and (d) same and oppositely charged muons with 30 GeV p_{T}.

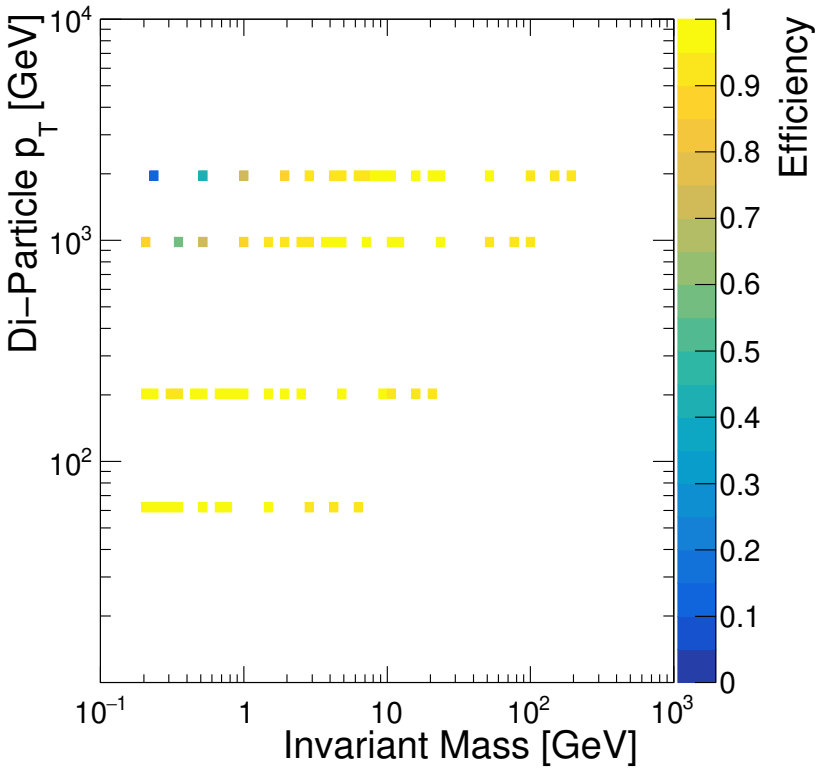


Figure 4.9: The ID di-track reconstruction efficiency for invariant mass versus p_{T}.

4.3 Prototype Analysis using $J/\psi \to \mu^+\mu^-$ Decays

The decay $J/\psi \to \mu^+\mu^-$ with boosted J/ψ production is proposed as a probe to measure the efficiency of the ID to reconstruct charged particle pairs with a small separation. Currently the tracking efficiency is evaluated primarily in simulation. A data-driven method would help validate these results and be able to calibrate the simulation. A tag-and-probe method is proposed, a method that uses di-object resonances to measure efficiencies based on whether the selected probe passes a test. Here the tag and the probe are the muons from the decay $J/\psi \to \mu^+\mu^-$, and the method exploits the capability of the ATLAS detector to reconstruct muons independently in the ID and in the MS, as described in Section 3.3.4. The tag is a high purity combined-type (CB) muon object, where the separate ID and MS tracks associated with a muon are combined to improve its reconstruction. The probe is a muon object that must be reconstructed in the MS and at least has a muon-spectrometer extrapolated (ME) track associated with it, which is available regardless of whether or not the improved CB track exists for the muon such

that the probe selection is unbiased in this regard: this is vital for an effective tag-and-probe test. The test of the efficiency of the ID to reconstruct pairs of charged particles is to check if the probe muon has an available CB track, meaning that the muon was also reconstructed in the ID. If the probe passes this test then the ID successfully resolved the two muons; if the probe fails this test then the ID failed to resolve the two muons and only reconstructed a single, merged muon track.

The efficiency of the ID to reconstruct two separate tracks, the ID di-track reconstruction efficiency, is the ratio of the pass yield to the total yield, where the yield in each case corresponds to the number of detected J/ψ decays. This is

$$\varepsilon_{ID} = \frac{n_{\text{pass}}}{n_{\text{pass}} + n_{\text{fail}}}.$$

where n_{pass} is the number $J/\psi \to \mu^+\mu^-$ decays reconstructed with two CB muons, and n_{fail} is the number of $J/\psi \to \mu^+\mu^-$ decays reconstructed with just one CB muon (the tag) and one ME muon (the probe). The values of n_{pass} and n_{fail} are measured independently using a binned maximum-likelihood fit of the dimuon invariant mass to calculate the number of J/ψ candidates. The dependence of ε_{ID} on particle p_{T} and angular separation ΔR can be studied by categorising events into bins of each variable and measuring the number of pass-case and fail-case events in each category. This section explorates the feasibility of applying this method on Run 2 data to measure the ID di-track reconstruction efficiency for close-by particles, including a description of the event selection, the models used for the signal in the pass and fail cases, the development of a background model for the high-p_{T} phase space required by the selection, and a look at a preliminary measurement of the efficiency.

4.3.1 Event Selection and Categorisation

The full ATLAS proton–proton collision dataset collected between 2015–2018 at $\sqrt{s} =$ 13 TeV during Run 2 is considered, with all relevant detector systems functional and stable beam conditions [103]. A single trigger is used, requiring a single high-energy

muon identified at the software-based high-level trigger with $p_{\mathrm{T}}^{\mu} > 50$ GeV. This trigger, called `HLT_mu50`, was available throughout Run 2. As well as the trigger requirement, data events are required to pass the 'Good Runs List' (GRL) requirements described in 3.3.1. The total integrated luminosity of the search is 139.0 ± 2.4 fb^{-1} where primary luminosity measurements are performed by the LUCID-2 detector [190] and the uncertainty on this measurement is calculated using the method in Refs. [191, 192]. To streamline analyses in the ATLAS experiment, data may be processed through derivations as described in Section 3.4. In this analysis the `STDM4` derivation is used, a general purpose derivation from the Standard Model ATLAS group for analyses involving at least one lepton.

Events must meet several additional selection criteria to be considered in the efficiency measurements, based on the kinematic properties of the muons. There must be at least two muons in the event with pseudorapidity $|\eta_{\mu}| < 2.4$. The highest p_{T} muon in the event is the tag μ candidate and it must pass the tight quality criteria [193], which includes the requirement of the muon to have a combined track, and have $p_{\mathrm{T}}^{\mu} > 50$ GeV, which is the requirement of the trigger. The second highest p_{T} muon in the event is the probe μ candidate and it must have opposite charge to the tag, and have at least a muon-spectrometer extrapolated track and a $p_{\mathrm{T}} > 4$ GeV. The two muon candidates are combined to reconstruct the J/ψ candidate. If the probe muon has a reconstructed combined muon track, as in the pass-case events, this CB track is used to reconstruct the J/ψ candidate as it has an improved resolution compared to ME tracks. However, in the fail case there is no available CB track for the probe, and instead the lower-resolution ME track is used to reconstruct the J/ψ candidate.

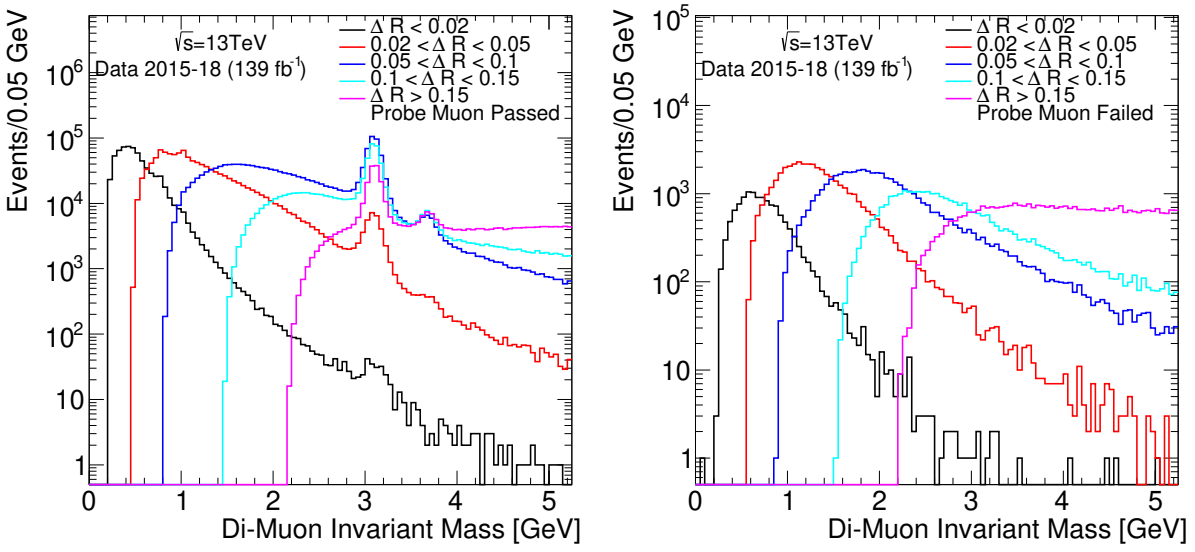
Candidate events are categorised according to the ΔR separation between the muon pairs and the p_{T} of the probe muon when measuring the efficiency versus either property. In total there are five ΔR categories and three p_{T} categories, listed in Table 4.2. The categories in ΔR are inclusive in probe p_{T}, and vice versa.

Figure 4.10 shows the dimuon invariant mass of the event yield from Run 2 data separated into ΔR categories. For the pass case in Figure 4.10(a), distinct J/ψ peaks at 3.097 GeV

Table 4.2: Bins of muon Δ_R and p_{T} used in $J/\psi \to \mu^+\mu^-$ Analysis

Variable	Categories
ΔR	$\Delta R < 0.02$
	$0.02 \leq \Delta R < 0.05$
	$0.05 \leq \Delta R < 0.10$
	$0.10 \leq \Delta R < 0.15$
	$\Delta R \geq 0.15$
Probe p_{T}	$p_{\mathrm{T}} < 10$ GeV
	10 GeV $\leq p_{\mathrm{T}} < 20$ GeV
	$p_{\mathrm{T}} \geq 20$ GeV

are visible in each of the ΔR categories; this is not true for the fail case in Figure 4.10(b), where there are few events for $\Delta R < 0.02$ where the decrease in efficiency is expected according to the Monte Carlo study in Section 4.2.

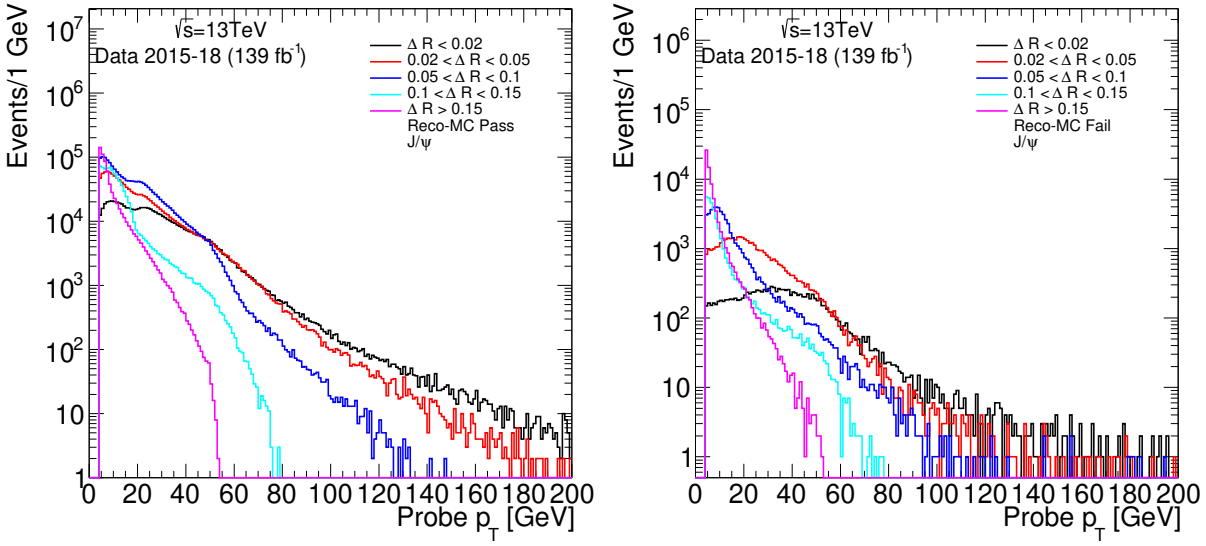


(a) (b)

Figure 4.10: Event yield from Run 2 Data (a) for passing probe muons and (b) for failing probe muons.

Figure 4.11 shows the probe p_{T} of the event yield from Run 2 data, inclusive of the dimuon invariant mass and separated into the ΔR categories. As ΔR gets smaller, the high tail of the p_{T} spectrum gets larger. For the probe fail case in Figure 4.11(b) there are few events with $p_{\mathrm{T}} > 100$ GeV, where the efficiency is expected to decrease. As a result, based on the Monte Carlo study, the Run 2 dataset itself is not expected to be sensitive to a decrease in ID di-track reconstruction efficiency. However, the study is

an interesting prospect for the large datasets expected in the high-luminosity phase of the LHC (HL-LHC) and provides an opportunity to investigate background modelling techniques in boosted searches with high-p_{T} phase spaces.



(a) (b)

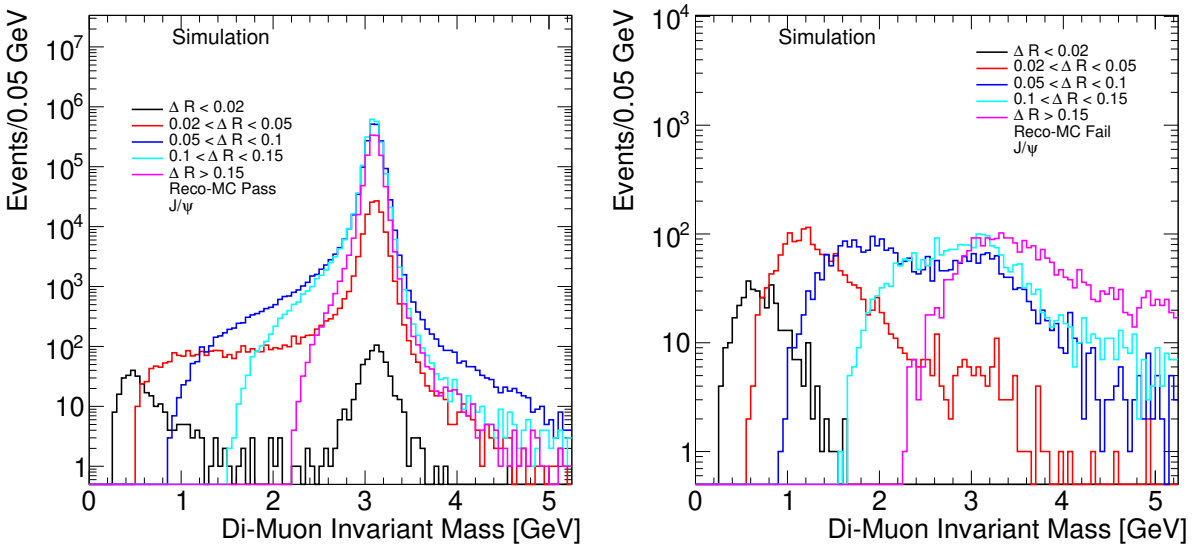
Figure 4.11: Probe p_{T} of Run 2 Data (a) for passing probe muons and (b) for failing probe muons.

4.3.2 Signal Modelling

The signal in the tag-and-probe study is modelled with simulated MC events. For n_{pass} the signal is J/ψ events that were reconstructed with two CB muons, whereas for n_{fail} the signal is J/ψ events that were reconstructed with one CB muon and one ME muon, which are worse resolution. The Pythia 8.212 event generator was used to model $J/\psi \to \mu^+\mu^-$ decays, using the A14 set of tuned parameters [194] for hadronisation and the underlying event, and the CTWQ6L1 set of parton distribution functions [195]. Events are filtered at generator level such that they require two muons, one with $p_{\mathrm{T}}^{\mu} > 45$ GeV and a second with $p_{\mathrm{T}}^{\mu} > 3$ GeV, and both muons are required to have $|\eta_{\mu}| < 2.5$. In addition, the minimum invariant p_{T} in the $2 \to 2$ hard process was set to 40 GeV, which is the variable `PtHatMin`.

The generator-level output files were analysed with a basic Athena [138] analysis to extract the four-vectors of the J/ψ and the muons in the $J/\psi \to \mu^+\mu^-$ decay. These were

used to create slimmed HepMC events, containing only this information, for simulation in the ATLAS detector and reconstruction. This was done to reduce the computational time of the reconstruction compared to full Pythia 8.212 events as fully simulated events are not necessary for this exploratory study; using skimmed events the simulation and reconstruction time is reduced by a factor of approximately 10. The events were simulated with ATLFAST-II, which uses the full Geant4 simulation for the ID and the MS but parameterises the calorimeter response, and reconstructed with no pile-up as in the Monte Carlo efficiency estimate in Section 4.2. Figures 4.12(a) and 4.12(b) show the yield of simulated events for the pass-case and fail-case events, respectively. From a sample of 10M truth Monte Carlo events, the event yield was 5M reconstructed events when applying the tighter analysis cuts from Section 4.3.1.The normalisation of the signal is extracted directly from data, which is the measurement of n_{pass} and n_{fail}.

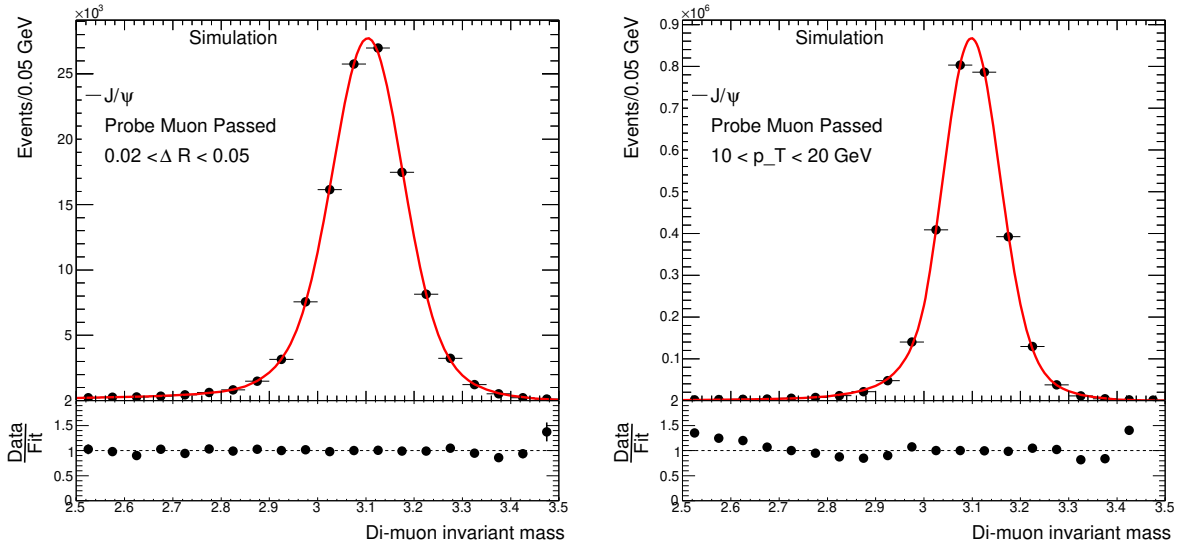


(a) (b)

Figure 4.12: Signal MC yield (a) for passing probe muons and (b) for failing probe muons.

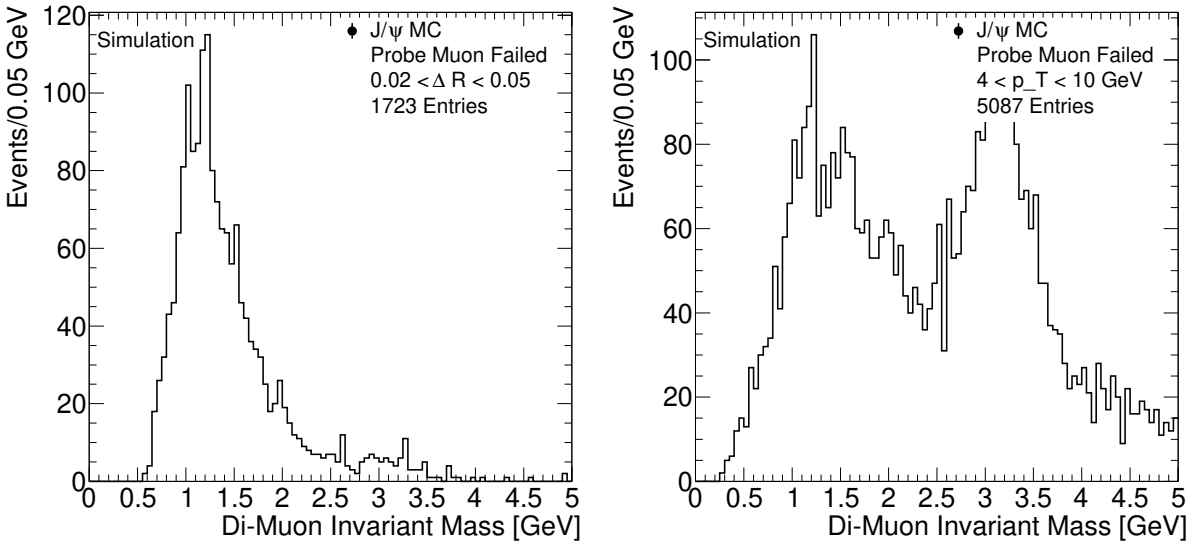
For pass-case events where J/ψ mesons are reconstructed well, signal peaks are modelled as a Gaussian + Crystal-Ball shape with their parameters extracted from a binned maximum-likelihood fit to the simulated events, examples of which are in Figure 4.13. For fail-case events the J/ψ mesons are reconstructed poorly as expected, and many events are not in the typical resonance window. These distributions, examples of which are in

Figure 4.14, are difficult to model with analytical lineshape, so the simulated distributions are used directly to model the probability density functions.



(a) (b)

Figure 4.13: Fits to pass-case signal Monte Carlo in selected categories:(a) $0.02 < \Delta R < 0.05$; (b) $10 <$ probe $p_{\mathrm{T}} < 20$ GeV.



(a) (b)

Figure 4.14: Fail-case signal Monte Carlo histograms in selected categories:(a) $0.02 < \Delta R < 0.05$; (b) $10 <$ probe $p_{\mathrm{T}} < 20$ GeV.

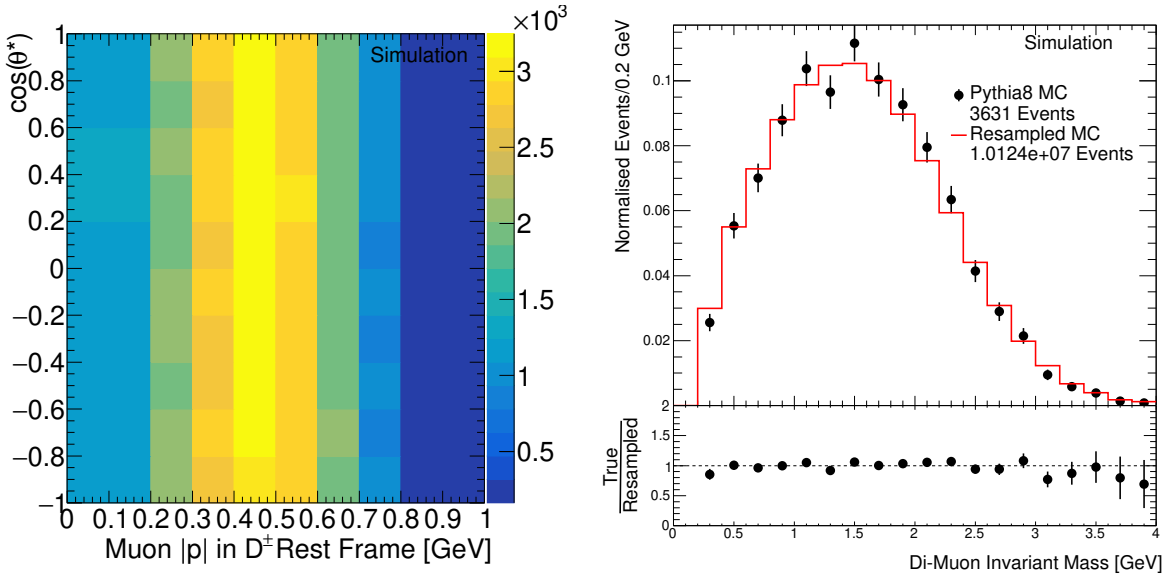
4.3.3 Background Modelling

The background in this analysis is mainly from bottom and charm hadron decays to semi-muonic final states in hard $b\bar{b}$ and $c\bar{c}$ events. Standard Monte Carlo generation of these events is limited due to the phase-space requirements, and a parametric data-driven background model is difficult due to the kinematic turn-on of the background distribution in each p_{T} and ΔR category. To overcome these challenges the production and the decay of the hadrons were split, and a generative resampling method was developed. Large $b\bar{b}$ and $c\bar{c}$ event samples were generated in the kinematic range of interest using a standalone version of Pythia 8.240, configured using a `PtHatMin` value of 50 GeV and allowing only hard QCD $b\bar{b}$ events on for the $b\bar{b}$ background model, and only hard QCD $c\bar{c}$ events for the $c\bar{c}$ background model.

To get the properties of hadron decays to muons, a 2M event hard $b\bar{b}$ sample was produced. The events were cycled through and decays of b- and c-hadrons to muons were selected. For each decay the muon was boosted into the rest frame of the decaying hadron, and the $\cos(\theta^*)$ versus $|p|$ kinematics were saved in two-dimensional histograms to form a 2D probability density function (PDF) of the kinematics of the decay. Here, θ^* is the boost angle: the angle between the line-of-flight of the muon in the rest frame of the decaying hadron, and the line-of-flight of the hadron in the lab frame. $|p|$ is the magnitude of the muon momentum in the decaying hadron's rest frame. Histograms are built by filling kinematic variables separately for each of the decaying hadron species. An example muon kinematic distribution is in Figure 4.15(a). In the current samples the $D^{\pm}$, D^0 and $D_s^{\pm}$ meson decays are resampled.

A 50M event hard $b\bar{b}$ sample and a 200M event hard $c\bar{c}$ sample were generated for the hadron production sample. For each sample, the events are cycled over and the hadrons are selected. For every appropriate c-hadron in each event (i.e $D^{\pm}$, D^0 and $D_s^{\pm}$) a custom muon decay is sampled by randomly sampling $\cos(\theta^*)$ and $|p|$ from the decay distributions and then boosting the muon into the lab frame. A ϕ co-ordinate is needed to generate a complete four-momentum for the muon; this is sampled uniformly between $-\pi$ and π.

Each event is resampled many times and every qualifying dimuon combination in each event is saved as a separate HepMC event containing only the two muon four-vectors and the identity of the parent hadron. A comparison of the invariant mass of resampled events compared to the true Pythia 8.240 events from which they were resampled is shown in Figure 4.15(b). The shapes are compatible, and the resampled events have a significant increase in statistics (a factor of approximately 2500).

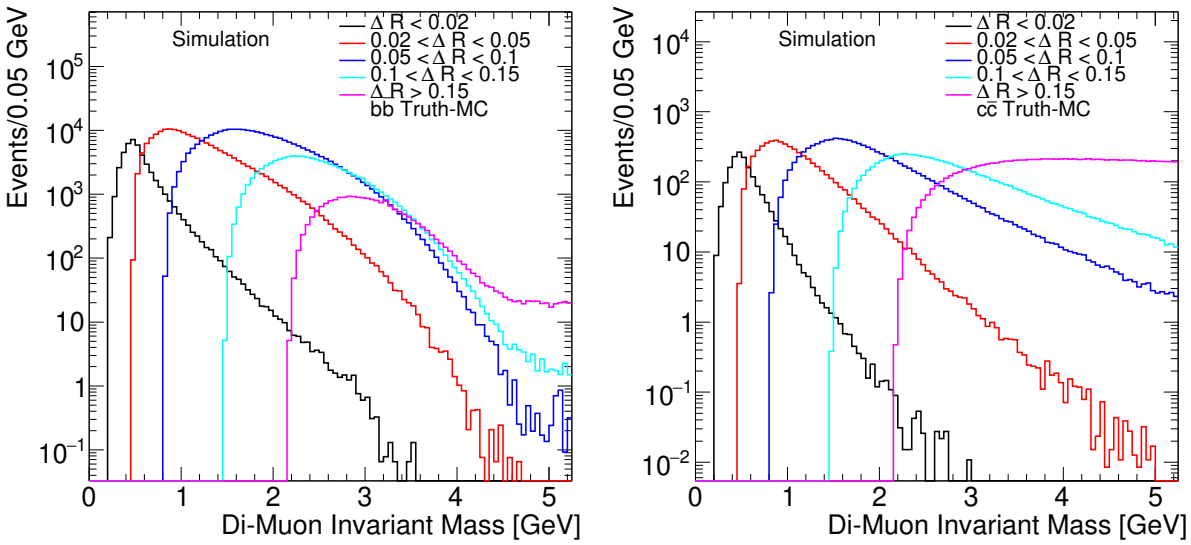


(a) (b)

Figure 4.15: (a) $\cos\theta^*$ of muons versus their total momentum $|p|$ in the rest-frame of the decay of $D^{\pm}$ mesons, where θ^* is the angle of the muon with respect to the $D^{\pm}$ line-of-flight in the lab frame. (b) dimuon invariant mass for (black) full standard Pythia 8.240 hard $b\bar{b}$ events and (red) resampled events generated from the same sample.

To avoid dealing with correlations of muons in $b \to c$ decay chains, resampling is only applied in the c-hadron decay; $B \to \mu + X$ is taken from hadron production sample. Although b-hadron decays are not resampled this way, sufficient statistics are produced. Events are reweighted using the product of the branching fractions of each decaying c-hadron, where the branching ratios are taken from the Pythia 8.240 samples used to generate the muon distributions. Figure 4.16 shows the truth Monte Carlo yield from resampling, when applying the 50 GeV tag and 4 GeV probe muon cuts from Section 4.3.1. The hard $b\bar{b}$ events in Figure 4.16(a) were generated by resampling each event in the 50M event sample 100 times, yielding 8M events; the hard $c\bar{c}$ events in Figure 4.16(b) were generated by resampling each event in the 200M event sample 1000 times, yielding 4.7M

events.



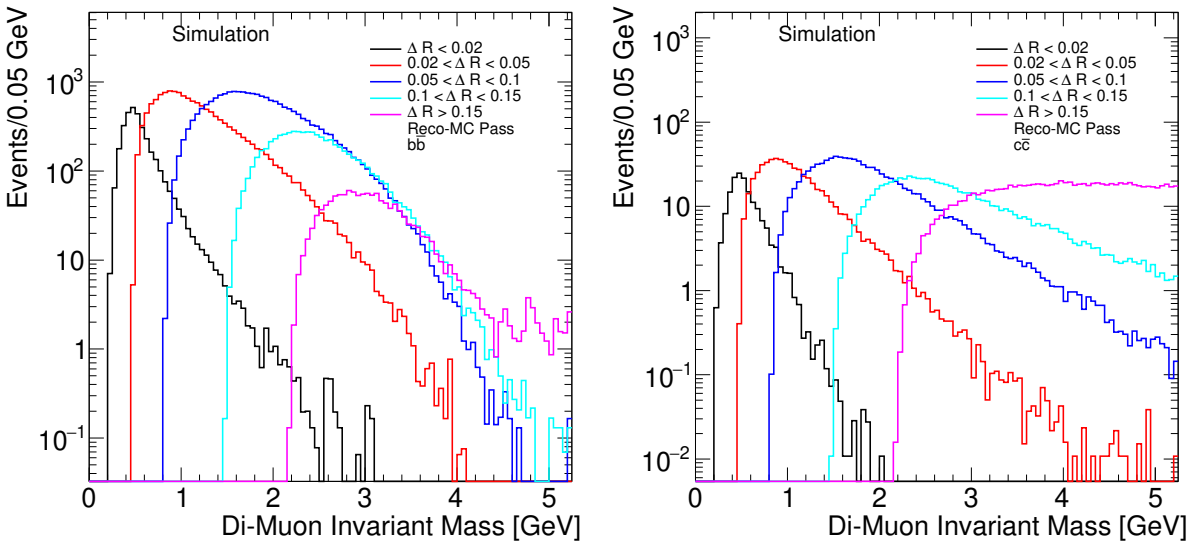
(a) (b)

Figure 4.16: Background truth MC yield (a) for hard $b\bar{b}$ events and (b) for hard $c\bar{c}$ events.

Loose requirements on the generator-level properties of each event is used to select focused HepMC events for reconstruction, where the tag muon must have $p_{\mathrm{T}} > 40$ GeV and the dimuon invariant mass must statisfy $m_{\mu^+\mu^-} < 10$ GeV; there are no requirements on the probe p_{T}. The chosen HepMC events are simulated with ATLFAST-II and reconstructed with no pile-up. This is the same method used for the Monte Carlo estimate in Section 4.2 and the signal model in Section 4.3.2. Figure 4.17 shows the pass case yield for the hard $b\bar{b}$ and $c\bar{c}$ samples; Figure 4.18 shows the corresponding fail case yield. In total 2M truth events each of the truth $b\bar{b}$ and $c\bar{c}$ Monte Carlo events were reconstructed, with a yield of approximately 600k $b\bar{b}$ and approximately 500k $c\bar{c}$ events when applying the tighter analysis selection.

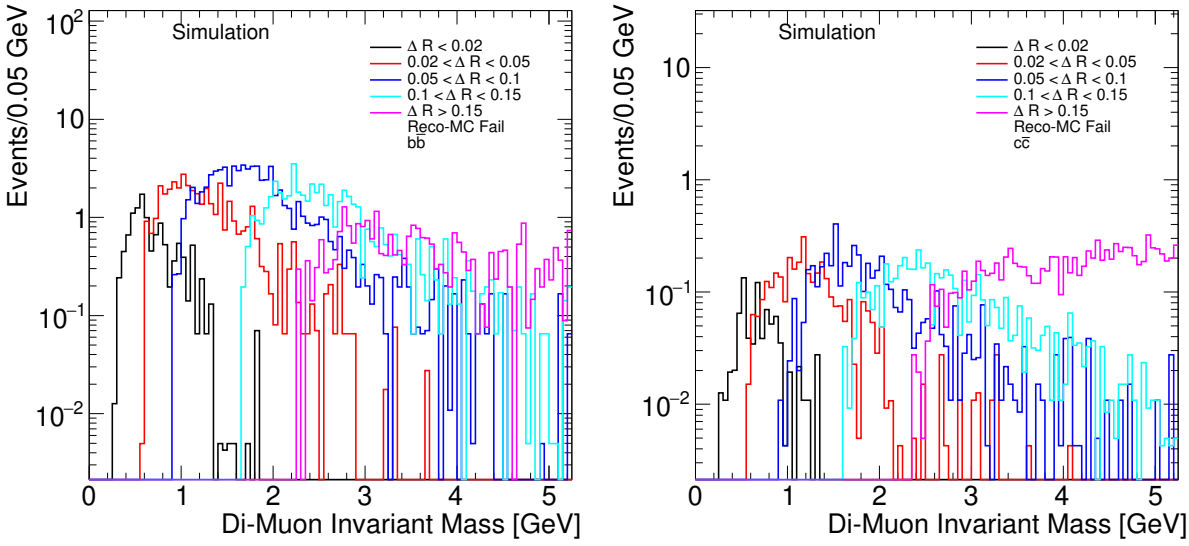
4.3.4 Results

The data are fit using the shapes from the Monte Carlo signal and background events. In the case of n_{pass} the signal is modelled with a Gaussian + Crystal-Ball shape, where the parameters are fixed to the signal Monte Carlo fits but the normalisation is a free parameter. For n_{fail} the signal is modelled by taking the shape of the signal Monte Carlo



(a) (b)

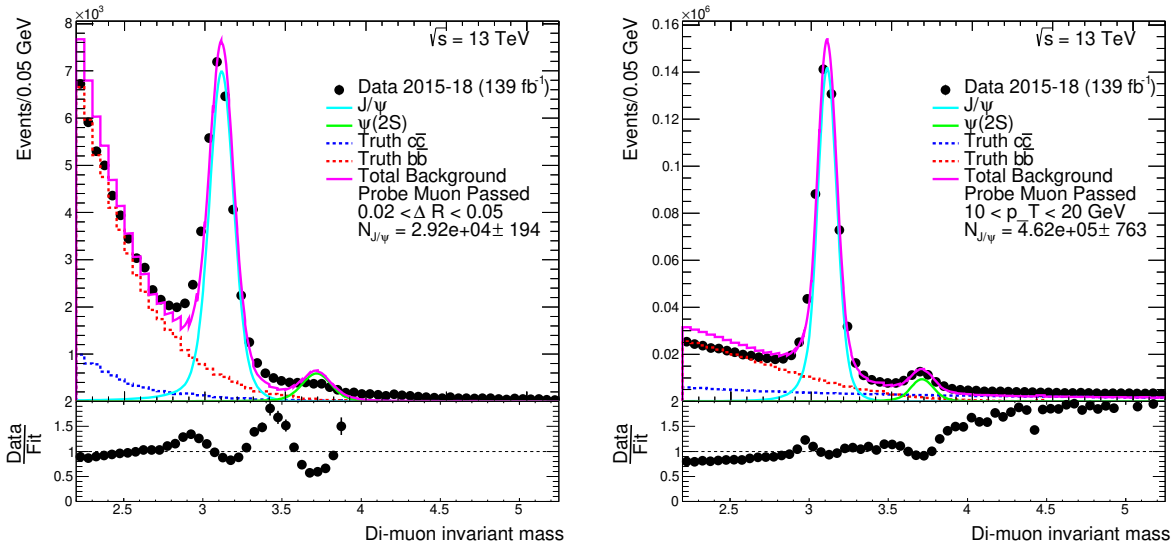
Figure 4.17: Background reco MC passing probe yield (a) for hard $b\bar{b}$ events and (b) for hard $c\bar{c}$ events.



(a) (b)

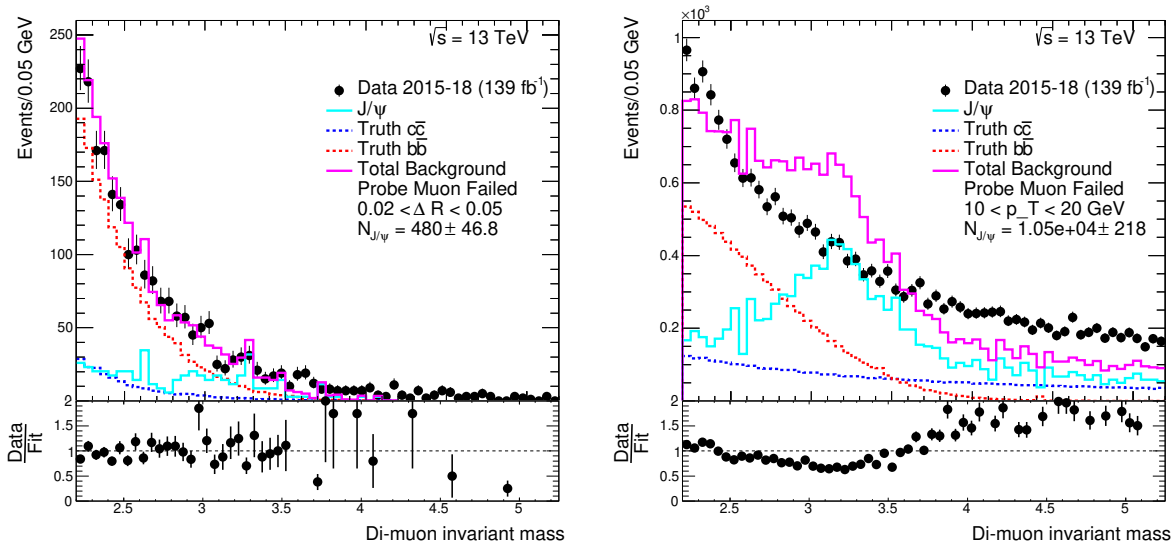
Figure 4.18: Background reco MC failing probe yield (a) for hard $b\bar{b}$ events and (b) for hard $c\bar{c}$ events.

histogram directly and allowing the normalisation to float. For the background shape the truth Monte Carlo hard $b\bar{b}$ and $c\bar{c}$ templates are used. The relative normalisation of $b\bar{b}$ to $c\bar{c}$ events is extracted from a fit to events inclusive in muon ΔR and probe p_{T}. This normalisation is taken and fixed in the fits to the ΔR and probe p_{T} categories according to the proportion of events in each category in the inclusive shape. This gives a fixed combined hard $b\bar{b} + c\bar{c}$ background template, the total normalisation of which is free in the fit in each category. Figure 4.19 shows example fits for the n_{pass} case; Figure 4.20 shows example fits for the n_{fail} case. The $\psi(2S)$ peak near 3.6 GeV is also seen in the pass-case events, this is modelled by using the Gaussian + Crystal Ball shape of the J/ψ, with the width and mean parameters scaled by the mass ratio of the two resonances from the Review of Particle Physics [26]. The fit works well in the pass case, but the signal model and data in the fail case are statistically limited, giving a poor match. Further work would be required in a full analysis to improve the modelling, particularly for the fail case events, but Figure 4.21 shows a crude calculation of the ID efficiency versus ΔR using the fit results of the pass case and fail case with the current models to explore the result. As predicted by the Monte Carlo estimate, the Run 2 dataset of $J/\psi \to \mu^+\mu^-$ candidates is not sensitive to a decrease in the ID di-track reconstruction efficiency.



(a) (b)

Figure 4.19: Fits to pass case data in selected categories using truth Monte Carlo templates.



(a) (b)

Figure 4.20: Fits to fail case data in selected categories using truth Monte Carlo templates.

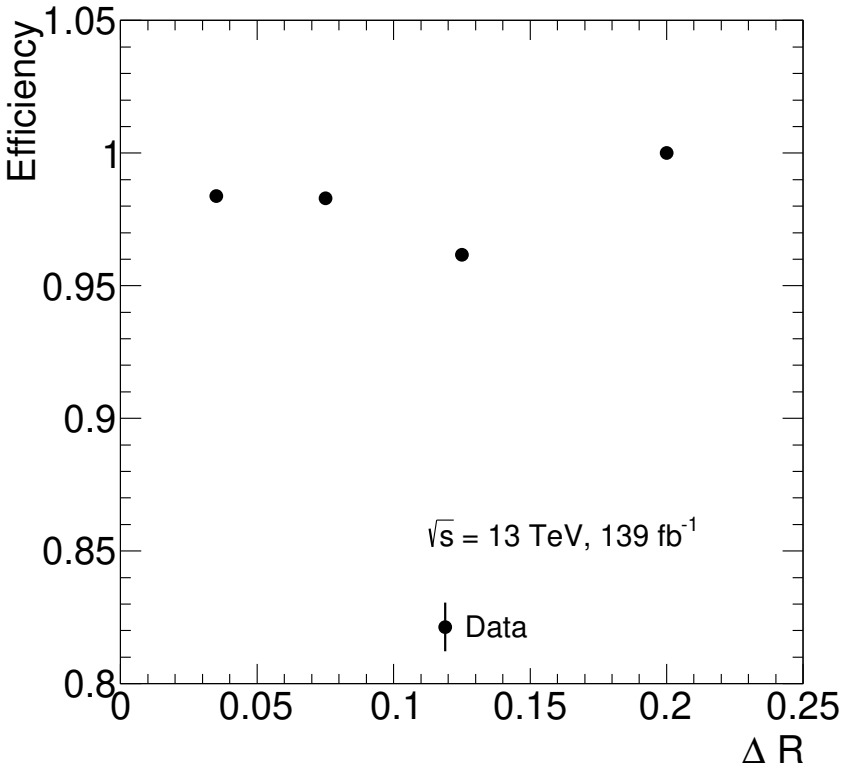
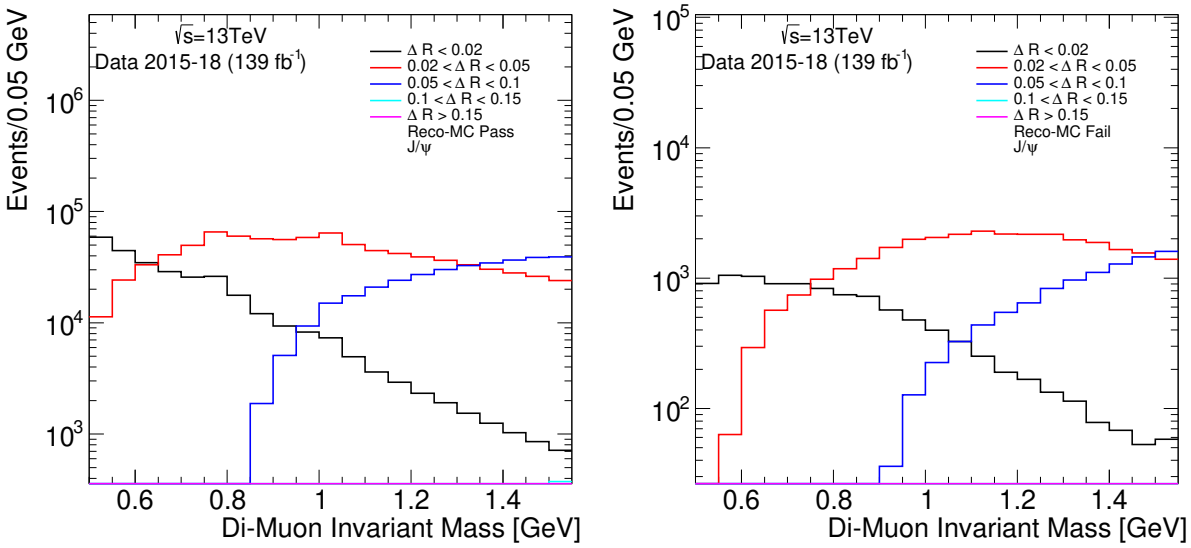


Figure 4.21: Prototype measurement of ID tracking efficiency versus ΔR.

4.4 Feasibility of using $\phi \to \mu^+\mu^-$ Decays

The decay $\phi \to \mu^+\mu^-$ with boosted ϕ mesons offers a potential alternative probe of the ID di-track reconstruction efficiency, where the smaller mass of the ϕ at 1.019 GeV compared to the J/ψ at 3.097 GeV allows the efficiency to be probed at smaller ΔR. To investigate the feasibility of measuring the ID di-track reconstruction efficiency in Run 2 data the same triggers and event selection requirements as for the $J/\psi \to \mu^+\mu^-$ analysis in Section 4.3.1 were used.

Figure 4.22 shows the Run 2 data yield near the $\phi \to \mu^+\mu^-$ resonance categorised according to the ΔR angular separation between the muon pairs. In the case of the ϕ meson, the events all have $\Delta R < 0.1$ which is the region of interest, however the peak at 1.02 GeV is less prominent than for the J/ψ. Although the overall statistics are larger at ΔR for the $\phi \to \mu^+\mu^-$ channel, these are mostly background events, and the smaller signal-to-background ratio compared to the $J/\psi \to \mu^+\mu^-$ resonance would make an efficiency measurement more challenging. Further, the ϕ decay suffers the same setback as the J/ψ analysis, in that there are too few events with $p_{\mathrm{T}} > 100$ GeV in Figure 4.11 where we expect to see a decrease in efficiency.



(a) (b)

Figure 4.22: Event yield from Run 2 Data near the ϕ resonance (a) for passing-probe muons and (b) for failing-probe muons.

4.5 Further Considerations for the Tag-and-Probe Method

The selection for the tag-and-probe data-driven analysis in Section 4.3 relies on the performance of the MS to accurately probe the ID di-track reconstruction efficiency. For the efficiency measured in the data-driven analysis, $\varepsilon_{\text{analysis}}$, to directly probe the ID di-track reconstruction efficiency, ε_{ID}, the two efficiencies must be equal such that $\varepsilon_{\text{analysis}} = \varepsilon_{\text{ID}}$. The following study investigates the additional effects that cause this equality to break down, using the same PARTICLE GUN samples as in Section 4.2. For an event to be selected in the analysis, the tag must be a combined-type muon. This means that both a MS and an ID track were formed for the muon, and these were combined to make an improved track. The probe muon must have opposite charge to the tag, and must at least have an associated track in the MS. The test whether the probe was reconstructed in the ID is to check if the probe was a combined-type muon. The efficiency measured by the data analysis is therefore the efficiency to have two combined muons, given that there are two MS tracks, and that these two tracks are correctly assigned opposite charge. Mathematically,

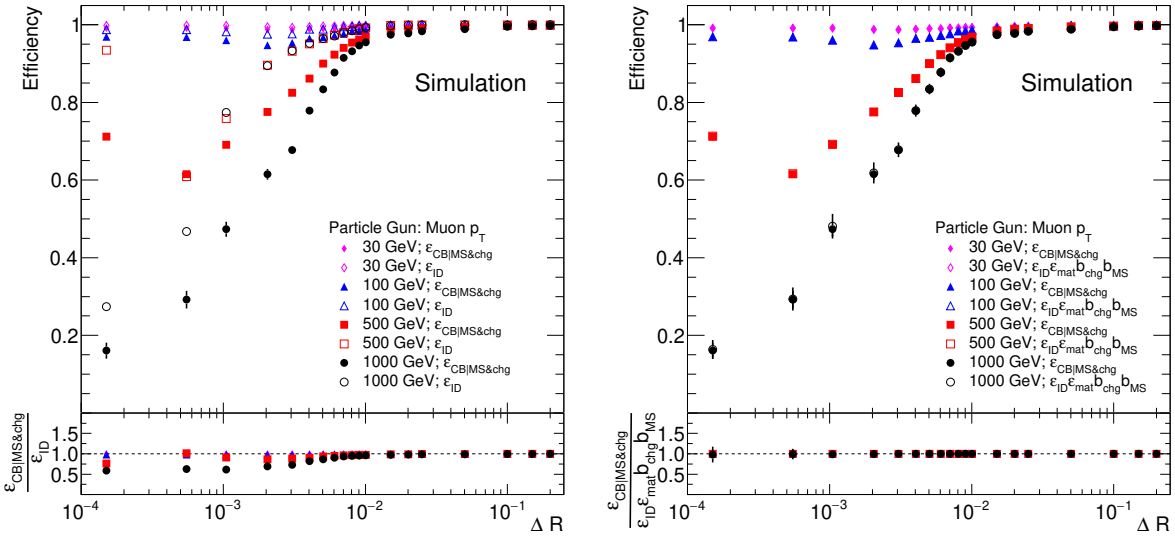
$$\varepsilon_{\text{analysis}} = \varepsilon_{\text{CB|MS\&chg}},$$

where ε_{CB} is combined muon di-track efficiency, ε_{MS} is MS di-track efficiency, and ε_{chg} is the efficiency for the combined track of the tag muon to be correctly assigned as oppositely charged to the ME track of the probe muon. Figure 4.23(a) compares $\varepsilon_{\text{analysis}}$ (filled makers) to ε_{ID} (unfilled markers). As muon p_{T} increases, and ΔR decreases, the two efficiencies begin to diverge. Three effects to cause this break down in equality: the MS- to ID-track matching efficiency, ε_{mat}; bias introduced by requiring two distinct MS tracks, b_{MS}; and bias introduced by requiring the tag and probe muons to be successfully assigned opposite charges, b_{chg}. Accounting for these effects, the relationship between $\varepsilon_{\text{analysis}}$ and ε_{ID} becomes

$$\varepsilon_{\text{analysis}} = \varepsilon_{\text{ID}} \times \varepsilon_{\text{mat}} \times b_{\text{MS}} \times b_{\text{chg}}.$$

Figure 4.23(b) compares the left- and right-hand sides of this equality and demonstrates it success in relating ε_{ID} to $\varepsilon_{\text{analysis}}$. To calculate ε_{ID} from $\varepsilon_{\text{analysis}}$, the above is rearranged to become

$$\varepsilon_{\text{ID}} = \frac{\varepsilon_{\text{analysis}}}{\varepsilon_{\text{mat}} \times b_{\text{MS}} \times b_{\text{chg}}}.$$



(a) (b)

Figure 4.23: Comparison, versus ΔR and with varying p_{T}, of the efficiency measured in the analysis, $\varepsilon_{\text{analysis}}$, (filled markers) to (a) the ID di-track reconstruction efficiency, ε_{ID}, and to (b) the product of ε_{ID} with the additional effects that enter the analysis, each with hollow markers.

Below is a detailed description of each of the three effects that must be considered in a data driven analysis to relate the measured efficiency to the ID di-track reconstruction efficiency. The first effect is the matching, or combination, efficiency, which is the probability for two combined muon tracks to be formed in an event, given that both the MS and the ID successfully reconstructed two muon tracks each. Mathematically,

$$\varepsilon_{\text{mat}} = \varepsilon_{\text{CB|MS\&ID}}.$$

If $\varepsilon_{\text{mat}} < 1$, in some events the ID successfully reconstructs two tracks, but they were not associated with the MS track of the probe to form a combined muon, which is required for

an event to pass the test. The result of this is that some successful events may appear as fail-case events, to reduce $\varepsilon_{\text{analysis}}$ compared to ε_{ID}. The value of ε_{mat} is measured in the Monte Carlo analysis by selecting events in the analysis with exactly two MS and two ID tracks, and testing whether one (fail) or two (pass) combined muon tracks were formed. Figure 4.24 shows the matching efficiency for the Particle Gun events. The decrease in ε_{mat} with increasing muon p_{T} and decreasing ΔR is comparable to ε_{ID} in Figure 4.23(a).

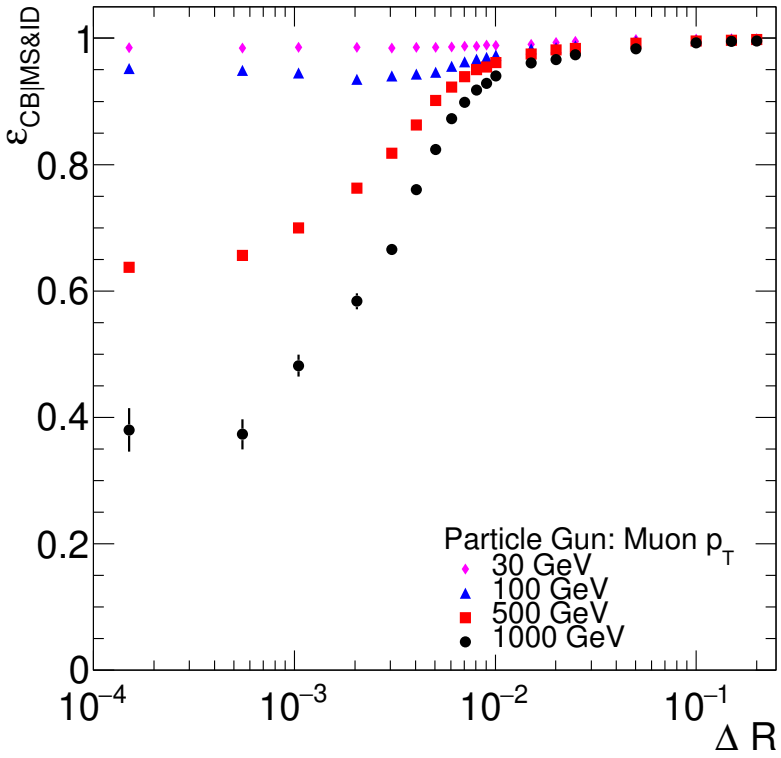


Figure 4.24: The ID-MS track matching efficiency, ε_{mat}, versus ΔR at different muon p_{T}.

The second effect, b_{MS}, accounts for the bias introduced by requiring the two separate MS tracks to be reconstructed in each event. The desired value of $b_{\text{MS}} = 1$ occurs when the di-track reconstruction efficiency of the MS is independent to that of the ID. The value $\varepsilon_{\text{ID|MS}}$ is the probability to reconstruct two ID tracks given that there are two MS tracks in the event. If $\varepsilon_{\text{ID|MS}} > \varepsilon_{\text{ID}}$, then the ID is more likely to have reconstructed two muon tracks if the MS successfully reconstructed two. Figure 4.25(a) compares these two efficiencies and their ratio versus ΔR and p_{T} . For small ΔR the success of the ID reconstructing two tracks becomes more dependent on the success of the MS to reconstruct two tracks. The effect of this is that the analysis preferentially selects di-track events, and so $\varepsilon_{\text{analysis}}$

is increased compared to the desired efficency. To take this bias into account with b_{MS} the reverse situation is required. According to Bayes' theorem,

$$\varepsilon_{\mathrm{ID|MS}} = b_{\mathrm{MS}} \times \varepsilon_{\mathrm{ID}} = \frac{\varepsilon_{\mathrm{MS|ID}}}{\varepsilon_{\mathrm{MS}}} \times \varepsilon_{\mathrm{ID}},$$

such that,

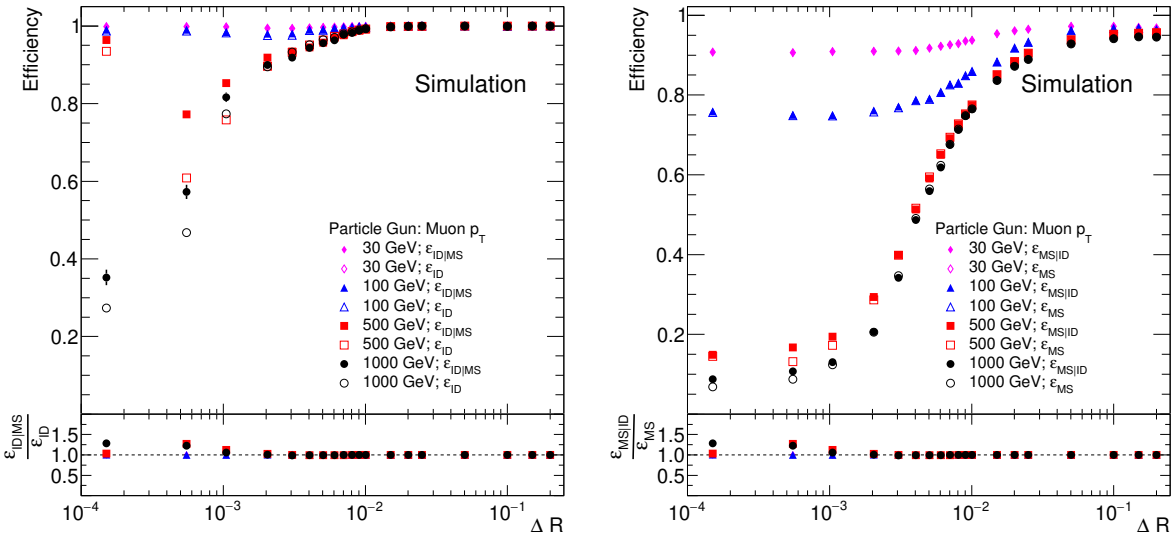
$$b_{\mathrm{MS}} = \frac{\varepsilon_{\mathrm{MS|ID}}}{\varepsilon_{\mathrm{MS}}}.$$

A value $b_{\mathrm{MS}} > 1$ means that if two tracks were formed in the ID, it is more likely that the MS successfully discerned the two muons. The value of $\varepsilon_{\mathrm{MS}}$ is calculated as the portion of total events with two MS tracks, and $\varepsilon_{\mathrm{MS|ID}}$ is calculated as the portion of events with two MS tracks from the events with exactly two ID tracks. Figure 4.25(b) shows each of these efficiencies as well as their ratio, b_{MS}, at the bottom of the plot, which becomes greater than one at small ΔR. Further, the reduced MS di-track reconstruction efficiency, $\varepsilon_{\mathrm{MS}}$, at small ΔR reduces the available statistics in data to probe $\varepsilon_{\mathrm{ID}}$ in this region.

The final effect, b_{chg}, accounts for the bias introduced by the relative probability to successfully assign the two muons as oppositely charged in pass-case and fail-case events. A value $b_{\mathrm{chg}} = 1$ means that successful charge assignment does not depend on whether the event has one or two combined muon tracks. Mathematically,

$$b_{\mathrm{chg}} = \frac{\varepsilon_{\mathrm{chg|CB}}}{\varepsilon_{\mathrm{chg}}}.$$

A value of $b_{\mathrm{chg}} > 1$ means that the muon tracks in pass-case events (events with two CB muon tracks) are more likely to be correctly assigned opposite charge. As events with muons of the same charge are not selected, the analysis preferentially selects successful events and $\varepsilon_{\mathrm{analysis}}$ is increased compared to the desired value. The value of $\varepsilon_{\mathrm{chg}}$ is calculated as the portion of events where the combined muon track of the tag muon has opposite charge to the ME track of the probe muon, given that at least one combined



(a) (b)

Figure 4.25: Correlation between the MS di-track reconstruction efficiency and the ID di-track reconstruction efficiency versus ΔR at different p_{T}. (a) ID efficiency in filled markers, compared to ID efficiency given successful MS di-track reconstruction in hollow markers. (b) MS efficiency in filled markers, compared to MS efficiency given successful ID di-track reconstruction in hollow markers. The ratio values in (b) are equal to b_{MS}.

muon and exactly two MS tracks are in the event. The value of $\varepsilon_{\mathrm{chg|CB}}$ is calculated in the same way, with the additional requirement that the event has exactly two combined muons. Figure 4.26 shows these two efficiencies as well as their ratio, b_{chg}, which becomes greater than one at small ΔR.

As the matching efficiency is the most prevalent effect, the result when taking the product of these three effects is $\varepsilon_{\mathrm{analysis}} < \varepsilon_{\mathrm{ID}}$ across ΔR and p_{T}. For small p_{T} and large ΔR, $\varepsilon_{\mathrm{analysis}} \approx \varepsilon_{\mathrm{ID}}$. To accurately probe $\varepsilon_{\mathrm{ID}}$ across the entire ΔR range however, these three effects must be accounted for.

The quality of the reconstructed ID tracks is also important in a data-driven study to be able to successfully model the signal and background with robust models. Figure 4.27 indicates the quality of the reconstructed ID tracks by showing some of their properties. In the reconstruction of a full CB muon it is possible for its charge to be reassigned compared to the charges of the individual ID or MS tracks. Figure 4.27(a) shows the probability of specifically the ID tracks belonging to the muon objects to be reconstructed

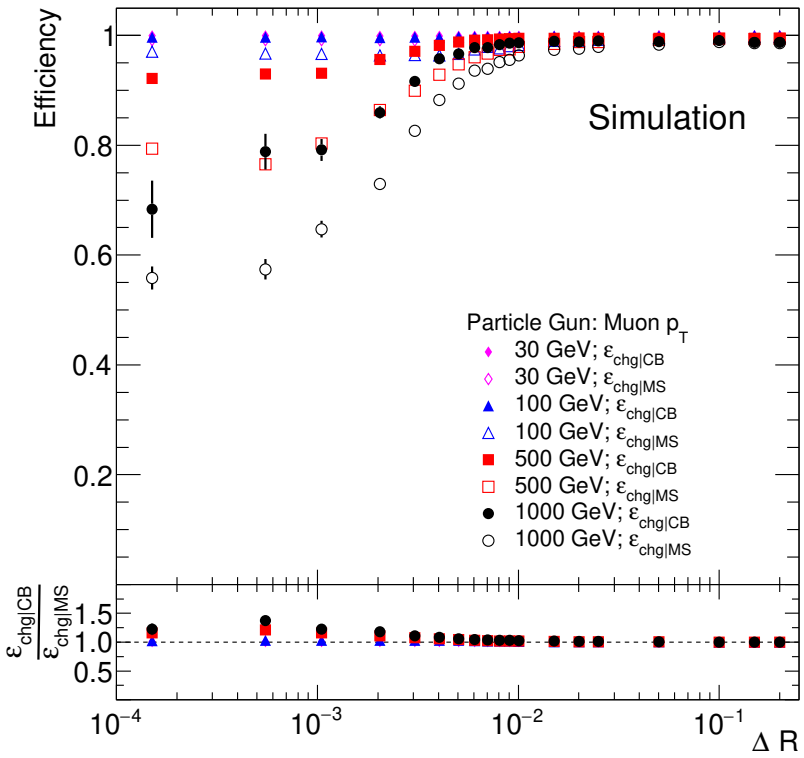


Figure 4.26: Comparison of charge assignment efficiency in successful events compared to total events, versus ΔR at different p_{T}. Hollow markers show the overall efficiency for opposite charge assignment; filled markers show the efficiency in events with two CB tracks. The ratio of these efficiencies is equal to b_{chg}.

as oppositely charged, given that two tracks were reconstructed. In addition, the relative p_{T} resolution of the ID is defined as

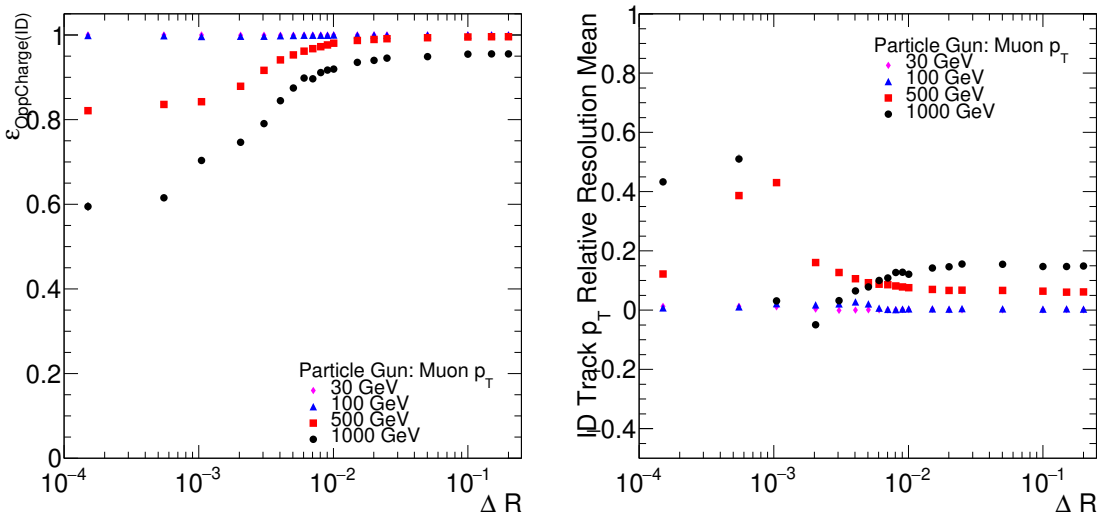
$$p_{\mathrm{T}}(\mathrm{Res}) = \frac{p_{\mathrm{T}}(\mathrm{Reco}) - p_{\mathrm{T}}(\mathrm{Truth})}{p_{\mathrm{T}}(\mathrm{Truth})}.$$

Figure 4.27(b) shows the mean of the relative ID p_{T} resolution, indicating how biased the ID is to reconstructing the p_{T} as higher than the true value at generator level. Figure 4.27(c) shows the root-mean-square (RMS) of the relative ID p_{T} resolution, indicating the overall resolution of the ID tracks.

One further consideration for the tag-and-probe method presented here is that J/ψ production at high p_{T} mostly arises in $B \to J/\psi + X$ decays of b-hadrons, such that J/ψ candidates are often produced close to b-jets. The other particles in these decays can affect the track reconstruction efficiency if their trajectories overlap with the muons and form merged clusters, and this is not taken into account in this study. The production of b-jets containing J/ψ states could be used as an alternative probe of dense environments, based on the properties of the jets such as their p_{T} or their number of contained tracks. Adapting the tag-and-probe method in this way could make the measurement less reliant on the formation of dense environments by the muons alone in $J/\psi \to \mu^+\mu^-$ production. This is a limiting factor in the sensitivity of the Run 2 dataset due to the small statistics of high-p_{T} muons.

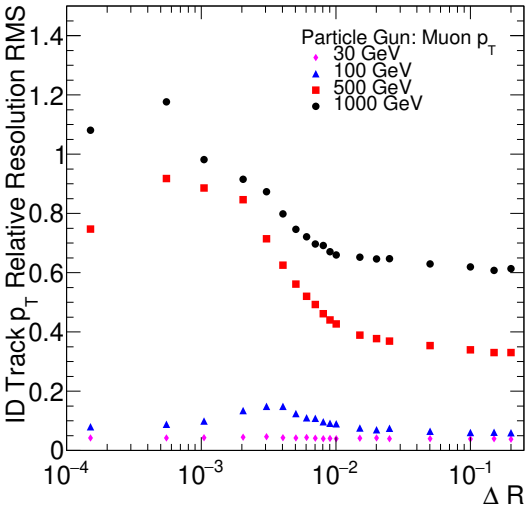
4.6 Outlook

The Monte Carlo study of charged particles produced close-by highlighted the significance of the magnetic field in the ID di-track reconstruction efficiency. For particles with $p_{\mathrm{T}} < 100$ GeV, the decrease in efficiency versus particle ΔR is insignificant for oppositely charged particles. Below this threshold, the separation caused by the bending of the oppositely charged particles by the magnetic field in the ATLAS detector is larger than the granularity of the pixels of the ID. For high-p_{T} muons, where the bending is small, a decrease in reconstruction efficiency is seen for $\Delta R < 0.01$. Thus, to be sensitive



(a)

(b)



(c)

Figure 4.27: Quality of ID track reconstruction in terms of (a) the opposite charge assignment efficiency for events with two ID tracks, (b) the p_{T} resolution bias and (c) the RMS of reconstructed ID tracks.

to a decrease in efficiency for close-by charged particles, analyses with light resonances requires statistics both with $\Delta R < 0.01$ and muon $p_{\mathrm{T}} > 100$ GeV.

In the case of the $J/\psi \to \mu^+\mu^-$ resonance, in the probe muon fail case there are fewer than 5 events per 0.05 GeV bin in the J/ψ mass region (near 3.1 GeV) for $\Delta R < 0.02$ in the Run 2 dataset. Comparatively, the $\phi \to \mu^+\mu^-$ resonance (near 1.0 GeV) has larger statistics for $\Delta R < 0.02$, with more than 100 events per bin, but the signal to background ratio is significantly smaller than for the J/ψ resonance. Regardless, each resonance suffers from a lack of statistics at high muon p_{T}: inclusive of dimuon invariant mass, there are fewer than 10 events per 1 GeV bin of probe p_{T} above 100 GeV. As a result, with the Run 2 dataset neither the J/ψ nor the ϕ analyses are sensitive to the expected decrease in ID reconstruction efficiency seen in the Monte Carlo efficiency estimate, but the technique remains an interesting prospect for the HL-LHC era. Further, there are several additional efficiencies and biases that affect the data-driven technique suggested here, which need to be taken in to account in a full analysis. These are the ID–MS track matching efficiency, the bias from the requirement that the muons are reconstructed separately in the MS, and the bias from the requirement that the two muons are oppositely charged.

In this study an effective resampling technique was developed to model the background in the J/ψ analysis. This technique allows the efficient generation of truth Monte Carlo events in a high-p_{T} phase space that is statistically limited with standard MC event generation, and could potentially be adapted for use in other, similar analyses. An alternative approach to measure the ID track reconstruction efficiency in dense environments could be to base the measurement around the properties of the b-jets produced alongside J/ψ states. In this case $J/\psi \to \mu^+\mu^-$ production could still provide the muons for a tag-and-probe approach, but the jets would form the dense environment such that the measurement would be less reliant on the production of high-p_{T} J/ψ states.

5 Searches for H and Z Boson Decays into a Vector Quarkonium State and a Photon

Vector quarkonium states, $\mathcal{Q}$, are a type of flavourless meson, and are split into bottomonium and charmonium categories. Bottomonium states are mesons consisting of a $b\bar{b}$-quark pair, and charmonium states are mesons consisting of a $c\bar{c}$-quark pair. Properties of each of the vector quarkonium states considered in these searches are summarised in Table 5.1. As discussed in Section 2.3, the rare SM decays of the Higgs boson to a charmonium state, J/ψ or $\psi(2S)$, and a photon offer a probe of the magnitude and sign of the c-quark Yukawa coupling, which has not yet been observed. Similarly, the rare SM decays of the Higgs boson to a bottomonium state, $\Upsilon(1S), \Upsilon(2S)$, or $\Upsilon(3S)$, and a photon offer a probe of the magnitude and sign of the b-quark Yukawa coupling. Searches for each of these exclusive decays are complementary to the corresponding searches to $H \to b\bar{b}$ [50] and $H \to c\bar{c}$ [56, 57] in the study of b- and c-quark couplings, which are sensitive mostly to the magnitude of the Yukawa couplings.

Table 5.1: Properties of the vector quarkonium states considered in these searches [26]. Uncertainties on the quarkonium masses are not shown as they are negligible compared to the central value, of order 1 MeV or smaller.

Quarkonium	Composition	Mass [GeV]	Width [keV]	$\mathcal{B}(Q \to \mu^+\mu^-)$
J/ψ	$c\bar{c}$	3.10	92.9 ± 2.8	$(5.96 \pm 0.03)\%$
$\psi(2S)$	$c\bar{c}$	3.69	294.0 ± 8.0	$(0.80 \pm 0.06)\%$
$\Upsilon(1S)$	$b\bar{b}$	9.46	54.0 ± 1.3	$(2.48 \pm 0.05)\%$
$\Upsilon(2S)$	$b\bar{b}$	10.02	32.0 ± 2.6	$(1.93 \pm 0.17)\%$
$\Upsilon(3S)$	$b\bar{b}$	10.36	20.3 ± 1.9	$(2.18 \pm 0.21)\%$

Feynman diagrams of the direct, $\mathcal{A}_{\text{dir}}$, and indirect, $\mathcal{A}_{\text{ind}}$, contributions to the $H \to \mathcal{Q}\gamma$ decay amplitude are shown in Figure 2.6 in Section 2.3. Recent SM predictions of the branching ratios for the J/ψ and $\Upsilon(1S, 2S, 3S)$ decay channels are presented in Table 5.2. The branching ratio of $H \to \psi(2S)\gamma$ is predicted to be $(1.03 \pm 0.06) \times 10^{-6}$, obtained by private communication from the authors of Ref. [74]. This was calculated by using an estimate of the value of the order-ν^2 non-relativistic QCD long-distance matrix element, where ν is the velocity of the charm quarks in the rest frame of the $\psi(2S)$.

Table 5.2: Recent calculations of the $H \to \mathcal{Q}\gamma$ branching fractions expected in the Standard Model. From Ref. [94].

Vector quarkonium state	SM branching fraction, $\mathcal{B}(H \to \mathcal{Q}\gamma)$		
	Ref. [71] (2015)	Refs. [73, 74] (2017)	Ref. [76] (2019)
J/ψ	$2.95^{+0.17}_{-0.17} \times 10^{-6}$	$2.99^{+0.16}_{-0.15} \times 10^{-6}$	$3.01^{+0.15}_{-0.15} \times 10^{-6}$
$\Upsilon(1S)$	$4.61^{+1.76}_{-1.23} \times 10^{-9}$	$5.22^{+2.02}_{-1.70} \times 10^{-9}$	$9.97^{+4.04}_{-3.03} \times 10^{-9}$
$\Upsilon(2S)$	$2.34^{+0.76}_{-1.00} \times 10^{-9}$	$1.42^{+0.72}_{-0.57} \times 10^{-9}$	$2.62^{+1.39}_{-0.91} \times 10^{-9}$
$\Upsilon(3S)$	$2.13^{+0.76}_{-1.13} \times 10^{-9}$	$0.91^{+0.48}_{-0.38} \times 10^{-9}$	$1.87^{+1.05}_{-0.69} \times 10^{-9}$

The branching ratios of the charmonium decays are of order 10^{-6}, where the indirect amplitude dominates and $\mathcal{A}_{\text{ind}} \approx 20 \times \mathcal{A}_{\text{dir}}$. This is typically the case for the rare SM Higgs boson decays into a meson and a photon. The branching ratios of the bottomonium decays are much smaller, of order 10^{-9}, because of an almost-perfect cancellation between $\mathcal{A}_{\text{ind}}$ and $\mathcal{A}_{\text{dir}}$ in the SM. This makes these channels particularly sensitive to modifications from BSM physics.

The corresponding decays of the Z boson to a vector quarkonium state and a photon offer a probe of the light-cone distribution amplitudes (LCDAs) of the charmonium and bottomonium states, as discussed in Section 2.3.2. The direct and indirect contributions to the decay amplitude, analogous to the $H \to \mathcal{Q}\gamma$ decays, are shown in Figure 2.7 in Section 2.3. Recent calculations of the SM expectations of the branching fractions for the J/ψ and $\Upsilon(1S, 2S, 3S)$ decay channels are shown in Table 5.3, where a value of the branching ratio for the $\psi(2S)$ decay channel is not currently available in the literature. Each of the branching ratios are of order 10^{-8}.

Table 5.3: Recent calculations of the $Z \to \mathcal{Q}\gamma$ branching fractions expected in the Standard Model. From Ref. [94].

Vector quarkonium state	SM branching fraction, $\mathcal{B}(Z \to \mathcal{Q}\gamma)$		
	Ref. [88] (2015)	Ref. [87] (2015)	Ref. [89] (2018)
J/ψ	$8.02^{+0.46}_{-0.44} \times 10^{-8}$	$9.96^{+1.86}_{-1.86} \times 10^{-8}$	$8.96^{+1.51}_{-1.38} \times 10^{-8}$
$\Upsilon(1S)$	$5.39^{+0.17}_{-0.15} \times 10^{-8}$	$4.93^{+0.51}_{-0.51} \times 10^{-8}$	$4.80^{+0.26}_{-0.25} \times 10^{-8}$
$\Upsilon(2S)$	-	-	$2.44^{+0.14}_{-0.13} \times 10^{-8}$
$\Upsilon(3S)$	-	-	$1.88^{+0.11}_{-0.10} \times 10^{-8}$

This chapter discusses the latest searches for the decays $H(Z) \to \mathcal{Q}\gamma$, which use 139 fb^{-1}

of ATLAS data collected at $\sqrt{s} = 13$ TeV. The content of this chapter is largely based on the publication for this search in Ref. [94], for which I am a primary editor, and covers more detail on many aspects of the analyses. The results, summarised previously in Section 2.3.3, are an improvement by a factor of approximately 2 on the previous ATLAS result, which used 36.1 fb^{-1} of ATLAS data collected at $\sqrt{s} = 13$ TeV [92]. These searches target the dimuon decays of the vector quarkonium states, $\mathcal{Q} \to \mu^+\mu^-$, leading to $\mu^+\mu^-\gamma$ final states. The experimental signature of these searches is shown in Figure 5.1. A high-energy photon and $\mathcal{Q}$ state interact back-to-back in the detector following the decay of the H or Z boson, and there is a resonance in dimuon mass, $m_{\mu^+\mu^-}$, in the reconstruction of the quarkonium state, and a second resonance in three-body mass, $m_{\mu^+\mu^-\gamma}$, in the reconstruction of the boson. The backgrounds in these searches are treated as two distinct sources, called the 'exclusive' and 'inclusive' backgrounds. The exclusive background originates from $\mu^+\mu^-\gamma$ events produced via the Drell-Yan process; the inclusive background originates mostly from multi-jet and γ+jet events involving $\mathcal{Q}$ or non-resonant dimuon production, and is the dominant background. Two-dimensional fits are performed in $m_{\mu^+\mu^-\gamma}$ and $m_{\mu^+\mu^-}$ when extracting the final results to discern all of the signals from each other and from each of the sources of background.

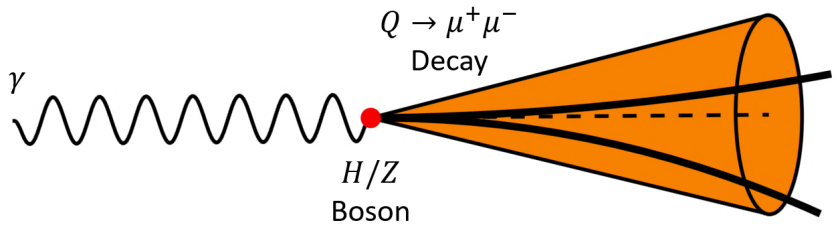


Figure 5.1: Experimental signature of the $H(Z) \to \mathcal{Q}\gamma$ decays, where the quarkonium state decays into a muon pair, $\mathcal{Q} \to \mu^+\mu^-$.

Throughout this chapter, where no distinction is relevant, the J/ψ and $\psi(2S)$ states are collectively denoted by $\psi(nS)$, and the $\Upsilon(1S, 2S, 3S)$ states are denoted by $\Upsilon(nS)$. The symbol $\mathcal{Q}$, meaning quarkonium, denotes the $\psi(nS)$ and $\Upsilon(nS)$ states collectively. Section 5.1 describes the data sample and event selection used in these searches, and Section 5.2 describes the models used for the signal decays. Sections 5.3 and 5.4 describe the models used for the exclusive and inclusive components of the backgrounds in these

searches, respectively. Section 5.5 describes the statistical treatment and likelihood functions used to extract the 95% confidence level upper limits of each decay channel and a full description of the observed results and their interpretation in the κ framework.

5.1 Event Selection

This section describes the requirements imposed on data to be considered candidate events in the searches for $H \to \mathcal{Q}\gamma$ and $Z \to \mathcal{Q}\gamma$. These are based on data quality requirements and available triggers, as well as geometric acceptance of the ATLAS detector. Several kinematic thresholds are also optimised to maximise the signal-to-background ratio of the searches.

The requirements for the H decay channels are the same as the Z signal channels, such that both share a background model. The requirements used in the $\psi(nS)$ analyses are the same as the requirements in the $\Upsilon(nS)$ analyses, with the exception of the $m_{\mu^+\mu^-}$ window and the $p_{\mathrm{T}}^{\mu^+\mu^-}$ thresholds of the candidate events.

5.1.1 Data Sample and Triggers

The full ATLAS pp collision dataset collected at $\sqrt{s} = 13$ TeV, with stable beam conditions and relevant detector systems functional [103] between 2015–2018, is considered in this analysis. As well as the trigger requirements described below, data events are required to pass the GRL requirements described in Section 3.1.1. These exclusive decay searches use triggers dedicated to the detection of these experimental signatures, and require a single photon and at least one muon in the event triggers. These dedicated triggers were developed as the momentum of the decay products in these decay channels are too low to be triggered on by unprescaled single object triggers, such as the single-photon triggers, and the unique topology of the decays provided the opportunuty to develop triggers with combined photon and muon requirements with much reduced p_{T} thresholds to increase signal acceptance.

The instantaneous luminosity increased during the operation of the LHC in Run 2. To

handle the increased dataflow, the transverse momentum thresholds and object identification requirements of some triggers were modified during the data taking period. Available throughout the entire 2015–2018 run period was a trigger requiring a 'medium' identification photon [196] with tranverse momentum $p_{\mathrm{T}}^{\gamma} > 25$ GeV and at least one muon identified at the level-1 trigger with $p_{\mathrm{T}}^{\mu} > 24$ GeV. During the 2015–2016 run period this trigger was complemented by a trigger requiring a 'loose' identification photon [196] with $p_{\mathrm{T}}^{\gamma} > 35$ GeV and a muon identified by the software-based high-level trigger with $p_{\mathrm{T}}^{\mu} > 18$ GeV. During the 2017–2018 run periods the trigger was complemented by two additional triggers. The first is a trigger requiring a 'tight' identification photon [196] with $p_{\mathrm{T}}^{\gamma} > 35$ GeV and a muon identified by the high-level trigger with $p_{\mathrm{T}}^{\mu} > 18$ GeV. The second is a trigger requiring a 'loose' identification photon with $p_{\mathrm{T}}^{\gamma} > 35$ GeV, one muon identified at the level-1 trigger with $p_{\mathrm{T}}^{\mu} > 15$ GeV and a second muon identified at the high-level trigger with $p_{\mathrm{T}}^{\mu} > 2$ GeV. These triggers are summarised in Table 5.4, along with their integrated luminosities and periods of operation.

Table 5.4: The dedicated triggers used to select candidate $H \to \mathcal{Q}\gamma$ and $Z \to \mathcal{Q}\gamma$ events from 2015–2018. GRLs are applied in the calculation of the integrated luminosities.

Period	Trigger	Luminosity (fb^{-1})
2015–2018	`HLT_g25_medium_mu24`	139.0
2015–2016	`HLT_g35_loose_L1EM22VHI_mu18noL1`	36.2
2017–2018	`HLT_g35_tight_icalotight_L1EM24VHI_mu18noL1`	102.8
2017–2018	`HLT_g35_loose_L1EM24VHI_mu15_mu2noL1`	102.8

The total integrated luminosity of the search, taking into account available triggers and the data quality requirements, is 139.0 ± 2.4 fb^{-1}. Primary luminosity measurements are performed by the LUCID-2 detector [190] and the uncertainty on this measurement is calculated using the method in Refs. [191, 192].

To streamline analyses in the ATLAS experiment, data may be processed through derivations as described in Section 3.4. In this analysis, data must meet the loose requirements of the `HIGG2D5` derivation, which is purpose-built to search for exclusive decays of the H and Z bosons to a meson and a photon. In the case of the $\mathcal{Q}\gamma$ decays, the `HIGG2D5` derivation requires that each event must contain at least one oppositely charged dimuon pair.

The muon with a larger p_{T}, called the leading muon, must satisfy $p_{\mathrm{T}}^{\mu} > 15$ GeV, and the muon with smaller p_{T}, called the subleading muon, must satisfy $p_{\mathrm{T}}^{\mu} > 2.5$ GeV. A fit of the dimuon vertex [197] must have $\chi^2 < 200$. The invariant mass of the dimuon system, which is the reconstructed quarkonium candidate, must satisfy 2.0 GeV $< m_{\mu^+\mu^-} <$ 4.3 GeV for the $\psi(nS)\,\gamma$ decay channels or 8.0 GeV $< m_{\mu^+\mu^-} <$ 12.0 GeV for the $\Upsilon(nS)\,\gamma$ decay channels. These values are chosen such that they enclose the mass of each of the quarkonium states, summarised in Table 5.1, with sufficient sidebands to use as control regions. The events must also contain at least one photon with $p_{\mathrm{T}}^{\gamma} > 15$ GeV.

5.1.2 Selection Requirements

Events which pass the trigger and data quality requirements, and requirements of the `HIGG2D5` derivation, must satisfy several additional selection criteria to be classed as a candidate event. These requirements are based on the kinematic and isolation properties of the photons and the muons in the event, as well as how they combine to reconstruct the quarkonium and boson candidates. Several requirements overlap with the `HIGG2D5` derivation criteria, but are reapplied explicitly in the offline selection to ensure consistency between candidate muons and photons chosen within each event. In general, requirements on photon and muon $|\eta|$ are determined by detector geometry, whilst requirements on photon and muon p_{T} are imposed by the p_{T} thresholds of the triggers.

Reconstructed muons must be either 'combined' or 'segment-tagged', described in Section 3.3.4, and have pseudorapidity $|\eta_{\mu}| < 2.5$: the geometric acceptance of the inner detector (ID). There must be at least one pair of oppositely charged muons in each event, where the leading muon in the pair has $p_{\mathrm{T}}^{\mu} > 18$ GeV and the subleading muon has $p_{\mathrm{T}}^{\mu} > 3$ GeV. The invariant mass of the dimuon system, which forms the reconstructed quarkonium candidate, must satisfy 2.4 GeV $< m_{\mu^+\mu^-} <$ 4.3 GeV in the searches for $\psi(nS)\,\gamma$ signals or 8.0 GeV $< m_{\mu^+\mu^-} <$ 12.0 GeV in the searches for $\Upsilon(nS)\,\gamma$ signals.

Several isolation and vertex requirements are also imposed on the dimuon system. The variable `ptvarcone30` is defined, which is the p_{T} sum of all of the ID tracks within a variable $\Delta R = \sqrt{(\Delta\phi)^2 + (\Delta\eta)^2}$ cone size of $\Delta R = \min\{10\text{ GeV}/(p_{\mathrm{T}}^{\mu}\,[\text{GeV}]), 0.3\}$ around

the leading muon. The sum excludes the p_{T} of the leading muon itself, as well as the p_{T} of the subleading muon if it lies within the ΔR cone, and only ID tracks originating from the primary vertex are considered.[4] The `FixedCutTightTrackOnly` muon isolation working point is imposed [198], which requires `ptvarcone30` $< 6\%$ of $p_{\mathrm{T}}^{\mu^+\mu^-}$, the transverse momentum of the reconstructed quarkonium candidate. The transverse decay length variable L_{xy} is defined for the vertex requirements. This is the signed projection of the vector leading from the primary vertex to the dimuon vertex onto the direction of $p_{\mathrm{T}}^{\mu^+\mu^-}$. To suppress contributions from events with displaced vertices originating from B-hadron decays, candidate $\mathcal{Q} \to \mu^+\mu^-$ decays are required to satisfy the L_{xy} significance criterion $|L_{xy}/\sigma_{L_{xy}}| < 3$, where $\sigma_{L_{xy}}$ is the uncertainty on L_{xy}. If there is more than one eligible pair of muons in the event, the dimuon pair with its mass closest to the J/ψ mass in Table 5.1 is used. This occurs in fewer than 2% of events which pass the trigger requirements.

Reconstructed photons must pass the 'tight' quality criteria [196], described in Section 3.3.3, have pseudorapidity $|\eta_\gamma| < 2.37$, excluding the calorimeter barrel to endcap transition region $1.37 < |\eta_\gamma| < 1.52$, and have a transverse momentum $p_{\mathrm{T}}^{\gamma} > 35$ GeV. Photons must also pass track- and calorimeter-isolation requirements. The variable `ptcone20` is defined as the p_{T} sum of the ID tracks within a cone of $\Delta R = 0.2$ of the photon candidate, and the variable `topoetcone40` is defined as the sum of the transverse energy E_{T} of the topological calorimeter energy clusters within $\Delta R = 0.4$ of the photon candidate.[5] The `FixedCutTight` photon isolation working point is imposed [196], which requires a track isolation of `ptcone20` $< 5\%$ of p_{T}^{γ} and a calorimeter isolation of `topoetcone40` $<$ (2.45 GeV + 2.2% of p_{T}^{γ} [GeV]). If there is more than one elegible photon in the event, the photon with the largest p_{T} is selected. This occurs in a negligible portion, $\sim 0.1\%$, of events which pass the trigger requirements.

Candidate photons and quarkonium states are combined to reconstruct the boson candidate. To suppress events where the $\mathcal{Q}$ candidate and the photon candidate are collimated

[4] The primary vertex is defined as the reconstructed vertex in the event with the highest $\sum p_{\mathrm{T}}^2$ of all tracks associated with the formation of the vertex.

[5] This calorimeter isolation variable is corrected to account for contributions from other pp interactions in the same bunch crossing [196].

(have small angular separation), combinations must satisfy $|\Delta\phi(\mathcal{Q},\gamma)| > \pi/2$, where $\Delta\phi(\mathcal{Q},\gamma)$ is the separation in azimuthal angle between the two candidates. To maintain a common event selection for the H and Z boson signal searches whilst keeping an optimal sensitivity for each, a variable $p_{\mathrm{T}}^{\mu^+\mu^-}$ threshold is applied depending on the mass of the boson candidate, $m_{\mu^+\mu^-\gamma}$. For $\psi(nS)\,\gamma$ candidates the threshold is 40 GeV for $m_{\mu^+\mu^-\gamma} \leq 91$ GeV and 54.4 GeV for $m_{\mu^+\mu^-\gamma} \geq 140$ GeV. For $\Upsilon(nS)\,\gamma$ candidates the threshold is 34 GeV for $m_{\mu^+\mu^-\gamma} \leq 91$ GeV and 52.7 GeV for $m_{\mu^+\mu^-\gamma} \geq 140$ GeV. The $p_{\mathrm{T}}^{\mu^+\mu^-}$ threshold varies linearly between the two extremes in each of the $\psi(nS)\,\gamma$ and $\Upsilon(nS)\,\gamma$ analyses in the region 91 GeV $< m_{\mu^+\mu^-\gamma} <$ 140 GeV, and $p_{\mathrm{T}}^{\mu^+\mu^-}$ must be greater than the threshold value for the event to be considered a candidate. The thresholds on $p_{\mathrm{T}}^{\mu^+\mu^-}$ are chosen to optimise the significance of potential signals at the Higgs and Z boson masses. These were optimised by maximising the figure-of-merit $S/\sqrt{B}$, where S is the number of signal events and B is the number of background events for a given threshold. If an event meets all of these criteria, it is considered as a candidate event in the signal region of these searches.

5.1.3 Event Categorisation

Candidate events in the search for the $\Upsilon(nS)\,\gamma$ signals are separated into categories based on the location of the two muons. Events where both muons interacted in the barrel of the ATLAS detector, in the region $|\eta|_\mu < 1.05$, constitute the barrel category (B). Events which do not meet this requirement contain at least one muon that interacted in the endcap of the ATLAS detector, and constitute the endcap category (EC). Categorising $\Upsilon(nS)$ events in this way improves the sensitivity of the analysis compared to a single inclusive category, as the improved resolution in the barrel helps resolve the separate $\Upsilon(1S, 2S, 3S)$ states. Conversely, a single inclusive category (INC) is used in the search for the $\psi(nS)\,\gamma$ signals since the J/ψ and $\psi(2S)$ resonances have a large mass difference and do not overlap. In this case there is no significant benefit in categorising the events.

5.2 Signal Modelling

To model the signal, MC events were simulated and subjected to the event selection described in Section 5.1, and the resulting signal distributions in dimuon and three-body mass were fitted with analytical functions to produce the shapes used in the maximum-likelihood fit in Section 5.5 to extract the final results. This section describes the procedure used to generate the signal events and produce the final model shapes, with details on the signal acceptance and resolution and the systematic uncertainties considered in the normalisation of the signal.

5.2.1 Event Generation and Simulation

Separate Higgs boson samples were produced for the main production modes to account for differences in kinematic properties between modes. In order of largest-to-smallest production cross section, these are gluon-gluon fusion (ggH), vector boson fusion (VBF), and associated production with a Z boson (ZH), $W^{\pm}$ boson (WH), or a $t\bar{t}$-pair ($t\bar{t}H$). The ZH and WH samples are known collectively as VH, where V is a vector boson. The $t\bar{t}H$ samples are further divided in to subcategories to account for the different possible decays of the two t-quarks. These categories are for where both decay leptonically (`dilep`), both decay hadronically (`allhad`), and for one leptonic decay and one hadronic decay (`semilep`). The small contribution from associated production of the Higgs boson with a $b\bar{b}$-pair ($b\bar{b}H$) is not modelled explicitly, but is accounted for in the normalisation of the ggH sample. The production of Z boson events is modelled in the $q\bar{q} \to Z$ production mode; contribution by the $gg \to Z$ production mode is taken into account in the normalisation of the sample. The subsequent decays of the H and Z bosons to $\mathcal{Q}[\to \mu^+\mu^-]\,\gamma$ are included in the generated events. Separate samples are produced for the two charmonium states, J/ψ and $\psi(2S)$, whereas the three bottomonium states, $\Upsilon(1S, 2S, 3S)$, are grouped.

The Powheg Box v2 MC event generator [199–203] was used to model the ggH and VBF Higgs boson production mechanisms and the Z boson production, calculated up to next-to-leading order (NLO) in α_s, the coupling constant of the strong force. This was

interfaced with Pythia 8.212 [141, 142], which used a set of tuned parameters called the AZNLO tune [204] to model the parton shower, hadronisation, and underlying event, and the CTEQ6L1 parton distribution functions [195]. Pythia8.212 was used to model the two VH production mechanisms, with the A14 event tune [194] for hadronisation and the underlying event, and the NNPDF2.3lo parton distribution functions [205]. The MadGraph5_aMC@NLO 2.2.2 [206] event generator was used to model the three $t\bar{t}H$ samples, using Pythia8.212 to model the parton shower with the same event tune and parton distribution functions as the VH production mechanisms. The generator configuration used to generate each sample is summarised in Table 5.5. In all cases the subsequent decays of the H and Z bosons to $\mathcal{Q}[\to \mu^+\mu^-]\,\gamma$ are modelled as a cascade of two-body decays. The resulting simulated events are passed through the detailed full-sim Geant4 simulation of the ATLAS detector [144, 145], and processed with the same software used to reconstruct and select the data. Separate samples were produced for the 2015–2016 (`mc16a`), 2017 (`mc16d`), and 2018 (`mc16e`) run periods to take into account the changing conditions in the ATLAS detector throughout Run 2. Each sample is normalised according to the integrated luminosity of the corresponding run period: 36.2 fb^{-1} for 2015–2016, 44.3 fb^{-1} for 2017, and 58.5 fb^{-1} for 2018.

Table 5.5: The Monte Carlo generator configuration used to generate each of the $H(Z) \to \mathcal{Q}\,\gamma$ samples. PDF is an abbreviation of parton distribution function.

Production Mode	Generator	Parton Showering	Event Tune	PDF
$H : ggH$	Powheg Box v2	Pythia8.212	AZNLO	CTEQ6L1
H : VBF	Powheg Box v2	Pythia8.212	AZNLO	CTEQ6L1
$H : ZH$	Pythia8.212	Pythia8.212	A14	NNPDF2.3lo
$H : WH$	Pythia8.212	Pythia8.212	A14	NNPDF2.3lo
$H : t\bar{t}H_{\text{allhad}}$	MadGraph5_aMC@NLO	Pythia8.212	A14	NNPDF2.3lo
$H : t\bar{t}H_{\text{semilep}}$	MadGraph5_aMC@NLO	Pythia8.212	A14	NNPDF2.3lo
$H : t\bar{t}H_{\text{dilep}}$	MadGraph5_aMC@NLO	Pythia8.212	A14	NNPDF2.3lo
$Z : q\bar{q}$	Powheg Box v2	Pythia8.212	AZNLO	CTEQ6L1

With the exception of $t\bar{t}H$ production mechanism, each of the $H(Z) \to J/\psi\,\gamma$ samples contain 50k events and each of the $H(Z) \to \Upsilon(nS)\,\gamma$ samples contain 100k events. The $\Upsilon(nS)$ samples were chosen to have higher statistics than the corresponding J/ψ samples to obtain sufficient statistics for the individual $\Upsilon(1S, 2S, 3S)$ states. The $H(Z) \to \psi(2S)\,\gamma$ samples have different statistics depending on run period, prioritising statistics according

to luminosity. Excluding $t\bar{t}H$, the $\psi(2S)$ samples contain 20k events for `mc16a`, and 40k events each for `mc16d` and `mc16e`. All of the $t\bar{t}H$ samples across $\mathcal{Q}$ states contain 10k events for each of the `dilep`, `allhad`, and `semilep` top-quark decay modes. The statistics of each sample are summarised in Table 5.6.

Table 5.6: The number of events generated per production mechanism for the $H(Z) \to \mathcal{Q}\gamma$ samples, split by MC period.

	Number of Events			
Production Mode	2015–2016	2017	2018	Total
$H \to J/\psi\,\gamma : ggH, \text{VBF}, ZH, WH$	50k	50k	50k	150k
$H \to J/\psi\,\gamma : ttH_{\text{allhad,semilep,dilep}}$	10k	10k	10k	30k
$H \to J/\psi\,\gamma$: Total	230k	230k	230k	690k
$Z \to J/\psi\,\gamma : q\bar{q}$	50k	50k	50k	150k
$H \to \psi(2S)\,\gamma : ggH, \text{VBF}, ZH, WH$	20k	40k	40k	100k
$H \to \psi(2S)\,\gamma : ttH_{\text{allhad,semilep,dilep}}$	10k	10k	10k	30k
$H \to \psi(2S)\,\gamma$: Total	110k	190k	190k	490k
$Z \to \psi(2S)\,\gamma : q\bar{q}$	20k	40k	40k	100k
$H \to \Upsilon(nS)\,\gamma : ggH, \text{VBF}, ZH, WH$	100k	100k	100k	300k
$H \to \Upsilon(nS)\,\gamma : ttH_{\text{allhad,semilep,dilep}}$	10k	10k	10k	30k
$H \to \Upsilon(nS)\,\gamma$: Total	430k	430k	430k	1290k
$Z \to \Upsilon(nS)\,\gamma : q\bar{q}$	100k	100k	100k	300k

The Higgs boson signal samples are normalised according to cross sections calculated for a Standard Model H with a mass of $m_H = 125.09$ GeV at a centre-of-mass energy of $\sqrt{s} = 13$ TeV [30, 86]. The ggH samples are normalised to a total cross section predicted by a next-to-next-to-next-to-leading-order (N^{3}LO) QCD calculation with NLO electroweak corrections [207–210]. The VBF samples are normalised to an approximate next-to-next-to-leading-order (NNLO) QCD cross section with NLO electroweak corrections [211–213]. The VH samples are normalised to cross sections calculated at NNLO in QCD with NLO electroweak corrections [214, 215] including the NLO QCD corrections [216] for $gg \to ZH$. The $t\bar{t}H$ samples are normalised to cross sections calculated at NLO in QCD with NLO electroweak corrections [30], and the production cross section used to scale the ggH sample to account for the $b\bar{b}H$ mechanism was calculated at a mix of NNLO and NLO accuracy in QCD, with no electroweak corrections [30]. The production rate for the Z boson is normalised to the total cross section between 66 GeV and 116 GeV obtained from the measurement in Ref. [85], which uses 81 pb^{-1} of ATLAS data

collected at $\sqrt{s} = 13$ TeV. The details of the production cross sections assumed in this analysis are summarised in Table 5.7. Values for the $\mathcal{Q} \to \mu^+\mu^-$ branching ratios used in sample normalisation are summarised in Table 5.1 and are taken from the Review of Particle Physics [26], along with the branching ratios for the t-quark decays, summarised in Table 5.8, which are used in the normalisation of the $t\bar{t}H$ samples.

Table 5.7: The various cross sections used in sample normalisation. Values are from Refs. [30, 85, 86].

			Order of Calculation	
Production Mode	Cross Section [pb]	Uncertainty [%]	QCD	EW
$H : ggH$	48.61	6.26%	N^{3}LO	NLO
H : VBF	3.766	2.13%	NNLO	NLO
$H : ZH$	0.880	3.50%	NNLO	NLO
$H : WH$	1.358	1.44%	NNLO	NLO
$H : t\bar{t}H$	0.5065	9.32%	NLO	NLO
$H : b\bar{b}H$	0.4863	22.0%	NNLO+NLO	–
H : Total	55.6068	5.98%	–	–
Z : Inclusive	58858.0	2.9%	Data Measurement	

Table 5.8: t-quark branching ratios used in the normalisation of the $t\bar{t}H$ samples. Values are from Ref. [26].

Decay Mode	Branching Ratio
$t\bar{t}$ →hadrons	$(44.22 \pm 1.86)\%$
$t\bar{t}$ →hadron and lepton	$(44.16 \pm 1.24)\%$
$t\bar{t}$ →leptons	$(11.02 \pm 0.41)\%$

The signal samples are produced assuming no polarisation of the boson decay products. The effects of quarkonium polarisation on the kinematic distributions of the muons in each event are instead accounted for via a reweighting of the events. The quarkonium states in the $H \to \mathcal{Q}\gamma$ signals are expected to be transversely polarised and are reweighted as $\frac{3}{4}(1 + \cos^2\theta')$, calculated using the method described in Ref. [217]. Here, θ' is the angle between the μ^+ in the rest frame of the $\mathcal{Q}$ state and the $\mathcal{Q}$ state in the rest frame of the H. The quarkonium states in the $Z \to \mathcal{Q}\gamma$ signals are expected to be longitudinally polarised, as the transversely polarised meson vanishes to leading order in $m_\mathcal{Q}^2/m_Z^2$ [87]. The Z boson signals are reweighted as $\frac{9}{8}(1 - \cos^2\theta\cos^2\theta' - \frac{1}{4}\sin 2\theta \sin 2\theta' \cos[\phi - \phi'])$, as derived in Ref. [218]. Here, the θ and ϕ angles are defined in the Collins-Soper frame of the Z boson, where the z-axis is aligned with the bisector of the angle between one

proton beam and the opposite of the second beam in the Z boson rest frame; the θ' and ϕ' angles are defined in the cloned cascade frame, where the co-ordinate axes are an exact geometrical clone as in the Collins-Soper frame but used now in the $\mathcal{Q}$ rest frame. Further scale factors are applied on an event-by-event basis to account for differences between data and MC in the trigger efficiency, photon and muon reconstruction, and to account for pile-up. Pile-up was modelled by overlaying each event with inelastic pp events generated with Pythia8.186, using the A3 tune and NNPDF2.3LO parton distribution functions [219].

5.2.2 Signal Acceptance and Efficiency

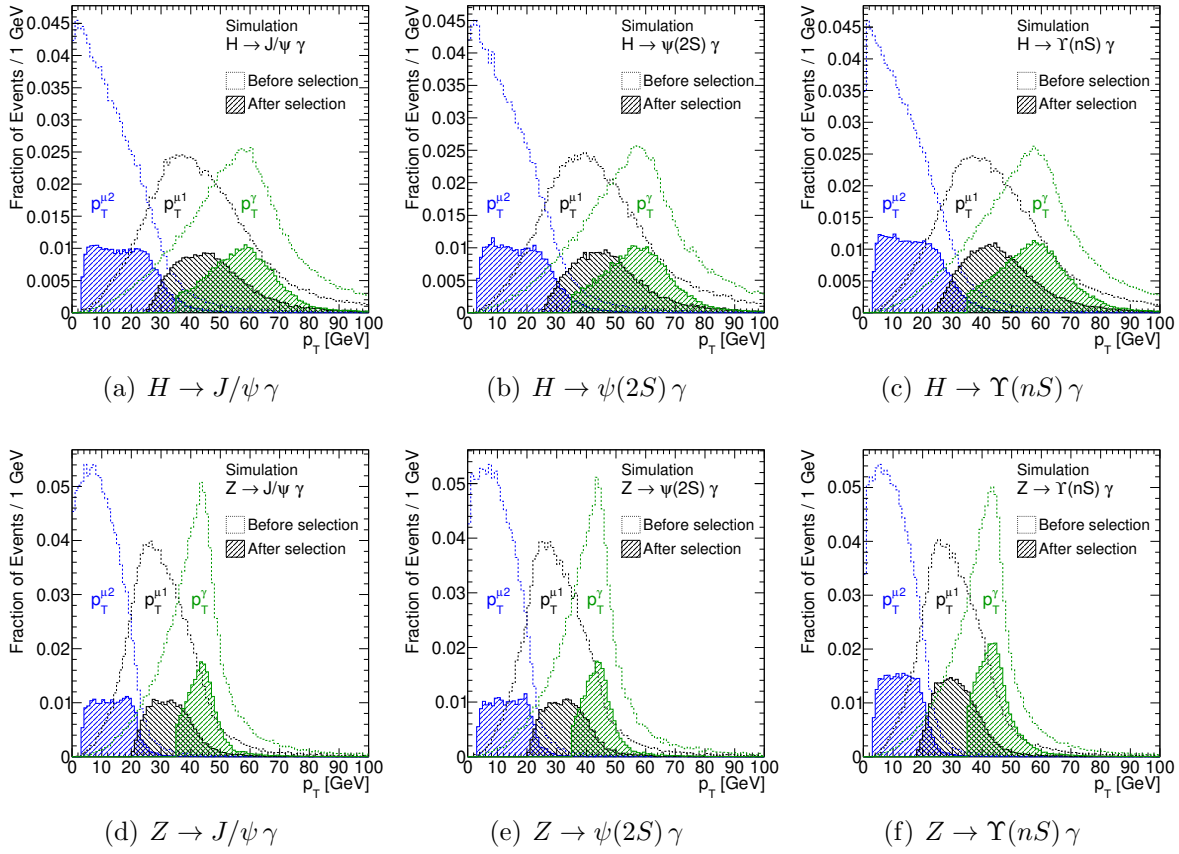
Simulated events are processed with the `HDBS2` derivation, which is a port of the `HIGG2D5` described in Section 5.1.1. For reconstructed events to pass the `HDBS2` derivation criteria they must contain at least one pair of oppositely charged muons, where the leading muon satisfies $p_{\mathrm{T}}^{\mu} > 17$ GeV and the subleading muon satisfies $p_{\mathrm{T}}^{\mu} > 2.5$ GeV. A fit of the dimuon vertex [197] must have $\chi^2 < 200$. The invariant mass of the dimuon system must be between 2.4 GeV $< m_{\mu^+\mu^-} <$ 4.3 GeV for the $\psi(nS)\,\gamma$ final states or 8.0 GeV $< m_{\mu^+\mu^-} <$ 12.0 GeV for the $\Upsilon(nS)\,\gamma$ final states, and the transverse momentum of the dimuon system must satisfy $p_{\mathrm{T}}^{\mu^+\mu^-} > 27$ GeV. The events must also contain at least one photon with $p_{\mathrm{T}}^{\gamma} > 27$ GeV. These selections are implemented to reduce the storage space taken by `HDBS2` samples; however the thresholds are sufficiently loose that the efficiency for signal events is close to 100% with respect to the offline selection. If the event does not meet this criteria the reconstruction-level information is not retained; however for simulated events generator-level information, that is the true physics properties of the event which the detector aims to reconstruct (also known as truth-level), is always retained. It is noted that the requirements for events to pass the `HDBS2` derivation are tighter than for the `HIGG2D5` derivation. However the selection criteria described in 5.1.2 are more stringent than either derivation, such that when the full requirements are imposed the event yields from both derivations are identical. As a result, the two derivations are equivalent in the scope of these analyses.

Signal acceptance is defined as the fraction of signal events which meet the geometric and kinematic requirements defined in Section 5.1 at generator level, before any effects from event reconstruction are taken into account. These are the events that would be detectable in an ideal detector with perfect reconstruction capabilities. Table 5.9 shows the acceptance of the $H(Z) \to \mathcal{Q}\gamma$ signals collectively for the $\psi(nS)\,\gamma$ and $\Upsilon(nS)\,\gamma$ channels. In particular, each of the requirements on p_{T}, η and $m_{\mu^+\mu^-}$ are applied, but not the isolation, vertex quality, or object quality requirements. The ggH mechanism has the largest acceptance in the case of the H boson decays, followed by VBF. In general the signal acceptance is larger for H signals compared to Z signals: as the mass of the Higgs boson is larger than that of the Z boson, their decay products have higher p_{T} and are more likely to meet the kinematic thresholds. This is demonstrated in Figure 5.2 by comparing the generator-level p_{T} of the H and Z boson signals in the histograms labelled 'before selection', which show the simulated events which meet the geometric acceptance requirements on η at generator-level. This is also true for the increased acceptance of the $\Upsilon(nS)$ channels over the $\psi(nS)$ channels, but the effect is smaller.

Table 5.9: Generator-level acceptance for $H(Z) \to \psi(nS)\,\gamma$ and $H(Z) \to \Upsilon(nS)\,\gamma$ decays, where only the kinematic selections on p_{T} and geometric selections on η from Section 5.1 are applied.

Decay	Production Mode	Signal Acceptance [%]
$H \to \psi(nS)\,\gamma$	ggH	37.25 ± 0.15
$H \to \psi(nS)\,\gamma$	VBF	26.72 ± 0.12
$H \to \psi(nS)\,\gamma$	WH	26.22 ± 0.12
$H \to \psi(nS)\,\gamma$	ZH	26.39 ± 0.12
$H \to \psi(nS)\,\gamma$	$t\bar{t}H$	22.29 ± 0.12
$H \to \psi(nS)\,\gamma$	Total	35.96 ± 0.06
$Z \to \psi(nS)\,\gamma$	Total	24.73 ± 0.10
$H \to \Upsilon(nS)\,\gamma$	ggH	40.18 ± 0.14
$H \to \Upsilon(nS)\,\gamma$	VBF	28.04 ± 0.11
$H \to \Upsilon(nS)\,\gamma$	WH	27.87 ± 0.11
$H \to \Upsilon(nS)\,\gamma$	ZH	27.87 ± 0.11
$H \to \Upsilon(nS)\,\gamma$	$t\bar{t}H$	23.36 ± 0.18
$H \to \Upsilon(nS)\,\gamma$	Total	38.71 ± 0.06
$Z \to \Upsilon(nS)\,\gamma$	Total	32.65 ± 0.11

Total signal efficiency is defined as the fraction of events which pass the full event selection in Section 5.1, meaning that they were successfully reconstructed. This is the product of the signal acceptance and the signal reconstruction efficiency, which is the probability



(a) $H \to J/\psi\,\gamma$ (b) $H \to \psi(2S)\,\gamma$ (c) $H \to \Upsilon(nS)\,\gamma$

(d) $Z \to J/\psi\,\gamma$ (e) $Z \to \psi(2S)\,\gamma$ (f) $Z \to \Upsilon(nS)\,\gamma$

Figure 5.2: Generator-level transverse momentum (p_{T}) distributions of the photon and muon candidates for (a) $H \to J/\psi\,\gamma$, (b) $H \to \psi(2S)\,\gamma$, (c) $H \to \Upsilon(nS)\,\gamma$, (d) $Z \to J/\psi\,\gamma$, (e) $Z \to \psi(2S)\,\gamma$ and (f) $Z \to \Upsilon(nS)\,\gamma$ simulated events, respectively. The leading muon candidate is labelled $p_{\mathrm{T}}^{\mu 1}$ (black), the subleading candidate $p_{\mathrm{T}}^{\mu 2}$ (blue), and the photon candidate p_{T}^{γ} (green). The 'before selecton' distributions, denoted with dashed lines and clear fills, show the events at generator level which fall within the analysis geometric acceptance (both muons are required to have $|\eta^{\mu}| < 2.5$, while the photon is required to have $|\eta^{\gamma}| < 2.37$, excluding the region $1.37 < |\eta^{\gamma}| < 1.52$), and are each normalised to unity. The 'after selection' distributions, denoted with solid lines and hatched fills, show the fraction of these events which pass the full analysis event selection described in Section 5.1. The relative difference between the two sets of distributions corresponds to the effects of reconstruction, identification, trigger, isolation, and event selection efficiencies including the kinematic requirements. From Ref. [94].

to reconstruct an event given that it is within the kinematic and geometric acceptance at generator level. Table 5.10 shows the total signal efficiency for each of the individual signal decays considered in these analyses, taking into accout the kinematic and geometric acceptance as well as the experimental trigger, reconstruction, identification, and isolation efficiencies. The total signal efficiency for the $J/\psi\,\gamma \to \mu^+\mu^-\,\gamma$ and $\psi(2S)\,\gamma \to \mu^+\mu^-\,\gamma$ final states is 19% for the Higgs boson decays and 10% for the Z boson decays. The corresponding efficiency for the $\Upsilon(1S, 2S, 3S)\,\gamma \to \mu^+\mu^-\,\gamma$ final states is 21% for the Higgs boson decays and 13% for the Z boson decays. The 'after selection' histograms in Figure 5.2 show the subset of signal events which meet the geometric requirements at truth-level that are successfully reconstructed and pass the full signal region criteria.

Table 5.10: Estimated reconstruction-level efficiencies in signal events following the full event selection.

Decay	Total Efficiency
$H \to J/\psi\,\gamma$	19.1%
$H \to \psi(2S)\,\gamma$	19.1%
$Z \to J/\psi\,\gamma$	10.1%
$Z \to \psi(2S)\,\gamma$	9.9%
$H \to \Upsilon(1S)\,\gamma$	21.2%
$H \to \Upsilon(2S)\,\gamma$	20.9%
$H \to \Upsilon(3S)\,\gamma$	20.7%
$Z \to \Upsilon(1S)\,\gamma$	13.3%
$Z \to \Upsilon(2S)\,\gamma$	13.0%
$Z \to \Upsilon(3S)\,\gamma$	13.3%

Table 5.11 shows the total trigger efficiency, which is defined as the fraction of events that pass the trigger requirements given that they pass the offline analysis selection described in Section 5.1.2. It is a measure of the performance of the trigger to successfully select events that fall in the analysis selection and is overall larger than 97% for each decay channel. In general, trigger efficiency decreases for events with smaller muon- and photon-candidate p_{T}, near the trigger kinematic thresholds, as shown in Figure 5.3. In all cases the efficiency in each p_{T} bin is of order 94% or greater.

The Z boson has a large natural width of 2.4952 ± 0.0023 GeV [26]. The decay products of low-mass Z bosons are softer than those of high-mass Z bosons, and since the p_{T} of the decay products are near the kinematic thresholds of these searches, this results in a

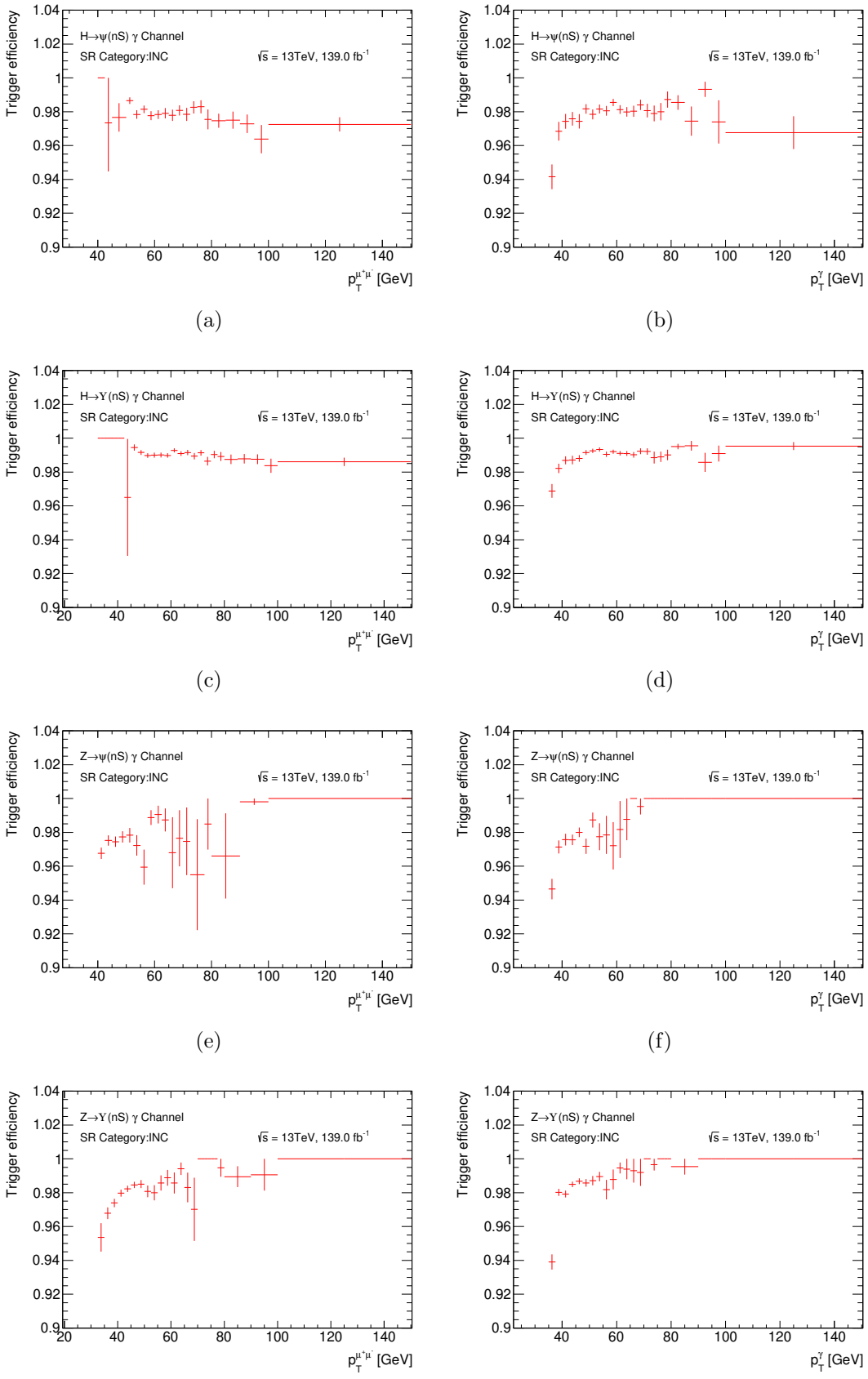


Figure 5.3: The trigger efficiency as a function of $p_{\mathrm{T}}^{\mu\mu}$ (left) and p_{T}^{γ} (right), with respect to the offline analysis selection defined in Section 5.1.2, calculated from simulated $H(Z) \to \mathcal{Q}\gamma$ events.

Table 5.11: The trigger efficiency with respect to the offline analysis selection for the $\psi(nS)\,\gamma$ and $\Upsilon(nS)\,\gamma$ decay channels, calculated from simulation.

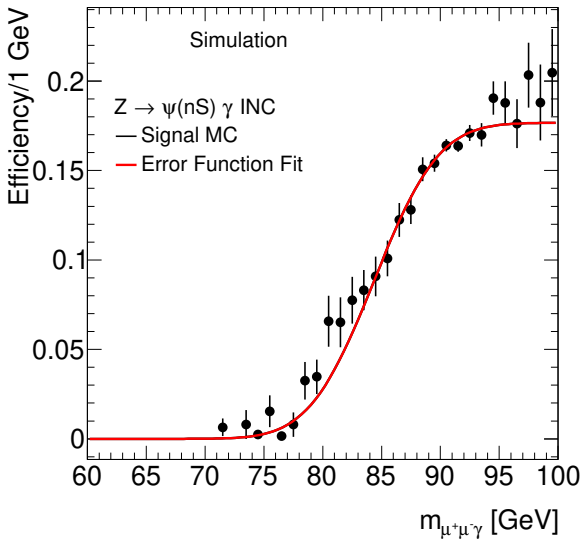
Channel	Trigger Efficiency
$H \to \psi(nS)\,\gamma$	$97.9 \pm 0.8\%$
$Z \to \psi(nS)\,\gamma$	$97.4 \pm 0.8\%$
$H \to \Upsilon(nS)\,\gamma$	$99.0 \pm 0.8\%$
$Z \to \Upsilon(nS)\,\gamma$	$97.9 \pm 0.8\%$

turn-on curve in efficiency of the $Z \to \mathcal{Q}\,\gamma$ signals with respect to generator-level Z mass, shown in Figure 5.4, which has a large natural width. This efficiency is modelled as an error function, which has a width parameter to model the slope of the turn-on curve and a mean parameter to model the central location in mass for the turn-on curve.

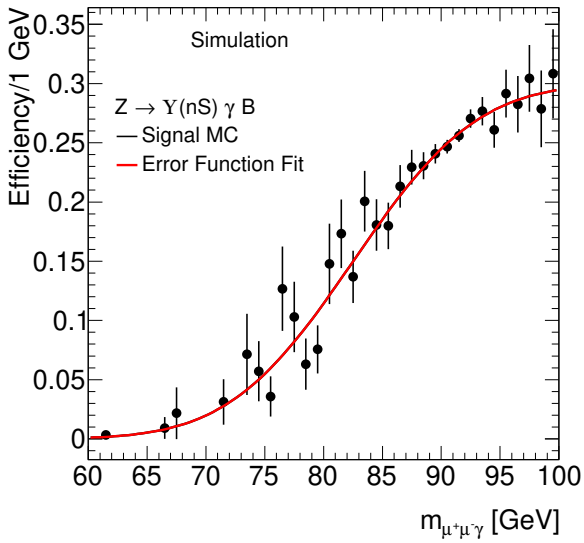
5.2.3 Signal Shape and Resolution

The two-dimensional (2D) mass distributions in $m_{\mu^+\mu^-}$ versus $m_{\mu^+\mu^-\gamma}$ of simulated signal events that pass all requirements in Section 5.1 are shown in Figure 5.5. Distinct resonances are seen in each dimension for all of the signal decays. For the $H \to \mathcal{Q}\,\gamma$ decays there is a correlation of approximately 60% between $m_{\mu^+\mu^-\gamma}$ and $m_{\mu^+\mu^-}$, whereas for the $Z \to \mathcal{Q}\,\gamma$ the correlation is only of order 10%, because the natural width of the Z is comparible to the resolution of the detector. For each of the final states a 2D probability density function (PDF) is used to model these distributions.

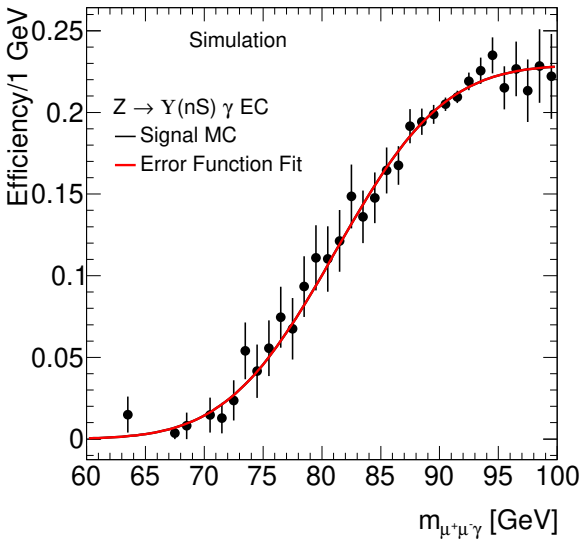
The resolution in $m_{\mu^+\mu^-\gamma}$ is $1.6\% - 1.8\%$ for each of the Higgs boson decays, where mass distributions are shown in Figure 5.6 for each category using J/ψ and $\Upsilon(1S)$ signal channels as an example. The Higgs boson signals are modelled with the sum of two bivariate Gaussian distributions, which describe the correlations between $m_{\mu^+\mu^-\gamma}$ and $m_{\mu^+\mu^-}$ as well as the effects of detector resolution. The parameters for each of these shapes are extracted from a fit to the simulated event samples and are shown in Table 5.12. Each of the Gaussian distributions have a σ parameter describing the standard deviation of the signal as well as a mean μ parameter to describe the central mass value. The correlation between $m_{\mu^+\mu^-\gamma}$ and $m_{\mu^+\mu^-}$ for the H signals is described by a ρ parameter, and an f parameter is used to describe the relative contribution between the broader and narrower



(a) $\psi(nS)$ Total

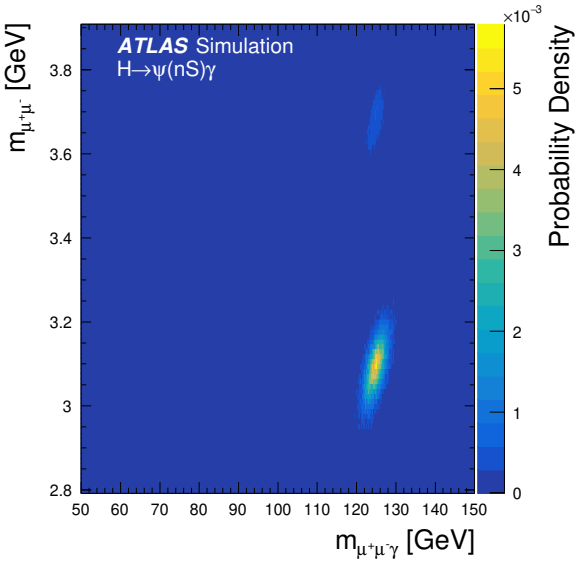


(b) $\Upsilon(nS)$ Barrel

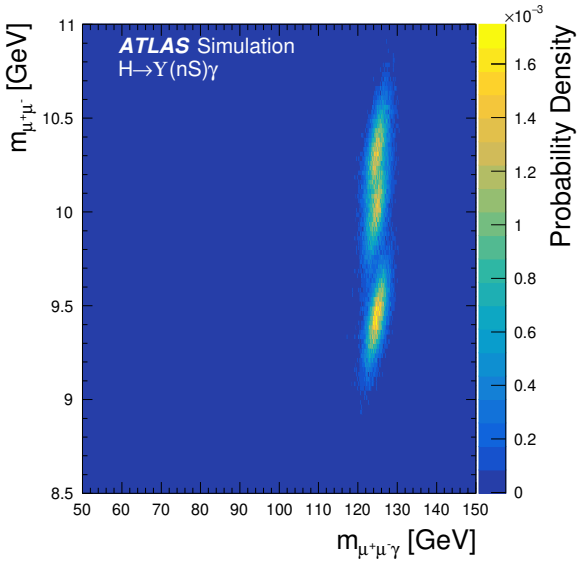


(c) $\Upsilon(nS)$ Endcap

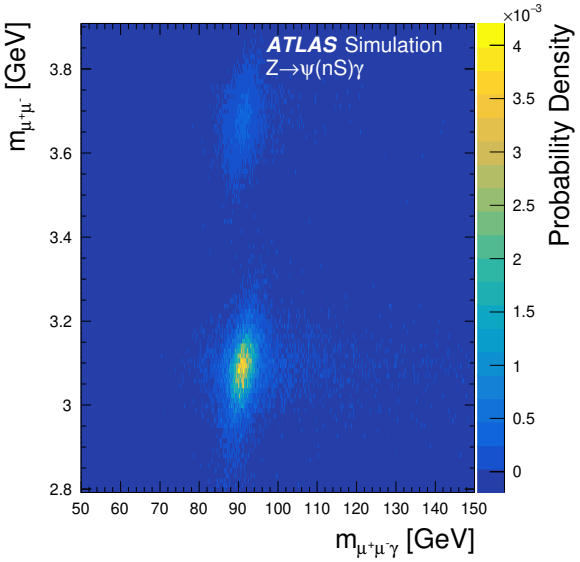
Figure 5.4: The Z boson mass-dependent efficiency function derived from the truth acceptance of the $\psi(nS)$ signals (a) and $\Upsilon(nS)$ signals in the barrel (b) and endcap (c) categories, respectively. The turn-on shape is a result of the kinematic thresholds on the photon and the two muons in the event, as the decay products of low-mass Z bosons are softer than those of high-mass Z bosons such that it is more difficult for them to meet the selection and trigger requirements.



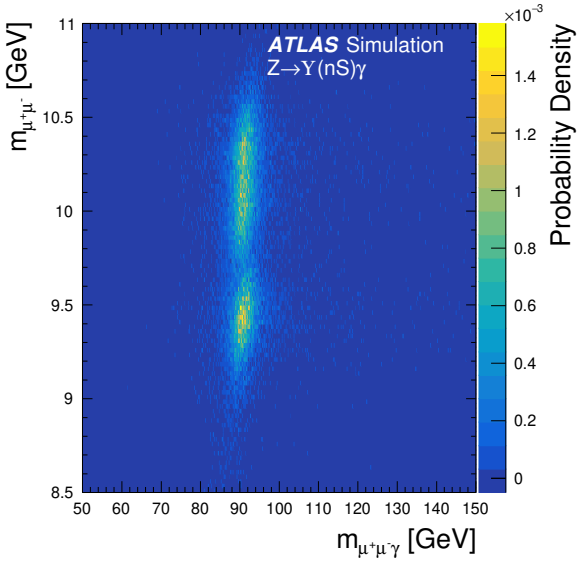
(a) $H \to \psi(nS)\gamma$



(b) $H \to \Upsilon(nS)\gamma$



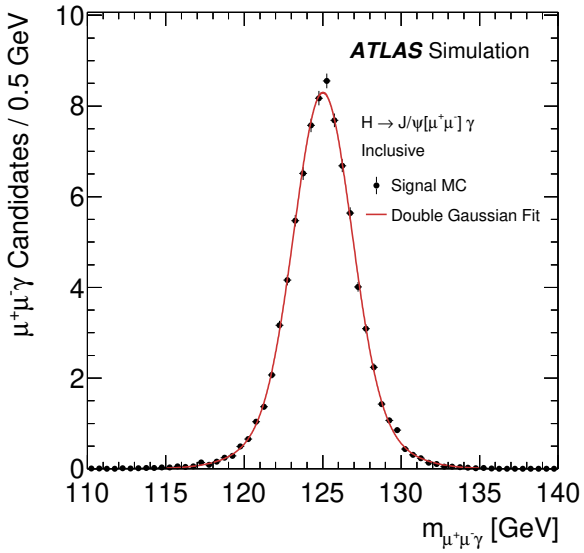
(c) $Z \to \psi(nS)\gamma$



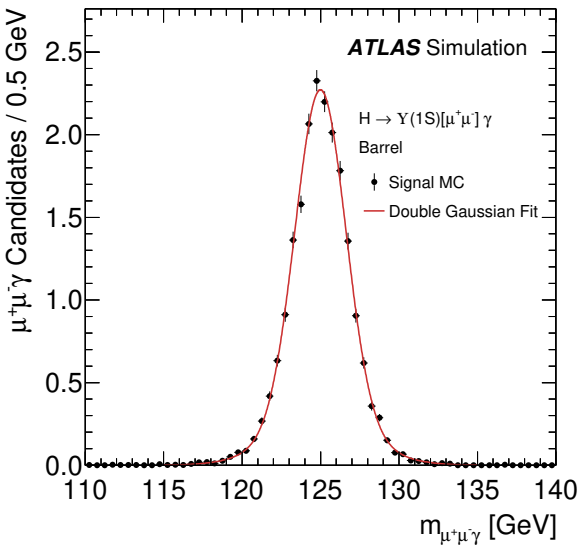
(d) $Z \to \Upsilon(nS)\gamma$

Figure 5.5: Two-dimensional distributions of $m_{\mu^+\mu^-\gamma}$ versus $m_{\mu^+\mu^-}$ for (a) $H \to \psi(nS)\gamma$, (b) $H \to \Upsilon(nS)\gamma$, (c) $Z \to \psi(nS)\gamma$, and (d) $Z \to \Upsilon(nS)\gamma$ simulated signal events which pass the signal region criteria. From Ref. [94].

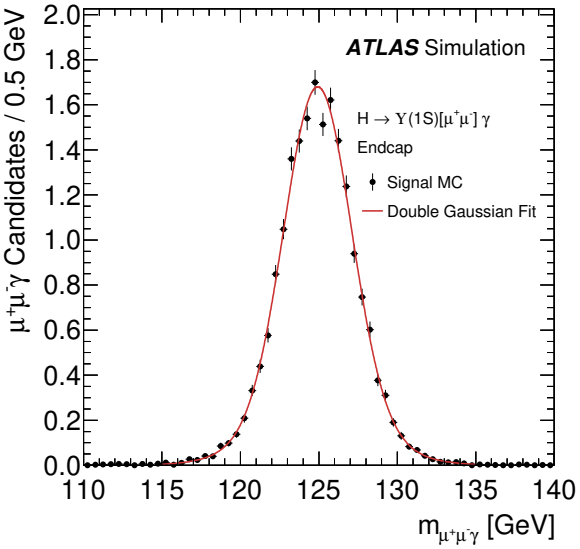
bivariate Gaussian distributions.



(a) $\psi(nS)$ Total



(b) $\Upsilon(nS)$ Barrel



(c) $\Upsilon(nS)$ Endcap

Figure 5.6: The resolution in $m_{\mu^+\mu^-\gamma}$ of the Higgs boson mass for (a) $H \to J/\psi\,\gamma$, (b) $H \to \Upsilon(1S)\,\gamma$ in the barrel category, and (c) $H \to \Upsilon(1S)\,\gamma$ in the endcap category for simulated events which meet the signal region criteria. The shape of the signal fit is a double Gaussian distribution. From Ref. [94].

The resolution in $m_{\mu^+\mu^-\gamma}$ is also $1.6\% - 1.8\%$ for each of the Z boson decays, where example mass distributions are shown in Figure 5.7. For the Z boson decays, $m_{\mu^+\mu^-\gamma}$ and $m_{\mu^+\mu^-}$ are treated as uncorrelated. The $m_{\mu^+\mu^-\gamma}$ distributions are modelled with the sum of two Voigtian distributions, which are a convolution of a Breit-Wigner distribution (to

Table 5.12: Parameters of the bivariate Gaussian shapes used to model the Higgs boson signals.

	$\mu_{m_{\mu^+\mu^-\gamma}}$	$\mu_{m_{\mu^+\mu^-}}$	$\sigma^1_{m_{\mu^+\mu^-\gamma}}$	$\sigma^2_{m_{\mu^+\mu^-\gamma}}$	$\sigma^1_{m_{\mu^+\mu^-}}$	$\sigma^2_{m_{\mu^+\mu^-}}$	$\rho_{m_{\mu^+\mu^-\gamma} m_{\mu^+\mu^-}}$	f_{Gaus1}
$H \to J/\psi$	125.03	3.095	2.986	1.714	0.0868	0.0498	0.611	0.351
$H \to \psi(2S)$	124.98	3.682	2.890	1.666	0.0977	0.0588	0.625	0.400
$H \to \Upsilon(1S)$ B	125.00	9.453	1.536	2.925	0.131	0.221	0.602	0.765
$H \to \Upsilon(2S)$ B	125.01	10.02	1.538	2.720	0.135	0.217	0.595	0.743
$H \to \Upsilon(3S)$ B	125.00	10.34	1.573	2.881	0.144	0.231	0.604	0.778
$H \to \Upsilon(1S)$ EC	124.93	9.442	3.246	1.967	0.282	0.181	0.645	0.358
$H \to \Upsilon(2S)$ EC	124.88	9.999	3.292	1.970	0.301	0.191	0.652	0.355
$H \to \Upsilon(3S)$ EC	124.91	10.33	2.038	3.491	0.202	0.332	0.646	0.736

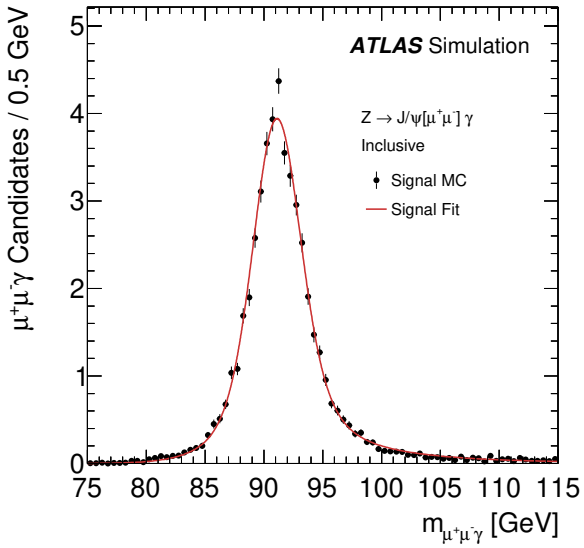
take into account the natural width of the Z boson) and a Gaussian distribution (to take into account detector resolution), multiplied by an efficiency factor, shown by the red error functions in Figure 5.4, to take into account the turn-on in signal efficiency with Z boson mass. The $m_{\mu^+\mu^-}$ distributions of the Z boson signals are modelled with the sum of two Gaussian distributions, which take into account detector resolution. The parameters for each of these shapes are extracted from a fit to the simulated event samples and are shown in Table 5.13 for the Z boson signal PDFs. Each of the Gaussian distributions, including the Gaussian component of the Voigtian functions, have a σ parameter describing the standard deviation of the signal as well as a mean μ parameter to describe the central mass value. The width of the Breit-Wigner component of the reconstructed Z boson mass is fixed to the natural width of the Z boson and the mean is set to be the same as for the Gaussian component. Two f parameters are used to describe the relative contribution between the broader and narrower Gaussian and Voigtian distributions.

Table 5.13: Parameters of the double Voigtian and double Gaussian models used for the Z signal.

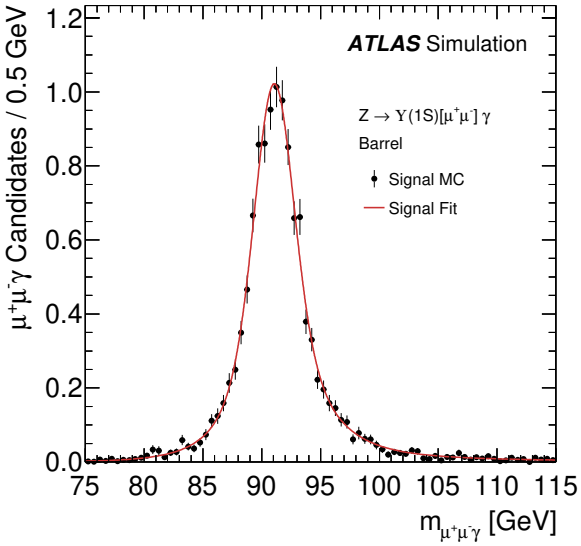
	$\mu_{m_{\mu^+\mu^-\gamma}}$	$\sigma^1_{m_{\mu^+\mu^-\gamma}}$	$\sigma^2_{m_{\mu^+\mu^-\gamma}}$	f_{Voigt2}	$\mu_{m_{\mu^+\mu^-}}$	$\sigma^1_{m_{\mu^+\mu^-}}$	$\sigma^2_{m_{\mu^+\mu^-}}$	f_{Gaus1}
$Z \to J/\psi$	90.969	1.663	9.316	0.0688	3.090	0.105	0.0500	0.239
$Z \to \psi(2S)$					3.677	0.108	0.0556	0.306
$Z \to \Upsilon(1S)$ B					9.434	0.129	0.414	0.897
$Z \to \Upsilon(2S)$ B	90.939	1.345	4.937	0.0786	9.996	0.136	0.433	0.892
$Z \to \Upsilon(3S)$ B					10.33	0.500	0.141	0.129
$Z \to \Upsilon(1S)$ EC					9.425	0.379	0.176	0.204
$Z \to \Upsilon(2S)$ EC	90.865	1.737	6.936	0.0673	9.987	0.182	0.301	0.612
$Z \to \Upsilon(3S)$ EC					10.32	0.191	0.500	0.749

5.2.4 Systematic Uncertainties

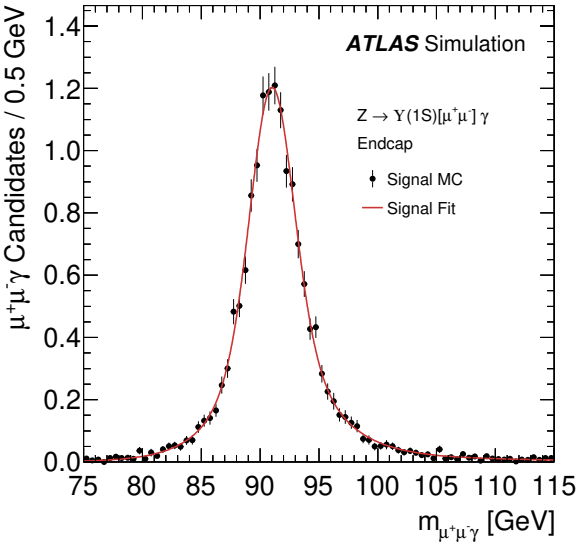
Systematic uncertainties in the signal event yield are taken into account in the maximum likelihood, and come from both theoretical and experimental sources. The uncertainty in the total integrated luminosity of these searches is 1.7% [191, 192] as discussed in Sec-



(a) $\psi(nS)$ Total



(b) $\Upsilon(nS)$ Barrel



(c) $\Upsilon(nS)$ Endcap

Figure 5.7: The resolution in $m_{\mu^+\mu^-\gamma}$ of the Z boson mass for (a) $Z \to J/\psi\,\gamma$, (b) $Z \to \Upsilon(1S)\,\gamma$ in the barrel category, and (c) $Z \to \Upsilon(1S)\,\gamma$ in the endcap category for simulated events which meet the signal region criteria. The shape of the signal fit is a double Voigtian distribution multiplied by an efficiency factor which varies with $m_{\mu^+\mu^-\gamma}$. From Ref. [94].

tion 5.1.1. The theoretical uncertainties in the Higgs boson cross sections for each production mode are taken from Ref. [30], for a Higgs boson mass of $m_H = 125.09$ GeV and for a centre-of-mass energy $\sqrt{s} = 13$ TeV. The QCD scale uncertainties on the production cross section are $+4.3\%(-6.5\%)$ for the ggH production mechanism, $+0.4\%(-0.3\%)$ for VBF, $+0.5\%(-0.5\%)$ for WH, $+3.5\%(-2.7\%)$ for ZH, and $+5.8\%(-9.2\%)$ for $t\bar{t}H$. The uncertainty on each production cross section from the uncertainties in the parton distribution functions and strong coupling constant, α_s, is $\pm 3.2\%$ for ggH, $\pm 2.1\%$ for VBF, $\pm 1.4\%$ for WH, $\pm 1.6\%$ for ZH, and $\pm 3.6\%$ for $t\bar{t}H$. For the $b\bar{b}H$ production mechanism the total uncertainty on the cross section due to QCD scale, parton distribution function and strong coupling constant uncertainties is $+20.1\%(-23.9\%)$. The total theoretical uncertainty on the Higgs boson cross section, combining the above by summing each source in quadrature and assuming each source is uncorrelated, is taken as 5.8%. The uncertainty in the Z boson cross section between 66 GeV and 116 GeV is taken as 2.9% [85], where the luminosity component of the uncertainty in the Z boson production cross-section measurement is treated as uncorrelated with the uncertainty of the integrated luminosity of the dataset used in these searches.

The uncertainty in the kinematics of the $H \to \mathcal{Q}\gamma$ signals, and how this impacts signal acceptance, due to the effect of uncertainties in the QCD scale, parton distribution functions, tuned parameters for the underlying event, and in the parton shower is estimated by applying variations at the generator level for the ggH process, which is the dominant production process. The effect of uncertainties in QCD scale are evaluated by applying 26 variations around the nominal from NNLOPS and are combined in quadrature. For the uncertainty in the parton distribusion functions, up and down variations of α_s and 30 variations given by the PDF4LHC recommendations are applied [220]. The uncertainty associated with the choice of the underlying event tune, in this case AZNLO [204], is estimated by showering the events with alternative event tunes, for which the following variations are available: Renormalisation, Var1, Var2 and MPI. The uncertainty associated with the choice of the parton shower model, in this case Pythia8.212, is estimated by showering the generated events with an alternative generator, namely Herwig7.

The changes in signal acceptance due to each of these theory uncertainties are summarised in Table 5.14. The total uncertainty in the acceptance of the Higgs boson signals from these sources is 1.8% when summed in quadrature, assuming each source is uncorrelated. The equivalent uncertainty in the signal acceptance for the $Z \to \mathcal{Q}\gamma$ boson signals is 1.0% and is estimated by comparing the Z boson kinematic distributions in simulated events with measurements in data [221], and propagating the differences through to the signal acceptance.

Table 5.14: $H \to \mathcal{Q}\gamma$ signal acceptance uncertainties from uncertainties in theoretical modelling.

Systematic Variation	Acceptance Uncertainty
Parton Distribution Function: α_s	0.5%
Parton Distribution Function: `pdf4lhc`	0.7%
QCD Scales: `NNLOPS`	1.3%
Parton Showering: `Herwig7` and `AZNLO` tune	0.8%

On the experimental side, the uncertainty in the trigger efficiency is 0.8% from the efficiencies in the muon and photon triggers [222, 223] as shown in Table 5.11, primarily from the uncertainty in the photon trigger efficiency which is estimated from samples enriched with $Z \to e^+e^-$ events in data [224]. Photon identification efficiencies are determined using the enriched $Z \to e^+e^-$ event samples, inclusive photon events, and $Z \to \ell^+\ell^-\gamma$ events [225, 226]. These total 1.7%–1.9% for the Higgs and Z boson signals. The effect of the equivalent muon reconstruction and identification efficiency uncertainties is 2.2%–2.4% [131]. The photon energy scale uncertainty, determined from $Z \to e^+e^-$ events and validated using $Z \to \ell^+\ell^-\gamma$ events [227, 228], is propagated through the simulated samples as a function of η^γ and p_{T}^γ, and has a 0.1%–0.2% effect on the Higgs and Z boson signal yields. Similarly, the systematic uncertainty associated with the scale of the muon momentum measurement has a 0.1%–0.5% effect on the signal yields [131], and the uncertainty associated with the muon resolution in the inner detector and the muon spectrometer is $< 0.1\%$. The effect of uncertainty in the pile-up is assessed by varying the average number of pile-up interactions in the simulation, and the corresponding uncertainty on the Higgs and Z boson signal yields is 0.7%–1.1%. The systematic uncertainties in the yield of the $H \to \mathcal{Q}\gamma$ and $Z \to \mathcal{Q}\gamma$ signals are summarised in Table 5.15 and are

taken into account in the final maximum likelihood fit using nuisance parameters with standard Gaussian constraints.

Table 5.15: Summary of the systematic uncertainties in the expected signal yields taken into account via Gaussian constraints in the likelihood fit. From Ref. [94].

Source of systematic uncertainty	Signal yield uncertainty			
	$H \to \psi(nS)$	$H \to \Upsilon(nS)$	$Z \to \psi(nS)$	$Z \to \Upsilon(nS)$
Total cross section	5.8%		2.9%	
Integrated luminosity	1.7%		1.7%	
Signal acceptance	1.8%		1.0%	
Muon reconstruction	2.3%	2.2%	2.4%	2.4%
Photon identification	1.7%	1.7%	1.9%	1.9%
Pile-up uncertainty	0.8%	0.7%	1.1%	1.1%
Trigger efficiency	0.7%	0.7%	0.8%	0.8%
Photon energy scale	0.1%	0.1%	0.2%	0.2%
Muon momentum scale	0.1%	0.1%	0.5%	0.2%
Muon momentum resolution (ID)	<0.01%	0.01%	0.06%	0.02%
Muon momentum resolution (MS)	0.02%	0.01%	0.04%	0.01%

The effect of each source of systematic uncertainty on the shape of each signal was also investigated, but each were on the order of a 0.05% shift in the mean, or smaller. As a result, the signal shape systematics were deemed negligible and are neglected. At this stage the event selection is now defined, as well as the signal models for each of the $H(Z) \to Q\gamma$ decay channels. The remaining items are to develop the background model and perform the statistical analysis of the data.

5.3 Exclusive Background Modelling

The exclusive background is the first of two distinct contributions modelled in these searches. It originates from $q\bar{q} \to \gamma^*/Z^* \to \mu^+\mu^-\gamma$ events produced via the Drell-Yan process, where a highly energetic photon typically arises from final-state radiation of one of the muons, such that the dimuon mass lies near the $\psi(nS)$ or $\Upsilon(nS)$ resonances whilst the three-body mass lies near the H and Z boson masses in the range 50 GeV–300 GeV considered in these analyses. This background exhibits a characteristic resonant structure in the $m_{\mu^+\mu^-\gamma}$ distribution, due to the contribution from on-shell Z bosons, with a non-resonant structure in the $m_{\mu^+\mu^-}$ distribution. Similarly to the signal models in Section 5.2, this background contribution is modelled using events simulated with MC

that are subjected to the event selection in Section 5.1. The resulting three-body and dimuon mass distributions are fitted with analytical functions to produce the shapes used in the final unbinned maximum-likelihood fit in Section 5.5. The smooth analytical shapes are beneficial to avoid false peak-like structures that could be introduced due to statistical fluctiations in the MC. This section describes the procedure used to generate exclusive background events, the analytical functions used to model them, and the systematic shape variations used to account for uncertainties in the analytical shapes. The normalisation of the exclusive background component is extracted directly from the fit to the data in each search.

5.3.1 Event Generation and Simulation

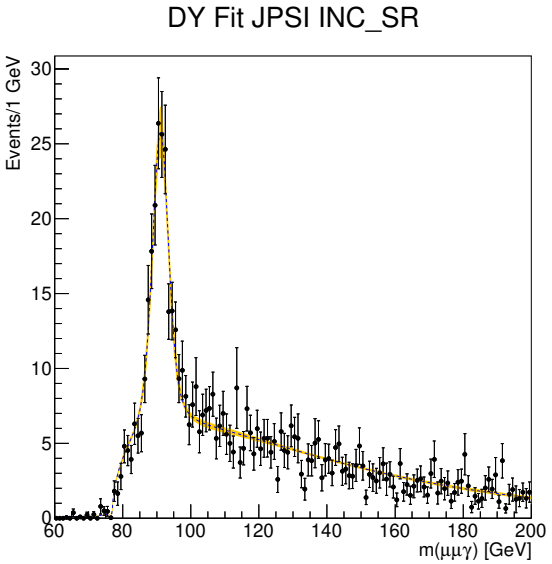
To simulate exclusive background events, the Sherpa 2.2.10 [143] event generator is used with leading-order matrix elements and the NNPDF3.0 set of parton distribution functions. Two samples are generated: the first in the $m_{\mu^+\mu^-}$ region 1.2 GeV–5.3 GeV around the $\psi(nS)$ resonances, and the second in the $m_{\mu^+\mu^-}$ region 7.0 GeV–13.0 GeV around the $\Upsilon(nS)$ resonances. These windows are larger than the nominal selection requirements to account for losses near the mass boundaries due to detector resolution. Requirements of $m_{\mu^+\gamma} > 1$ GeV and $m_{\mu^-\gamma} > 1$ GeV are applied during generation for computational reasons; these do not impact the expected yield of the exclusive background in the signal region as the $\Delta\phi(\mathcal{Q},\gamma) > \pi/2$ selection imposes a large opening angle between each muon and the photon, such that the invariant mass of each muon–photon system is large. The resulting simulated events are passed through the detailed Geant4 simulation of the ATLAS detector [144, 145], and processed with the same software used to reconstruct and select the data. The total sample statistics are 100k events each in the $\psi(nS)$ mass window and $\Upsilon(nS)$ mass window, split as 20k:40k:40k across the 2015–2016, 2017, and 2018 run periods, similarly to the $H(Z) \to \psi(2S)\,\gamma$ samples in Table 5.6. The final normalisation of the exclusive background is determined directly from the data in the maximum-likelihood fit, but reference values are predicted using production cross sections estimated by the Sherpa 2.2.10 generator.

5.3.2 Analytical Shapes of $m_{\mu^+\mu^-\gamma}$ and $m_{\mu^+\mu^-}$

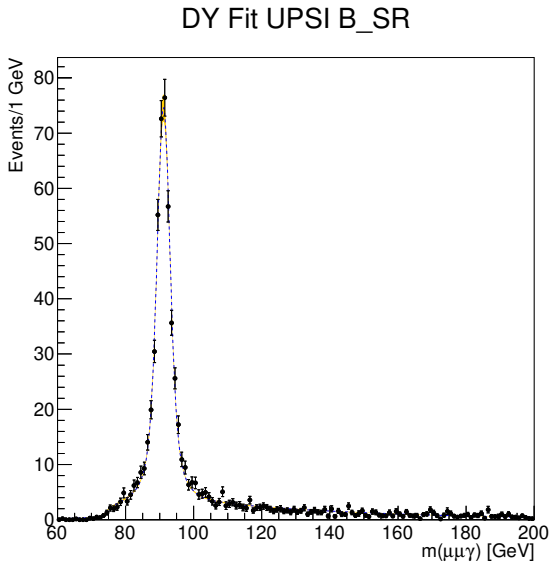
The event selection described in Section 5.1 is applied to the simulated exclusive background samples to obtain the $m_{\mu^+\mu^-\gamma}$ and $m_{\mu^+\mu^-}$ distributions in the signal regions of these analyses. The resulting $m_{\mu^+\mu^-\gamma}$ distribution in each category is modelled analytically as the sum of a Voigtian function, which describes the on-shell Z production, and a threshold function defined as $f(x) = \sqrt{x - x_0}\, e^{-A(x-x_0)}$, which describes the off-shell γ^*/Z^* production. In the threshold function A and x_0 are constants, $f(x) = 0$ for $x < x_0$, and x is the three-body mass $m_{\mu^+\mu^-\gamma}$. Alternative forms of the threshold function were considered, but the above function provided the best description of the background shape. The on-shell component is dominant in the $\Upsilon(nS)\,\gamma$ signal searches, whilst the off-shell component dominates in the $\psi(nS)\,\gamma$ signal searches. The parameters of the analytical functions are extracted from a fit to the simulated events, with the width of the Breit-Wigner component set to the natural width of the Z [26]. The width of the Gaussian component of the Voigtian function, the overall mean of the Voigtian function, and the A and x_0 parameters of the threshold function are free in each fit, as well as the overall fraction of on-shell events versus off-shell events. The $m_{\mu^+\mu^-\gamma}$ distributions in each signal region category as well as the results of each analytical fit are shown in Figure 5.8.

The $m_{\mu^+\mu^-}$ distributions after the full event selection is applied are non-resonant and are modelled using a linear shape with a single parameter a_0 to describe the gradient. The $m_{\mu^+\mu^-}$ distributions in each signal region as well as the results of each analytical fit are shown in Figure 5.9.

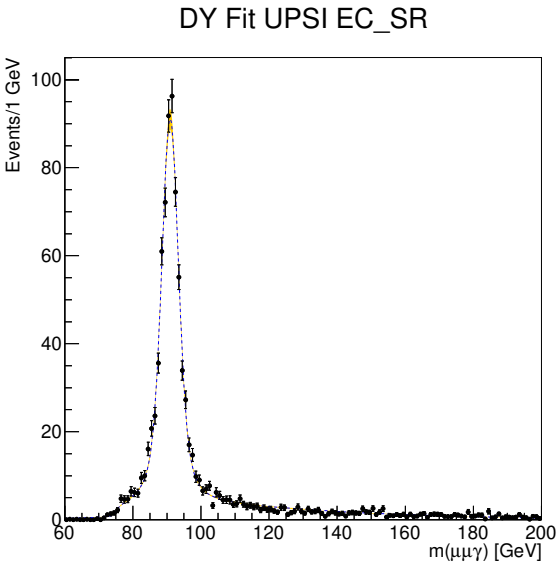
The two-dimensional probability density functions in $m_{\mu^+\mu^-}$ versus $m_{\mu^+\mu^-\gamma}$ for the exclusive background are shown in Figure 5.10. The $m_{\mu^+\mu^-}$ and $m_{\mu^+\mu^-\gamma}$ masses are treated as uncorrelated for the exclusive background, and the 2D model is constructed as a product of the independent models for the two mass dimensions. For visualisation, these plots are generated using the exclusive background PDFs extracted from the fits to the simulated samples, and not the simulated samples themselves.



(a) $\psi(nS)\,\gamma$ Total

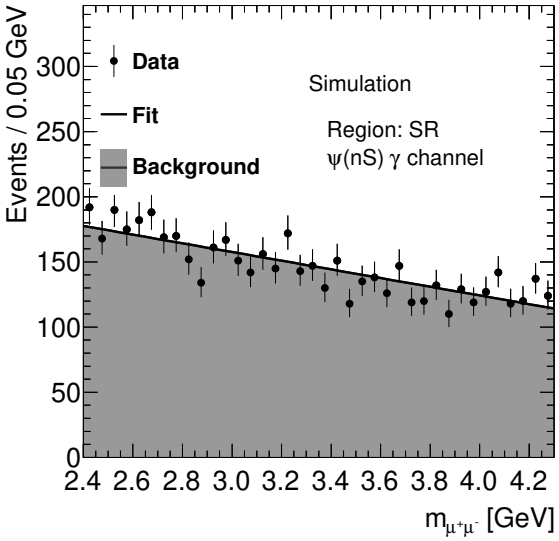


(b) $\Upsilon(nS)\,\gamma$ Barrel

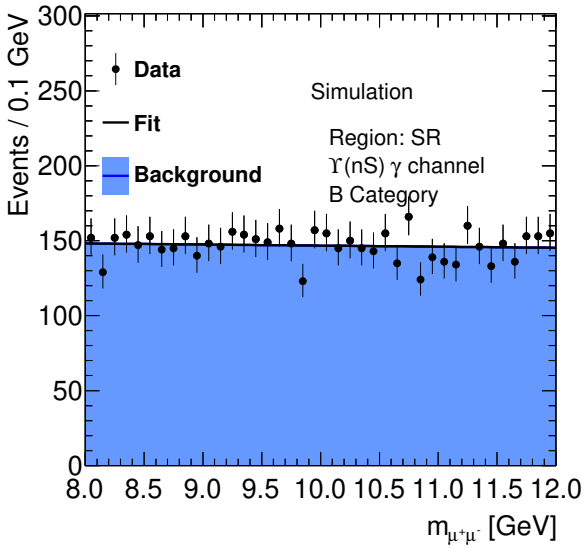


(c) $\Upsilon(nS)\,\gamma$ Endcap

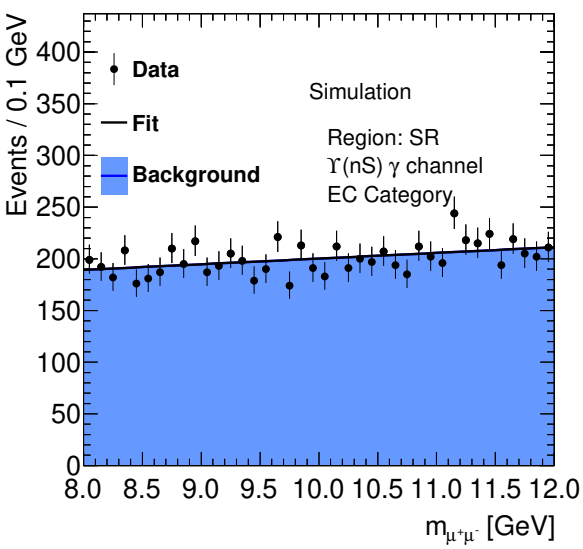
Figure 5.8: The results of the analytical lineshape fits to the $m_{\mu^+\mu^-\gamma}$ distribution of simulated exclusive background events that pass the event selection in the $\psi(nS)\,\gamma$ analysis and in the $\Upsilon(nS)\,\gamma$ analysis.



(a) $\psi(nS)\,\gamma$ Total

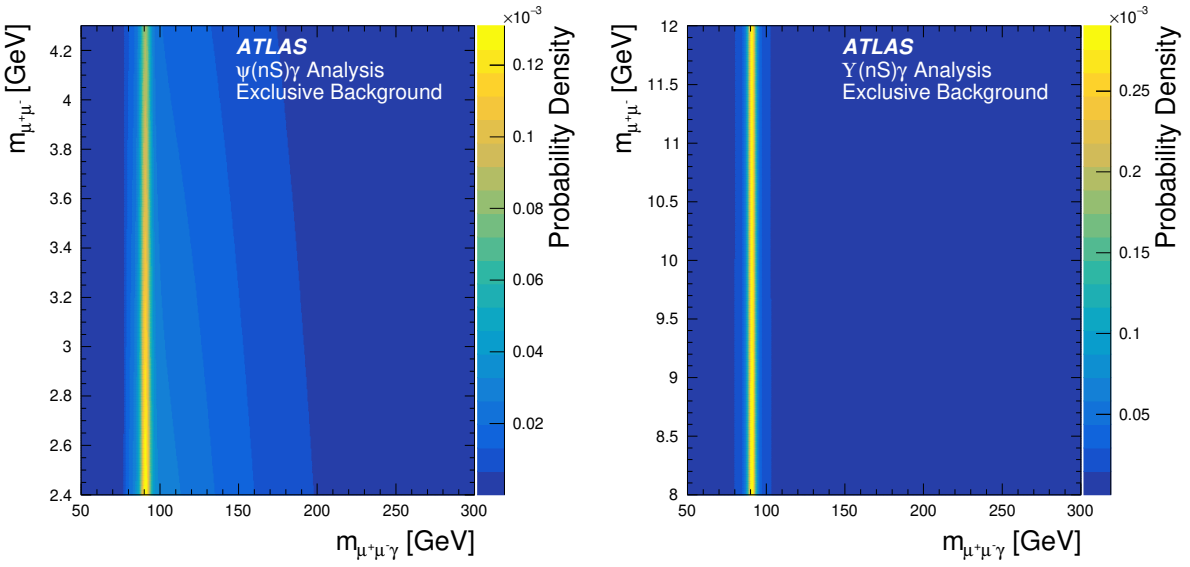


(b) $\Upsilon(nS)\,\gamma$ Barrel



(c) $\Upsilon(nS)\,\gamma$ Endcap

Figure 5.9: The $m_{\mu^+\mu^-}$ distributions of simulated exclusive background events for (a) $\psi(nS)\,\gamma$, (b) $\Upsilon(nS)\,\gamma$ in the barrel category and (c) $\Upsilon(nS)\,\gamma$ in the endcap category. Candidates satisfy the requirements of the signal region selection defined in Section 5.1. The error bars on the data points denote their statistical uncertainty and the fit lines are first-order Chebyshev polynomials.



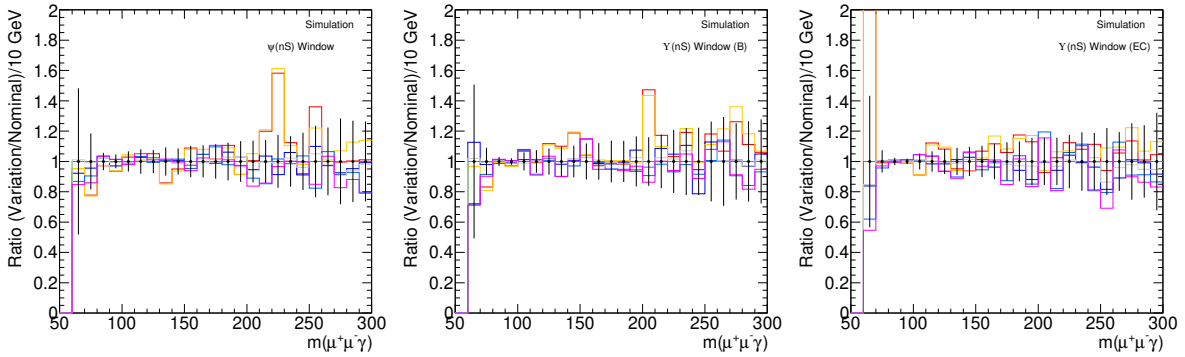
(a) (b)

Figure 5.10: The two-dimensional $m_{\mu^+\mu^-\gamma}$ versus $m_{\mu^+\mu^-}$ probability density functions in the signal region for the exclusive background in the (a) $\psi(nS)\,\gamma$ and (b) $\Upsilon(nS)\,\gamma$ analyses. The barrel and endcap categories are summed for the $\Upsilon(nS)\,\gamma$ model. From Ref. [94].

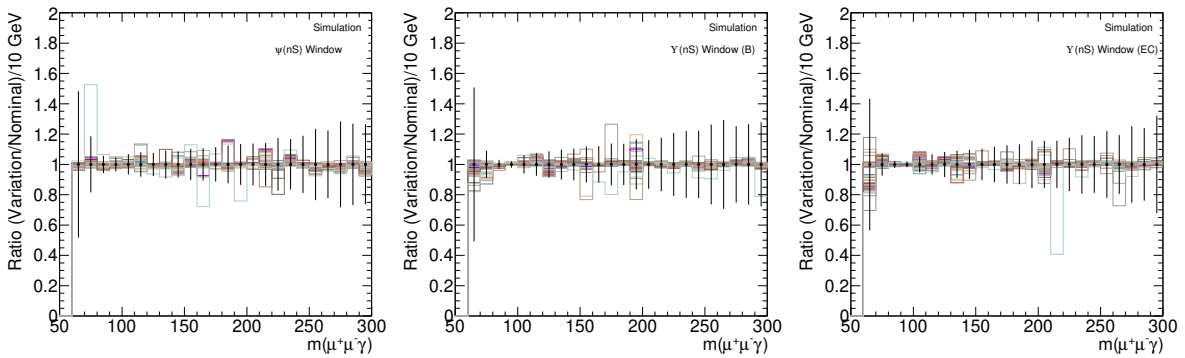
5.3.3 Systematic Uncertainties

The effect of theoretical and experimental uncertainties on the shape of the exclusive background were investigated. Theoretical uncertainties include the 7-point variations of the renormalisation and factorisation scales in Sherpa and variations in the parton distribution functions, and experimental uncertainties include the photon and muon reconstruction efficiency, scale, and resolution uncertainties. The effect of each variation on the shape of the exclusive background was found to be smaller than, or comparable to, the statistical uncertainty of the Sherpa samples and did not show any consistent trend. This is shown in Figure 5.11 for the theoretical uncertainties in the shape of the exclusive background, and in Figure 5.12 for the experimental uncertainties. The dominant uncertainty in the shape of the exclusive background arises from the limited statistics of the available Sherpa samples. As a result, the statistical uncertainty associated with the parameters of the $m_{\mu^+\mu^-\gamma}$ shape function are used to account for uncertainties in the shape of the exclusive background, via Gaussian constraints in the likelihood fit in Section 5.5. The size of the uncertainty associated with each parameter is shown in Table 5.16. Although systematic uncertainties in the shape of the exclusive background

are implemented in the maximum-likelihood fit, they are found to have a negligible effect on the result. No systematic uncertainties are considered in the normalisations of the exclusive backgrounds as these are extracted directly from data.



(a) $\psi(nS)$ 7-point variations (b) $\Upsilon(nS)$ 7-point variations (B) (c) $\Upsilon(nS)$ 7-point variations (EC)

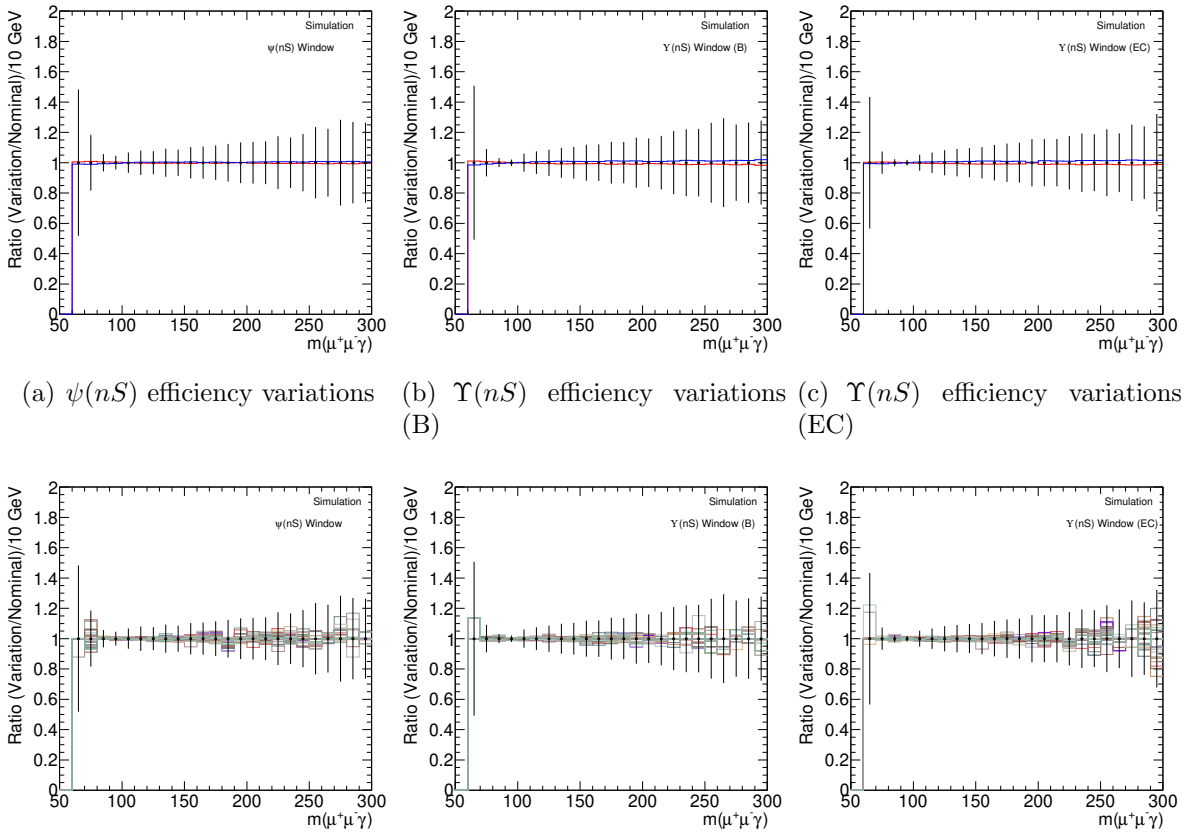


(d) $\psi(nS)$ PDF variations (e) $\Upsilon(nS)$ PDF variations (B) (f) $\Upsilon(nS)$ PDF variations (EC)

Figure 5.11: Effect of the theoretical systematic uncertainties on the shape of the exclusive background. Plots (a), (b), and (c) show the effect of the 7-point variations of the renormalisation and factorisation scales in Sherpa on the exclusive background shape, whilst plots (d), (e), and (f) show the effect of the PDF variations. The plots show the ratio of the varied shape divided by the nominal shape, where the error bars represent the statistical uncertainty of the Sherpa sample, and the collection of coloured histograms represent the variations due to the modelling uncertainties.

5.4 Inclusive Background Modelling

The inclusive background is the second of two distinct contributions modelled in these searches. It originates from a mixture of multi-jet and γ+jet sources which involve the production of genuine $\mathcal{Q}$ states, which subsequently decay to $\mu^+\mu^-$, or the production of non-resonant dimuon pairs such as from the Drell-Yan process or from random combinations of muons. The photon candidate may be genuine, as in the γ+jet events,



(a) $\psi(nS)$ efficiency variations (b) $\Upsilon(nS)$ efficiency variations (B) (c) $\Upsilon(nS)$ efficiency variations (EC)

(d) $\psi(nS)$ scale/resolution variations (e) $\Upsilon(nS)$ scale/resolution variations (B) (f) $\Upsilon(nS)$ scale/resolution variations (EC)

Figure 5.12: Effect of the experimental systematic uncertainties on the shape of the exclusive background. Plots (a), (b), and (c) show the effect of the muon and photon efficiency systematic uncertainties on the exclusive background shape, whilst plots (d), (e), and (f) show the effect of the muon and photon scale and resolution systematic uncertainties. The plots show the ratio of the varied shape divided by the nominal shape, where the error bars represent the statistical uncertainty of the Sherpa sample, and the collection of coloured histograms represent the variations due to the modelling uncertainties.

Table 5.16: Statistical uncertainty in the exclusive background shape parameters for each analysis category. These are accounted for in the final fit via nuisance parameters with Gaussian constraints.

	Uncertainty		
Parameter	$\psi(nS)$ Analysis	$\Upsilon(nS)$ Analysis (B)	$\Upsilon(nS)$ Analysis (EC)
Voigt/Threshold Fraction	2.2%	3.4%	3.5%
Threshold Amplitude, A	4.3%	4.2%	3.9%
Threshold, x_0	0.12%	0.13%	0.0055%
Voigt Mean	0.23%	0.057%	0.057%
Voigt Sigma	15%	5.2%	3.5%

or more typically a misidentified jet, as in the multi-jet events. The contribution from Drell-Yan production of dimuons in the inclusive background is separate from the exclusive $q\bar{q} \to \mu^+\mu^-\gamma$ background in Section 5.3, as the latter involves a genuine photon candidate whereas the former involves a jet misidentified as a photon.

The complicated mixture of contributions to the inclusive background, which involves QCD proceses and misidentification of physics objects, and the highly selective kinematic phase-space of these searches make this background challenging to model accurately with simulation. In addition, the inclusive background shape exhibits a broad kinematic peak near the location of a possible $Z \to \mathcal{Q}\gamma$ signal. When combined with the low number of events in the signal region, this makes the modelling of this background through direct fits of parametric models to the data unsuitable. To overcome each of these challenges, a non-parametric data-driven model is used to describe the inclusive background, which is a generative approach to obtain the $m_{\mu^+\mu^-\gamma}$ distribution of the background contribution. This method is described in detail in Ref. [229] and is based around the construction of a 'kernel' from a dataset. This kernel represents a description of the distributions of kinematic variables, as well as the correlations between them, relevant in the reconstruction of particles in the particular analysis. Isolation variables relevant in the event selection may also be included. Data structures called pseudocandidates can be sampled from this kernel, such that an ensemble of pseudocandidate events will respect the same variable distributions and correlations as the dataset used in its construction. In the ideal case this kernel will have as many dimensions as there are variables, to form a complete description of the background, however this is not practical. To minimise the impact of statistical fluctuations in data it is necessary to factorise the kernel from a single distribution of high dimensionality into several distributions of low dimensionality, whilst keeping an explicit description of the most important correlations among the variables. The pseudocandidate events are then generated from this factorised kernel using an ancestral sampling technique, and these are used to obtain the required background distribution. Several previous searches for exclusive decays of the H and Z bosons to a meson and a photon have used this method to model their backgrounds [90–93].

This section describes the application and validation of this method in describing the $m_{\mu^+\mu^-\gamma}$ shape of the inclusive background in these searches, as well as the allowed shape variations in the final fit in Section 5.5. This section also describes the parametric model used to model the $m_{\mu^+\mu^-}$ distribution of the inclusive background. The normalisation of the inclusive background component is extracted directly from the fit to the data in each search, similarly to the exclusive background.

5.4.1 Generation and Validation Region Selection Criteria

The generation of the non-parametric data-driven background model relies on the definition of a more relaxed event selection compared to the signal region (SR) requirements defined in Section 5.1.2. This background model generation region (GR) is defined in this way such that the selected events are expected to be dominated by background events, and any effect on model generation from the potential contamination of the region by signal events is negligible. This allows the events around the H and Z boson mass in $m_{\mu^+\mu^-\gamma}$ to be left unblinded during preparation of the model. This is vital to accurately estimate the shape of the background under potential signal peaks in the SR, which is blinded (in that the data points in the $m_{\mu^+\mu^-\gamma}$ ranges 86 GeV–96 GeV and 122 GeV–128 GeV are hidden) during the preparation of the analysis to avoid biasing the result.

The GR selection applies the SR selection defined in Section 5.1 but with three changes to loosen the selection. The first is that the variable threshold on $p_{\mathrm{T}}^{\mu^+\mu^-}$ is not applied, and instead a smaller, constant threshold of $p_{\mathrm{T}}^{\mu^+\mu^-} > 30$ GeV is imposed. The second is that the $\mathcal{Q}$-candidate isolation requirement is loosened to a threshold of `ptvarcone30` $< 40\%$ of $p_{\mathrm{T}}^{\mu^+\mu^-}$. The third is that the photon isolation requirements are loosened to a threshold of `ptcone20` $< 20\%$ of p_{T}^{γ} for the track isolation, and a threshold of `topoetcone40` < 2.45 GeV $+ 40\%$ of p_{T}^{γ} [GeV] for the calorimeter isolation.

Further validation regions (VRs) are defined to assess model performance when each of the three tighter SR requirements are applied to the generated model in turn. VR1 is defined as the GR selection with the variable $p_{\mathrm{T}}^{\mu^+\mu^-}$ threshold from the SR, VR2 is defined as the GR selection with the tight $\mathcal{Q}$ isolation requirements from the SR, and VR3 is

defined as the GR selection with the tight photon isolation requirements from the SR. Each of the selection regions is summarised in Table 5.17, and the overlap of each region is illustrated in the Venn diagram in Figure 5.13 for visualisation.

Table 5.17: A summary of the selection regions used in the analysis for the generation of the inclusive background model. The term 'Full' indicates the corresponding requirement applied in the SR, and discussed in Section 5.1.2. The Relaxed $\mathcal{Q}$-candidate isolation requires `ptvarcone30` $< 40\%$ of $p_{\mathrm{T}}^{\mu^+\mu^-}$. The Relaxed photon isolation requires `ptcone20` $< 20\%$ of p_{T}^{γ}, and `topoetcone40` $< (2.45\ \mathrm{GeV} + 40\%$ of p_{T}^{γ} [GeV]). From Ref. [94].

Region		$p_{\mathrm{T}}^{\mu^+\mu^-}$	Photon Isolation	$\mathcal{Q}$ Isolation
Generation Region	(GR)	> 30 GeV	Relaxed	Relaxed
Validation Region 1	(VR1)	Full	Relaxed	Relaxed
Validation Region 2	(VR2)	> 30 GeV	Relaxed	Full
Validation Region 3	(VR3)	> 30 GeV	Full	Relaxed
Signal Region	(SR)	Full	Full	Full

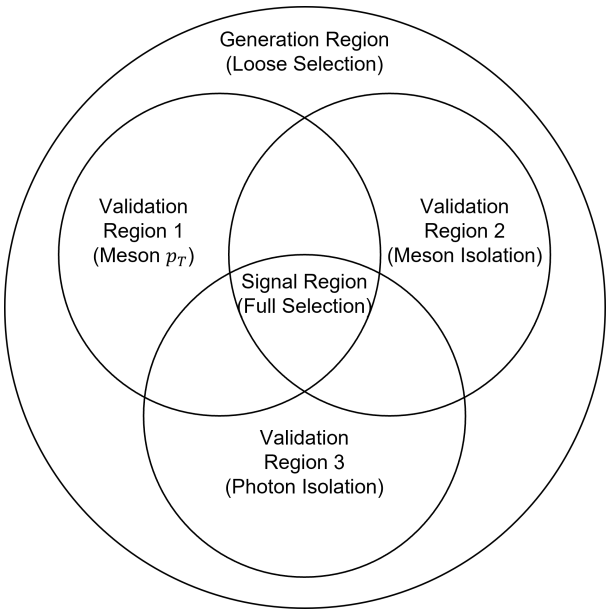


Figure 5.13: Illustrative Venn diagram showing the overlap between the different selection regions defined for the generation of the inclusive background model in these searches. The signal region (SR) selection is the most stringent, followed by the validation regions (VRs) and then the generation region (GR) which has the loosest selection, and is dominated by background events. The relative areas of each selection region are not to scale.

5.4.2 Non-Parametric Data-Driven Method for $m_{\mu^+\mu^-\gamma}$

The application of the GR selection criteria on the ATLAS Run 2 dataset yields approximately 1.8×10^4 events for the $\psi(nS)\,\gamma$ searches and 8.9×10^3 events for the $\Upsilon(nS)\,\gamma$ searches for use in the generation of the inclusive background model. To prepare for the

construction of the model, the exclusive background is subtracted from the GR datasets, where the normalisation of the inclusive and exclusive background components are extracted from the data. PDFs are constructed from the prepared data to describe the kinematics of the quarkonium and photon candidates, the relevant isolation variables, and the most important correlations between each variable. These PDFs are sampled using the ancestral sampling technique shown in Figure 5.14 to generate pseudocandidate events, each with complete $\mathcal{Q}$ and γ four-vectors, necessary to reconstruct the three-body mass, $m_{\mu^+\mu^-\gamma}$, and their associated isolation values, necessary for the application of the VR and SR selection requirements. The sampling scheme is as follows, where $\mathcal{Q}$ is equivalent to the notation of the dimuon system, $\mu^+\mu^-$, used to describe variables elswhere in this chapter:

1. The angular co-ordinates and mass of the quarkonium candidate, $\eta_{\mathcal{Q}}$, $\phi_{\mathcal{Q}}$ and $m_{\mathcal{Q}}$ are each sampled from independent one-dimensional PDFs, and the photon and quarkonium tranverse momenta, p_{T}^{γ} and $p_{\mathrm{T}}^{\mathcal{Q}}$, are sampled simultaneously from a two-dimensional PDF which describes their correlation.

2. The value drawn for $p_{\mathrm{T}}^{\mathcal{Q}}$ is used as an input to a three-dimensional (3D) PDF which describes the correlations between $p_{\mathrm{T}}^{\mathcal{Q}}$, the photon calorimeter isolation (γ calo-iso), and $\Delta\eta(\mathcal{Q},\gamma)$, which is the separation in η between the photon and quarkonium candidates, and γ calo-iso and $\Delta\eta(\mathcal{Q},\gamma)$ are sampled simultaneously.

3. The values of $p_{\mathrm{T}}^{\mathcal{Q}}$ and γ calo-iso are used as inputs to two separate 3D PDFs, where the first is used to sample the quarkonium isolation ($\mathcal{Q}$ track-iso) and the second is used to sample $\Delta\phi(\mathcal{Q},\gamma)$, which is the separation in ϕ between the photon and quarkonium candidates.

4. The values of $\Delta\eta(\mathcal{Q},\gamma)$ and $\Delta\phi(\mathcal{Q},\gamma)$ are summed with $\eta_{\mathcal{Q}}$ and $\phi_{\mathcal{Q}}$ to generate the angular co-ordinates of the photon candidate, η_{γ} and ϕ_{γ}, and the $\mathcal{Q}$ track-iso and γ calo-iso are used as inputs to a 3D PDF to sample the photon track isolation (γ track-iso).

In practice, the PDFs described in Figure 5.14 are constructed using a series of one-

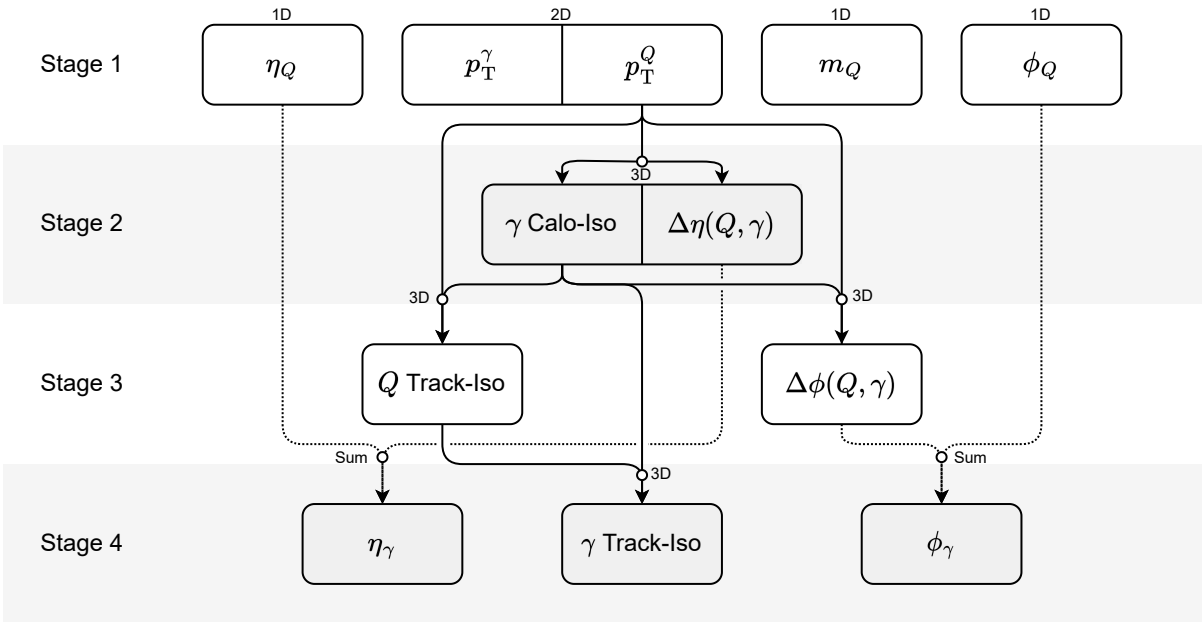


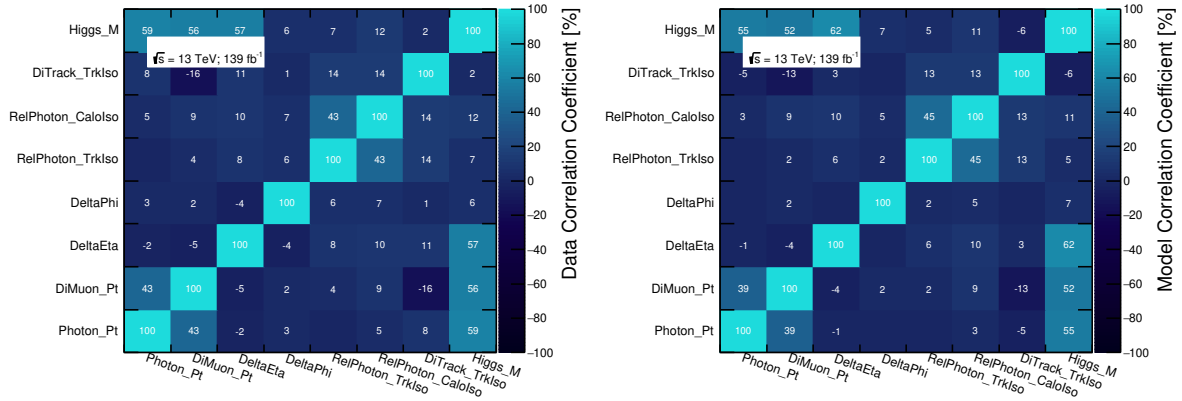
Figure 5.14: The data-driven ancestral sampling method used to generate pseudocandidate events to model the inclusive background. Variables labelled '1D' and '2D' refer to the dimensionality of the PDFs used in their generation. Vertices labelled '3D' signify that the output variable (or variables), identifed by the arrow leaving the vertex, is sampled from a three-dimensional PDF described in bins of the input variable (or variables), identifed by the lines leading into the vertex. Vertices labelled 'Sum' signify that the output variable is calculated directly from the sum of the input variables. If two variables share a border, they are sampled simultaneously from a combined PDF. From Ref. [94].

and two-dimensional histograms which are filled using data in the GR. These histograms are sampled to generate the value of a given variable, or pair of values in the case of 2D simultaneously sampled variables. Variables that are downstream from the vertices labelled 3D are described in an array of histograms, separated in bins of the input variable or variables. If a particular variable is used as an input in the generation of another variable, the histogram corresponding to the bin that contains the generated input value is used to sample the downstream variable, thus retaining their correlation.

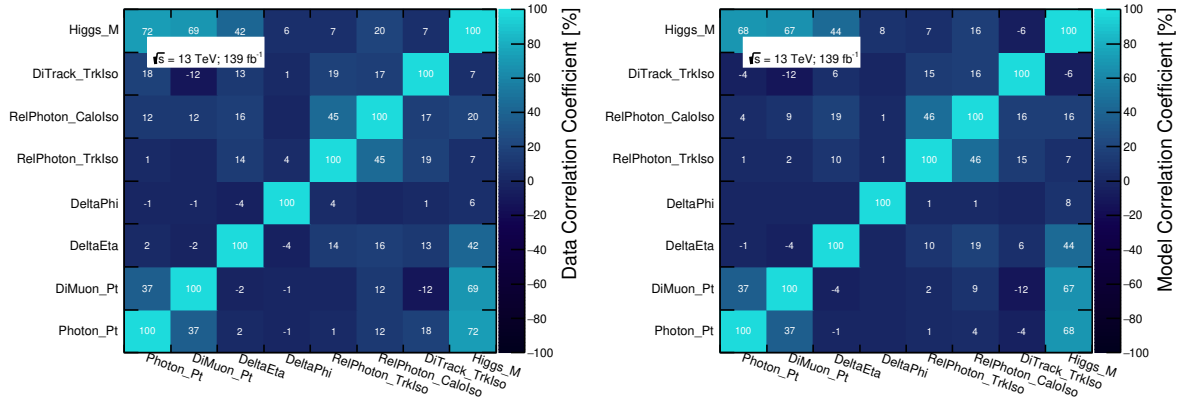
The specific sampling scheme used to model the correlations, as well as binning of each PDF, are hyperparameters of the model. These hyperparameters are optimised based on the statistics of the available GR dataset as well as on studies of the important correlations in data, shown in Figure 5.15 alongside the correlations in the pseudocandidate events. The performance of a particular model procedure is assessed by comparing the correlations in the data and in the pseudocandidate events to check if the important correlations are retained.[6] The variables that are most correlated with three-body mass are the p_{T} of the photon and quarkonium candidates, and their separation in $\Delta\eta$. It is noted that despite the large correlation between $m_{\mu^+\mu^-\gamma}$ and $\Delta\eta$, the correlation between $m_{\mu^+\mu^-\gamma}$ and $\Delta\phi$, which is the angular separation between the photon and quarkonium candidates in the transverse plane, is small. The application of explicit cuts on object p_{T} and $\Delta\phi$ restrict the $\Delta\phi$ distribution in data whilst no analogous cuts on $\Delta\eta$ or object total momentum are applied, such that the $\Delta\eta$ distribution has more freedom. This results in larger correlations between $\Delta\eta$ and $m_{\mu^+\mu^-\gamma}$ compared to $\Delta\phi$ and $m_{\mu^+\mu^-\gamma}$.

Large samples of 10M pseudocandidate events each were generated for the $\psi(nS)\,\gamma$ and $\Upsilon(nS)\,\gamma$ searches, and the three-body mass distributions were reconstructed from the pseudo $\mathcal{Q}$ and γ candidates. The sample sizes are chosen to be large to obtain a smooth $m_{\mu^+\mu^-\gamma}$ distribution for the inclusive background model, which is smoothed further using Gaussian kernel density estimation (KDE). The resulting $m_{\mu^+\mu^-\gamma}$ distributions in the GR are shown in Figure 5.16, where the contribution of from the exclusive background is also

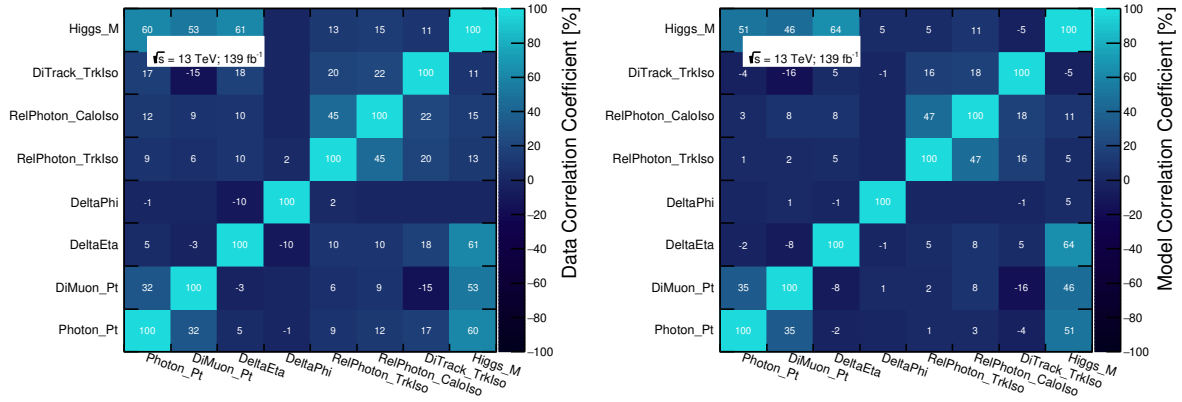
[6] Control distributions comparing the model to the data in several kinematic and isolation variables in each selection region are also used to assist in the optimisation production of the model, but these are outside of the scope of this discussion.



(a) $\psi(nS)$ Total



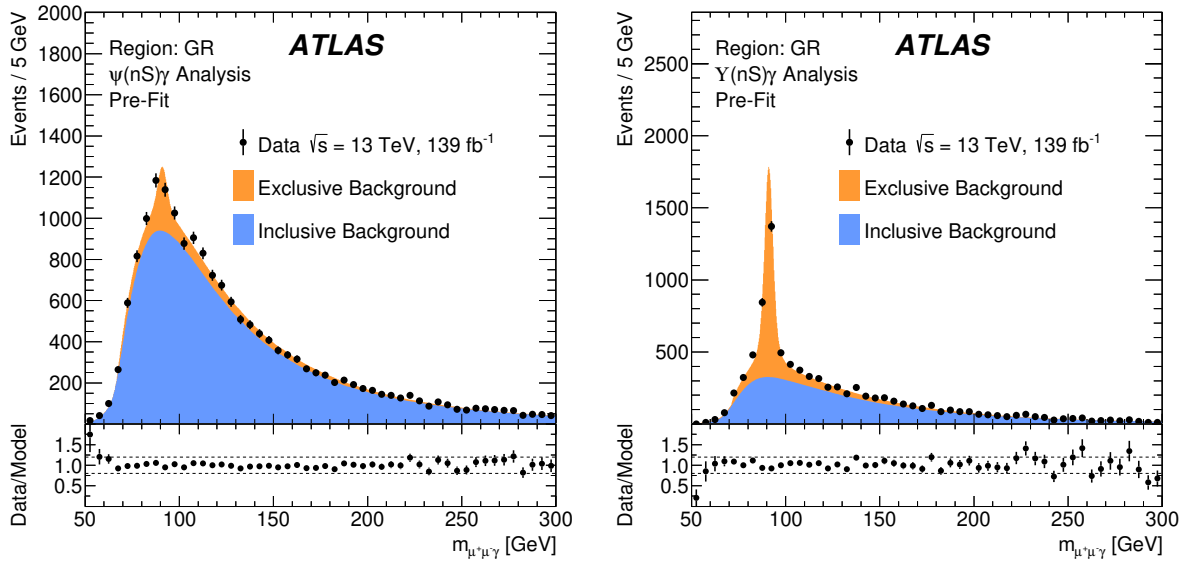
(b) $\Upsilon(nS)$ Barrel



(c) $\Upsilon(nS)$ Endcap

Figure 5.15: Linear correlations between the variables used in the inclusive background model with the GR selection applied. Correlations for the data (left) and pseudo candidate events (right) are shown for the (a) $\psi(nS)\,\gamma$ analysis, and for the $\Upsilon(nS)\,\gamma$ analysis in the (b) barrel and (c) endcap categories. The values in each bin are indicative of strength of the correlation between the two variables, where bins are left unlabelled if their correlation is smaller than 1%. Here, `Higgs_M` refers to the three-body mass $m_{\mu^+\mu^-\gamma}$.

included. The total background model accurately predicts the data in the generation region, which is expected since this is the data sample used to produce the model.



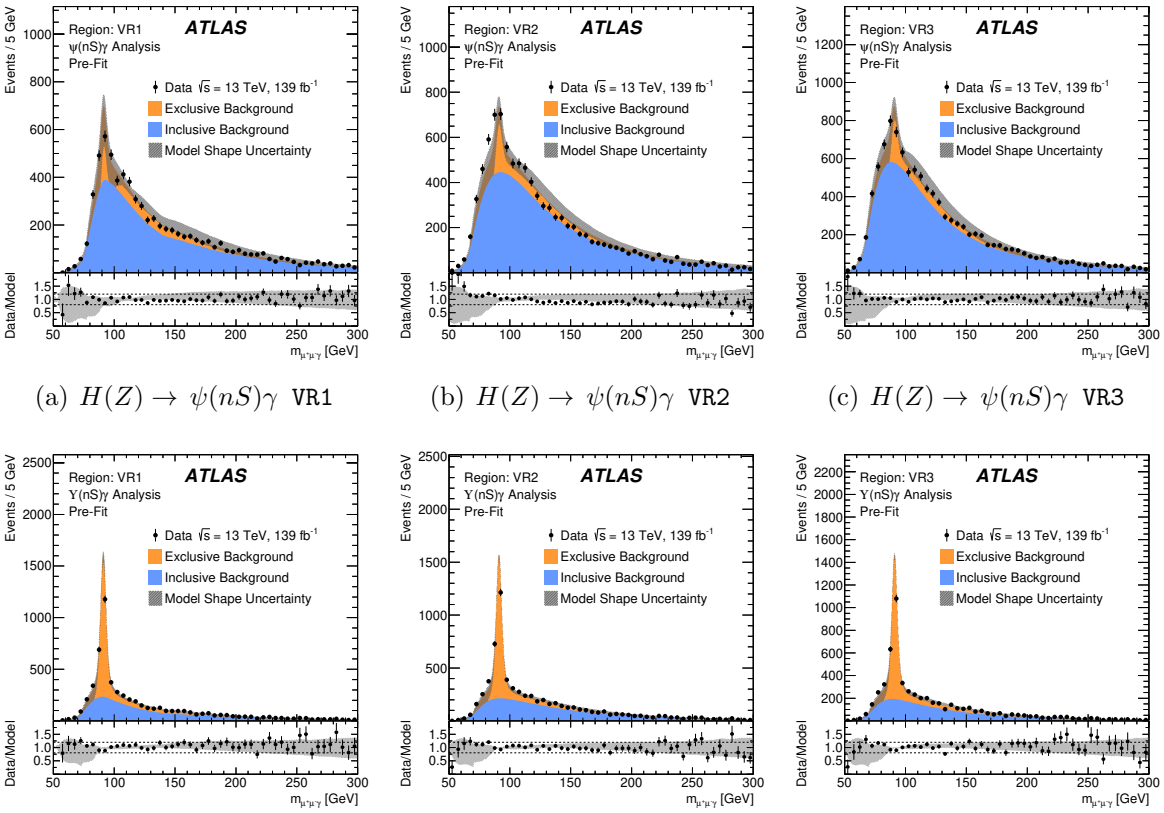
(a) $H(Z) \to \psi(nS)\gamma$ GR

(b) $H(Z) \to \Upsilon(nS)\gamma$ GR

Figure 5.16: The distribution of $m_{\mu^+\mu^-\gamma}$ in data compared to the prediction of the total background model for (a) $H(Z) \to \psi(nS)\,\gamma$ and (b) $H(Z) \to \Upsilon(nS)\,\gamma$ in the GR. The total background is normalised to the observed number of events within each region shown, where the ratio of the exclusive and inclusive background components are extrapolated from data in the GR. The dashed lines in the ratio plots of each figure indicate 1.2 and 0.8 on the y-axis. It should be noted that these plots are pre-fit, where the shape of the inclusive and exclusive background components are fixed to the nominal template. From Ref. [94].

The performance of the models in predicting the data when applying the additional signal region requirements are assessed in the three VRs, and the comparison of data versus the model are shown in Figure 5.17. The model accurately describes the data even before any fits are performed to adjust the normalisation of the inclusive and exclusive background components or to apply shape variations in the models.

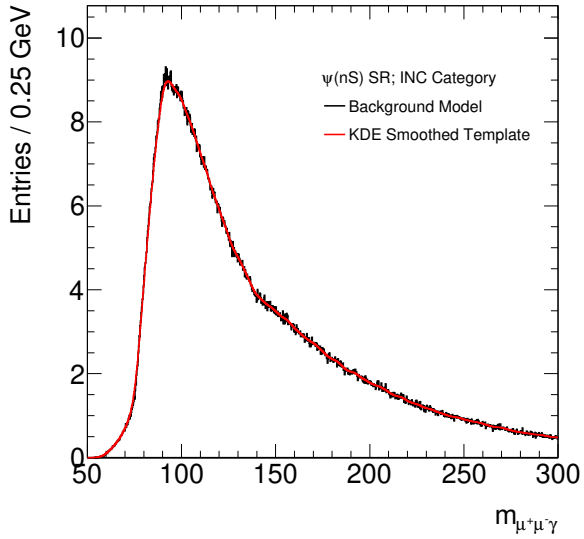
The final model PDFs used in the fits to the data in the signal region, obtained from applying the SR requirements to the pseudocandidate events and smoothing the resulting $m_{\mu^+\mu^-\gamma}$ distribution with KDE, are shown in Figure 5.18. The shapes before and after the KDE smoothing are compared, and the smoothing successfully retains the shape of the background distribution.



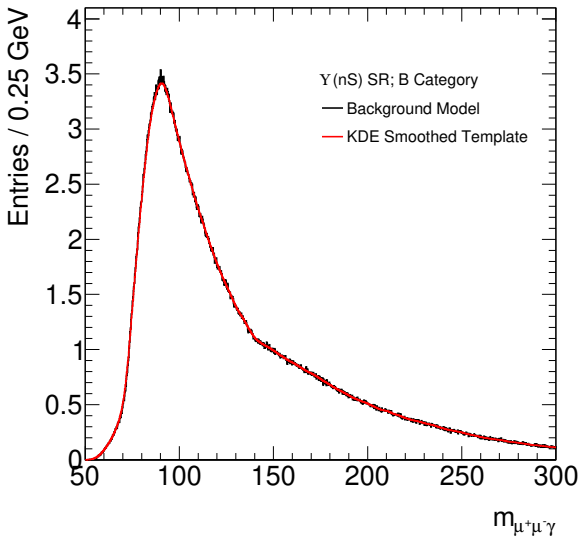
(a) $H(Z) \to \psi(nS)\gamma$ VR1 (b) $H(Z) \to \psi(nS)\gamma$ VR2 (c) $H(Z) \to \psi(nS)\gamma$ VR3

(d) $H(Z) \to \Upsilon(nS)\gamma$ VR1 (e) $H(Z) \to \Upsilon(nS)\gamma$ VR2 (f) $H(Z) \to \Upsilon(nS)\gamma$ VR3

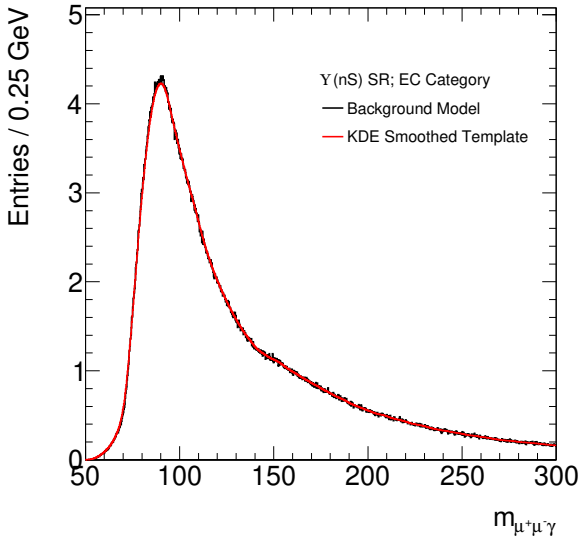
Figure 5.17: The distribution of $m_{\mu^+\mu^-\gamma}$ in data compared to the prediction of the total background model for ((a), (b) and (c)) $H(Z) \to \psi(nS)\,\gamma$ and ((d), (e) and (f)) $H(Z) \to \Upsilon(nS)\,\gamma$ in the VR1, VR2 and VR3 validation regions, respectively. The total background is normalised to the observed number of events within each region shown, where the ratio of the exclusive and inclusive background components are extrapolated from data in the GR. The uncertainty band corresponds to the uncertainty envelope derived from variations in the inclusive background modelling procedure described in Section 5.4.4. The dashed lines in the ratio plot in each figure indicate 1.2 and 0.8 on the y-axis. It should be noted that these plots are pre-fit, where the shapes of the inclusive and exclusive background components are fixed to the nominal template. From Ref. [94].



(a) $\psi(nS)\,\gamma$ Total



(b) $\Upsilon(nS)\,\gamma$ Barrel



(c) $\Upsilon(nS)\,\gamma$ Endcap

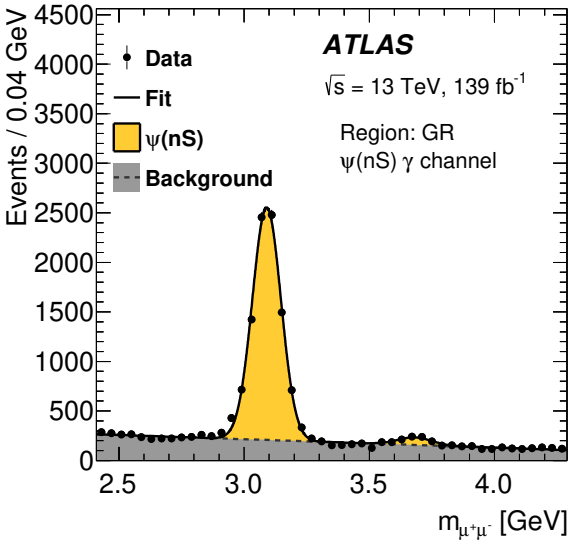
Figure 5.18: The smoothed $m_{\mu^+\mu^-\gamma}$ inclusive background KDE templates used in the likelihood fit to data in the signal region in the range $50 < m_{\mu^+\mu^-\gamma} < 300$ GeV.

5.4.3 Analytical Shape of $m_{\mu^+\mu^-}$

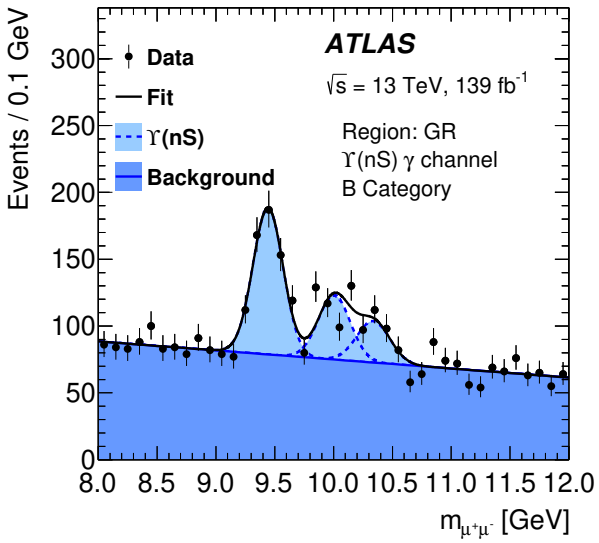
No significant correlations between $m_{\mu^+\mu^-}$ and $m_{\mu^+\mu^-\gamma}$ are observed for the inclusive background contribution, which allows the two distributions to be modelled independently.[7] The $m_{\mu^+\mu^-}$ distribution of the inclusive background model is described analytically as a sum of a first-order Chebyshev polynomial and several Gaussian distributions, one for each $\mathcal{Q}$ state in the $\psi(nS)$ and $\Upsilon(nS)$ analysis regions. The Chebyshev polynomial describes the non-resonant dimuon production component of the inclusive background, similarly to the $m_{\mu^+\mu^-}$ distribution of the exclusive background, and the Gaussian distributions describe each of the $\mathcal{Q}$ resonances. The width and mean parameters of the Gaussian components of each $m_{\mu^+\mu^-}$ distribution are fixed to values extracted from fits to the GR dataset, shown in Figure 5.19. The slope of each Chebyshev polynomial is also extracted in these fits, however these values are only used as a starting point and the slope parameter is free to adapt to the data in the maximum-likelihood fit to the SR in each search in Section 5.5. The GR selection is used to extract the Gaussian shape parameters instead of the SR selection to exploit the larger statistics of the GR dataset, and to reduce the number of free parameters in the maximum-likelihood fit to the signal region. The normalisation of the non-resonant dimuon contribution and each of the $\mathcal{Q}$ resonances is extracted directly from data in the signal region.

The two-dimensional model in $m_{\mu^+\mu^-}$ versus $m_{\mu^+\mu^-\gamma}$ for the inclusive background is the product of the two independently modelled mass distributions for each analysis. As the two mass distributions are uncorrelated, the shape of the $m_{\mu^+\mu^-\gamma}$ distribution is set to be the same for each of the genuine $\mathcal{Q}$ components and the non-resonant dimuon component of the inclusive background. The resulting 2D probability density functions, with relative normalisations extracted from data in the signal region, are shown in Figure 5.20.

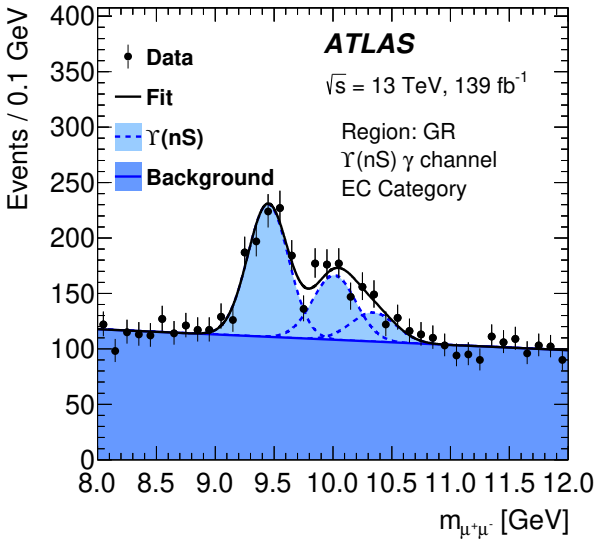
[7] Although values for $m_{\mu^+\mu^-}$ are sampled during the generation of the $m_{\mu^+\mu^-\gamma}$ model, these are not suitable to model the $m_{\mu^+\mu^-}$ distribution as it consists of several distinct components, some of which are resonant. The non-parametric data driven model generates a single template and typically smears out resonances, which is beneficial for modelling $m_{\mu^+\mu^-\gamma}$ but not for modelling $m_{\mu^+\mu^-}$.



(a)

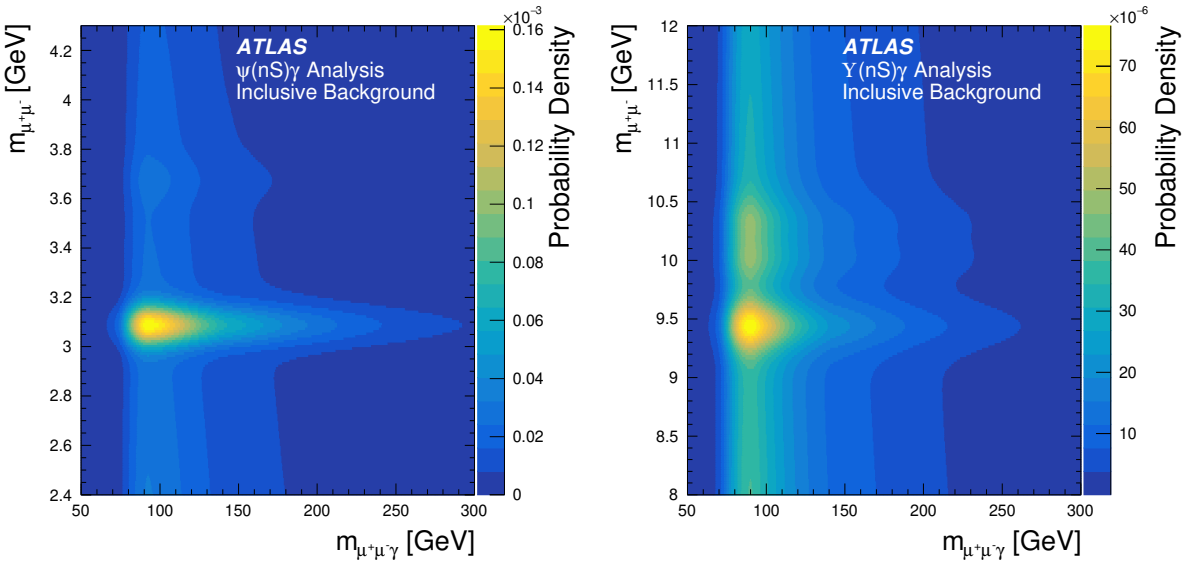


(b)



(c)

Figure 5.19: The $m_{\mu^+\mu^-}$ distributions in data satisfying the GR selection criteria for (a) $\psi(nS)\,\gamma$, (b) $\Upsilon(nS)\,\gamma$ in the barrel category, and (c) $\Upsilon(nS)\,\gamma$ in the endcap category. The error bars on the data points denote their statistical uncertainty. From Ref. [94].



(a) $\psi(nS)\,\gamma$ Total

(b) $\Upsilon(nS)\,\gamma$ Total

Figure 5.20: The two-dimensional $m_{\mu^+\mu^-\gamma}$ versus $m_{\mu^+\mu^-}$ probability density functions for the inclusive background in the (a) $\psi(nS)\,\gamma$ and (b) $\Upsilon(nS)\,\gamma$ analyses. The barrel and endcap categories are summed for the $\Upsilon(nS)\,\gamma$ model. From Ref. [94].

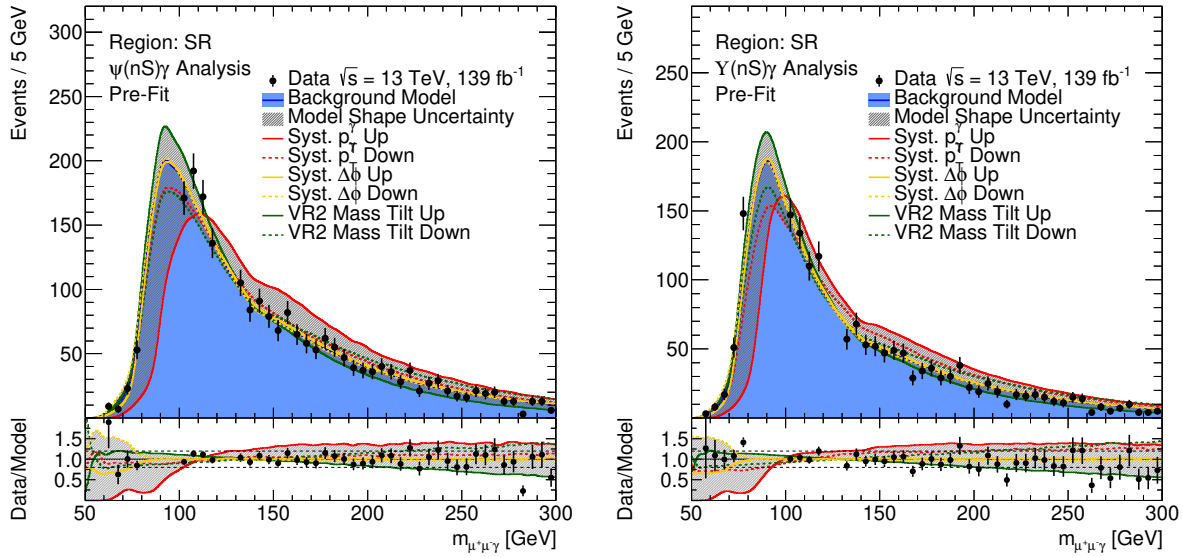
5.4.4 Systematic Uncertainties

To provide the inclusive background model with freedom to adapt to the data in the SR, the derived $m_{\mu^+\mu^-\gamma}$ distribution is allowed to vary around the nominal shape via three approximately orthogonal shape variations, called p_{T}^{γ}`-shift`, $\Delta\phi(\mathcal{Q},\gamma)$`-distortion`, and `mass-tilt`. The parameters controlling each systematic variation are treated as a nuisance parameters in the maximum-likelihood fit in Section 5.5. The alternative shapes are derived either by generating additional models with systematic variations in the underlying kinematics of the pseudocandidates and propagating the changes to the $m_{\mu^+\mu^-\gamma}$ distributions, as is the case in the p_{T}^{γ}`-shift` and the $\Delta\phi(\mathcal{Q},\gamma)$`-distortion` variations, or by the direct modification of the $m_{\mu^+\mu^-\gamma}$ final shape, as is the case in the `mass-tilt` variation. Several shapes are generated for each shape variation, and are arbitrarily designated as $\pm1\sigma$ and $\pm5\sigma$ variations, corresponding to relatively large changes in the shape to give the model sufficient freedom to adapt to data. The nuisance parameters are subsequently constrained by the data. The form of each shape variation is motivated by experience gained in previous searches for exclusive $H(Z)\to\mathcal{M}\gamma$ decays [90–93].

The alternate shapes for the p_{T}^{γ}`-shift` variation are generated by changing the scale of

the p_{T}^{γ} distribution of the model, artificially shifted by ± 6 GeV for the $\pm 1\sigma$ variations and by ± 12 GeV for the $\pm 5\sigma$ variations, and propagating this shift to the three-body mass distribution. This shape variation allows the peak of the $m_{\mu^+\mu^-\gamma}$ distribution to increase or decrease, and is constrained by a Gaussian term in the likelihood function. The alternate shapes for the $\Delta\phi(\mathcal{Q},\gamma)$`-distortion` variation are generated by a linear distortion of the $\Delta\phi(\mathcal{Q},\gamma)$ distribution of the model, implemented by reweighting the distribution by $\pi + 2 \times \Delta\phi(\mathcal{Q},\gamma)$ and $\pi + \frac{2}{5} \times (\pi - \Delta\phi(\mathcal{Q},\gamma))$ for the $\pm 1\sigma$ variations, and by $\pi + 10 \times \Delta\phi(\mathcal{Q},\gamma)$ and $\pi + 2 \times (\pi - \Delta\phi(\mathcal{Q},\gamma))$ for the $\pm 5\sigma$ variations, and propagating this distortion to the three-body mass distribution. This shape variation allows the peak of the $m_{\mu^+\mu^-\gamma}$ distribution to narrow or broaden, and is also constrained by a Gaussian term in the likelihood function. The alternate shapes for the `mass-tilt` variation are generated by directly reweighting the three-body mass distribution with a linear function around a pivot point near 123 GeV, defined as $-0.0013 \times m_{\mu^+\mu^-\gamma} + 1.16$ and $0.0013 \times m_{\mu^+\mu^-\gamma} + 0.84$ for the $\pm 1\sigma$ variations, and as $-0.0026 \times m_{\mu^+\mu^-\gamma} + 1.32$ and $0.0026 \times m_{\mu^+\mu^-\gamma} + 0.68$ for the $\pm 5\sigma$ variations. This shape variation allows the $m_{\mu^+\mu^-\gamma}$ distribution to adapt to slopes with respect to the data, and is left unconstrained in the likelihood function. The effect of each of the three systematic shape variations in the SR are demonstrated in Figure 5.21, where the H and Z mass peaks are blinded and the contribution by the exclusive background is ignored for purposes of demonstration. These systematic uncertainties are implemented in the maximum-likelihood fit using the interpolation technique described in Ref. [230] to morph the shape of the $m_{\mu^+\mu^-\gamma}$ distribution in the direction of each variation.

No systematic shape uncertainties are considered for the model of the $m_{\mu^+\mu^-}$ distribution, as the parameters are extracted directly from data. To test whether the shapes of the genuine $\mathcal{Q}$ components of inclusive background are consistent in the GR and the SR, the parameters of the Gaussian distributions describing each of the $\psi(nS)$ and $\Upsilon(nS)$ resonances in $m_{\mu^+\mu^-}$ were extracted from data in the SR under the background-only hypothesis and compared with the parameters found in the fit to the GR dataset: the two sets of parameters were compatible within the statistical error. The slope of the



(a) $\psi(nS)$ Window

(b) $\Upsilon(nS)$ Window

Figure 5.21: Illustration of the effect of each of the three systematic shape variations on the $m_{\mu^+\mu^-\gamma}$ distribution of the inclusive background in the (a) $\psi(nS)\,\gamma$ and (b) $\Upsilon(nS)\,\gamma$ analyses. The $\pm5\sigma$ shape variations are shown, where the solid lines show the positive variations and the dashed lines show the negative variations. The p_{T}^{γ}`-shift` variation is shown in red, the $\Delta\phi(\mathcal{Q},\gamma)$`-distortion` variation in yellow, and the `mass-tilt` variation in green. For demonstration purposes, the data points near potential H (86 GeV–96 GeV) and Z (122 GeV–128 GeV) boson signals are blinded and the exclusive background contribution is ignored. It should be noted that these plots are pre-fit, where the shape of the inclusive background is fixed to the nominal template.

first order Chebyshev polynomial describing the non-resonant dimuon component of the inclusive background is extracted directly from the SR in each search. Similarly, no systematic uncertainties on the normalisation of the inclusive background are considered as the normalisation of each component is extracted directly from the data in the signal region of each search.

5.5 Statistical Procedure and Results

To extract upper limits on the branching fractions of the $H(Z) \to \mathcal{Q}\,\gamma$ decay channels, two-dimensional unbinned maximum-likelihood fits are performed to data with $m_{\mu^+\mu^-\gamma} <$ 300 GeV in the signal region of each of the $\psi(nS)\,\gamma$ and $\Upsilon(nS)\,\gamma$ searches. Performing the fits in 2D, with $m_{\mu^+\mu^-\gamma}$ and $m_{\mu^+\mu^-}$ as the discriminant variables, allows potential $H(Z) \to \mathcal{Q}\,\gamma$ signals to be distinguished from each other as well as each of the components in the exclusive and inclusive background contributions. This section describes the form of the likelihood function and the method used to extract the 95% confidence level (CL) upper limits, the results of the fit with the observed 95% CL upper limits and significances, as well as the interpretation of the results in the κ framework described in Section 2.2.

5.5.1 Construction of the Likelihood Function

A likelihood function $\mathcal{L}$ is constructed for each of the $\psi(nS)\,\gamma$ and $\Upsilon(nS)\,\gamma$ analyses using the signal and background models described throughout Sections 5.2, 5.3 and 5.4. The likelihood for the $\psi(nS)\,\gamma$ analysis is described by

$$\begin{aligned}\mathcal{L}(\vec{\mu},\vec{b},\vec{\alpha},\vec{\theta},\theta') = \mathcal{P}(n|\sum_{i=1}^{4}\mu_i\cdot s_i(\vec{\alpha})+\sum_{j=1}^{4}b_j)\times\prod_r\mathcal{G}(\alpha_r|0,1)\\ \times\prod_{k=1}^{n}\left(\sum_{i=1}^{4}\mathcal{F}_i^s(\vec{\mu},\vec{\alpha},\vec{b})\mathcal{S}_i(m^k_{\mu^+\mu^-\gamma},m^k_{\mu^+\mu^-})+\sum_{j=1}^{4}\mathcal{F}_j^b(\vec{\mu},\vec{\alpha},\vec{b})\mathcal{R}_j(m^k_{\mu^+\mu^-\gamma}|\vec{\theta})\mathcal{M}_j(m^k_{\mu^+\mu^-}|\theta')\right)\\ \times\prod_l\mathcal{G}(\theta_l|0,1).\end{aligned}$$

The first line of the above equation describes the likelihood of observing n events, related

to the normalisation of the expected signal and background distributions. The symbol $\mathcal{P}$ represents the Poisson distribution to observe n events given the total signal and background, for which there are four distinct contributions each. The signals are counted by the index i and represent each of the signals, $H \to J/\psi\,\gamma$, $H \to \psi(2S)\,\gamma$, $Z \to J/\psi\,\gamma$ and $Z \to \psi(2S)\,\gamma$. The backgrounds are counted by the index j and represent each of the backgrounds, split into the exclusive and inclusive contributions, where the inclusive background is divided into three components: non-resonant dimuon production, J/ψ decays, and $\psi(2S)$ decays. The normalisation parameters associated with each of these background contributions are denoted by $\vec{b} = \{b_j\}$. These are not constrained and are determined directly from the fit to the data. The symbol $s_i(\vec{\alpha})$ represents the expected signal yield for signal i, as modified by the nuisance parameters $\vec{\alpha}$ for the signal normalisation systematics discussed in Section 5.2.4. These nuisance parameters are counted by index r and are constrained with Gaussian terms $\mathcal{G}$ where the mean and width parameters are set to the parameters of the standard normal distribution at 0 and 1, respectively. The expected signal yields are multiplied by the relative signal strength parameters $\vec{\mu} = \{\mu_i\}$ for each of the Higgs and Z boson signals, where $\mu_i = 1$ corresponds to an unmodified yield.[8] These are the parameters of interest in these searches and are used to determine the significances of each observed signal and the 95% CL upper limits on the branching fractions of each decay.

The second and third lines of the equation describe the likelihood of observing each individual event, represented by the index k, at its specific location, related to the PDFs of each signal and background contribution. The symbol $\mathcal{F}_i^s$ denotes the fraction of signal i in the total signal and background, and the symbol $\mathcal{F}_j^b$ denotes the fraction of background j in the total signal and background. The shape of the signal i in $m_{\mu^+\mu^-\gamma}$ versus $m_{\mu^+\mu^-}$ is given by the two-dimensional PDF $\mathcal{S}_i$. Similarly, the shape of the background component j is given by the product of one-dimensional PDFs $\mathcal{R}_j(m_{\mu^+\mu^-\gamma})$ and $\mathcal{M}_j(m_{\mu^+\mu^-})$,

[8]The exact values used in the normalisation of the expected signal yields $s_i(\vec{\alpha})$ are arbitrary as the signal strength parameters μ_i are free in the fit and constrained entirely by the data to adapt to the observed yield. Typically $s_i(\vec{\alpha})$ values are set to the expected yield in the SM, but in these analyses reference values corresponding to $\mathcal{B}(H \to \mathcal{Q}\gamma) = 10^{-3}$ and $\mathcal{B}(Z \to \mathcal{Q}\gamma) = 10^{-6}$ are used to set the normalisation of the expected signal yields in the limit setting, near the sensitivity of each search. This is helpful in the case of the $\psi(2S)\,\gamma$ channels where the SM expectations are not well known.

since the two mass distributions are not correlated in the backgrounds.[9] The nuisance parameters $\vec{\theta}$ represent the systematic variations of the background shapes in $m_{\mu^+\mu^-\gamma}$, as discussed for the exclusive background in Section 5.3.3 and for the inclusive background in Section 5.4.4. These parameters, counted by index l, are constrained by standard Gaussian terms similarly to the signal normalisation systematics. This is with the exception of the nuisance parameter for the `mass-tilt` shape variation which is not constrained. The nuisance parameter θ' represents the slope of in $m_{\mu^+\mu^-}$ of the non-resonant dimuon component of the inclusive background, which is also a free parameter in the fit.

The likelihood function for the $\Upsilon(nS)\,\gamma$ searches is defined similarly, but with the events divided further into the mutually exclusive barrel and endcap categories. In this case there are six signal contributions, three for $H \to \Upsilon(1S, 2S, 3S)\,\gamma$ and three for $Z \to \Upsilon(1S, 2S, 3S)\,\gamma$, and five background contributions. The backgrounds are split into the exclusive and inclusive backgrounds, where the inclusive background is divided into four components: non-resonant dimuon production, $\Upsilon(1S)$ decays, $\Upsilon(2S)$ decays, and $\Upsilon(3S)$ decays. Using analogous symbolism as for the $\psi(nS)\,\gamma$ likelihood function, the likelihood for the $\Upsilon(nS)\,\gamma$ analysis is described by

$$
\begin{aligned}
\mathcal{L}(\vec{\mu},\vec{b},\vec{\alpha},\vec{\theta},\vec{\theta'}) = \mathcal{P}(n|\sum_{i=1}^{6}\mu_i\cdot(s_i^{\mathrm{B}}(\vec{\alpha})+s_i^{\mathrm{EC}}(\vec{\alpha}))+\sum_{j=1}^{5}(b_j^{\mathrm{B}}+b_j^{\mathrm{EC}}))\times\prod_r\mathcal{G}(\alpha_r|0,1)\\
\times\prod_{k_{\mathrm{B}}=1}^{n_{\mathrm{B}}}\left(\sum_{i=1}^{6}\mathcal{F}_i^{s^{\mathrm{B}}}(\vec{\mu},\vec{\alpha},\vec{b_B})\mathcal{S}_i^{\mathrm{B}}(m^{k_{\mathrm{B}}}_{\mu^+\mu^-\gamma},m^{k_{\mathrm{B}}}_{\mu^+\mu^-})+\sum_{j=1}^{5}\mathcal{F}_j^{b^{\mathrm{B}}}(\vec{\mu},\vec{\alpha},\vec{b_{\mathrm{B}}})\mathcal{R}_j^{\mathrm{B}}(m^{k_{\mathrm{B}}}_{\mu^+\mu^-\gamma}|\vec{\theta_{\mathrm{B}}})\mathcal{M}_j^{\mathrm{B}}(m^{k_{\mathrm{B}}}_{\mu^+\mu^-}|\theta'_{\mathrm{B}})\right)\\
\times\prod_{k_{\mathrm{EC}}=1}^{n_{\mathrm{EC}}}\left(\sum_{i=1}^{6}\mathcal{F}_i^{s^{\mathrm{EC}}}(\vec{\mu},\vec{\alpha},\vec{b_{EC}})\mathcal{S}_i^{\mathrm{EC}}(m^{k_{\mathrm{EC}}}_{\mu^+\mu^-\gamma},m^{k_{\mathrm{EC}}}_{\mu^+\mu^-})+\sum_{j=1}^{5}\mathcal{F}_j^{b^{\mathrm{EC}}}(\vec{\mu},\vec{\alpha},\vec{b_{\mathrm{EC}}})\mathcal{R}_j^{\mathrm{EC}}(m^{k_{\mathrm{EC}}}_{\mu^+\mu^-\gamma}|\vec{\theta_{\mathrm{EC}}})\mathcal{M}_j^{\mathrm{EC}}(m^{k_{\mathrm{EC}}}_{\mu^+\mu^-}|\theta'_{\mathrm{EC}})\right)\\
\times\prod_l\mathcal{G}(\theta_l|0,1).
\end{aligned}
$$

In the above, the indices B and EC denote the specific barrel and endcap components of each term described in the likelihood, where the total signals and backgrounds are the sum of these two mutually exclusive categories, and the total number of events $n = n_{\mathrm{B}} + n_{\mathrm{EC}}$. The signal strength parameters $\vec{\mu}$ and nuisance parameters $\vec{\alpha}$, representing the

[9] This is also true in the case of the $Z \to \mathcal{Q}\gamma$ signal PDFs, which can be described as $\mathcal{S}_i = \mathcal{S}_i^1(m_{\mu^+\mu^-\gamma}) \times \mathcal{S}_i^2(m_{\mu^+\mu^-})$.

signal normalisation systematic uncertainties, scale the total signal yields. Conversely, the parameters associated with the background shape systematic uncertainties modify the background shapes separately in the B and EC categories, such that $\vec{\theta} = \{\vec{\theta_{\mathrm{B}}}, \vec{\theta_{\mathrm{EC}}}\}$ and $\vec{\theta'} = \{\theta'_{\mathrm{B}}, \theta'_{\mathrm{EC}}\}$.

The above functions are fit to the data to extract the observed significances for each signal in the data, as well as the 95% CL upper limits on the branching fractions for the H and Z boson decays into $\mathcal{Q}\gamma$. The background-only hypothesis refers to the situation where the set $\vec{\mu}$ of the signal strengths are set to 0, such that $\mathcal{L}$ consists only of terms relating to the background. The statistics-only hypothesis refers to the situation where the systematic uncertainties are neglected, such that $\vec{\alpha} = \vec{0}$ and $\vec{\theta} = \vec{0}$ and is used to assess the impact of the systematic uncertainties on the sensitivity of each search. For the limit setting, the CL_{s} modified frequentist formalism [231] is used with the profile-likelihood-ratio test statistic and the asymptotic approximations derived in Ref. [232]. The 95% CL upper limit corresponds to $CL_{\mathrm{s}} = 1 - \mathrm{CL} = 0.05$. Whilst setting the limits for a given signal, each of the other potential signal contributions are treated as nuisance parameters and are profiled in the fit. The profile-likelihood-ratio test statistic $\Lambda(\mu_i)$ for a given signal i is defined as

$$\Lambda(\mu_i) = \frac{\mathcal{L}(\mu_i, \hat{\hat{\vec{\beta}}}(\mu_i))}{\mathcal{L}(\hat{\mu}_i, \hat{\vec{\beta}})},$$

where $\vec{\beta}$ corresponds to the full set of nuisance parameters in the likelihood function $\mathcal{L}$, which is every parameter $\mathcal{L}$ is dependent on described above with the exception of the strength of the signal of interest μ_i. The symbols $\hat{\mu}_i$ and $\hat{\vec{\beta}}$ refer to the specific set of values of μ_i and $\vec{\beta}$ which maximise $\mathcal{L}$ overall, found via fits to the data. The symbol $\hat{\hat{\vec{\beta}}}(\mu_i)$ refers to the set of values of $\vec{\beta}$ which maximise $\mathcal{L}$ for a given value of μ_i. For technical and computational reasons, the fits themselves find the values of each parameter which minimize the negative log-likelihood function, defined as $-\ln(\mathcal{L})$, for a given condition. The observed local significance σ_i for a signal i is approximated by

taking the value $\sqrt{2 \times |\Delta[-\ln \mathcal{L}]|}$ for the situation where $\Delta[-\ln \mathcal{L}] = \ln[\mathcal{L}(0, \hat{\hat{\vec{\beta}}}(0))] - \ln[\mathcal{L}(\hat{\mu}_i, \hat{\vec{\beta}})]$. This compares the maximised likelihood value in the case where the signal i is fixed to $\mu_i = 0$ to the case where the signal is free in the fit. Signals are upward fluctuations if the corresponding best-fit value of μ_i is positive and downward fluctuations if the corresponding value of μ_i is negative.

To test the capability of the fit in finding potential signal contributions, signal injection tests were performed. Signals corresponding to a branching fraction of 5×10^{-4} for H boson signals and 5×10^{-7} for Z boson signals, such that $\mu_i = 0.5$ for all signals, were injected into an Asimov dataset [232] of the expected backgrounds obtained from a background-only fit to the signal region. Table 5.18 shows the results of a maximum-likelihood fit to the resulting Asimov datasets, and the fit successfully recovers the signal in each case, in that the best fit value of μ_i is found to be consistent with 0.5 in each case.

Table 5.18: μ values from the fit after injection of signals corresponding to a branching ratio of $5 \times 10^{-4}(10^{-7})$ for the Higgs (Z) boson decays. A binning of 1 GeV in $m_{\mu^+\mu^-\gamma}$ and 0.025 (0.05) GeV in $m_{\mu^+\mu^-}$ was used to construct the Asimov dataset for the $\psi(nS)$ ($\Upsilon(nS)$) analysis.

	post-fit μ (syst)
$H \to J/\psi\,\gamma$	0.499 ± 0.126
$H \to \psi(2S)\gamma$	0.500 ± 0.426
$Z \to J/\psi\,\gamma$	0.501 ± 0.324
$Z \to \psi(2S)\gamma$	0.497 ± 1.390
$H \to \Upsilon(1S)\gamma$	0.500 ± 0.303
$H \to \Upsilon(2S)\gamma$	0.496 ± 0.259
$H \to \Upsilon(3S)\gamma$	0.502 ± 0.257
$Z \to \Upsilon(1S)\gamma$	0.505 ± 0.676
$Z \to \Upsilon(2S)\gamma$	0.502 ± 0.454
$Z \to \Upsilon(3S)\gamma$	0.506 ± 0.492

5.5.2 Observed Significances and Upper Limits

In total, across the entire $m_{\mu^+\mu^-\gamma}$ and $m_{\mu^+\mu^-}$ mass ranges used in each search, 3394 events are observed in the signal region for the $\psi(nS)\,\gamma$ analysis, and 3577 events are observed in the signal region for the $\Upsilon(nS)\,\gamma$ analysis, which is the total of the barrel and endcap categories. The number of expected and observed background events in the

mass windows for individual signal resonances are shown in Table 5.19, along with the expected signal yields for reference branching ratios of 10^{-3} and 10^{-6} for each of the H and Z signals, respectively. The values for the expected backgrounds are obtained from a background-only fit to the data whereas the values for the expected signals given their reference branching ratios are obtained from the normalisation of the simulated samples. The contribution from the exclusive background to the total background around each resonance is approximately 10% for $H \to J/\psi\,\gamma$, 22% for $H \to \psi(2S)\,\gamma$, 21% for $Z \to J/\psi\,\gamma$, and 41% for $Z \to \psi(2S)\,\gamma$. For the $\Upsilon(nS)\,\gamma$ searches the exclusive background makes up 24%–29% of the total background near the Higgs boson signals and 75%–79% near the Z boson signals. The exclusive background comprises a larger portion of the total background near the Z signals primarily due to the contribution by on-shell $Z \to \mu^+\mu^-\gamma$ events, particularly in the $Z \to \Upsilon(nS)\,\gamma$ searches.

Table 5.19: Numbers of expected and observed background events for the $m_{\mu^+\mu^-\gamma}$ versus $m_{\mu^+\mu^-}$ ranges of interest. Each expected background its corresponding uncertainty is obtained from a background-only fit to the data; the uncertainty does not take into account statistical fluctuations in each mass range. Expected H and Z boson signal contributions are shown for reference branching fractions of 10^{-3} and 10^{-6}, respectively, with their corresponding total systematic uncertainty. The ranges in $m_{\mu^+\mu^-\gamma}$ are centred around each boson resonance whereas the ranges in $m_{\mu^+\mu^-}$ are centred around each quarkonium resonance, with widths driven by the resolution of the detector. In particular, the ranges for the $\Upsilon(nS)$ resonances are based on the resolution in the endcaps, and the same window is used for the barrel category. From Ref. [94].

Category	$m_{\mu^+\mu^-}$ range [GeV]	Observed (expected) background $m_{\mu^+\mu^-\gamma}$ range [GeV] 86–96		122–128		Z signal for $\mathcal{B} = 10^{-6}$	H signal for $\mathcal{B} = 10^{-3}$
Inclusive	2.9–3.3	198	(185.6 ± 5.9)	61	(59.1 ± 1.6)	49.3 ± 2.4	87.8 ± 6.1
Inclusive	3.5–3.9	83	(82.5 ± 4.0)	21	(22.9 ± 0.9)	6.5 ± 0.3	11.8 ± 0.8
Barrel	9.0–9.8	125	(125.3 ± 4.7)	12	(11.6 ± 0.6)	11.4 ± 0.6	20.2 ± 1.4
Barrel	9.6–10.4	118	(121.9 ± 4.6)	14	(10.7 ± 0.6)	8.8 ± 0.4	15.3 ± 1.1
Barrel	9.9–10.7	102	(119.9 ± 4.5)	11	(10.2 ± 0.6)	10.1 ± 0.5	17.4 ± 1.2
Endcap	9.0–9.8	133	(162.9 ± 5.7)	16	(13.6 ± 0.7)	15.5 ± 0.8	20.5 ± 1.4
Endcap	9.6–10.4	150	(157.1 ± 5.6)	11	(11.7 ± 0.5)	11.7 ± 0.6	15.8 ± 1.1
Endcap	9.9–10.7	171	(156.7 ± 5.8)	7	(11.4 ± 0.6)	13.5 ± 0.7	17.6 ± 1.2

The results of the background-only fits are shown graphically in each mass dimension in Figure 5.22 for the $\psi(nS)\,\gamma$ analysis and in Figure 5.23 for the $\Upsilon(nS)\,\gamma$ analysis. These demonstrate the ability of the background model to accurately describe the data across the entire signal region of each analysis. In these figures the signal distributions are

normalised to the reference branching ratios of 10^{-3} for the Higgs boson signals and 10^{-6} for the Z boson signals.

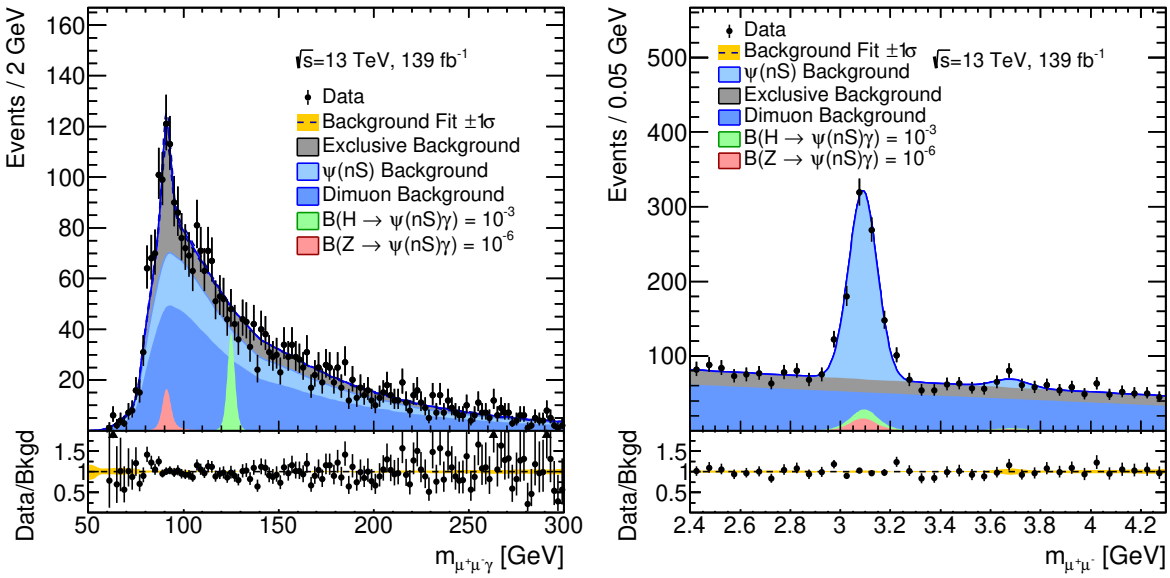


Figure 5.22: The $m_{\mu^+\mu^-\gamma}$ and $m_{\mu^+\mu^-}$ distributions for the selected events in the $\psi(nS)\,\gamma$ analysis. The results of the maximum-likelihood fits to the background-only models is also given, along with the ratio of the data to this fit. The dimuon background in the legend refers to the component of the inclusive background which is non-resonant $m_{\mu^+\mu^-}$; the $\psi(nS)$ background in the legend refers to the components of the inclusive background which are resonant in $m_{\mu^+\mu^-}$. The expected Z and Higgs boson contributions are shown for reference branching fraction values of 10^{-6} and 10^{-3}, respectively. From Ref. [94].

Expected 95% CL upper limits on the branching fractions, and their uncertainty bands, are calculated based on the construction of Asimov datasets and fitting these with the likelihood functions $\mathcal{L}$. Tables 5.20 and 5.21, for the $\psi(nS)\,\gamma$ and $\Upsilon(nS)\,\gamma$ searches, respectively, compare the expected limits obtained when accounting for the full set of systematic uncertainties in the maximum-likelihood fit to the expected limits obtained when only accounting for statistical uncertainties in the fit. The sensitivity of each search is dominated by the statistical uncertainty; the systematic uncertainties have a small effect in the expected limits. For $H \to J/\psi\,\gamma$ the systematic uncertainties result in a 0.8% increase of the expected 95% CL upper limit on the branching fraction compared to the statistics-only case, and 4.2% for $Z \to J/\psi\,\gamma$. The corresponding increases are 0.1% for $H \to \psi(2S)\,\gamma$, and 0.6% for $Z \to \psi(2S)\,\gamma$. Similarly, the sensitivity to the $H \to \Upsilon(1S, 2S, 3S)\,\gamma$ signals deteriorates by 0.1%–0.8% when accounting for systematic uncertainties, and by 0.3%–0.5% for the $Z \to \Upsilon(1S, 2S, 3S)\,\gamma$ signals. For $Z \to J/\psi\,\gamma$,

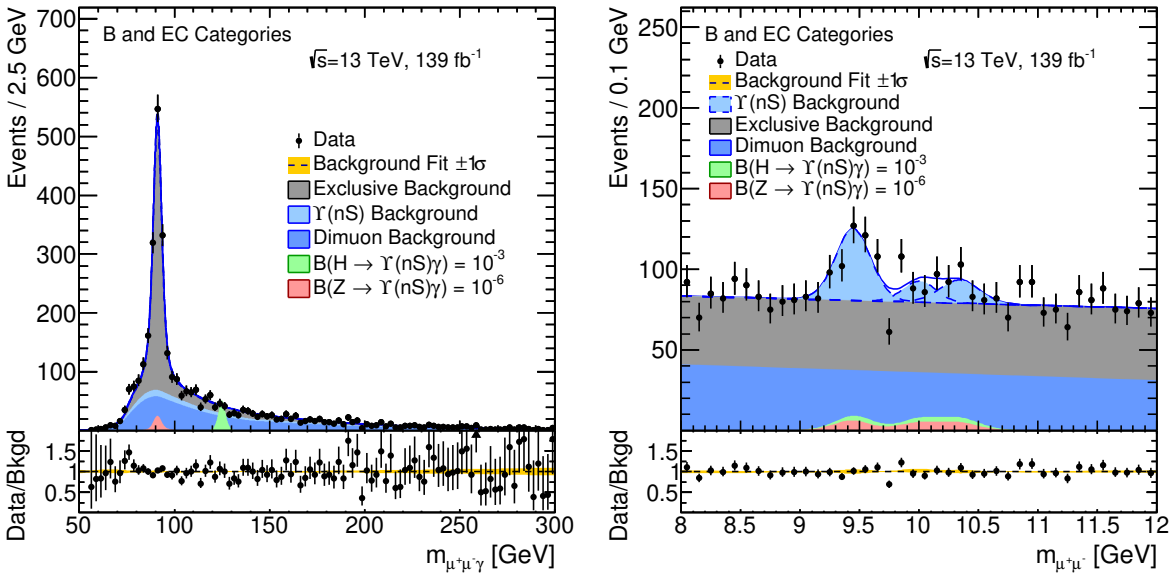


Figure 5.23: The $m_{\mu^+\mu^-\gamma}$ and $m_{\mu^+\mu^-}$ distributions for the selected events in the $\Upsilon(nS)\,\gamma$ analysis. The results of the maximum-likelihood fits to the background-only models is also given, along with the ratio of the data to this fit. The dimuon background in the legend refers to the component of the inclusive background which is non-resonant $m_{\mu^+\mu^-}$; the $\Upsilon(nS)$ background in the legend refers to the components of the inclusive background which are resonant in $m_{\mu^+\mu^-}$. The expected Z and Higgs boson contributions are shown for reference branching fraction values of 10^{-6} and 10^{-3}, respectively. From Ref. [94].

where systematic uncertainties have the largest impact on sensitivity, the uncertainties in the inclusive background shape dominate compared to the uncertainties in the exclusive background shape and in the normalisation of the signals.

Table 5.20: Post-fit expected branching fraction limit at 95% CL for the $\psi(nS)\,\gamma$ decays. The limits are estimated both with no systematic uncertainties, and with the complete normalisation and shape systematic uncertainties.

	Expected	$\pm1\sigma$	$\pm2\sigma$
$H \to J/\psi\,\gamma$ $[10^{-3}]$			
No Systematics	0.179	0.255/0.129	0.355/0.096
Shape+Norm	0.181	0.259/0.130	0.363/0.097
$H \to \psi(2S)\gamma$ $[10^{-3}]$			
No Systematics	0.813	1.176/0.586	1.680/0.436
Shape+Norm	0.814	1.178/0.586	1.686/0.437
$Z \to J/\psi\,\gamma$ $[10^{-6}]$			
No Systematics	0.636	0.900/0.458	1.227/0.341
Shape+Norm	0.663	0.937/0.477	1.281/0.356
$Z \to \psi(2S)\gamma$ $[10^{-6}]$			
No Systematics	3.024	4.317/2.179	5.953/1.623
Shape+Norm	3.041	4.351/2.191	6.021/1.632

The significance of each of the observed signal strengths is presented in Table 5.22, ob-

Table 5.21: Post-fit expected branching fraction limit at 95% CL for the $\Upsilon(nS)\,\gamma$ decays. The limits are estimated both with no systematic uncertainties, and with the complete normalisation and shape systematic uncertainties.

	Expected	$\pm1\sigma$	$\pm2\sigma$
$H \to \Upsilon(1S)\gamma$ $[10^{-3}]$			
No Systematics	0.270	0.389/0.195	0.552/0.145
Shape+Norm	0.272	0.394/0.196	0.564/0.146
$H \to \Upsilon(2S)\gamma$ $[10^{-3}]$			
No Systematics	0.340	0.490/0.245	0.699/0.182
Shape+Norm	0.340	0.491/0.245	0.701/0.183
$H \to \Upsilon(3S)\gamma$ $[10^{-3}]$			
No Systematics	0.298	0.431/0.215	0.615/0.160
Shape+Norm	0.298	0.432/0.215	0.617/0.160
$Z \to \Upsilon(1S)\gamma$ $[10^{-6}]$			
No Systematics	1.553	2.178/1.119	2.966/0.833
Shape+Norm	1.559	2.191/1.123	2.996/0.837
$Z \to \Upsilon(2S)\gamma$ $[10^{-6}]$			
No Systematics	2.109	2.934/1.519	3.988/1.132
Shape+Norm	2.119	2.958/1.527	4.032/1.137
$Z \to \Upsilon(3S)\gamma$ $[10^{-6}]$			
No Systematics	1.928	2.704/1.389	3.682/1.035
Shape+Norm	1.934	2.719/1.394	3.719/1.038

tained by comparing the signal-plus-background hypothesis to the background-only hypothesis. The observed data are consistent with the expected backgrounds in each search,[10] where the largest observed local excess is 1.9σ in the search for $Z \to J/\psi\,\gamma$ followed by 0.8σ in the search for $H \to \psi(2S)\,\gamma$.

Table 5.22: Post-fit observed significances. The p-value is calculated from a one-tailed test under the background-only hypothesis. For the upward fluctuations this corresponds to the probability of observing an as large or larger excess of events with respect to the background-only expectation; for the downward fluctuations this is the probability of observing an as large or larger deficit of events with respect to the background-only expectation.

	Local Significance (σ)	Direction of fluctuation	P-value (%)
$H \to J/\psi\,\gamma$	0.38	Up	35.3
$H \to \psi(2S)\,\gamma$	0.81	Up	20.8
$Z \to J/\psi\,\gamma$	1.90	Up	2.8
$Z \to \psi(2S)\,\gamma$	0.73	Down	23.4
$H \to \Upsilon(1S)\,\gamma$	0.38	Down	35.3
$H \to \Upsilon(2S)\,\gamma$	0.69	Up	24.4
$H \to \Upsilon(3S)\,\gamma$	0.64	Up	26.1
$Z \to \Upsilon(1S)\,\gamma$	1.21	Down	11.3
$Z \to \Upsilon(2S)\,\gamma$	1.69	Down	4.6
$Z \to \Upsilon(3S)\,\gamma$	0.63	Up	26.5

[10] In general, an excess of 3σ is required to claim that there is evidence of a signal, and an excess of 5σ is required to claim a discovery.

The results of the background-only fits projected into the individual mass windows near each signal resonance are shown in Figures 5.24 and 5.25 for the $\psi(nS)\,\gamma$ and $\Upsilon(nS)\,\gamma$ searches, respectively. The signal distributions shown in these plots are set to these observed 95% CL upper limits, which are highly sensitive to the number of events in the resonance windows shown. These are presented in Table 5.23 alongside the observed upper limits in terms of the H and Z production cross sections times branching fractions to a quarkonium state and a photon, where the cross section values are shown in Table 5.7 in Section 5.2.2. In general, the observed limits are an improvement by a factor of approximately two compared to the previous ATLAS result presented in Ref. [92], which used a smaller dataset 36.1 fb^{-1} of $\sqrt{s} = 13$ TeV proton–proton collision data. The improvement in the limits is consistent with the increase in integrated luminosity from 36.1 fb^{-1} to 139 fb^{-1}.

Table 5.23: Expected, with the corresponding $\pm1\sigma$ intervals, and observed 95% CL branching fraction upper limits for the Higgs and Z boson decays into a quarkonium state and a photon. Standard Model production of the Higgs boson is assumed. The corresponding upper limits on the production cross section times branching fraction $\sigma \times \mathcal{B}$ are also shown. From Ref. [94].

	95% CL upper limits					
	Branching fraction				$\sigma \times \mathcal{B}$	
Decay	Higgs boson [10^{-4}]		Z boson [10^{-6}]		Higgs boson [fb]	Z boson [fb]
channel	Expected	Observed	Expected	Observed	Observed	Observed
$J/\psi\,\gamma$	$1.8^{+0.8}_{-0.5}$	2.0	$0.7^{+0.3}_{-0.2}$	1.2	11	69
$\psi(2S)\,\gamma$	$8.1^{+3.6}_{-2.3}$	10.5	$3.0^{+1.3}_{-0.8}$	2.4	58	142
$\Upsilon(1S)\,\gamma$	$2.7^{+1.2}_{-0.8}$	2.5	$1.6^{+0.6}_{-0.4}$	1.1	14	62
$\Upsilon(2S)\,\gamma$	$3.4^{+1.5}_{-1.0}$	4.2	$2.1^{+0.8}_{-0.6}$	1.3	24	74
$\Upsilon(3S)\,\gamma$	$3.0^{+1.3}_{-0.8}$	3.4	$1.9^{+0.8}_{-0.5}$	2.4	19	143

5.5.3 Interpretation in κ Framework

The approach presented in Refs. [71, 78] is employed to interpret the results of these searches in terms of constraints on the charm- and bottom-quark Yukawa couplings, described in terms of the κ framework discussed in Section 2.2. The ratio of signal strength μ measurements between the $H \to J/\psi\,\gamma$ and $H \to \gamma\gamma$ decay channels, where μ is normalised such that $\mu = 1$ is the expected yield with SM branching ratios (not reference

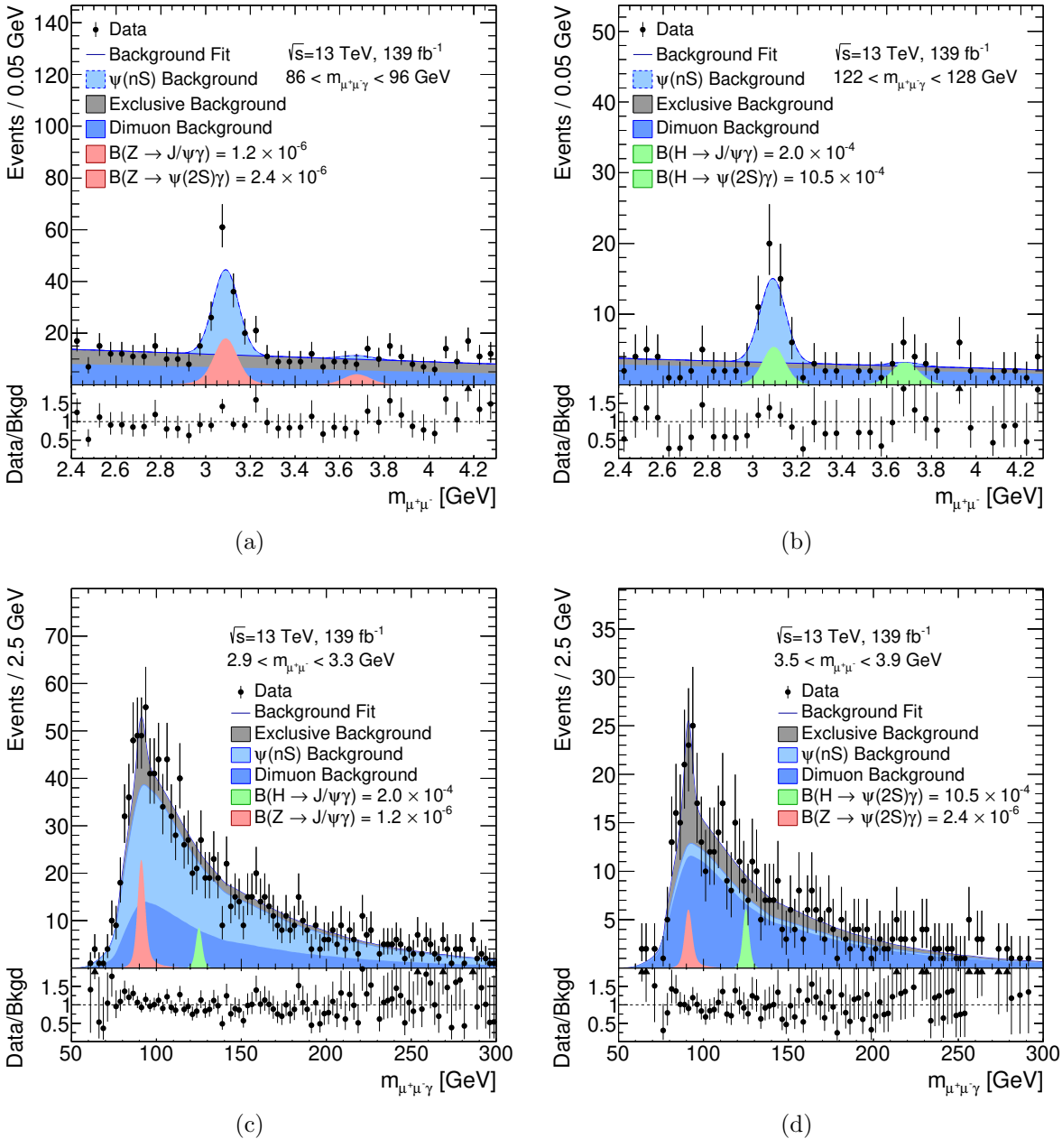


Figure 5.24: Projection of the background-only fit in the $\psi(nS)\,\gamma$ analysis in $m_{\mu^+\mu^-}$ for the (a) Z boson and (b) Higgs boson $m_{\mu^+\mu^-\gamma}$ regions, and in $m_{\mu^+\mu^-\gamma}$ for the (c) J/ψ and (d) $\psi(2S)$ $m_{\mu^+\mu^-}$ regions. The dimuon background in the legend refers to the component of the inclusive background which is non-resonant $m_{\mu^+\mu^-}$; the $\psi(nS)$ background in the legend refers to the components of the inclusive background which are resonant in $m_{\mu^+\mu^-}$. The branching fraction of each signal distributions is set to the corresponding observed 95% CL upper limit. From Ref. [94].

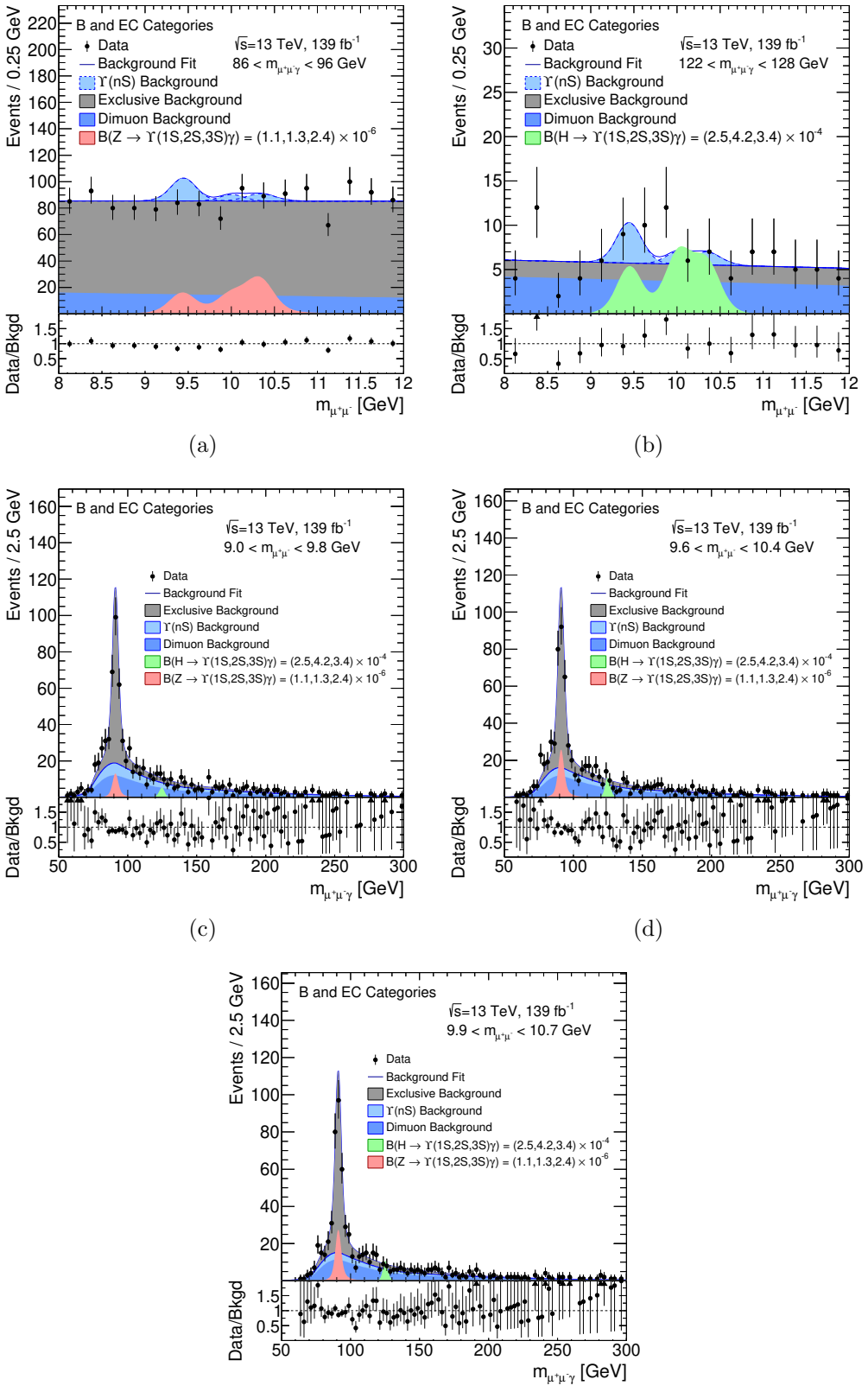


Figure 5.25: Projection of the background-only fit in the $\Upsilon(nS)\,\gamma$ analysis in $m_{\mu^+\mu^-}$ for the (a) Z boson and (b) Higgs boson $m_{\mu^+\mu^-\gamma}$ regions, and in $m_{\mu^+\mu^-\gamma}$ for the $\Upsilon(1S, 2S, 3S)$ $m_{\mu^+\mu^-}$ regions in (c), (d) and (e), respectively. The dimuon background in the legend refers to the component of the inclusive background which is non-resonant $m_{\mu^+\mu^-}$; the $\Upsilon(nS)$ background in the legend refers to the components of the inclusive background which are resonant in $m_{\mu^+\mu^-}$. The branching fraction of each signal distributions is set to the corresponding observed 95% CL upper limit. From Ref. [94].

branching ratios as in the limit setting), is equivalent to the ratio of measurements of their production cross section times branching fraction $\sigma \times \mathcal{B}$. This is approximately equal to the ratio of the respective partial decay widths, Γ, normalised to their expectation in the SM, Γ^{SM}, since the dependence on the production mechanism and Higgs total width cancels out. The ratio κ_c/κ_γ of the coupling modifiers, where κ is the ratio of each coupling with its value in the SM, for the charm-quark Yukawa coupling κ_c and the effective coupling of Higgs boson to photons κ_γ can be estimated as

$$\frac{\mu_{H\to J/\psi\,\gamma}}{\mu_{H\to\gamma\gamma}} = \frac{\sigma_H \mathcal{B}_{H\to J/\psi\,\gamma}/\sigma_H^{\mathrm{SM}}\mathcal{B}^{\mathrm{SM}}_{H\to J/\psi\,\gamma}}{\sigma_H \mathcal{B}_{H\to\gamma\gamma}/\sigma_H^{\mathrm{SM}}\mathcal{B}^{\mathrm{SM}}_{H\to\gamma\gamma}} \approx \frac{\Gamma_{H\to J/\psi\,\gamma}/\Gamma^{\mathrm{SM}}_{H\to J/\psi\,\gamma}}{\Gamma_{H\to\gamma\gamma}/\Gamma^{\mathrm{SM}}_{H\to\gamma\gamma}} = \frac{|\mathcal{A}_{\mathrm{ind}} + \mathcal{A}_{\mathrm{dir}}\kappa_c/\kappa_\gamma|^2}{\Gamma^{\mathrm{SM}}_{H\to J/\psi\,\gamma}}.$$

This parameterisation is used to derive a 95% CL interval of the κ_c/κ_γ ratio. The indirect and direct amplitudes, $\mathcal{A}_{\mathrm{ind}}$ and $\mathcal{A}_{\mathrm{dir}}$, for $H \to J/\psi\,\gamma$ and $H \to \Upsilon(nS)\,\gamma$ interfere destructively and are obtained from Ref. [76].[11] The signal strength for $H \to \gamma\gamma$ is obtained from Ref. [233] whereas the signal strengths for $H \to J/\psi\,\gamma$ and $H \to \Upsilon(nS)\,\gamma$ are from this search. An observed 95% CL interval of $(-133, 175)$ is obtained for κ_c/κ_γ, with an expected interval of $(-120, 161)$. This interval is dominated by the statistical uncertainty in the search for $H \to J/\psi\,\gamma$, where the theoretical uncertainties of the decay amplitudes enlarge the obtained interval by approximately 8%, mainly through the uncertainty in the real part of $\mathcal{A}_{\mathrm{dir}}$. The correlated components in the uncertainties of the two measurements were also removed, but this had negligible impact. The magnitude of $\mathcal{A}_{\mathrm{dir}}$, which is sensitive to the charm-quark Yukawa coupling, is significantly smaller in the most recent theory calculations [74, 76] compared to earlier ones [69], leading to much weaker constraints than those predicted when these searches were proposed. Very large values of κ_c lead to tensions with other ATLAS [234] and CMS [235] measurements of Higgs boson couplings [236].

A similar relation can be written for the ratio κ_b/κ_γ, where κ_b is the coupling modifier

[11] The corresponding values for $H \to \psi(2S)\,\gamma$ are not available in the literature, so this study cannot be performed for the $\psi(2S)$ channel.

for the bottom-quark Yukawa coupling. This relation is

$$\frac{\mu_{H\to\Upsilon(nS)\,\gamma}}{\mu_{H\to\gamma\gamma}} = \frac{\sigma_H \mathcal{B}_{H\to\Upsilon(nS)\,\gamma}/\sigma_H^{\rm SM}\mathcal{B}^{\rm SM}_{H\to\Upsilon(nS)\,\gamma}}{\sigma_H \mathcal{B}_{H\to\gamma\gamma}/\sigma_H^{\rm SM}\mathcal{B}^{\rm SM}_{H\to\gamma\gamma}} \approx \frac{\Gamma_{H\to\Upsilon(nS)\,\gamma}/\Gamma^{\rm SM}_{H\to\Upsilon(nS)\,\gamma}}{\Gamma_{H\to\gamma\gamma}/\Gamma^{\rm SM}_{H\to\gamma\gamma}} = \frac{|\mathcal{A}_{\rm ind} + \mathcal{A}_{\rm dir}\kappa_b/\kappa_\gamma|^2}{\Gamma^{\rm SM}_{H\to\Upsilon(nS)\,\gamma}}.$$

Combining the three $\Upsilon(1S, 2S, 3S)\,\gamma$ decays, and accounting for the -21% correlation between $\mu_{H\to\Upsilon(2S)\,\gamma}$ and $\mu_{H\to\Upsilon(3S)\,\gamma}$, a 95% CL interval of $(-37, 40)$ is obtained for κ_b/κ_γ, with an expected interval of $(-37, 39)$. The $\Upsilon(1S)\,\gamma$ decay contributes most of the sensitivity to κ_b/κ_γ since its indirect amplitude is the largest amongst the $\Upsilon(nS)\,\gamma$ decays. Similarly to the κ_c/κ_γ result, the statistical uncertainty in the searches for $H \to \Upsilon(nS)\,\gamma$ dominate the interval, where the theoretical uncertainties of the decay amplitudes enlarge the interval by 12%.

6 Searches for Flavour-Violating H and Z Boson Decays with a Displaced Vertex: $H \to D^*\gamma$, $Z \to D^0\gamma$, and $Z \to K_s\gamma$

Flavoured mesons consist of quarks of two different flavours, and their properties relevant for these exclusive decay searches are summarised in Table 6.1. As discussed in Section 2.3, the decays $H \to D^*\gamma$, $Z \to D^0\gamma$ and $Z \to K_s\gamma$ are forbidden at tree level in the SM, and loop contributions are very small [84]. The provides the opportunity to probe potential flavour-violating couplings of the Higgs and Z bosons, through the Feynman diagram shown in Figure 6.1 which proceeds via the flavour violating coupling.

Table 6.1: Properties of the flavoured mesons considered in these searches [26]. Uncertainties on the meson masses are not shown as they are negligible compared to the central value, of order 50 keV or smaller. Decay lengths are calculated from the proper lifetimes the K_s and D^0 by the speed of light. The lifetime of the K_s is $(8.954 \pm 0.004) \times 10^{-11}$ s and of the D^0 is $(4.103 \pm 0.010) \times 10^{-13}$ s. The anti-particles $\bar{D}^0$ and $\bar{D}^*$ are also considered.

Meson	Composition	Mass [MeV]	Decay Length	Targeted Decay
K_s	$\frac{1}{\sqrt{2}}(d\bar{s} - s\bar{d})$	498	2.686 cm	$\pi^+\pi^-(69.20 \pm 0.05)\%$
D^0	$c\bar{u}$	1865	0.123 mm	$K^-\pi^+(3.947 \pm 0.030)\%$
D^*	$c\bar{u}$	2007	Prompt	$D^0\pi^0(64.7 \pm 0.9)\%$ and $D^0\gamma(35.3 \pm 0.9)\%$

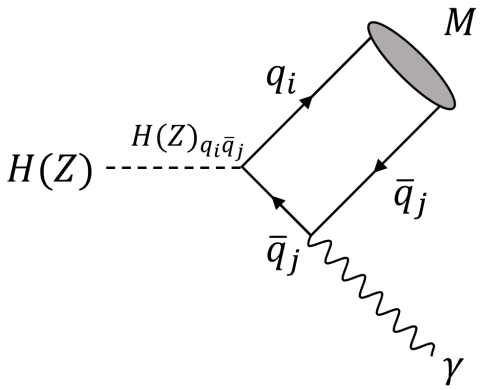


Figure 6.1: Feynman diagrams depicting the flavour-violating $H \to \mathcal{M}\gamma$ and $Z \to \mathcal{M}\gamma$ processes, where $\mathcal{M}$ is a flavoured meson. For Higgs boson decays, $\mathcal{M} = D^*$ or $\bar{D}^*$; for Z boson decays, $\mathcal{M} = D^0, \bar{D}^0$ or K_s. The indices i and j refer to the flavour of the quark, and $i \neq j$.

The three decays investigated in these searches each involve a displaced vertex, either through the decay of the D^0 in $H \to D^*\gamma$ and $Z \to D^0\gamma$ or the decay of the K_s in $Z \to K_s\gamma$. This provides a particularly distinct signature compared to the exclusive

decays in general, shown in Figure 6.2, as requirements on the vertex displacement can be used to reject prompt backgrounds which make up the vast majority of events at ATLAS. This signature, like other exclusive decays, includes a high-energy photon and a meson appearing approximately back-to-back in the detector following the decay of the H or Z boson, where there is a resonance in di-track mass to reconstruct the meson and in three-body mass to reconstruct the initial boson. As the mass difference between the D^0 and D^* is so small, 142 MeV, the additional π^0 or γ in the decay of the D^* is very soft and the majority of the energy goes to the D^0. This provides the opportunity to partially reconstruct the Higgs boson as the $D^0\,\gamma$ system, where the additional daughter particle is neglected, while still attaining a good mass resolution. This simplifies the search for the D^* decay as it allows it to share a common selection and background model with the $Z \to D^0\,\gamma$ search, and the reconstruction of a soft neutral particle is not required. The backgrounds in these searches are considered as a single inclusive source, and originate mostly from multi-jet and γ+jet events involving the production of the meson or a non-resonant di-track system near its mass.

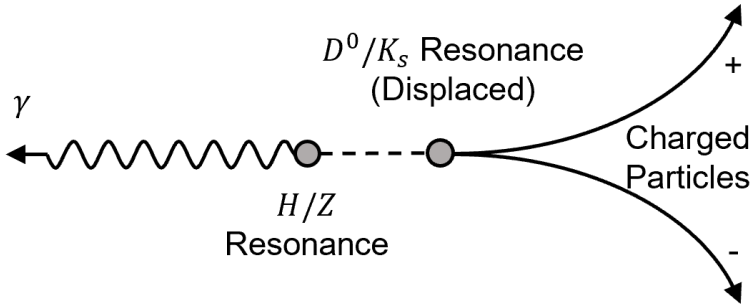


Figure 6.2: Experimental signature of the $H \to D^*\,\gamma$, $Z \to D^0\,\gamma$ and $Z \to K_s\,\gamma$ decays, where the displaced meson decays into a pair of charged particles.

This chapter discusses the ongoing development of the searches for the decays $H \to D^*\,\gamma$, $Z \to D^0\,\gamma$ (as well as the corresponding charge-conjugate decays $H \to \bar{D}^*\,\gamma$ and $Z \to \bar{D}^0\,\gamma$) and $Z \to K_s\,\gamma$, which use 135.2 fb^{-1} of ATLAS data collected at $\sqrt{s} = 13$ TeV. The LHCb experiment has searched for the decay $Z \to D^0\,\gamma$ using 2.0 fb^{-1} of data collected at $\sqrt{s} = 13$ TeV, yielding a 95% CL upper limit of 2.1×10^{-3} [98], but to the best of the author's knowledge there are no further previous constraints on these decays. Throughout this chapter, D^* collectively refers to the D^* and its anti-particle

$\bar{D}^*$, and D^0 collectively refers to the D^0 and its anti-particle $\bar{D}^0$, unless otherwise specified. Section 6.1.1 describes the data sample and event selection used in these searches, and Sections 6.2 and 6.3 describe the current treatment of the signal and background models, respectively. Section 6.4 describes the statistical approach used in these searches as well as the expected sensitivity based on blinded data.

6.1 Event Selection

This section describes the requirements imposed on data for them to be considered candidate events in the searches for $H \to D^* \gamma$, $Z \to D^0 \gamma$ and $Z \to K_s \gamma$. Similarly to the $H(Z) \to \mathcal{Q}\gamma$ event selection, these are based on data quality requirements and available triggers, as well as the geometric acceptance. Kinematic thresholds are also optimised to maximise the signal-to-background of the searches, and vertex requirements are imposed to exploit the displaced topology of the D^0 and K_s decays.

The requirements for the $H \to D^* \gamma$ and $Z \to D^0 \gamma$ searches are identical, as the additional π^0 or γ in the decay of the D^* is soft and the mass resolution of the Higgs boson does not deteriorate significantly if it is ignored as shown later in Section 5.2. The requirements for the $Z \to K_s \gamma$ search are similar to the others, but different triggers are used and the optimised kinematic and vertex significance thresholds differ slightly.

6.1.1 Data Sample and Triggers

The ATLAS proton–proton collision dataset collected between 2016–2018 at $\sqrt{s} = 13$ TeV is considered in these searches, with stable beam conditions and relevant detector systems functional [103]. The 2015 dataset is not included as the triggers described below were not available throughout this period. Data events are required to pass the GRL requirements described in Section 3.1.1. These decays searches also use dedicated triggers, but unlike the combined photon and muon triggers used for the $\mathcal{Q}\gamma$ final states in Chapter 5, these triggers are based on adapted τ-lepton trigger algorithms at the software-based HLT. The topology of the decays $D^0 \to K^-\pi^+$ and $K_s \to \pi^+\pi^-$ are similar to the topology of the τ-lepton decays, except these have two-pronged decays whereas the τ-lepton decays

are either one- or three-pronged. This was exploited to develop combined photon and 'τ-object' triggers dedicated to these searches, which are also used in the searches for other exclusive $\mathcal{M}\,\gamma$ decays with hadronically decaying mesons, such as $H(Z) \to (\phi, \rho)\,\gamma$ [91, 93]. On top of the typical kinematic requirements on the τ-object p_{T}, several additional variables are used to define the selection in the τ-object leg of these dedicated triggers. The standard τ-object selection variables used in the triggers include the number of tracks associated with the τ-object, the p_{T} of the leading track, and `EMPOverTrkSysPMax` which is the ratio of the p_{T} of the EM cluster associated with the τ-object over the total p_{T} of the tracks associated with the τ-object. Two further variables are defined for background reduction in the exclusive decay triggers: the invariant mass of the τ-object tracks, so that events near the mass of the meson are selected, and the invariant mass of the τ-object and photon system, to reduce combinatoric backgrounds. Applying optimised requirements on these two variables allowed the p_{T} thresholds for the τ-object and photon legs to be reduced as much as possible to increase the signal acceptance of the dedicated triggers.

In particular for the $D^*\,\gamma$ and $D^0\,\gamma$ searches, throughout the 2016 data taking period a trigger requiring a 'medium' identification photon [196] with $p_{\mathrm{T}}^{\gamma} > 35$ GeV, and a τ-object with a $p_{\mathrm{T}}^{\tau} > 25$ GeV was available. Throughout the 2017–2018 data taking period a trigger requiring a 'medium' identification photon with a looser selection of $p_{\mathrm{T}}^{\gamma} > 25$ GeV, a τ-object with $p_{\mathrm{T}}^{\tau} > 25$ GeV, and an invariant mass of the photon+τ-object system of $m_{\tau\gamma} > 50$ GeV was available. Each of these triggers also required the τ-object to have exactly two tracks associated with it which have an invariant mass 1800 MeV $< m_{K\pi} <$ 1930 MeV under a kaon-pion mass hypothesis,[12] a lead-track $p_{\mathrm{T}} > 15$ GeV, and `EMPOverTrkSysPMax` < 1. Analogous triggers for the 2016 and the 2017–2018 run periods were available for $K_s\,\gamma$, with the difference that the two tracks associated with the τ-object were required to have an invariant mass 460 MeV $< m_{\pi^+\pi^-} <$ 538 MeV under a dipion mass hypothesis. The available triggers are summarised in Table 6.2 alongside their integrated luminosities and run periods, and the total integrated luminosity of these searches is 135.2 fb^{-1}. In these searches, data must meet the loose requirements of the

[12] Both combinations are tried for the kaon-pion mass hypothesis, and the one closer to the mass of the D^0 is chosen.

dedicated HDBS2 derivation, which requires all tracks to have $p_{\mathrm{T}} > 5$ GeV, and a fit of the di-track vertex [197] must have $\chi^2 < 200$. The tracks must also be oppositely charged.

Table 6.2: The dedicated triggers used to select candidate $H \to D^* \gamma$, $Z \to D^0 \gamma$ and $Z \to K_s \gamma$ events from 2016–2018. GRLs are applied in the calculation of the integrated luminosities.

Period	Trigger	Luminosity (fb^{-1})
$H \to D^* \gamma$ and $Z \to D^0 \gamma$		
2016	HLT_g35_medium_tau25_kaonpi2_tracktwo_L1TAU12	32.4
2017–2018	HLT_g25_medium_L1EM24VHI_tau25_kaonpi2_tracktwo_50mVis10000	102.8
$H(Z) \to K_s \gamma$		
2016	HLT_g35_medium_tau25_dipion2_tracktwo_L1TAU12	32.4
2017–2018	HLT_g25_medium_L1EM24VHI_tau25_dipion2_tracktwo_50mVis10000	102.8

6.1.2 Selection Requirements

Events which pass the trigger, data quality requirements, and the HDBS2 derivation must satisfy several additional criteria to be selected as candidate events. Reconstructed tracks must satisfy the 'loose' selection working point [124], and have $|\eta| < 2.5$. There must be at least one pair of oppositely charged tracks in the event, where the leading track has $p_{\mathrm{T}} > 20$ GeV and the subleading track has $p_{\mathrm{T}} > 5$ GeV. The invariant mass of the di-track system must satisfy 1800 MeV $< m_{K\pi} <$ 1930 MeV under the kaon-pi hypothesis for D^0 candidates, and 460 MeV $< m_{\pi^+\pi^-} <$ 538 MeV under the dipion hypothesis for K_s candidates.

Several isolation and vertex requirements are also imposed on the di-track system. The variable ptcone20 is defined, which is the sum of the p_{T} of all the ID tracks within $\Delta R < 0.2$ of the leading track, excluding the p_{T} of the leading track itself and the subleading track if it lies within this cone. Only tracks compatible with originating from the primary vertex are considered. Candidate D^0 and K_s mesons must satisfy ptcone20 $< 10\%$ of $p_{\mathrm{T}}^{\mathcal{M}}$, where $\mathcal{M}$ is the meson candidate. To reject backgrounds originating from prompt decays, the transverse decay length significance must satisfy $|L_{xy}/\sigma_{L_{xy}}| > 3$ for the $H \to D^* \gamma$ and $Z \to D^0 \gamma$ searches, and must satisfy $|L_{xy}/\sigma_{L_{xy}}| > 5$ for the $Z \to K_s \gamma$ search. The transverse momentum of the di-track system for D^0 and K_s candidates must respectively satisfy $p_{\mathrm{T}}^{D^0} > 39$ GeV and $p_{\mathrm{T}}^{K_s} > 38$ GeV.

The requirements for the photon candidate are identical to those for the $H(Z) \to \mathcal{Q}\gamma$

searches in Section 5.1.2. To summarise, photons must pass the 'tight' identification criteria, have pseudorapidity $|\eta_\gamma| < 2.37$, excluding $1.37 < |\eta_\gamma| < 1.52$, and have a transverse momentum $p_{\mathrm{T}}^{\gamma} > 35$ GeV. The `FixedCutTight` photon isolation working point is imposed, which requires a track isolation of `ptcone20` $< 5\%$ of p_{T}^{γ} and a calorimeter isolation of `topoetcone40` $<$ (2.45 GeV + 2.2% of p_{T}^{γ} [GeV]).

Candidate photons and mesons are combined to reconstruct the boson candidates, where the additional π^0 or γ from the decay of the D^* are neglected in the search for $H \to D^* \gamma$, such that the $D^0 \gamma$ system is considered as the Higgs boson candidate. Good mass resolution is achieved for the Higgs boson candidate, despite its partial reconstruction, as shown in Section 6.2. To suppress events where the meson and the photon candidates are collimated, combinations must satisfy $|\Delta\phi(\mathcal{M}, \gamma)| > \pi/2$ similarly to the $H(Z) \to \mathcal{Q}\gamma$ searches in Section 5.1.2. Events which meet each of these requirements are considered candidate events for either the $H(Z) \to D^*(D^0)\gamma$ or the $Z \to K_s \gamma$ searches. As these analyses are still in development, events that have an invariant mass near the expected Higgs and Z boson resonances are blinded. For the Z boson in the $Z \to D^0 \gamma$ and the $Z \to K_s \gamma$ searches this window is 86 GeV $< m_{\mathcal{M}\gamma} <$ 96 GeV. For the Higgs boson in the $H \to D^* \gamma$ search this window is 116 GeV $< m_{\mathcal{M}\gamma} <$ 126 GeV, which is not centred around $m_H = 125$ GeV to take into account the shift in mass caused by the missing soft π^0 or γ in the decay of the D^*.

6.2 Signal Modelling

The signal model in these searches is produced by simulating signal events, imposing the event selection described in Section 6.1.1, and fitting the resulting distributions in three-body mass with analytical functions to extract shapes for use in the likelihood fit in Section 6.4. This section describes the procedure used to generate signal events and produce the analytical shapes, including details on signal resolution and acceptance. Systematic uncertainties on the signal shape and normalisation have not yet been taken into account in these searches, however based on previous exclusive decays searches these are expected to have a small effect on the expected limits.

6.2.1 Event Generation and Simulation

Similarly to the searches for $H \to \mathcal{Q}\gamma$, signal samples for $H \to D^*\gamma$ are separated according to the production mode of the Higgs boson. Samples were produced for the ggH, VBF, ZH, WH, and $t\bar{t}H$ (separated into `dilep`, `semilep` and `allhad` categories depending on the decays of the t-quark pair) production modes of the Higgs boson, and the $b\bar{b}H$ contribution is again taken into account in the normalisation of the ggH sample. Unlike in the searches for $H \to \mathcal{Q}\gamma$, in this search the WH mechanism samples are separated according to the charge of the $W^{\pm}$ boson, into W^+H and W^-H samples. The production of $Z \to D^0\gamma$ and $Z \to K_s\gamma$ decays are modelled in the $q\bar{q} \to Z$ production mode; contribution by the $gg \to Z$ production mode is taken into account in the normalisation of each sample. The subsequent decays of each of the D^*, D^0 and K_s mesons are included in the generated events and the searches for each decay channel have their own set of samples. The D^* and D^0 samples also include equal contributions from the equivalent anti-particle decays, $\bar{D}^*$ and $\bar{D}^0$.

The Powheg Box v2 MC event generator [199–203] was used to model the ggH and VBF Higgs boson production mechanisms and the Z boson production, calculated up to NLO in α_s. This was interfaced with Pythia 8.244 [141, 142], which used a set of tuned parameters called the AZNLO tune [204] to model the parton shower, hadronisation, and underlying event, and the CTEQ6L1 parton distribution functions [195]. The Powheg Box v2 and Pythia 8.244 combination was also used to model the three VH production mechanisms (ZH, W^+H, W^-H), but with the A14 event tune [194] for hadronisation and the underlying event, and the NNPDF2.3lo parton distribution functions [205]. The MadGraph5_aMC@NLO 2.2.2 [206] event generator was used to model the three $t\bar{t}H$ samples, using Pythia8.244 to model the parton shower with the same event tune and parton distribution functions as the VH production mechanisms. The generator configuration used to generate each sample is summarised in Table 6.3. In all cases the subsequent decays of the H and Z bosons to $\mathcal{M}\gamma$ are modelled as a cascade of two-body decays. The resulting simulated events are passed through the detailed full-sim Geant4 simulation of the ATLAS detector [144, 145], and processed with the

same software used to reconstruct and select the data, including the use of the HDBS2 derivation. Separate samples were produced for the 2016, 2017, and 2018 run periods and each sample is normalised according to the integrated luminosity of the corresponding run period: 32.4 fb^{-1} for 2016, 44.3 fb^{-1} for 2017, and 58.5 fb^{-1} for 2018.

Table 6.3: The Monte Carlo generator configuration used to generate of the Higgs and Z boson signal samples. In this table PDF is an abbreviation of parton distribution function.

Production Mode	Generator	Parton Showering	Event Tune	PDF
$H : ggH$	Powheg Box v2	Pythia8.244	AZNLO	CTEQ6L1
H : VBF	Powheg Box v2	Pythia8.244	AZNLO	CTEQ6L1
$H : ZH$	Powheg Box v2	Pythia8.244	A14	NNPDF2.3lo
$H : W^+H$	Powheg Box v2	Pythia8.244	A14	NNPDF2.3lo
$H : W^-H$	Powheg Box v2	Pythia8.244	A14	NNPDF2.3lo
$H : t\bar{t}H_{\text{allhad}}$	Madgraph5_aMC@NLO	Pythia8.244	A14	NNPDF2.3lo
$H : t\bar{t}H_{\text{semilep}}$	Madgraph5_aMC@NLO	Pythia8.244	A14	NNPDF2.3lo
$H : t\bar{t}H_{\text{dilep}}$	Madgraph5_aMC@NLO	Pythia8.244	A14	NNPDF2.3lo
$Z : q\bar{q}$	Powheg Box v2	Pythia8.244	AZNLO	CTEQ6L1

In total 779k $H \to D^*\gamma$, 100k $Z \to D^0\gamma$, and 499k $Z \to K_s\gamma$ signal events were generated to use in these searches. The number of events generated for each production mechanism and each run period is summarised in Table 6.4. In general the statistics prioritise years with higher luminosity, and production mechanisms with the highest cross section for the H boson decays.

Table 6.4: The number of events generated per production mechanism for the flavour-violating decay samples, split by MC period.

	Number of Events			
Production Mode	2016	2017	2018	Total
$H \to D^*\gamma : ggH$	39k	50k	90k	179k
$H \to D^*\gamma$: VBF	40k	50k	90k	180k
$H \to D^*\gamma : ZH, W^+H, W^-H$	20k	20k	30k	70k
$H \to D^*\gamma : ttH_{\text{allhad,semilep,dilep}}$	20k	20k	30k	70k
$H \to D^*\gamma$: Total	199k	220k	360k	779k
$Z \to D^0\gamma : q\bar{q}$	20k	30k	50k	100k
$Z \to K_s\gamma : q\bar{q}$	99k	150k	250k	499k

The Higgs and Z boson signal samples are normalised to the same production cross section values from Refs. [30, 85, 86] that were used for the $H(Z) \to \mathcal{Q}, \gamma$ analyses, withthe exception that the WH cross section is split into separate values for W^+H and W^-H. These two cross sections are also calculated at NNLO in QCD with NLO electroweak corrections [214, 215]. The details of the production cross sections assumed

in this analysis are summarised in Table 6.5. The branching ratios for the t-quark decays from the Review of Particle Physics [26] are used here as well, summarised in Table 5.8 in Section 5.2.

Table 6.5: The various cross sections used in sample normalisation. The uncertainty quoted for each H production mode is a sum in quadrature of the different sources of uncertainty, where the average value is taken for a given source of uncertainty if the positive and negative values differ. The total H cross section uncertainty is taken from the sum of the total uncertainties of each production mode, weighted according to its cross section. Values are from Refs. [30, 85, 86].

			Order of Calculation	
Production Mode	Cross Section [pb]	Uncertainty [%]	QCD	EW
$H : ggH$	48.61	6.26%	N^{3}LO	NLO
H : VBF	3.766	2.13%	NNLO	NLO
$H : ZH$	0.880	3.50%	NNLO	NLO
$H : W^+H$	0.831	1.94%	NNLO	NLO
$H : W^-H$	0.527	2.12%	NNLO	NLO
$H : ttH$	0.5065	9.32%	NLO	NLO
$H : bbH$	0.4863	22.0%	NNLO+NLO	–
H : Total	55.6068	6.00%	–	–
Z : Inclusive	58858.0	2.9%	Data Measurement	

The signal samples are produced assuming no polarisation of the boson decay products, which is true for the $Z \to D^0\,\gamma$ and $Z \to K_s\,\gamma$, following the method in Ref. [217]. However the decay products in $H \to D^*\,\gamma$ are polarised. The effect of this polarisation on the kinematic distributions of the decay products in each event is taken into account by reweighting the events as $\frac{3}{2}(1-\cos^2\theta')$. Further scale factors are applied on an event-by-event basis to account for differences between data and simulation in the trigger efficiency, photon and track reconstruction, and to account for pile-up. Pile-up was modelled by overlaying each event with inelastic pp events generated with Pythia8.186, using the A3 tune and NNPDF2.3lo parton distribution functions [219].

6.2.2 Signal Acceptance and Efficiency

Figure 6.3 shows the generator-level p_T distributions of the two tracks and the photon in each of the Higgs and Z boson signal decays, before and after implementing the full event selection of the analysis in Section 6.1.1. This illustrates the smaller p_T phase space of the Z decays compared to the H decay, which leads to a smaller acceptance for the Z

boson decay channels. The total signal efficiency for $H \to D^* \gamma$ is approximately 9%, for $Z \to D^0 \gamma$ is 4%, and for $Z \to K_s \gamma$ is 0.3%. The particularly small acceptance for the K_s decay channel is because many of the K_s mesons do not decay inside the beampipe due to their large lifetimes.

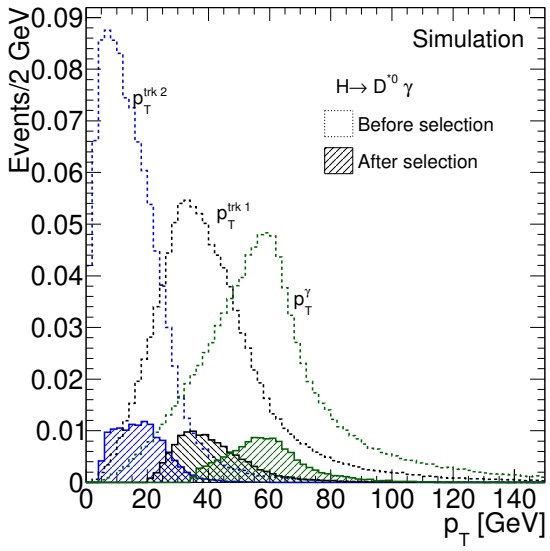
Similarly to the $Z \to \mathcal{Q} \gamma$ decays, the large natural width of the Z boson leads to a turn-on curve in efficiency of the $Z \to (D^0, K_s) \gamma$ signals versus Z boson mass. This is shown in Figure 6.4. This efficiency is modelled as an error function, which has a width parameter to model the slope of the turn-on curve and a mean parameter to model the central location in mass for the turn-on curve.

6.2.3 Signal Shape and Resolution

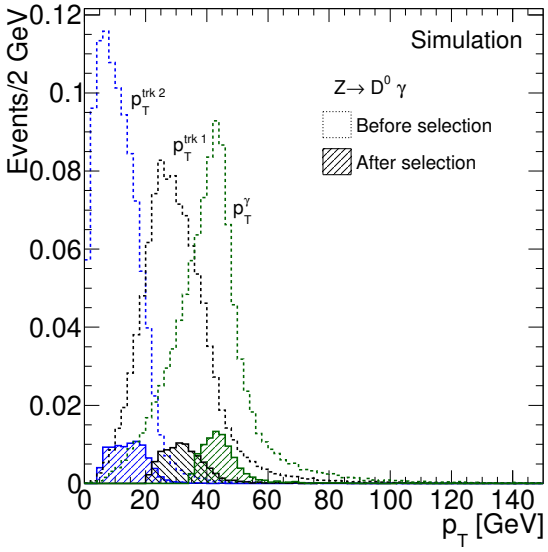
The $m_{K\pi\gamma}$ and $m_{\pi^+\pi^-\gamma}$ distributions are modelled using fits to the simulated events, shown in Figure 6.5. The resolution of the Higgs boson mass in $H \to D^* \gamma$ is 2.2% despite its partial reconstruction, which shifts the mean from 125 GeV to 121 GeV. The shape of the Higgs boson signal is modelled with the sum of two Gaussian distributions, ech of which have a σ parameter to describe the width and a μ parameter to describe the central mass value. An f parameter is used to describe the relative contribution between the broader and narrower Gaussian distributions. The resolution of the Z boson mass is 2.0% for $Z \to D^0 \gamma$ and 2.4% for $Z \to K_s \gamma$. The shapes of the Z boson signals are modelled with a Voigtian distribution multiplied by an efficiency factor, shown by the red error functions in Figure 5.4, to take into account the turn-on in signal efficiency with Z boson mass. As for the Higgs boson decay, the Gaussian components of the Voigtian functions also have σ and μ parameters. The width of the Breit-Wigner components of the Voigtian functions are fixed to the natural width of the Z boson and the mean is set to be the same as for the Gaussian component.

6.3 Background Modelling

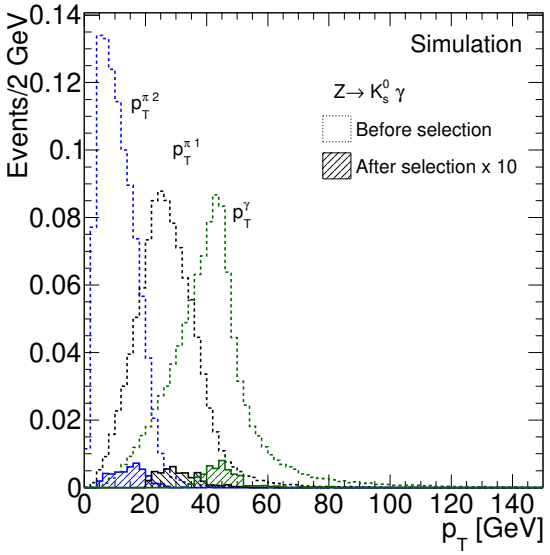
The main sources of background in the $H \to D^* \gamma$ and $Z \to D^0 \gamma$ searches form a non-resonant contribution to the three-body mass distribution, $m_{K\pi\gamma}$, and come from



(a) $H \to D^{*0}\,\gamma$

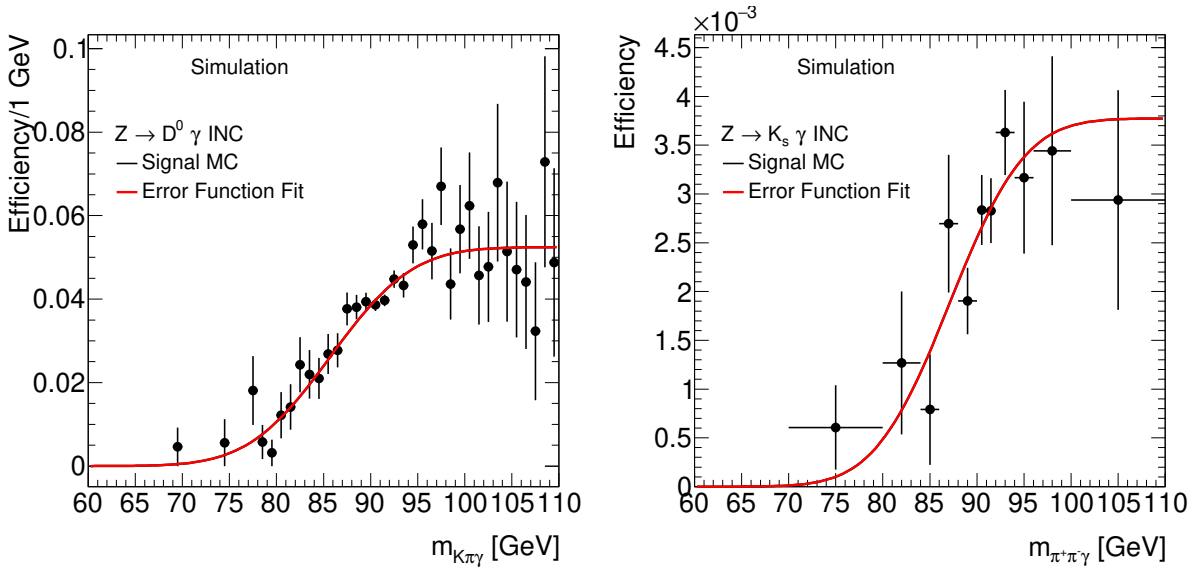


(b) $Z \to D^{0}\,\gamma$



(c) $Z \to K^{0}_{s}\,\gamma$

Figure 6.3: Generator-level transverse momentum (p_{T}) distributions of the photon and of the tracks, ordered in p_{T}, for (a) $H \to D^{*0}\,\gamma$, (b) $Z \to D^{0}\,\gamma$, and (c) $Z \to K_s\,\gamma$ simulated signal events. The leading track candidate is labelled $p_{\mathrm{T}}^{\mathrm{trk1}}$ (black), the subleading candidate $p_{\mathrm{T}}^{\mathrm{trk2}}$ (blue), and the photon candidate p_{T}^{γ} (green). For $Z \to K_s\,\gamma$ the tracks are both pions and are labelled $p_{\mathrm{T}}^{\pi 1}$ and $p_{\mathrm{T}}^{\pi 2}$. The 'before selecton' distributions, denoted with dashed lines and clear fills, show the events at generator level which fall within the analysis geometric acceptance (both tracks are required to have $|\eta^{\mu}| < 2.5$, while the photon is required to have $|\eta^{\gamma}| < 2.37$, excluding the region $1.37 < |\eta^{\gamma}| < 1.52$), and are each normalised to unity. The 'after selection' distributions, denoted with solid lines and hatched fills, show the fraction of these events which pass the full analysis event selection described in Section 6.1.1. The relative difference between the two sets of distributions corresponds to the effects of reconstruction, identification, trigger, isolation, and event selection efficiencies including the kinematic requirements.

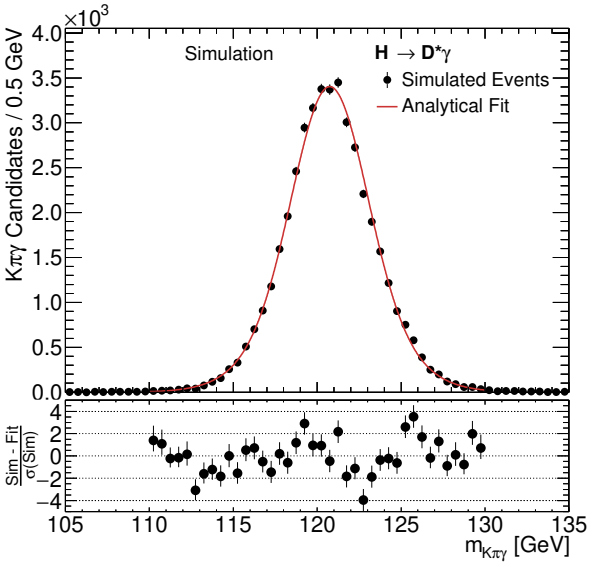


(a) $Z \to D^0\gamma$ (b) $Z \to K_s\gamma$

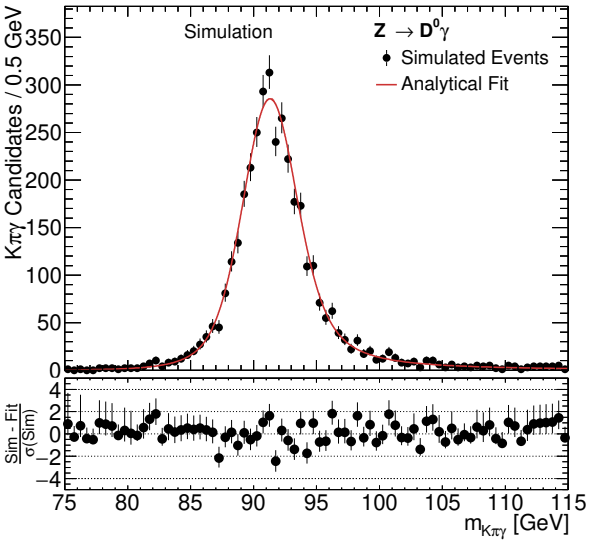
Figure 6.4: The Z boson mass-dependent efficiency function derived from the simulated $Z \to D^0\gamma$ and $Z \to K_s\gamma$ signals.

events involving inclusive multijet or photon + jet production, where a $D^0 \to K^-\pi^+$ (or $\bar{D}^0 \to K^+\pi^-$) candidate is reconstructed from the combination of two tracks associated with a jet: this can be a genuine D^0 state or a non-resonant di-track combination whose mass falls within the D^0 window. The photon candidate may be genuine, as in the γ + jet production, or a jet misidentified as a single photon, as in the multi-jet production. Isolation and vertex requirements help suppress these backgrounds, but as the production cross sections of the underlying mechanisms are very large, the contribution to the background remains significant. The sources of background in the search for $Z \to K_s\,\gamma$ are very similar, except a $K_s \to \pi^+\pi^-$ candidate is reconstructed from the combination of two tracks associated with a jet.

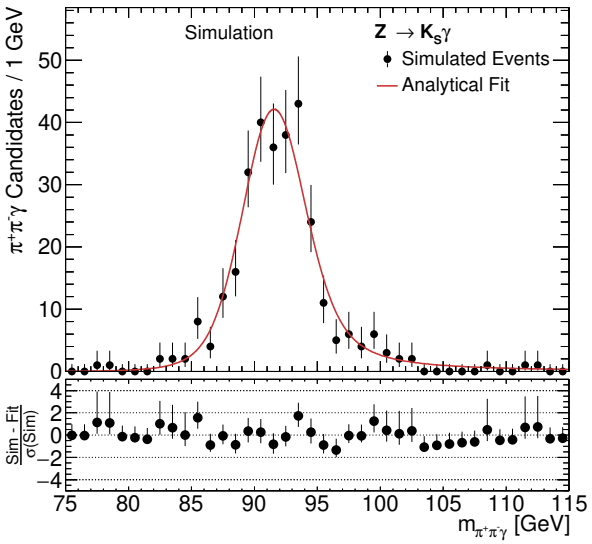
The shape of each background is modelled inclusively using a non-parametric data-driven sampling approach discussed in Ref. [229] and used in several previous exclusive decay searches [90–94]; this is done as the complicated nature of the processes involved in the background are difficult to model accurately with simulation or through direct fits of parametric models. The model procedure is analagous to the inclusive model three-body mass distribution for the $\mathcal{Q}\,\gamma$ searches described in Section 5.4. In this analysis the



(a) $H \to D^*\gamma$



(b) $Z \to D^0\gamma$



(c) $Z \to K_s\gamma$

Figure 6.5: The $m_{K\pi\gamma}$ and $m_{\pi^+\pi^-\gamma}$ distribution models for the Higgs and Z bosons in the decays $H \to D^*\gamma$, $Z \to D^0\gamma$ and $Z \to K_s\gamma$ respectively.

background model is shared by the $H \to D^* \gamma$ and $Z \to D^0 \gamma$ searches as both require the selection of a D^0 candidate and a high energy photon candidate to reconstruct the boson candidate. The normalisation of each background is extracted directly from the data.

6.3.1 Generation and Validation Region Selection Criteria

The generation of the non-parametric data-driven background model relies on the definition of a more relaxed event selection compared to the signal region (SR) requirements defined in Section 6.1.2, with the same motivations as for the $\mathcal{Q}\gamma$ inclusive background model. The generation region (GR) selection applies the SR selection defined in Section 6.1.1 but with three changes to loosen the selection. The first is that the threshold on the transverse momentum of the meson candidate is reduced to $p_{\mathrm{T}}^{\mathcal{M}} > 25$ GeV. The second is that the meson candidate isolation requirement is removed entirely. The third is that the photon isolation requirements are loosened to a threshold of `ptcone20` $< 20\%$ of p_{T}^{γ} for the track isolation, and a threshold of `topoetcone40` < 2.45 GeV$+40\%$ of p_{T}^{γ} [GeV] for the calorimeter isolation.

Further validation regions (VRs) are defined to assess model performance when each of the three tighter SR requirements are applied to the generated model in turn. VR1 is defined as the GR selection with the variable $p_{\mathrm{T}}^{\mathcal{M}}$ threshold from the SR, VR2 is defined as the GR selection with the tight meson isolation requirements from the SR, and VR3 is defined as the GR selection with the tight photon isolation requirements from the SR. Each of the selection regions is summarised in Table 6.6.

6.3.2 Non-Parametric Data-Driven Method

The application of the GR selection criteria yields approximately 15.8k events for use in the model generation for the $H \to D^* \gamma$ and $Z \to K_s \gamma$ searches, and approximately 2.7k events for use in the search for $Z \to K_s \gamma$. As in the $\mathcal{Q}\gamma$ searches, PDFs are constructed from the data to describe the kinematics of the meson and photon candidates, the relevant isolation variables, and the important correlations between each variable. These PDFs

Table 6.6: A summary of the selection regions used in the analysis for the generation of the inclusive background model. The term 'Full' indicates the corresponding requirement applied in the SR, and discussed in Section 6.1.2. The Relaxed photon isolation requires `ptcone20` $< 20\%$ of p_{T}^{γ}, and `topoetcone40` $<$ (2.45 GeV + 40% of p_{T}^{γ} [GeV]). Values in brackets denote the $p_{\mathrm{T}}^{\mathcal{M}}$ threshold used in the K_s search, otherwise they are selections used in the D^* and D^0 searches.

Region		$p_{\mathrm{T}}^{\mathcal{M}}$	Photon Isolation	$\mathcal{M}$ Isolation
Generation Region	(GR)	> 25 GeV	Relaxed	None
Validation Region 1	(VR1)	$> 39(38)$ GeV	Relaxed	None
Validation Region 2	(VR2)	> 25 GeV	Relaxed	Full
Validation Region 3	(VR3)	> 25 GeV	Full	None
Signal Region	(SR)	$> 39(38)$ GeV	Full	Full

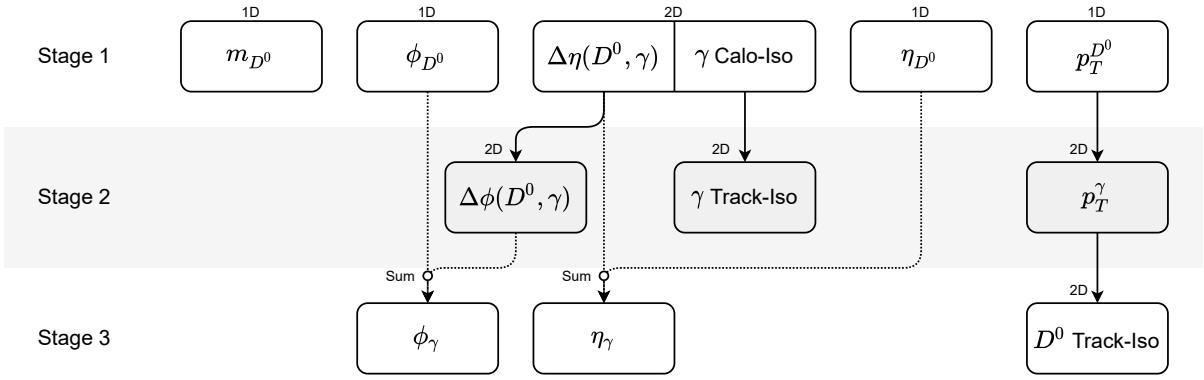
are sampled using the ancestral sampling techniques shown in Figure 6.6 for the D^0 and K_s searches to generate pseudocandidate events. Currently the sampling schemes for each background model are the same, and use the same scheme as for the $H(Z) \to \rho\gamma$ searches [93] as a starting point. The sampling scheme is as follows, where $\mathcal{M}$ collectively refers to the meson candidates D^0 and K_s:

1. Each of the $\mathcal{M}$ candidate four-momentum variables, $m_{\mathcal{M}}$, $\phi_{\mathcal{M}}$, $\eta_{\mathcal{M}}$, $p_{\mathrm{T}}^{\mathcal{M}}$, are sampled from independent one-dimensional (1D) PDFs, and values for the photon calorimeter isolation (γ calo-iso) and the separation in pseudorapidity between the $\mathcal{M}$ and photon candidates, $\Delta\eta(\mathcal{M},\gamma)$, are simultaneously sampled from a two-dimensional (2D) PDF.

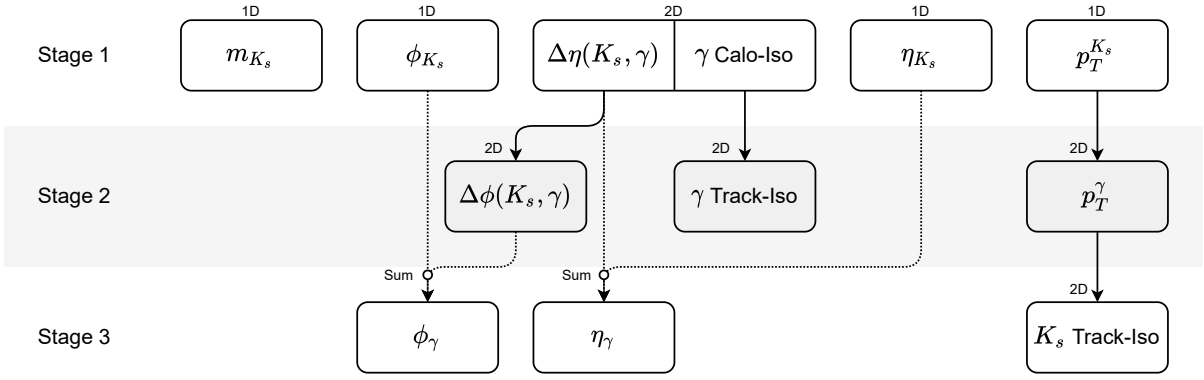
2. A value of the separation in ϕ between the $\mathcal{M}$ and photon candidates, $\Delta\phi(\mathcal{M},\gamma)$, is sampled from a 2D PDF using the previously sampled value of $\Delta\eta(\mathcal{M},\gamma)$ as an input, a value of the photon track isolation (γ track-iso) is sampled from a 2D PDF using the generated γ calo-iso variable as an input, and a value of p_{T}^{γ} is sampled from a 2D PDF using the generated $p_{\mathrm{T}}^{\mathcal{M}}$ as an input.

3. The ϕ_γ and η_γ variables are calculated from $\phi_{\mathcal{M}}$, $\phi_{\mathcal{M}}$, $\Delta\phi(\mathcal{M},\gamma)$ and $\Delta\eta(\mathcal{M},\gamma)$, and the $\mathcal{M}$ di-track isolation variable ($\mathcal{M}$ track-iso) is sampled from a 2D PDF using p_{T}^{γ} as an input.

The specific sampling schemes used for each background model are currently being optimised, however the correlations between variables in data and in the pseudocandidate



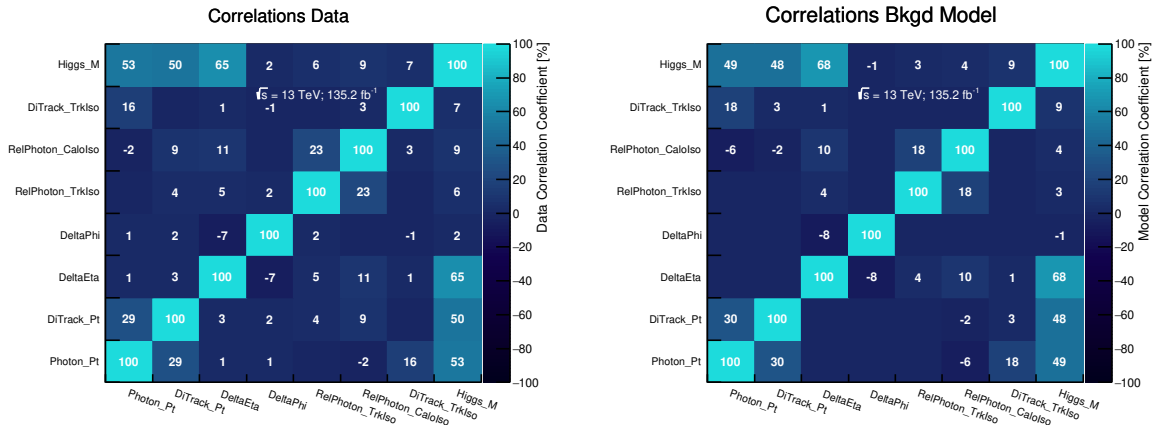
(a) $D^0\,\gamma$ Sampling Scheme



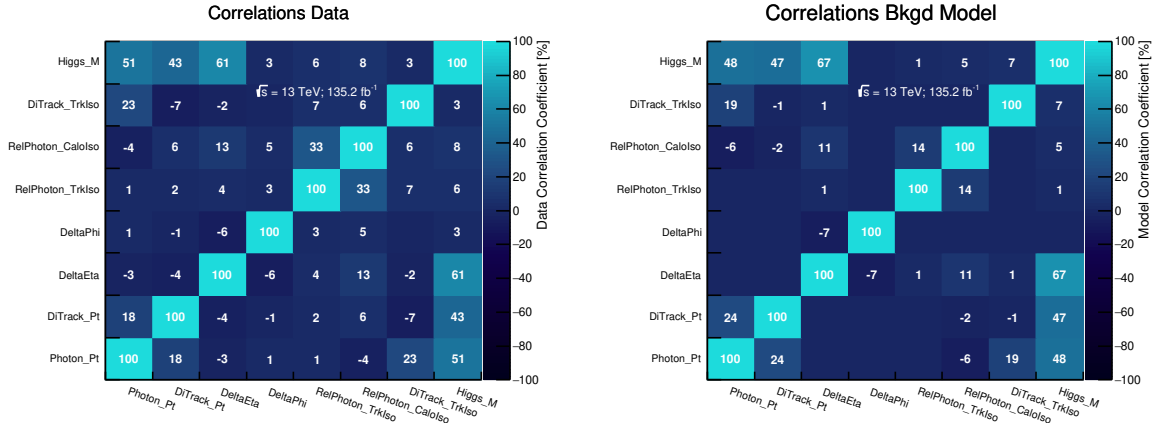
(b) $K_s\,\gamma$ Sampling Scheme

Figure 6.6: Sampling scheme used in the non-parametric data-driven model (a) for $H \to D^*\,\gamma$ and $Z \to D^0\,\gamma$, and (b) for $Z \to K_s\,\gamma$. The labels 1D and 2D refer to the dimensionality of the PDFs used to draw the adjacent variables. When two variables share a border this means that the values are sampled simultaneously from a combined PDF. Arrows leading into variables in Stages 2 and 3 mean that the variable is drawn from a PDF described in bins of the input variable. Vertices labelled Sum mean that the output variable, denoted by the arrow leading out of the vertex, is calculated as a sum of the input variables, denoted by the lines leading in to the vertex.

events in Figure 6.7 in general match quite well due to the robustness of the $\rho\,\gamma$ model procedure. Large samples of 1M pseudocandidate events each were generated for the D^0 and K_s background models, and the three-body mass distributions were reconstrructed from the pseudo meson- and photon-candidate four-momenta. The resulting $m_{K\pi\gamma}$ and $m_{\pi^+\pi^-\gamma}$ distributions in the GR are shown in Figure 6.8 which show a good match between data and the model as expected. Similarly the resulting three-body mass distributions in each of the VRs are shown in Figure 6.9 where in general there is good agreement between data and prediction.



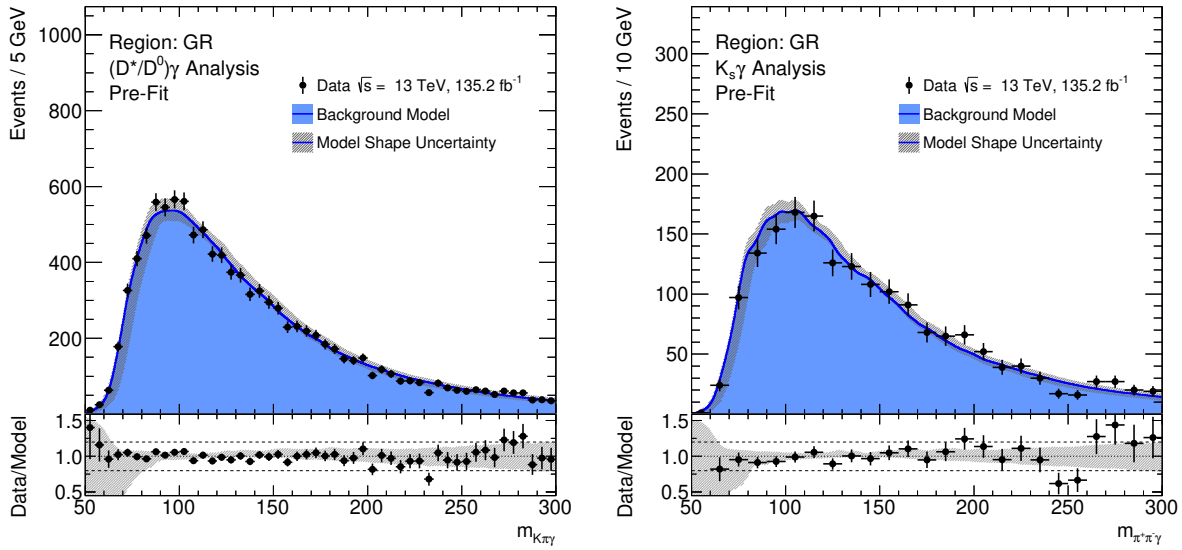
(a) $D^0\,\gamma$ Correlations



(b) $K_s\,\gamma$ Correlations

Figure 6.7: Linear correlations between variables used in the background modelling for (a) the D^0 analyses and (b) the K_s analysis. The distribution for the data is in the left panel and for the pseudocandidate events is in the right panel. These correlations are indicative of strength of the correlation between variables. It should be noted that 'Higgs_M' refers to the three-body mass used to reconstruct the boson candidates. Bins are left unlabelled if the correlation between the two variables is smaller than 1%.

The model PDFs used in the maximum-likelihood fits to the data in the signal region are



(a) $D^0\,\gamma$ GR

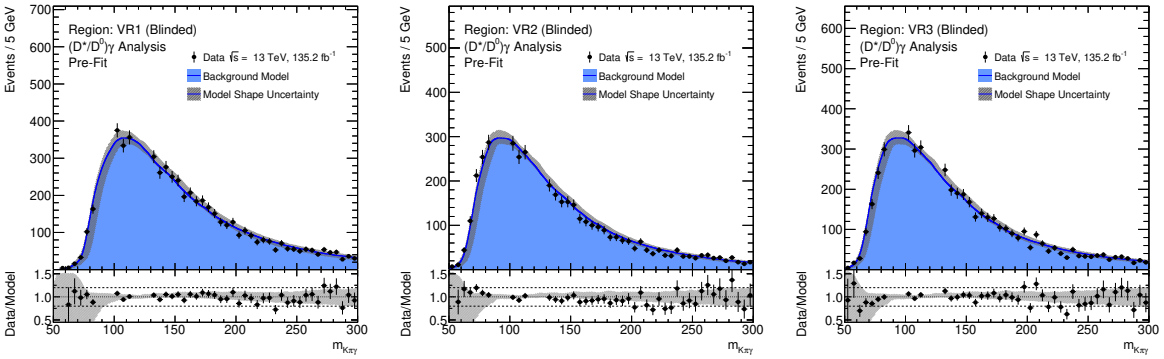
(b) $K_s\,\gamma$ GR

Figure 6.8: The three-body mass distribution in the GR of (a) $m_{K\pi\gamma}$ for the $H \to D^*\,\gamma$ and $Z \to D^0\,\gamma$ searches, and of (b) $m_{\pi^+\pi^-\gamma}$ for the $Z \to K_s\,\gamma$ search. The background model is normalised to the total number of observed events in the region shown, and the model shapes are set to the nominal template.

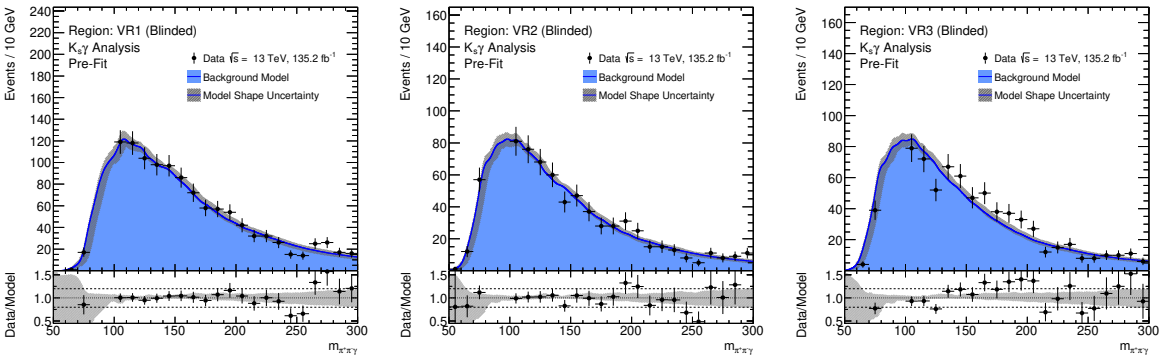
shown in Figure 6.10, obtained from applying the SR requirements to the pseudocandidate events and smoothing the resulting distributions with KDE. The smoothing successfully retains the shape of the background distribution whilst reducing the effects of statistical fluctuations.

6.3.3 Systematic Uncertainties

Three approximately orthogonal shape variations are derived to allow the background model to adapt to the data in the SR. The shape variations are currently generated using approaches identical to the variations defined for the $\mathcal{Q}\,\gamma$ inclusive background in Section 5.4.4, and are called the p_{T}^{γ}`-shift`, $\Delta\phi(\mathcal{M},\gamma)$`-distortion`, and `mass-tilt` variations. The $\Delta\phi(\mathcal{M},\gamma)$`-distortion` variation is analogous to the $\Delta\phi(\mathcal{Q},\gamma)$`-distortion` variation in the $\mathcal{Q}\,\gamma$ searches. The effect of each shape variation is demonstrated in Figure 6.11. Each variation is implemented through the use of a shape morphing technique [230] and has a corresponding nuisance parameter in the maximum-likelihood fit to the signal region which is constrained by the data.

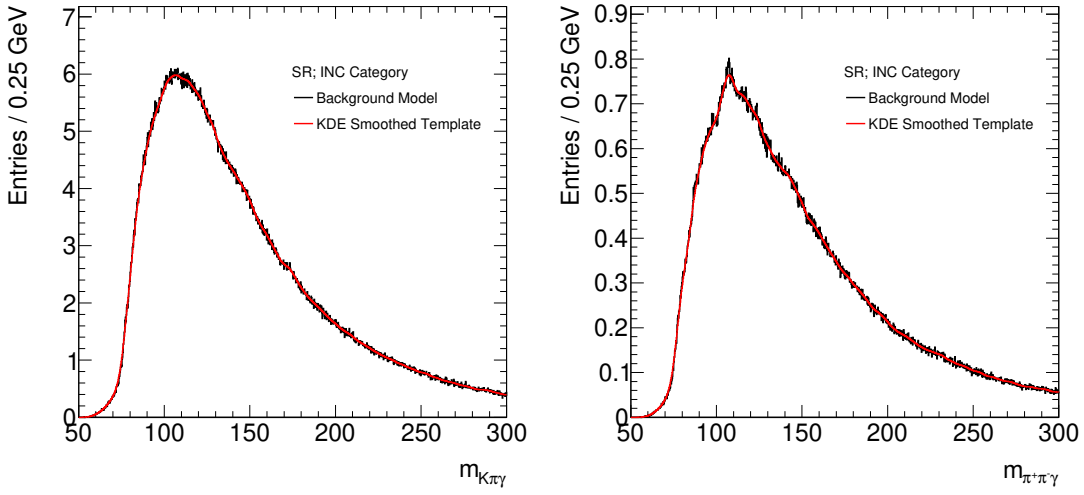


(a) $D^0\,\gamma$ VR1 (b) $D^0\,\gamma$ VR2 (c) $D^0\,\gamma$ VR3



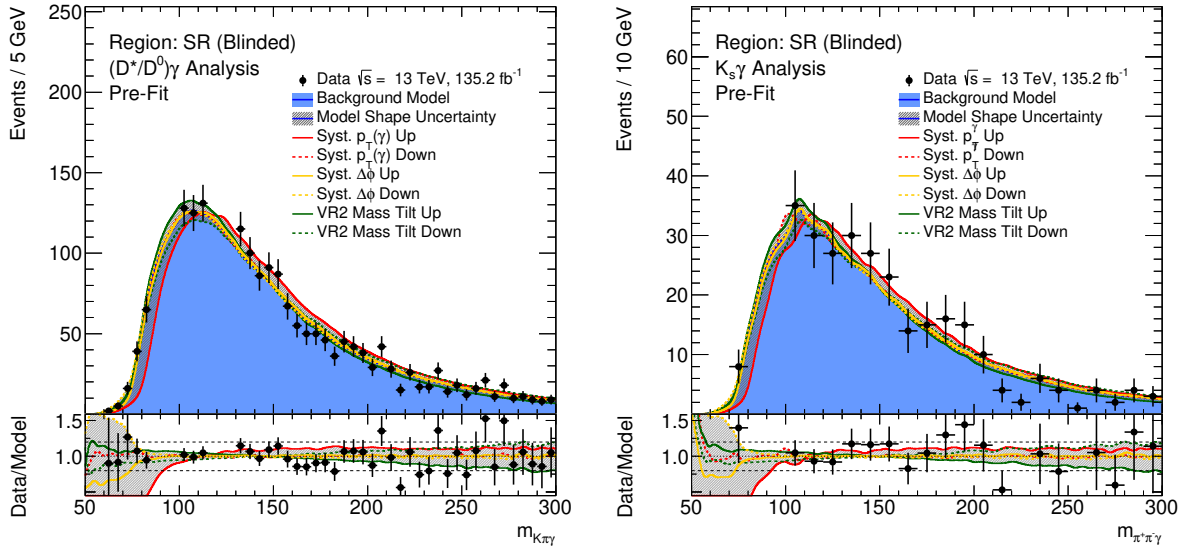
(d) $K_s\,\gamma$ VR1 (e) $K_s\,\gamma$ VR2 (f) $K_s\,\gamma$ VR3

Figure 6.9: Validation of the background model in (a) VR1, (b) VR2, and (c) VR3, for the $H \to D^*\,\gamma$ and $Z \to D^0\,\gamma$ searches, and in (d) VR1, (e) VR2, and (f) VR3, for the $Z \to K_s\,\gamma$ search. The background model is normalised to the total number of observed events in the region shown, and the model shapes are set to the nominal template.



(a) $D^0\,\gamma$ Background Model (b) $K_s\,\gamma$ Background Model

Figure 6.10: The smoothed three-body mass background KDE templates used in the likelihood fit to data in the signal region in the range $50 < m_{\mu^+\mu^-\gamma} < 300$ GeV.



(a) $D^0\,\gamma$ SR (b) $K_s\,\gamma$ SR

Figure 6.11: Illustration of the effect of each of the three systematic shape variations on the three-body mass distribution of the background (a) in the $H \to D^*\,\gamma$ and $Z \to D^0\,\gamma$ searches, and (b) in the $Z \to K_s\,\gamma$ search. The background model is normalised to the total number of observed events in the region shown, and the model shape is set to the nominal template.

6.4 Statistical Procedure and Results

One-dimensional unbinned maximum-likelihood fits to the blinded data in the signal region are used to extract expected upper limits on the branching fractions of the three decay channels. For $H \to D^*\,\gamma$ and $Z \to D^0\,\gamma$ this is to the $m_{K\pi\gamma}$ three-body mass distribution for events with $m_{K\pi\gamma} < 300$ GeV, and for $Z \to K_s\,\gamma$ this is to the $m_{\pi^+\pi^-\gamma}$ distribution for events with $m_{\pi^+\pi^-\gamma} < 300$ GeV. This section describes the likelihood functions and methods used to extract the expected 95% CL upper limits.

6.4.1 Construction of the Likelihood Function

A likelihood function $\mathcal{L}$ is constructed for each of the $D^0\,\gamma$ and $K_s\,\gamma$ analyses using the signal and background models described in Sections 6.2 and 6.3. The likelihood for the $D^0\,\gamma$ analysis, which includes the $H \to D^*\,\gamma$ and $Z \to D^0\,\gamma$ searches, is described by

$$\mathcal{L}(\vec{\mu}, b, \vec{\theta}) = \mathcal{P}(n|\sum_{i=1}^{2} \mu_i \cdot s_i + b) \times \prod_{k=1}^{n} \left(\sum_{i=1}^{2} \mathcal{F}_i^s(\vec{\mu}, b) \mathcal{S}_i(m_{K\pi\gamma}^k) + \mathcal{F}^b(\vec{\mu}, b) \mathcal{R}(m_{K\pi\gamma}^k|\vec{\theta}) \right) \times \prod_l \mathcal{G}(\theta_l|0,1).$$

The symbol $\mathcal{P}$ represents the Poisson distribution to observe n events given the total signal and background, for which there are two distinct signal contributions and one background contribution. The signals are counted by the index i and represent each of the signals, $H \to D^* \gamma$ and $Z \to D^0 \gamma$. The normalisation of the background is denoted by b which is unconstrained and determined directly from the fit to the data. The symbol s_i represents the expected signal yield for signal i for which there are currently no signal normalisation systematics. The expected signal yields are multiplied by the relative signal strength parameters $\vec{\mu} = \{\mu_i\}$ for each of the Higgs and Z boson signals, where $\mu_i = 1$ corresponds to an unmodified yield. These are the parameters of interest in these searches and are used to determine the expected 95% CL upper limits on the branching fractions of each decay. The likelihood of observing each individual event, represented by the index k, at its specific location is described by the remainder of the equation, and is related to the PDFs of each signal and background contribution. The symbol $\mathcal{F}_i^s$ denotes the fraction of signal i in the total signal and background, and the symbol $\mathcal{F}^b$ denotes the fraction of the background in the total signal and background. The shape of the signal i in $m_{K\pi\gamma}$ is given by the one-dimensional PDF $\mathcal{S}_i$. Similarly the shape of the background component is given by the one-dimensional PDF $\mathcal{R}$. The nuisance parameters $\vec{\theta}$ represent the systematic variations of the background shapes in $m_{K\pi\gamma}$, as discussed in Section 6.3.3. These parameters, counted by index l, are constrained by standard Gaussian terms $\mathcal{G}$ where the mean and width parameters are set to the parameters of the standard normal distribution at 0 and 1, respectively. This is with the exception of the nuisance parameter for the `mass-tilt` shape variation which is not constrained.

The likelihood for the $K_s \gamma$ analysis is defined similarly, except there is only one signal

contribution, removing the need to sum over i, and the discriminant variable is instead $m_{\pi^+\pi^-\gamma}$. Using analogous symbolism as for the $D^0\,\gamma$ likelihood function, the likelihood for the $K_s\,\gamma$ analysis is described by

$$\mathcal{L}(\mu, b, \vec{\theta}) = \mathcal{P}(n|\mu \cdot s + b) \times \prod_{k=1}^{n} \left(\mathcal{F}^s(\mu, b)\mathcal{S}(m^k_{\pi^+\pi^-\gamma}) + \mathcal{F}^b(\mu, b)\mathcal{R}(m^k_{\pi^+\pi^-\gamma}|\vec{\theta}) \right) \times \prod_l \mathcal{G}(\theta_l|0, 1).$$

The above functions are fit to the blinded data in the signal region to extract the expected 95% CL upper limits to evaluate the sensitivity of the searches to potential signals. The statistical approach used is the same as for the $\mathcal{Q}\,\gamma$ searches in Section 5.5.1, including the use of the CL_s modified frequentist formalism [231] with the profile-likelihood-ratio test statistic and the asymptotic approximations derived in Ref. [232]. The statistics-only and background-only hypotheses are defined similarly.

6.4.2 Expected Sensitivity

In total, across the entire three-body mass ranges in each search, 2774 events are observed in the signal region of the $H \to D^*\,\gamma$ and $Z \to D^0\,\gamma$ analysis and 384 events are observed in the signal region of the $Z \to K_s\,\gamma$ analysis. Expected 95% CL upper limits on the branching fractions and their uncertainties are calculated based on the construction of Asimov datasets [232] and fitting these with the likelihood functions $\mathcal{L}$. The Asimov datasets are constructed by fitting the blinded datasets in the signal region under the background-only hypothesis. Table 6.7 compares the expected limits obtained when accounting for the background model shape systematic uncertainties in the maximum-likelihood fit to the limits obtained under the statistics-only hypothesis. For $H \to D^*\,\gamma$ the systematic uncertainties result in a 2.0% increase of the expected 95% CL upper limit compared to the statistics-only case. For the Z boson decays the shape systematics have a larger effect on the sensitivity as the signals lie on the peak of the kinematic background. The increase in the expected limit compared to the statistics-only case is

15.1% for $Z \to D^0\,\gamma$ and 6.7% for $Z \to K_s\,\gamma$. The systematic uncertainties do not yet account for systematic variations in the shape or normalisation of the signal models, but based on previous exclusive searches these are expected to have a small effect. The expected branching fractions are of similar order to the previous results presented in Table 2.4 and Figure 2.8 in Section 2.3.

Table 6.7: Blinded post-fit expected branching fraction limit at 95% CL_s for each of the $H \to D^*\,\gamma$, $Z \to D^0\,\gamma$ and $Z \to K_s\,\gamma$ decays. The limits are estimated both without the inclusion of systematic uncertainties and with the complete background shape systematic uncertainties.

	Expected	$\pm1\sigma$	$\pm2\sigma$
$H \to D^*\,\gamma$ $[10^{-3}]$			
No Systematics	1.29	1.82/0.93	2.48/0.69
Background Shape	1.32	1.86/0.95	2.57/0.71
$Z \to D^0\,\gamma$ $[10^{-6}]$			
No Systematics	2.62	3.69/1.89	5.04/1.41
Background Shape	3.02	4.26/2.17	5.88/1.62
$Z \to K_s\,\gamma$ $[10^{-6}]$			
No Systematics	2.49	3.56/1.79	5.00/1.34
Background Shape	2.66	3.81/1.91	5.40/1.43

7 Conclusion

Since the discovery of the Higgs boson in 2012, the ATLAS experiment has continued to test the limits of the Standard Model and the search for new physics. So far, measurements of the properties of the observed Higgs boson are consistent with predictions by the SM, but much remains to be understood about this particle such as its couplings to quarks. One method to probe the Higgs boson couplings to quarks is through the study of its exclusive decays into a meson state and a photon. Analogous Z boson decays into a meson and a photon offer complementary search channels to aid in the development of analysis techniques but also are useful in tests of the QCD factorisation approach.

In this thesis, a performance study investigating the inner detector track reconstruction efficiency in dense environments was discussed, where the separation between tracks is of the order of the granularity of the inner detector. These environments are becoming increasingly important at the centre-of-mass energy of the LHC, and are used in a variety of new physics searches, precision SM measurements and performance studies. The exclusive decays of the Higgs and Z bosons for example often form dense environments. The study presented here investigates the feasiblity of a data-driven approach to measure the ID efficiency using the tag-and-probe method with boosted resonances. The Run 2 dataset had too few statistics to be sensitive to the expected drop in efficiency, based on simulation, but a promising background method was developed and the study remains an interesting prospect for the high luminosity LHC.

The latest searches for the exclusive decays of the Higgs and Z bosons to a vector quarkonium state and a photon were presented in this thesis, which use the full 139 fb^{-1} ATLAS Run 2 dataset collected at $\sqrt{s} = 13$ TeV. The observed data are compatible with expected backgrounds and 95% CL upper limits are set on the branching fractions of each decay channel. For the charmonium decay channels of the Higgs boson, $H \to J/\psi\,\gamma$ and $H \to \psi(2S)\,\gamma$, these limits are 2.0×10^{-4} and 10.5×10^{-4}. For the corresponding decay channels of the Z boson, $Z \to J/\psi\,\gamma$ and $Z \to \psi(2S)\,\gamma$, these are 1.2×10^{-6} and 2.4×10^{-6}. In the bottomonium sector, the upper limits on the Higgs

boson decays $H \to \Upsilon(1S, 2S, 3S)\,\gamma$ are $(2.5, 4.2, 3.4) \times 10^{-4}$, and for the Z boson decays $Z \to \Upsilon(1S, 2S, 3S)\,\gamma$ are $(1.1, 1.3, 2.4) \times 10^{-6}$. These upper limits represent an improvement by a factor of approximately two over the previous ATLAS result, which used a partial Run 2 dataset of 36.1 fb^{-1} collected at $\sqrt{s} = 13$ TeV.

The current progress of the searches for the three flavour-violating decays $H \to D^{*0}\gamma$, $Z \to D^0\gamma$, and $Z \to K^0_S\gamma$, was also discussed. These use 135.2 fb^{-1} of ATLAS data collected at $\sqrt{s} = 13$ TeV between 2016–2018. The analysis is blinded as it is in the process of being optimised, but expected 95% CL upper limits are set on the branching fractions of each decay channel to evaluate the sensitivity of the analyses to potential signals. For $H \to D^*\,\gamma$ the expected 95% CL upper limit is $13.2^{+5.4}_{-3.7} \times 10^{-4}$, and for $Z \to D^0\,\gamma$ the expected limit is $3.0^{+1.2}_{-0.8} \times 10^{-6}$. For $Z \to K_s\,\gamma$ the expected limit is $2.7^{+1.2}_{-0.7} \times 10^{-6}$. These expected limits are similar to the sensitivity of previous exclusive decays searches, and when the analysis is unblinded will represent the first limits on these decay channels. The next steps of the analyses are to optimise the background models and to evaluate systematic uncertainties in the signal shape and normalisation, which are expected to have a small effect.

References

[1] Mark Thomson. *Modern particle physics*. New York: Cambridge University Press, 2013. ISBN: 978-1-107-03426-6.

[2] ATLAS Collaboration. "Observation of a new particle in the search for the Standard Model Higgs boson with the ATLAS detector at the LHC". In: *Phys. Lett. B* 716 (2012), p. 1. DOI: 10.1016/j.physletb.2012.08.020. arXiv: 1207.7214 [hep-ex].

[3] CMS Collaboration. "Observation of a new boson at a mass of 125 GeV with the CMS experiment at the LHC". In: *Phys. Lett. B* 716 (2012), p. 30. DOI: 10.1016/j.physletb.2012.08.021. arXiv: 1207.7235 [hep-ex].

[4] ATLAS Collaboration. "The ATLAS Experiment at the CERN Large Hadron Collider". In: *JINST* 3 (2008), S08003. DOI: 10.1088/1748-0221/3/08/S08003.

[5] CMS Collaboration. "The CMS Experiment at the CERN LHC". In: *JINST* 3 (2008), S08004. DOI: 10.1088/1748-0221/3/08/S08004.

[6] Lyndon Evans and Philip Bryant. "LHC Machine". In: *JINST* 3 (2008), S08001. DOI: 10.1088/1748-0221/3/08/S08001.

[7] ATLAS Collaboration. "A detailed map of Higgs boson interactions by the ATLAS experiment ten years after the discovery". In: *Nature* 607.7917 (2022), pp. 52–59. DOI: 10.1038/s41586-022-04893-w. arXiv: 2207.00092 [hep-ex].

[8] CMS Collaboration. "A portrait of the Higgs boson by the CMS experiment ten years after the discovery". In: *Nature* 607.7917 (2022), pp. 60–68. DOI: 10.1038/s41586-022-04892-x. arXiv: 2207.00043 [hep-ex].

[9] S.L. Glashow. "Partial Symmetries of Weak Interactions". In: *Nucl. Phys.* 22 (1961), pp. 579–588. DOI: 10.1016/0029-5582(61)90469-2.

[10] Steven Weinberg. "A Model of Leptons". In: *Phys. Rev. Lett.* 19 (1967), pp. 1264–1266. DOI: 10.1103/PhysRevLett.19.1264.

[11] Abdus Salam. "Weak and Electromagnetic Interactions". In: *Conf. Proc. C* 680519 (1968), pp. 367–377. DOI: 10.1142/9789812795915_0034.

[12] Gerard 't Hooft and M. J. G. Veltman. "Regularization and Renormalization of Gauge Fields". In: *Nucl. Phys. B* 44 (1972), pp. 189–213. DOI: 10.1016/0550-3213(72)90279-9.

[13] F. Englert and R. Brout. "Broken Symmetry and the Mass of Gauge Vector Mesons". In: *Phys. Rev. Lett.* 13 (1964). Ed. by J. C. Taylor, pp. 321–323. DOI: 10.1103/PhysRevLett.13.321.

[14] Peter W. Higgs. "Broken symmetries, massless particles and gauge fields". In: *Phys. Lett.* 12 (1964), pp. 132–133. DOI: 10.1016/0031-9163(64)91136-9.

[15] Peter W. Higgs. "Broken Symmetries and the Masses of Gauge Bosons". In: *Phys. Rev. Lett.* 13 (1964). Ed. by J. C. Taylor, pp. 508–509. DOI: 10.1103/PhysRevLett.13.508.

[16] G. S. Guralnik, C. R. Hagen and T. W. B. Kibble. "Global Conservation Laws and Massless Particles". In: *Phys. Rev. Lett.* 13 (1964). Ed. by J. C. Taylor, pp. 585–587. DOI: 10.1103/PhysRevLett.13.585.

[17] Peter W. Higgs. "Spontaneous Symmetry Breakdown without Massless Bosons". In: *Phys. Rev.* 145 (1966), pp. 1156–1163. DOI: 10.1103/PhysRev.145.1156.

[18] T. W. B. Kibble. "Symmetry breaking in nonAbelian gauge theories". In: *Phys. Rev.* 155 (1967). Ed. by J. C. Taylor, pp. 1554–1561. DOI: 10.1103/PhysRev.155.1554.

[19] MissMJ and Cush. *Standard model of elementary particles: the 12 fundamental fermions and 5 fundamental bosons*. https://commons.wikimedia.org/wiki/File:Standard_Model_of_Elementary_Particles.svg. [Online; accessed 16-September-2020]. 2020.

[20] LHCb Collaboration. "Observation of the resonant character of the $Z(4430)^-$ state". In: *Phys. Rev. Lett.* 112.22 (2014), p. 222002. DOI: 10.1103/PhysRevLett.112.222002. arXiv: 1404.1903 [hep-ex].

[21] LHCb Collaboration. "Observation of $J/\psi p$ Resonances Consistent with Pentaquark States in $\Lambda_b^0 \to J/\psi K^- p$ Decays". In: *Phys. Rev. Lett.* 115 (2015), p. 072001. DOI: 10.1103/PhysRevLett.115.072001. arXiv: 1507.03414 [hep-ex].

[22] UA1 Collaboration. "Experimental Observation of Isolated Large Transverse Energy Electrons with Associated Missing Energy at $\sqrt{s} = 540$ GeV". In: *Phys. Lett. B* 122 (1983), pp. 103–116. DOI: 10.1016/0370-2693(83)91177-2.

[23] UA2 Collaboration. "Observation of Single Isolated Electrons of High Transverse Momentum in Events with Missing Transverse Energy at the CERN anti-p p Collider". In: *Phys. Lett. B* 122 (1983), pp. 476–485. DOI: 10.1016/0370-2693(83)91605-2.

[24] UA1 Collaboration. "Experimental Observation of Lepton Pairs of Invariant Mass Around 95-GeV/c**2 at the CERN SPS Collider". In: *Phys. Lett. B* 126 (1983), pp. 398–410. DOI: 10.1016/0370-2693(83)90188-0.

[25] UA2 Collaboration. "Evidence for $Z^0 \to e^+e^-$ at the CERN $\bar{p}p$ Collider". In: *Phys. Lett. B* 129 (1983), pp. 130–140. DOI: 10.1016/0370-2693(83)90744-X.

[26] P. Zyla et al. (Particle Data Group). "Review of Particle Physics". In: *PTEP* 2020.8 (2020). and 2021 update, p. 083C01. DOI: 10.1093/ptep/ptaa104.

[27] CDF Collaboration. "High-precision measurement of the W boson mass with the CDF II detector". In: *Science* 376.6589 (2022), pp. 170–176. DOI: 10.1126/science.abk1781.

[28] John Ellis. "Higgs Physics". In: *2013 European School of High-Energy Physics*. 2015, pp. 117–168. DOI: 10.5170/CERN-2015-004.117. arXiv: 1312.5672 [hep-ph].

[29] Yoichiro Nambu and G. Jona-Lasinio. "Dynamical Model of Elementary Particles Based on an Analogy with Superconductivity. 1." In: *Phys. Rev.* 122 (1961). Ed. by T. Eguchi, pp. 345–358. DOI: 10.1103/PhysRev.122.345.

[30] D. de Florian et al. "Handbook of LHC Higgs Cross Sections: 4. Deciphering the Nature of the Higgs Sector". In: 2/2017 (Oct. 2016). DOI: 10.23731/CYRM-2017-002. arXiv: 1610.07922 [hep-ph].

[31] ATLAS and CMS Collaborations. "Combined Measurement of the Higgs Boson Mass in pp Collisions at $\sqrt{s} = 7$ and 8 TeV with the ATLAS and CMS Experi-

ments". In: *Phys. Rev. Lett.* 114 (2015), p. 191803. DOI: 10.1103/PhysRevLett.114.191803. arXiv: 1503.07589 [hep-ex].

[32] ATLAS Collaboration. "Measurement of the Higgs boson mass in the $H \to ZZ^* \to 4\ell$ and $H \to \gamma\gamma$ channels with $\sqrt{s} = 13\,\text{TeV}$ pp collisions using the ATLAS detector". In: *Phys. Lett. B* 784 (2018), p. 345. DOI: 10.1016/j.physletb.2018.07.050. arXiv: 1806.00242 [hep-ex].

[33] CMS Collaboration. "A measurement of the Higgs boson mass in the diphoton decay channel". In: *Phys. Lett. B* 805 (2020), p. 135425. DOI: 10.1016/j.physletb.2020.135425. arXiv: 2002.06398 [hep-ex].

[34] ATLAS Collaboration. "Combined measurement of differential and total cross sections in the $H \to \gamma\gamma$ and the $H \to ZZ^* \to 4\ell$ decay channels at $\sqrt{s} = 13\,\text{TeV}$ with the ATLAS detector". In: *Phys. Lett. B* 786 (2018), p. 114. DOI: 10.1016/j.physletb.2018.09.019. arXiv: 1805.10197 [hep-ex].

[35] ATLAS Collaboration. "Measurement of the total and differential Higgs boson production cross-sections at $\sqrt{s} = 13$ TeV with the ATLAS detector by combining the $H \to ZZ^* \to 4\ell$ and $H \to \gamma\gamma$ decay channels". In: (July 2022). arXiv: 2207.08615. URL: http://cds.cern.ch/record/2816107.

[36] CMS Collaboration. "Measurement and interpretation of differential cross sections for Higgs boson production at $\sqrt{s} = 13\,\text{TeV}$". In: *Phys. Lett. B* 792 (2019), p. 369. DOI: 10.1016/j.physletb.2019.03.059. arXiv: 1812.06504 [hep-ex].

[37] CMS Collaboration. "Measurement of the Higgs boson inclusive and differential fiducial production cross sections in the diphoton decay channel with pp collisions at $\sqrt{s} = 13$ TeV". In: (Aug. 2022). arXiv: 2208.12279. URL: https://cds.cern.ch/record/2825355.

[38] ATLAS Collaboration. "Study of the spin and parity of the Higgs boson in diboson decays with the ATLAS detector". In: *Eur. Phys. J. C* 75 (2015), p. 476. DOI: 10.1140/epjc/s10052-015-3685-1. arXiv: 1506.05669 [hep-ex]. Erratum: in: *Eur. Phys. J. C* 76 (2016), p. 152. DOI: 10.1140/epjc/s10052-016-3934-y.

[39] CMS Collaboration. "Constraints on the spin-parity and anomalous HVV couplings of the Higgs boson in proton collisions at 7 and 8 TeV". In: *Phys. Rev. D* 92 (2015), p. 012004. DOI: 10.1103/PhysRevD.92.012004. arXiv: 1411.3441 [hep-ex].

[40] ATLAS Collaboration. "Constraints on the off-shell Higgs boson signal strength in the high-mass ZZ and WW final states with the ATLAS detector". In: *Eur. Phys. J. C* 75 (2015), p. 335. DOI: 10.1140/epjc/s10052-015-3542-2. arXiv: 1503.01060 [hep-ex].

[41] CMS Collaboration. "Search for Higgs boson off-shell production in proton–proton collisions at 7 and 8 TeV and derivation of constraints on its total decay width". In: *JHEP* 09 (2016), p. 051. DOI: 10.1007/JHEP09(2016)051. arXiv: 1605.02329 [hep-ex].

[42] CMS Collaboration. "Limits on the Higgs boson lifetime and width from its decay to four charged leptons". In: *Phys. Rev. D* 92 (2015), p. 072010. DOI: 10.1103/PhysRevD.92.072010. arXiv: 1507.06656 [hep-ex].

[43] CMS Collaboration. "First evidence for off-shell production of the Higgs boson and measurement of its width". In: (2022). arXiv: 2202.06923 [hep-ex].

[44] ATLAS Collaboration. "Evidence for Higgs boson decays to a low-mass dilepton system and a photon in pp collisions at $\sqrt{s} = 13$ TeV with the ATLAS detector". In: *Phys. Lett. B* 819 (2021), p. 136412. DOI: 10.1016/j.physletb.2021.136412. arXiv: 2103.10322 [hep-ex].

[45] CMS Collaboration. "Search for the decay of a Higgs boson in the $\ell\ell\gamma$ channel in proton–proton collisions at $\sqrt{s} = 13$ TeV". In: *JHEP* 11 (2018), p. 152. DOI: 10.1007/JHEP11(2018)152. arXiv: 1806.05996 [hep-ex].

[46] ATLAS Collaboration. "A search for the $Z\gamma$ decay mode of the Higgs boson in pp collisions at $\sqrt{s} = 13$ TeV with the ATLAS detector". In: *Phys. Lett. B* 809 (2020), p. 135754. DOI: 10.1016/j.physletb.2020.135754. arXiv: 2005.05382 [hep-ex].

[47] CMS Collaboration. "Search for Higgs boson decays to a Z boson and a photon in proton–proton collisions at $\sqrt{s} = 13\,\text{TeV}$". In: (2022). arXiv: 2204.12945 [hep-ex].

[48] ATLAS Collaboration. "Observation of Higgs boson production in association with a top quark pair at the LHC with the ATLAS detector". In: *Phys. Lett. B* 784 (2018), p. 173. DOI: 10.1016/j.physletb.2018.07.035. arXiv: 1806.00425 [hep-ex].

[49] CMS Collaboration. "Observation of $t\bar{t}H$ Production". In: *Phys. Rev. Lett.* 120 (2018), p. 231801. DOI: 10.1103/PhysRevLett.120.231801. arXiv: 1804.02610 [hep-ex].

[50] ATLAS Collaboration. "Observation of $H \to b\bar{b}$ decays and VH production with the ATLAS detector". In: *Phys. Lett. B* 786 (2018), p. 59. DOI: 10.1016/j.physletb.2018.09.013. arXiv: 1808.08238 [hep-ex].

[51] CMS Collaboration. "Observation of Higgs Boson Decay to Bottom Quarks". In: *Phys. Rev. Lett.* 121 (2018), p. 121801. DOI: 10.1103/PhysRevLett.121.121801. arXiv: 1808.08242 [hep-ex].

[52] ATLAS Collaboration. "Measurements of Higgs boson production cross-sections in the $H \to \tau^+\tau^-$ decay channel in pp collisions at $\sqrt{s} = 13\,\text{TeV}$ with the ATLAS detector". In: (2022). arXiv: 2201.08269 [hep-ex].

[53] CMS Collaboration. "Measurements of Higgs boson production in the decay channel with a pair of τ leptons in proton–proton collisions at $\sqrt{s} = 13\,\text{TeV}$". In: (2022). arXiv: 2204.12957 [hep-ex].

[54] CMS Collaboration. "Evidence for Higgs boson decay to a pair of muons". In: *JHEP* 01 (2021), p. 148. DOI: 10.1007/JHEP01(2021)148. arXiv: 2009.04363 [hep-ex].

[55] ATLAS Collaboration. "A search for the dimuon decay of the Standard Model Higgs boson with the ATLAS detector". In: *Phys. Lett. B* 812 (2021), p. 135980. DOI: 10.1016/j.physletb.2020.135980. arXiv: 2007.07830 [hep-ex].

[56] ATLAS Collaboration. "Search for the Decay of the Higgs Boson to Charm Quarks with the ATLAS Experiment". In: *Phys. Rev. Lett.* 120 (2018), p. 211802. DOI: 10.1103/PhysRevLett.120.211802. arXiv: 1802.04329 [hep-ex].

[57] ATLAS Collaboration. "Direct constraint on the Higgs-charm coupling from a search for Higgs boson decays into charm quarks with the ATLAS detector". In: (Jan. 2022). arXiv: 2201.11428 [hep-ex].

[58] CMS Collaboration. "A search for the standard model Higgs boson decaying to charm quarks". In: *JHEP* 03 (2020), p. 131. DOI: 10.1007/JHEP03(2020)131. arXiv: 1912.01662 [hep-ex].

[59] CMS Collaboration. "Search for Higgs boson decay to a charm quark-antiquark pair in proton-proton collisions at $\sqrt{s} = 13$ TeV". In: (May 2022). arXiv: 2205.05550 [hep-ex].

[60] ATLAS Collaboration. "Search for the Higgs boson decays $H \to ee$ and $H \to e\mu$ in pp collisions at $\sqrt{s} = 13\,\text{TeV}$ with the ATLAS detector". In: *Phys. Lett. B* 801 (2020), p. 135148. DOI: 10.1016/j.physletb.2019.135148. arXiv: 1909.10235 [hep-ex].

[61] CMS Collaboration. "Search for a standard model-like Higgs boson in the $\mu^+\mu^-$ and e^+e^- decay channels at the LHC". In: *Phys. Lett. B* 744 (2015), p. 184. DOI: 10.1016/j.physletb.2015.03.048. arXiv: 1410.6679 [hep-ex].

[62] LHC Higgs Cross Section Working Group. "Handbook of LHC Higgs Cross Sections: 3. Higgs Properties". In: (July 2013). Ed. by S Heinemeyer et al. DOI: 10.5170/CERN-2013-004. arXiv: 1307.1347 [hep-ph].

[63] ATLAS Collaboration. "Search for top quark decays $t \to qH$, with $H \to \gamma\gamma$, in $\sqrt{s} = 13\,\text{TeV}$ pp collisions using the ATLAS detector". In: *JHEP* 10 (2017), p. 129. DOI: 10.1007/JHEP10(2017)129. arXiv: 1707.01404 [hep-ex].

[64] ATLAS Collaboration. "Search for flavor-changing neutral currents in top quark decays $t \to Hc$ and $t \to Hu$ in multilepton final states in proton–proton collisions at $\sqrt{s} = 13\,\text{TeV}$ with the ATLAS detector". In: *Phys. Rev. D* 98 (2018), p. 032002. DOI: 10.1103/PhysRevD.98.032002. arXiv: 1805.03483 [hep-ex].

[65] CMS Collaboration. "Search for flavor-changing neutral current interactions of the top quark and the Higgs boson decaying to a bottom quark-antiquark pair at $\sqrt{s}$ =13 TeV". In: *JHEP* 02 (2021), p. 169. DOI: 10.1007/JHEP02(2022)169. arXiv: 2112.09734 [hep-ex].

[66] CMS Collaboration. "Search for flavor-changing neutral current interactions of the top quark and Higgs boson in final states with two photons in proton–proton collisions at $\sqrt{s} = 13$ TeV". In: (2021). arXiv: 2111.02219 [hep-ex].

[67] ATLAS Collaboration. "Searches for lepton-flavour-violating decays of the Higgs boson in $\sqrt{s} = 13$ TeV pp collisions with the ATLAS detector". In: *Phys. Lett. B* 800 (2020), p. 135069. DOI: 10.1016/j.physletb.2019.135069. arXiv: 1907.06131 [hep-ex].

[68] CMS Collaboration. "Search for lepton-flavor violating decays of the Higgs boson in the $\mu\tau$ and eτ final states in proton-proton collisions at $\sqrt{s} = 13$ TeV". In: *Phys. Rev. D* 104.3 (2021), p. 032013. DOI: 10.1103/PhysRevD.104.032013. arXiv: 2105.03007 [hep-ex].

[69] Geoffrey Bodwin et al. "Higgs boson decays to quarkonia and the $H\bar{c}c$ coupling". In: *Phys. Rev. D* 88.5 (2013), p. 053003. DOI: 10.1103/PhysRevD.88.053003. arXiv: 1306.5770 [hep-ph].

[70] M.N. Doroshenko et al. "Vector quarkonium in decays of heavy Higgs particles". In: *Yad. Fiz.* 46 (1987), pp. 864–868.

[71] Matthias Konig and Matthias Neubert. "Exclusive Radiative Higgs Decays as Probes of Light-Quark Yukawa Couplings". In: *JHEP* 08 (2015), p. 012. DOI: 10.1007/JHEP08(2015)012. arXiv: 1505.03870 [hep-ph].

[72] Geoffrey T. Bodwin et al. "Relativistic corrections to Higgs boson decays to quarkonia". In: *Phys. Rev. D* 90.11 (2014), p. 113010. DOI: 10.1103/PhysRevD.90.113010. arXiv: 1407.6695 [hep-ph].

[73] Geoffrey T. Bodwin et al. "New approach to the resummation of logarithms in Higgs-boson decays to a vector quarkonium plus a photon". In: *Phys. Rev. D*

95.5 (2017), p. 054018. DOI: 10.1103/PhysRevD.95.054018. arXiv: 1603.06793 [hep-ph].

[74] Geoffrey T. Bodwin et al. "Addendum: New approach to the resummation of logarithms in Higgs-boson decays to a vector quarkonium plus a photon [Phys. Rev. D 95, 054018 (2017)]". In: *Phys. Rev. D* 96 (2017), p. 116014. DOI: 10.1103/PhysRevD.96.116014. arXiv: 1710.09872 [hep-ph].

[75] Chao Zhou et al. "Next-to-leading order QCD corrections to Higgs boson decay to quarkonium plus a photon". In: *Chin. Phys. C* 40.12 (2016), p. 123105. DOI: 10.1088/1674-1137/40/12/123105. arXiv: 1607.02704 [hep-ph].

[76] Nora Brambilla et al. "Order v^4 corrections to Higgs boson decay into $J/\psi + \gamma$". In: *Phys. Rev. D* 100.5 (2019), p. 054038. DOI: 10.1103/PhysRevD.100.054038. arXiv: 1907.06473 [hep-ph].

[77] Aditya Batra, Sanjoy Mandal and Rahul Srivastava. "$h \to \Upsilon\gamma$ Decay: Smoking Gun Signature of Wrong-Sign $hb\bar{b}$ Coupling". In: (Sept. 2022). arXiv: 2209.01200 [hep-ph].

[78] Gilad Perez et al. "Constraining the charm Yukawa and Higgs-quark coupling universality". In: *Phys. Rev. D* 92.3 (2015), p. 033016. DOI: 10.1103/PhysRevD.92.033016. arXiv: 1503.00290 [hep-ph].

[79] C. D. Froggatt and Holger Bech Nielsen. "Hierarchy of quark masses, cabibbo angles and CP violation". In: *Nucl. Phys. B* 147 (1979), pp. 277–298. DOI: 10.1016/0550-3213(79)90316-X.

[80] Lisa Randall and Raman Sundrum. "A Large mass hierarchy from a small extra dimension". In: *Phys. Rev. Lett.* 83 (1999), pp. 3370–3373. DOI: 10.1103/PhysRevLett.83.3370. arXiv: hep-ph/9905221.

[81] G. D'Ambrosio et al. "Minimal flavor violation: an effective field theory approach". In: *Nucl. Phys. B* 645 (2002), pp. 155–187. DOI: 10.1016/S0550-3213(02)00836-2. arXiv: hep-ph/0207036.

[82] Gian F. Giudice and Oleg Lebedev. "Higgs-dependent Yukawa couplings". In: *Phys. Lett. B* 665 (2008), pp. 79–85. DOI: 10.1016/j.physletb.2008.05.062. arXiv: 0804.1753 [hep-ph].

[83] Michael J. Dugan, Howard Georgi and David B. Kaplan. "Anatomy of a composite Higgs model". In: *Nucl. Phys. B* 254 (1985), p. 299. DOI: 10.1016/0550-3213(85)90221-4.

[84] J. I. Aranda et al. "Revisiting the rare $H \to q_i q_j$ decays in the standard model". In: *J. Phys. G* 47.12 (2020), p. 125001. DOI: 10.1088/1361-6471/abb44d. arXiv: 2009.07166 [hep-ph].

[85] ATLAS Collaboration. "Measurement of $W^{\pm}$ and Z-boson production cross sections in pp collisions at $\sqrt{s} = 13\,\text{TeV}$ with the ATLAS detector". In: *Phys. Lett. B* 759 (2016), p. 601. DOI: 10.1016/j.physletb.2016.06.023. arXiv: 1603.09222 [hep-ex].

[86] Andrea Dainese et al. "Report on the Physics at the HL-LHC, and Perspectives for the HE-LHC". In: (2019). DOI: 10.23731/CYRM-2019-007. URL: https://cds.cern.ch/record/2703572.

[87] Ting-Chung Huang and Frank Petriello. "Rare exclusive decays of the Z-boson revisited". In: *Phys. Rev. D* 92.1 (2015), p. 014007. DOI: 10.1103/PhysRevD.92.014007. arXiv: 1411.5924 [hep-ph].

[88] Yuval Grossman, Matthias König and Matthias Neubert. "Exclusive Radiative Decays of W and Z Bosons in QCD Factorization". In: *JHEP* 04 (2015), p. 101. DOI: 10.1007/JHEP04(2015)101. arXiv: 1501.06569 [hep-ph].

[89] Geoffrey T. Bodwin et al. "Z-boson decays to a vector quarkonium plus a photon". In: *Phys. Rev. D* 97.1 (2018), p. 016009. DOI: 10.1103/PhysRevD.97.016009. arXiv: 1709.09320 [hep-ph].

[90] ATLAS Collaboration. "Search for Higgs and Z Boson Decays to $J/\psi\gamma$ and $\Upsilon(n\text{S})\gamma$ with the ATLAS Detector". In: *Phys. Rev. Lett.* 114 (2015), p. 121801. DOI: 10.1103/PhysRevLett.114.121801. arXiv: 1501.03276 [hep-ex].

[91] ATLAS Collaboration. "Search for Higgs and Z Boson Decays to $\phi\gamma$ with the ATLAS Detector". In: *Phys. Rev. Lett.* 117 (2016), p. 111802. DOI: 10.1103/PhysRevLett.117.111802. arXiv: 1607.03400 [hep-ex].

[92] ATLAS Collaboration. "Searches for exclusive Higgs and Z boson decays into $J/\psi\gamma$, $\psi(2S)\gamma$, and $\Upsilon(nS)\gamma$ at $\sqrt{s} = 13\,\text{TeV}$ with the ATLAS detector". In: *Phys. Lett. B* 786 (2018), p. 134. DOI: 10.1016/j.physletb.2018.09.024. arXiv: 1807.00802 [hep-ex].

[93] ATLAS Collaboration. "Search for exclusive Higgs and Z boson decays to $\phi\gamma$ and $\rho\gamma$ with the ATLAS detector". In: *JHEP* 07 (2018), p. 127. DOI: 10.1007/JHEP07(2018)127. arXiv: 1712.02758 [hep-ex].

[94] ATLAS Collaboration. "Searches for exclusive Higgs and Z boson decays into a vector quarkonium state and a photon using 139 fb^{-1} of ATLAS $\sqrt{s} = 13$ TeV proton−proton collision data". In: (Aug. 2022). arXiv: 2208.03122 [hep-ex].

[95] CMS Collaboration. "Search for a Higgs boson decaying into $\gamma^*\gamma \to \ell\ell\gamma$ with low dilepton mass in pp collisions at $\sqrt{s} = 8\,\text{TeV}$". In: *Phys. Lett. B* 753 (2016), p. 341. DOI: 10.1016/j.physletb.2015.12.039. arXiv: 1507.03031 [hep-ex].

[96] CMS Collaboration. "Search for rare decays of Z and Higgs bosons to J/ψ and a photon in proton-proton collisions at $\sqrt{s} = 13$ TeV". In: *Eur. Phys. J.* C79.2 (2019), p. 94. DOI: 10.1140/epjc/s10052-019-6562-5. arXiv: 1810.10056 [hep-ex].

[97] CMS Collaboration. "Search for the rare decay of the W boson into a pion and a photon in proton–proton collisions at $\sqrt{s} = 13\,\text{TeV}$". In: *Phys. Lett. B* 819 (2020), p. 136409. DOI: 10.1016/j.physletb.2021.136409. arXiv: 2011.06028 [hep-ex].

[98] LHCb Collaboration. "Search for the rare decays $W^+ \to D_s^+\gamma$ and $Z \to D^0\gamma$ at LHCb". In: (Dec. 2022). arXiv: 2212.07120 [hep-ex].

[99] ATLAS Collaboration. "Search for Higgs Boson Decays into a Z Boson and a Light Hadronically Decaying Resonance Using 13 TeV pp Collision Data from the

ATLAS Detector". In: *Phys. Rev. Lett.* 125 (2020), p. 221802. DOI: 10.1103/PhysRevLett.125.221802. arXiv: 2004.01678 [hep-ex].

[100] CMS Collaboration. "Search for Higgs and Z boson decays to J/ψ or Υ pairs in the four-muon final state in proton–proton collisions at $\sqrt{s} = 13\,\text{TeV}$". In: *Phys. Lett. B* 797 (2019), p. 134811. DOI: 10.1016/j.physletb.2019.134811. arXiv: 1905.10408 [hep-ex].

[101] LHCb Collaboration. "The LHCb Detector at the LHC". In: *JINST* 3 (2008), S08005. DOI: 10.1088/1748-0221/3/08/S08005.

[102] ALICE Collaboration. "The ALICE experiment at the CERN LHC". In: *JINST* 3 (2008), S08002. DOI: 10.1088/1748-0221/3/08/S08002.

[103] ATLAS Collaboration. "ATLAS data quality operations and performance for 2015–2018 data-taking". In: *JINST* 15 (2020), P04003. DOI: 10.1088/1748-0221/15/04/P04003. arXiv: 1911.04632 [physics.ins-det].

[104] ATLAS Collaboration. *ATLAS Magnet System: Magnet Project Technical Design Report, Volume 1*. ATLAS-TDR-6; CERN-LHCC-97-018. 1997. URL: https://cds.cern.ch/record/338080.

[105] ATLAS Collaboration. *ATLAS Barrel Toroid: Magnet Project Technical Design Report, Volume 2*. ATLAS-TDR-7; CERN-LHCC-97-019. 1997. URL: https://cds.cern.ch/record/331065.

[106] ATLAS Collaboration. *ATLAS End-Cap Toroids: Magnet Project Technical Design Report, Volume 3*. ATLAS-TDR-8; CERN-LHCC-97-020. CERN, 1997. URL: https://cds.cern.ch/record/331066.

[107] ATLAS Collaboration. *ATLAS Central Solenoid: Magnet Project Technical Design Report, Volume 4*. ATLAS-TDR-9; CERN-LHCC-97-021. CERN, 1997. URL: https://cds.cern.ch/record/331067.

[108] ATLAS Collaboration. *ATLAS Inner Detector: Technical Design Report, Volume 1*. ATLAS-TDR-4; CERN-LHCC-97-016. 1997. URL: https://cds.cern.ch/record/331063.

[109] ATLAS Collaboration. *ATLAS Inner Detector: Technical Design Report, Volume 2*. ATLAS-TDR-5, CERN-LHCC-97-017. 1997. URL: https://cds.cern.ch/record/331064.

[110] ATLAS Collaboration. *ATLAS Insertable B-Layer: Technical Design Report*. ATLAS-TDR-19; CERN-LHCC-2010-013. 2010. URL: https://cds.cern.ch/record/1291633. Addendum: ATLAS-TDR-19-ADD-1; CERN-LHCC-2012-009. 2012. URL: https://cds.cern.ch/record/1451888.

[111] B. Abbott et al. "Production and integration of the ATLAS Insertable B-Layer". In: *JINST* 13 (2018), T05008. DOI: 10.1088/1748-0221/13/05/T05008. arXiv: 1803.00844 [physics.ins-det].

[112] ATLAS Collaboration. "Study of the material of the ATLAS inner detector for Run 2 of the LHC". In: *JINST* 12 (2017), P12009. DOI: 10.1088/1748-0221/12/12/P12009. arXiv: 1707.02826 [hep-ex].

[113] ATLAS Collaboration. *ATLAS Pixel Detector: Technical Design Report*. ATLAS-TDR-11; CERN-LHCC-98-013. 1998. URL: https://cds.cern.ch/record/381263.

[114] ATLAS Collaboration. "Performance of the ATLAS Transition Radiation Tracker in Run 1 of the LHC: tracker properties". In: *JINST* 12 (2017), P05002. DOI: 10.1088/1748-0221/12/05/P05002. arXiv: 1702.06473 [hep-ex].

[115] ATLAS Collaboration. *ATLAS Calorimeter Performance: Technical Design Report*. ATLAS-TDR-1; CERN-LHCC-96-040. 1996. URL: https://cds.cern.ch/record/331059.

[116] ATLAS Collaboration. *ATLAS Liquid Argon Calorimeter: Technical Design Report*. ATLAS-TDR-2; CERN-LHCC-96-041. 1996. URL: https://cds.cern.ch/record/331061.

[117] ATLAS Collaboration. *ATLAS Tile Calorimeter: Technical Design Report*. ATLAS-TDR-3; CERN-LHCC-96-042. 1996. URL: https://cds.cern.ch/record/331062.

[118] ATLAS Collaboration. *ATLAS Muon Spectrometer: Technical Design Report*. ATLAS-TDR-10; CERN-LHCC-97-022. CERN, 1997. URL: https://cds.cern.ch/record/331068.

[119] ATLAS Collaboration. "Performance of the ATLAS trigger system in 2015". In: *Eur. Phys. J. C* 77 (2017), p. 317. DOI: 10.1140/epjc/s10052-017-4852-3. arXiv: 1611.09661 [hep-ex].

[120] ATLAS Collaboration. "Operation of the ATLAS trigger system in Run 2". In: *JINST* 15 (2020), P10004. DOI: 10.1088/1748-0221/15/10/P10004. arXiv: 2007.12539 [hep-ex].

[121] T. Cornelissen et al. "Concepts, Design and Implementation of the ATLAS New Tracking (NEWT)". In: (Mar. 2007). Ed. by A. Salzburger. URL: https://cds.cern.ch/record/1020106.

[122] T. Cornelissen et al. "The new ATLAS track reconstruction (NEWT)". In: *J. Phys. Conf. Ser.* 119 (2008). Ed. by Randall Sobie, Reda Tafirout and Jana Thomson, p. 032014. DOI: 10.1088/1742-6596/119/3/032014.

[123] R. Fruhwirth. "Application of Kalman filtering to track and vertex fitting". In: *Nucl. Instrum. Meth. A* 262 (1987), pp. 444–450. DOI: 10.1016/0168-9002(87)90887-4.

[124] ATLAS Collaboration. "Early Inner Detector tracking performance in the 2015 data at $\sqrt{s} = 13$ TeV". In: *ATL-PHYS-PUB-2015-051* (Dec. 2015). URL: http://cds.cern.ch/record/2110140.

[125] ATLAS Collaboration. *Performance of primary vertex reconstruction in proton–proton collisions at $\sqrt{s} = 7$ TeV in the ATLAS experiment*. ATLAS-CONF-2010-069. 2010. URL: https://cds.cern.ch/record/1281344.

[126] ATLAS Collaboration. *Vertex Reconstruction Performance of the ATLAS Detector at $\sqrt{s} = 13$ TeV*. ATL-PHYS-PUB-2015-026. 2015. URL: https://cds.cern.ch/record/2037717.

[127] ATLAS Collaboration. "Electron and photon energy calibration with the ATLAS detector using 2015–2016 LHC proton–proton collision data". In: *JINST* 14 (2019), P03017. DOI: 10.1088/1748-0221/14/03/P03017. arXiv: 1812.03848 [hep-ex].

[128] ATLAS Collaboration. "Electron reconstruction and identification in the ATLAS experiment using the 2015 and 2016 LHC proton–proton collision data at $\sqrt{s} = 13\,\text{TeV}$". In: *Eur. Phys. J. C* 79 (2019), p. 639. DOI: 10.1140/epjc/s10052-019-7140-6. arXiv: 1902.04655 [hep-ex].

[129] ATLAS Collaboration. "Electron and photon performance measurements with the ATLAS detector using the 2015-2017 LHC proton-proton collision data". In: (2019). arXiv: 1908.00005 [hep-ex].

[130] ATLAS Collaboration. "Measurement of the photon identification efficiencies with the ATLAS detector using LHC Run 2 data collected in 2015 and 2016". In: *Eur. Phys. J. C* 79 (2019), p. 205. DOI: 10.1140/epjc/s10052-019-6650-6. arXiv: 1810.05087 [hep-ex].

[131] ATLAS Collaboration. "Muon reconstruction performance of the ATLAS detector in proton–proton collision data at $\sqrt{s} = 13\,\text{TeV}$". In: *Eur. Phys. J. C* 76 (2016), p. 292. DOI: 10.1140/epjc/s10052-016-4120-y. arXiv: 1603.05598 [hep-ex].

[132] J. Illingworth and J. Kittler. "A survey of the hough transform". In: *Computer Vision, Graphics, and Image Processing* 44.1 (1988), pp. 87–116. ISSN: 0734-189X. DOI: https://doi.org/10.1016/S0734-189X(88)80033-1. URL: https://www.sciencedirect.com/science/article/pii/S0734189X88800331.

[133] ATLAS Collaboration. "Search for high-mass dilepton resonances in pp collisions at $\sqrt{s} = 8\,\text{TeV}$ with the ATLAS detector". In: *Phys. Rev. D* 90 (2014), p. 052005. DOI: 10.1103/PhysRevD.90.052005. arXiv: 1405.4123 [hep-ex].

[134] ATLAS Collaboration. "Search for new particles in events with one lepton and missing transverse momentum in pp collisions at $\sqrt{s} = 8\,\text{TeV}$ with the ATLAS detector". In: *JHEP* 09 (2014), p. 037. DOI: 10.1007/JHEP09(2014)037. arXiv: 1407.7494 [hep-ex].

[135] ATLAS Collaboration. "Measurements of Higgs boson production and couplings in the four-lepton channel in pp collisions at center-of-mass energies of 7 and 8 TeV with the ATLAS detector". In: *Phys. Rev. D* 91 (2015), p. 012006. DOI: 10.1103/PhysRevD.91.012006. arXiv: 1408.5191 [hep-ex].

[136] ATLAS Collaboration. "Muon reconstruction and identification efficiency in ATLAS using the full Run 2 pp collision data set at $\sqrt{s} = 13$ TeV". In: *Eur. Phys. J. C* 81 (2021), p. 578. DOI: 10.1140/epjc/s10052-021-09233-2. arXiv: 2012.00578 [hep-ex].

[137] ATLAS Collaboration. *The ATLAS Computing Model*. Tech. rep. ATL-SOFT-2004-007. Geneva: CERN, Dec. 2004. DOI: 10.5170/CERN-2005-002.1007. URL: https://cds.cern.ch/record/811058.

[138] ATLAS Collaboration. *The ATLAS Collaboration Software and Firmware*. ATL-SOFT-PUB-2021-001. 2021. URL: https://cds.cern.ch/record/2767187.

[139] Marco Clemencic et al. "Recent developments in the LHCb software framework Gaudi". In: *J. Phys. Conf. Ser.* 219 (2010). Ed. by Jan Gruntorad and Milos Lokajicek, p. 042006. DOI: 10.1088/1742-6596/219/4/042006.

[140] I. Antcheva et al. "ROOT: A C++ framework for petabyte data storage, statistical analysis and visualization". In: *Comput. Phys. Commun.* 180 (2009), pp. 2499–2512. DOI: 10.1016/j.cpc.2009.08.005. arXiv: 1508.07749 [physics.data-an].

[141] Torbjorn Sjostrand, Stephen Mrenna and Peter Z. Skands. "A Brief Introduction to PYTHIA 8.1". In: *Comput. Phys. Commun.* 178 (2008), pp. 852–867. DOI: 10.1016/j.cpc.2008.01.036. arXiv: 0710.3820 [hep-ph].

[142] Törbjorn Sjöstrand, Stephen Mrenna and Peter Z. Skands. "PYTHIA 6.4 physics and manual". In: *JHEP* 05 (2006), p. 026. DOI: 10.1088/1126-6708/2006/05/026. arXiv: hep-ph/0603175.

[143] T. Gleisberg et al. "Event generation with SHERPA 1.1". In: *JHEP* 02 (2009), p. 007. DOI: 10.1088/1126-6708/2009/02/007. arXiv: 0811.4622 [hep-ph].

[144] S. Agostinelli et al. "GEANT4: a simulation toolkit". In: *Nucl. Instrum. Meth. A* 506 (2003), pp. 250–303. DOI: 10.1016/S0168-9002(03)01368-8.

[145] ATLAS Collaboration. "The ATLAS Simulation Infrastructure". In: *Eur. Phys. J. C* 70 (2010), p. 823. DOI: 10.1140/epjc/s10052-010-1429-9. arXiv: 1005.4568 [physics.ins-det].

[146] W. Lukas. "Fast Simulation for ATLAS: Atlfast-II and ISF". In: *J. Phys. Conf. Ser.* 396 (2012). Ed. by Michael Ernst et al., p. 022031. DOI: 10.1088/1742-6596/396/2/022031.

[147] ATLAS Collaboration. "Measurement of inclusive jet and dijet production in pp collisions at $\sqrt{s} = 7\,\text{TeV}$ using the ATLAS detector". In: *Phys. Rev. D* 86 (2012), p. 014022. DOI: 10.1103/PhysRevD.86.014022. arXiv: 1112.6297 [hep-ex].

[148] ATLAS Collaboration. "Measurement of inclusive jet and dijet cross-sections in proton–proton collisions at $\sqrt{s} = 13\,\text{TeV}$ with the ATLAS detector". In: *JHEP* 05 (2018), p. 195. DOI: 10.1007/JHEP05(2018)195. arXiv: 1711.02692 [hep-ex].

[149] Jonathan M. Butterworth et al. "Jet substructure as a new Higgs search channel at the LHC". In: *Phys. Rev. Lett.* 100 (2008), p. 242001. arXiv: 0802.2470 [hep-ph].

[150] ATLAS Collaboration. "A search for high-mass resonances decaying to $\tau^+\tau^-$ in pp collisions at $\sqrt{s} = 7\,\text{TeV}$ with the ATLAS detector". In: *Phys. Lett. B* 719 (2013), p. 242. DOI: 10.1016/j.physletb.2013.01.040. arXiv: 1210.6604 [hep-ex].

[151] ATLAS Collaboration. "A search for high-mass resonances decaying to $\tau^+\tau^-$ in pp collisions at $\sqrt{s} = 8\,\text{TeV}$ with the ATLAS detector". In: *JHEP* 07 (2015), p. 157. DOI: 10.1007/JHEP07(2015)157. arXiv: 1502.07177 [hep-ex].

[152] ATLAS Collaboration. "Search for high-mass diboson resonances with boson-tagged jets in proton–proton collisions at $\sqrt{s} = 8\,\text{TeV}$ with the ATLAS detector". In: *JHEP* 12 (2015), p. 055. DOI: 10.1007/JHEP12(2015)055. arXiv: 1506.00962 [hep-ex].

[153] ATLAS Collaboration. "Search for diboson resonances with boson-tagged jets in pp collisions at $\sqrt{s} = 13\,\text{TeV}$ with the ATLAS detector". In: *Phys. Lett. B* 777 (2018), p. 91. DOI: 10.1016/j.physletb.2017.12.011. arXiv: 1708.04445 [hep-ex].

[154] ATLAS Collaboration. "Search for a high-mass Higgs boson decaying to a W boson pair in pp collisions at $\sqrt{s} = 8\,\text{TeV}$ with the ATLAS detector". In: *JHEP* 01 (2016), p. 032. DOI: 10.1007/JHEP01(2016)032. arXiv: 1509.00389 [hep-ex].

[155] ATLAS Collaboration. "Search for anomalous electroweak production of WW/WZ in association with a high-mass dijet system in pp collisions at $\sqrt{s} = 8\,\text{TeV}$ with the ATLAS detector". In: *Phys. Rev. D* 95 (2017), p. 032001. DOI: 10.1103/PhysRevD.95.032001. arXiv: 1609.05122 [hep-ex].

[156] ATLAS Collaboration. "Search for the electroweak diboson production in association with a high-mass dijet system in semileptonic final states in pp collisions at $\sqrt{s} = 13\,\text{TeV}$ with the ATLAS detector". In: *Phys. Rev. D* 100 (2019), p. 032007. DOI: 10.1103/PhysRevD.100.032007. arXiv: 1905.07714 [hep-ex].

[157] ATLAS Collaboration. *Observation of leading ϕ-mesons in high p_T jets with the ATLAS detector at $\sqrt{s} = 7$ TeV*. ATLAS-CONF-2011-146. 2011. URL: https://cds.cern.ch/record/1390495.

[158] ATLAS Collaboration. "The differential production cross section of the $\phi(1020)$ meson in $\sqrt{s} = 7\,\text{TeV}$ pp collisions measured with the ATLAS detector". In: *Eur. Phys. J. C* 74 (2014), p. 2895. DOI: 10.1140/epjc/s10052-014-2895-2. arXiv: 1402.6162 [hep-ex].

[159] ATLAS Collaboration. "Time-dependent angular analysis of the decay $B_s^0 \to J/\psi\phi$ and extraction of $\Delta\Gamma_s$ and the CP-violating weak phase ϕ_s by ATLAS". In: *JHEP* 12 (2012), p. 072. DOI: 10.1007/JHEP12(2012)072. arXiv: 1208.0572 [hep-ex].

[160] ATLAS Collaboration. *Observation of the B_d^0 and B_s^0 mesons in the decays $B_d^0 \to J/\psi K^{*0}$ and $B_s \to J/\psi\phi$ in ATLAS*. ATLAS-CONF-2011-050. 2011. URL: https://cds.cern.ch/record/1341815.

[161] ATLAS Collaboration. *Measurement of the B_d^0 and B_s^0 lifetimes in the decay modes $B_d^0 \to J/\psi K^{*0}$ and $B_s^0 \to J/\psi\phi$ in ATLAS*. ATLAS-CONF-2011-092. 2011. URL: https://cds.cern.ch/record/1363779.

[162] ATLAS Collaboration. *Flavour tagged time dependent angular analysis of the $B_s^0 \to J/\psi\phi$ decay and extraction of $\Delta\Gamma_s$ and the weak phase ϕ_s in ATLAS*. ATLAS-CONF-2013-039. 2013. URL: https://cds.cern.ch/record/1541823.

[163] ATLAS Collaboration. "Flavour tagged time-dependent angular analysis of the $B_s^0 \to J/\psi\phi$ decay and extraction of $\Delta\Gamma_s$ and the weak phase ϕ_s in ATLAS". In: *Phys. Rev. D* 90 (2014), p. 052007. DOI: 10.1103/PhysRevD.90.052007. arXiv: 1407.1796 [hep-ex].

[164] ATLAS Collaboration. "Measurement of the CP-violating phase ϕ_s and the B_s^0 meson decay width difference with $B_s^0 \to J/\psi\phi$ decays in ATLAS". In: *JHEP* 08 (2016), p. 147. DOI: 10.1007/JHEP08(2016)147. arXiv: 1601.03297 [hep-ex].

[165] ATLAS Collaboration. "Measurement of the CP-violating phase ϕ_s in $B_s^0 \to J/\psi\phi$ decays in ATLAS at 13 TeV". In: *Eur. Phys. J. C* 81 (2020), p. 342. DOI: 10.1140/epjc/s10052-021-09011-0. arXiv: 2001.07115 [hep-ex].

[166] ATLAS Collaboration. "Jet energy resolution in proton–proton collisions at $\sqrt{s} =$ 7 TeV recorded in 2010 with the ATLAS detector". In: *Eur. Phys. J. C* 73 (2013), p. 2306. DOI: 10.1140/epjc/s10052-013-2306-0. arXiv: 1210.6210 [hep-ex].

[167] ATLAS Collaboration. "Jet mass and substructure of inclusive jets in $\sqrt{s} = 7$ TeV pp collisions with the ATLAS experiment". In: *JHEP* 05 (2012), p. 128. DOI: 10.1007/JHEP05(2012)128. arXiv: 1203.4606 [hep-ex].

[168] ATLAS Collaboration. "Jet energy measurement and its systematic uncertainty in proton–proton collisions at $\sqrt{s} = 7$ TeV with the ATLAS detector". In: *Eur. Phys. J. C* 75 (2015), p. 17. DOI: 10.1140/epjc/s10052-014-3190-y. arXiv: 1406.0076 [hep-ex].

[169] ATLAS Collaboration. "Identification of boosted, hadronically decaying W bosons and comparisons with ATLAS data taken at $\sqrt{s} = 8$ TeV". In: *Eur. Phys. J. C* 76 (2016), p. 154. DOI: 10.1140/epjc/s10052-016-3978-z. arXiv: 1510.05821 [hep-ex].

[170] ATLAS Collaboration. "Performance of jet substructure techniques for large-R jets in proton–proton collisions at $\sqrt{s} = 7$ TeV using the ATLAS detector". In:

JHEP 09 (2013), p. 076. DOI: 10.1007/JHEP09(2013)076. arXiv: 1306.4945 [hep-ex].

[171] ATLAS Collaboration. "Measurement of the cross-section of high transverse momentum vector bosons reconstructed as single jets and studies of jet substructure in pp collisions at $\sqrt{s} = 7\,\text{TeV}$ with the ATLAS detector". In: *New J. Phys.* 16 (2014), p. 113013. DOI: 10.1088/1367-2630/16/11/113013. arXiv: 1407.0800 [hep-ex].

[172] ATLAS Collaboration. "Measurement of jet-substructure observables in top quark, W boson and light jet production in proton–proton collisions at $\sqrt{s} = 13\,\text{TeV}$ with the ATLAS detector". In: *JHEP* 08 (2019), p. 033. DOI: 10.1007/JHEP08(2019)033. arXiv: 1903.02942 [hep-ex].

[173] ATLAS Collaboration. "Light-quark and gluon jet discrimination in pp collisions at $\sqrt{s} = 7\,\text{TeV}$ with the ATLAS detector". In: *Eur. Phys. J. C* 74 (2014), p. 3023. DOI: 10.1140/epjc/s10052-014-3023-z. arXiv: 1405.6583 [hep-ex].

[174] ATLAS Collaboration. *Discrimination between Light Quark and Gluon Jets in pp collisions at $\sqrt{s} = 8$ TeV with the ATLAS Detector*. ATLAS-CONF-2016-034. 2016. URL: https://cds.cern.ch/record/2200202.

[175] ATLAS Collaboration. *Quark versus Gluon Jet Tagging Using Charged-Particle Constituent Multiplicity with the ATLAS Detector*. ATL-PHYS-PUB-2017-009. 2017. URL: https://cds.cern.ch/record/2263679.

[176] ATLAS Collaboration. "A new method to distinguish hadronically decaying boosted Z bosons from W bosons using the ATLAS detector". In: *Eur. Phys. J. C* 76 (2016), p. 238. DOI: 10.1140/epjc/s10052-016-4065-1. arXiv: 1509.04939 [hep-ex].

[177] ATLAS Collaboration. "ATLAS b-jet identification performance and efficiency measurement with $t\bar{t}$ events in pp collisions at $\sqrt{s} = 13\,\text{TeV}$". In: *Eur. Phys. J. C* 79 (2019), p. 970. DOI: 10.1140/epjc/s10052-019-7450-8. arXiv: 1907.05120 [hep-ex].

[178] ATLAS Collaboration. "Performance of b-jet identification in the ATLAS experiment". In: *JINST* 11 (2016), P04008. DOI: 10.1088/1748-0221/11/04/P04008. arXiv: 1512.01094 [hep-ex].

[179] ATLAS Collaboration. *b-tagging in dense environments*. ATL-PHYS-PUB-2014-014. 2014. URL: https://cds.cern.ch/record/1750682.

[180] ATLAS Collaboration. *Calibration of ATLAS b-tagging algorithms in dense jet environments*. ATLAS-CONF-2016-001. 2015. URL: https://cds.cern.ch/record/2127958.

[181] ATLAS Collaboration. "Identification and energy calibration of hadronically decaying tau leptons with the ATLAS experiment in pp collisions at $\sqrt{s} = 8\,\text{TeV}$". In: *Eur. Phys. J. C* 75 (2015), p. 303. DOI: 10.1140/epjc/s10052-015-3500-z. arXiv: 1412.7086 [hep-ex].

[182] ATLAS Collaboration. "Reconstruction of hadronic decay products of tau leptons with the ATLAS experiment". In: *Eur. Phys. J. C* 76 (2016), p. 295. DOI: 10.1140/epjc/s10052-016-4110-0. arXiv: 1512.05955 [hep-ex].

[183] ATLAS Collaboration. "A neural network clustering algorithm for the ATLAS silicon pixel detector". In: *JINST* 9 (2014), P09009. DOI: 10.1088/1748-0221/9/09/P09009. arXiv: 1406.7690 [hep-ex].

[184] ATLAS Collaboration. *The Optimization of ATLAS Track Reconstruction in Dense Environments*. ATL-PHYS-PUB-2015-006. 2015. URL: https://cds.cern.ch/record/2002609.

[185] ATLAS Collaboration. "Performance of the ATLAS track reconstruction algorithms in dense environments in LHC Run 2". In: *Eur. Phys. J. C* 77 (2017), p. 673. DOI: 10.1140/epjc/s10052-017-5225-7. arXiv: 1704.07983 [hep-ex].

[186] ATLAS Collaboration. *Measurement of performance of the pixel neural network clustering algorithm of the ATLAS experiment at* $\sqrt{s} = 13$ *TeV*. ATL-PHYS-PUB-2015-044. 2015. URL: https://cds.cern.ch/record/2054921.

[187] ATLAS Collaboration. *Measurement of track reconstruction inefficiencies in the core of jets via pixel dE/dx with the ATLAS experiment using* $\sqrt{s} = 13$ *TeV pp*

collision data. ATL-PHYS-PUB-2016-007. 2016. URL: https://cds.cern.ch/record/2140460.

[188] ATLAS Collaboration. *Modelling of Track Reconstruction Inside Jets with the 2016 ATLAS* $\sqrt{s} = 13$ *TeV pp Dataset*. ATL-PHYS-PUB-2017-016. 2017. URL: https://cds.cern.ch/record/2275639.

[189] ATLAS Collaboration. *Training and validation of the ATLAS pixel clustering neural networks*. ATL-PHYS-PUB-2018-002. 2018. URL: https://cds.cern.ch/record/2309474.

[190] G. Avoni et al. "The new LUCID-2 detector for luminosity measurement and monitoring in ATLAS". In: *JINST* 13.07 (2018), P07017. DOI: 10.1088/1748-0221/13/07/P07017.

[191] ATLAS Collaboration. "Luminosity determination in pp collisions at $\sqrt{s} = 8$ TeV using the ATLAS detector at the LHC". In: *Eur. Phys. J. C* 76 (2016), p. 653. DOI: 10.1140/epjc/s10052-016-4466-1. arXiv: 1608.03953 [hep-ex].

[192] ATLAS Collaboration. *Luminosity determination in pp collisions at* $\sqrt{s} = 13$ *TeV using the ATLAS detector at the LHC*. ATLAS-CONF-2019-021. 2019. URL: https://cds.cern.ch/record/2677054.

[193] "Muon reconstruction performance of the ATLAS detector in proton–proton collision data at $\sqrt{s}$ =13 TeV". In: *Eur. Phys. J.* C76.5 (2016), p. 292. DOI: 10.1140/epjc/s10052-016-4120-y. arXiv: 1603.05598 [hep-ex].

[194] ATLAS Collaboration. "ATLAS Pythia8 tunes to 7 TeV data". In: ATL-PHYS-PUB-2014-021 (Nov. 2014). URL: https://cds.cern.ch/record/1966419.

[195] J. Pumplin et al. "New Generation of Parton Distributions with Uncertainties from Global QCD Analysis". In: *JHEP* 07 (2002), p. 012. DOI: 10.1088/1126-6708/2002/07/012. arXiv: hep-ph/0201195.

[196] ATLAS Collaboration. "Electron and photon performance measurements with the ATLAS detector using the 2015–2017 LHC proton-proton collision data". In: *JINST* 14.12 (2019), P12006. DOI: 10.1088/1748-0221/14/12/P12006. arXiv: 1908.00005 [hep-ex].

[197] V. Kostyukhin. *VKalVrt - package for vertex reconstruction in ATLAS*. ATL-PHYS-2003-031. CERN, Aug. 2003. URL: https://cds.cern.ch/record/685551.

[198] ATLAS Collaboration. "Muon reconstruction and identification efficiency in ATLAS using the full Run 2 *pp* collision data set at $\sqrt{s} = 13$ TeV". In: *Eur. Phys. J. C* 81.7 (2021), p. 578. DOI: 10.1140/epjc/s10052-021-09233-2. arXiv: 2012.00578 [hep-ex].

[199] Paolo Nason. "A new method for combining NLO QCD with shower Monte Carlo algorithms". In: *JHEP* 11 (2004), p. 040. DOI: 10.1088/1126-6708/2004/11/040. arXiv: hep-ph/0409146.

[200] Stefano Frixione, Paolo Nason and Carlo Oleari. "Matching NLO QCD computations with parton shower simulations: the POWHEG method". In: *JHEP* 11 (2007), p. 070. DOI: 10.1088/1126-6708/2007/11/070. arXiv: 0709.2092 [hep-ph].

[201] Simone Alioli et al. "A general framework for implementing NLO calculations in shower Monte Carlo programs: the POWHEG BOX". In: *JHEP* 06 (2010), p. 043. DOI: 10.1007/JHEP06(2010)043. arXiv: 1002.2581 [hep-ph].

[202] Simone Alioli et al. "NLO Higgs boson production via gluon fusion matched with shower in POWHEG". In: *JHEP* 04 (2009), p. 002. DOI: 10.1088/1126-6708/2009/04/002. arXiv: 0812.0578 [hep-ph].

[203] Paolo Nason and Carlo Oleari. "NLO Higgs boson production via vector-boson fusion matched with shower in POWHEG". In: *JHEP* 02 (2010), p. 037. DOI: 10.1007/JHEP02(2010)037. arXiv: 0911.5299 [hep-ph].

[204] ATLAS Collaboration. "Measurement of the Z/γ^* boson transverse momentum distribution in *pp* collisions at $\sqrt{s} = 7$ TeV with the ATLAS detector". In: *JHEP* 09 (2014), p. 145. DOI: 10.1007/JHEP09(2014)145. arXiv: 1406.3660 [hep-ex].

[205] NNPDF Collaboration. "Parton distributions with LHC data". In: *Nucl. Phys. B* 867 (2013), pp. 244–289. DOI: 10.1016/j.nuclphysb.2012.10.003. arXiv: 1207.1303 [hep-ph].

[206] J. Alwall et al. "The automated computation of tree-level and next-to-leading order differential cross sections, and their matching to parton shower simulations". In: *JHEP* 07 (2014), p. 079. DOI: 10.1007/JHEP07(2014)079. arXiv: 1405.0301 [hep-ph].

[207] Charalampos Anastasiou et al. "Higgs Boson Gluon-Fusion Production in QCD at Three Loops". In: *Phys. Rev. Lett.* 114 (2015), p. 212001. DOI: 10.1103/PhysRevLett.114.212001. arXiv: 1503.06056 [hep-ph].

[208] Charalampos Anastasiou et al. "High precision determination of the gluon fusion Higgs boson cross-section at the LHC". In: *JHEP* 05 (2016), p. 058. DOI: 10.1007/JHEP05(2016)058. arXiv: 1602.00695 [hep-ph].

[209] Stefano Actis et al. "NLO electroweak corrections to Higgs boson production at hadron colliders". In: *Phys. Lett. B* 670 (2008), pp. 12–17. DOI: 10.1016/j.physletb.2008.10.018. arXiv: 0809.1301 [hep-ph].

[210] Charalampos Anastasiou, Radja Boughezal and Frank Petriello. "Mixed QCD-electroweak corrections to Higgs boson production in gluon fusion". In: *JHEP* 04 (2009), p. 003. DOI: 10.1088/1126-6708/2009/04/003. arXiv: 0811.3458 [hep-ph].

[211] M. Ciccolini, A. Denner and S. Dittmaier. "Strong and Electroweak Corrections to the Production of a Higgs Boson + 2 Jets via Weak Interactions at the Large Hadron Collider". In: *Phys. Rev. Lett.* 99 (2007), p. 161803. DOI: 10.1103/PhysRevLett.99.161803. arXiv: 0707.0381 [hep-ph].

[212] Mariano Ciccolini, Ansgar Denner and Stefan Dittmaier. "Electroweak and QCD corrections to Higgs production via vector-boson fusion at the LHC". In: *Phys. Rev. D* 77 (2008), p. 013002. DOI: 10.1103/PhysRevD.77.013002. arXiv: 0710.4749 [hep-ph].

[213] Paolo Bolzoni et al. "Higgs Boson Production via Vector-Boson Fusion at Next-to-Next-to-Leading Order in QCD". In: *Phys. Rev. Lett.* 105 (2010), p. 011801. DOI: 10.1103/PhysRevLett.105.011801. arXiv: 1003.4451 [hep-ph].

[214] Oliver Brein, Abdelhak Djouadi and Robert Harlander. "NNLO QCD corrections to the Higgs-strahlung processes at hadron colliders". In: *Phys. Lett. B* 579 (2004), pp. 149–156. DOI: 10.1016/j.physletb.2003.10.112. arXiv: hep-ph/0307206 [hep-ph].

[215] Ansgar Denner et al. "Electroweak corrections to Higgs-strahlung off W/Z bosons at the Tevatron and the LHC with HAWK". In: *JHEP* 03 (2012), p. 075. DOI: 10.1007/JHEP03(2012)075. arXiv: 1112.5142 [hep-ph].

[216] Lukas Altenkamp et al. "Gluon-induced Higgs-strahlung at next-to-leading order QCD". In: *JHEP* 02 (2013), p. 078. DOI: 10.1007/JHEP02(2013)078. arXiv: 1211.5015 [hep-ph].

[217] R. Kutschke. *An Angular Distribution Cookbook*. home.fnal.gov/~kutschke/Angdist/angdist.ps. [Online; accessed 16-September-2020]. 1996.

[218] Pietro Faccioli and Carlos Lourenço. *Particle Polarization in High Energy Physics*. Springer Cham, 2022. DOI: 10.1007/978-3-031-08876-6. URL: https://link.springer.com/book/10.1007/978-3-031-08876-6.

[219] ATLAS Collaboration. "The Pythia 8 A3 tune description of ATLAS minimum bias and inelastic measurements incorporating the Donnachie-Landshoff diffractive model". In: (Aug. 2016). URL: https://cds.cern.ch/record/2206965.

[220] Jon Butterworth et al. "PDF4LHC recommendations for LHC Run II". In: *J. Phys. G* 43 (2016), p. 023001. DOI: 10.1088/0954-3899/43/2/023001. arXiv: 1510.03865 [hep-ph].

[221] ATLAS Collaboration. "Measurement of the transverse momentum distribution of Drell–Yan lepton pairs in proton–proton collisions at $\sqrt{s} = 13\,\text{TeV}$ with the ATLAS detector". In: *Eur. Phys. J. C* 80 (2020), p. 616. DOI: 10.1140/epjc/s10052-020-8001-z. arXiv: 1912.02844 [hep-ex].

[222] ATLAS Collaboration. "Performance of electron and photon triggers in ATLAS during LHC Run 2". In: *Eur. Phys. J. C* 80 (2020), p. 47. DOI: 10.1140/epjc/s10052-019-7500-2. arXiv: 1909.00761 [hep-ex].

[223] ATLAS Collaboration. "Performance of the ATLAS muon triggers in Run 2". In: *JINST* 15 (2020), P09015. DOI: 10.1088/1748-0221/15/09/p09015. arXiv: 2004.13447 [hep-ex].

[224] ATLAS Collaboration. "Performance of the Electron and Photon Trigger in p-p Collisions at $\sqrt{s} = 7$ TeV with the ATLAS Detector at the LHC". In: *ATLAS-CONF-2011-114* ATLAS-CONF-2011-114 (Aug. 2011). URL: http://cds.cern.ch/record/1375551.

[225] ATLAS Collaboration. "Measurement of the photon identification efficiencies with the ATLAS detector using LHC Run-1 data". In: *Eur. Phys. J. C* 76.12 (2016), p. 666. DOI: 10.1140/epjc/s10052-016-4507-9. arXiv: 1606.01813 [hep-ex].

[226] ATLAS Collaboration. *Photon identification in 2015 ATLAS data*. ATL-PHYS-PUB-2016-014. Geneva: CERN, Aug. 2016. URL: https://cds.cern.ch/record/2203125.

[227] ATLAS Collaboration. "Electron and photon energy calibration with the ATLAS detector using LHC Run 1 data". In: *Eur. Phys. J. C* 74.10 (2014), p. 3071. DOI: 10.1140/epjc/s10052-014-3071-4. arXiv: 1407.5063 [hep-ex].

[228] ATLAS Collaboration. *Electron and photon energy calibration with the ATLAS detector using data collected in 2015 at* $\sqrt{s}$ *=13 TeV*. ATL-PHYS-PUB-2016-015. Geneva: CERN, Aug. 2016. URL: https://cds.cern.ch/record/2203514.

[229] A. Chisholm et al. "Non-Parametric Data-Driven Background Modelling using Conditional Probabilities". In: (Dec. 2021). arXiv: 2112.00650 [hep-ex].

[230] Max Baak et al. "Interpolation between multi-dimensional histograms using a new non-linear moment morphing method". In: (2014). DOI: 10.1016/j.nima.2014.10.033. arXiv: 1410.7388 [physics.data-an].

[231] Alexander L. Read. "Presentation of search results: the CL_s technique". In: *J. Phys. G* 28 (2002), pp. 2693–2704. DOI: 10.1088/0954-3899/28/10/313.

[232] Glen Cowan et al. "Asymptotic formulae for likelihood-based tests of new physics". In: *EPJC* 71 (2011), p. 1554. DOI: 10.1140/epjc/s10052-011-1554-0. arXiv:

1007.1727 [physics.data-an]. Erratum: in: *EPJC* 73 (2013), p. 2501. DOI: 10.1140/epjc/s10052-013-2501-z.

[233] ATLAS Collaboration. "Measurement of the properties of Higgs boson production at $\sqrt{s}$=13 TeV in the $H \to \gamma\gamma$ channel using 139 fb^{-1} of pp collision data with the ATLAS experiment". In: (Aug. 2020). URL: https://cds.cern.ch/record/2725727.

[234] ATLAS Collaboration. "Combined measurements of Higgs boson production and decay using up to 80 fb^{-1} of proton–proton collision data at $\sqrt{s} = 13$ TeV collected with the ATLAS experiment". In: *Phys. Rev. D* 101 (2020), p. 012002. DOI: 10.1103/PhysRevD.101.012002. arXiv: 1909.02845 [hep-ex].

[235] CMS Collaboration. "Combined measurements of Higgs boson couplings in proton–proton collisions at $\sqrt{s} = 13$ TeV". In: *Eur. Phys. J. C* 79 (2019), p. 421. DOI: 10.1140/epjc/s10052-019-6909-y. arXiv: 1809.10733 [hep-ex].

[236] Nina M. Coyle, Carlos E. M. Wagner and Viska Wei. "Bounding the charm Yukawa coupling". In: *Phys. Rev. D* 100.7 (2019), p. 073013. DOI: 10.1103/PhysRevD.100.073013. arXiv: 1905.09360 [hep-ph].